A Quantum Light Source for Quantum Information Applications in the Telecom *C*-Band

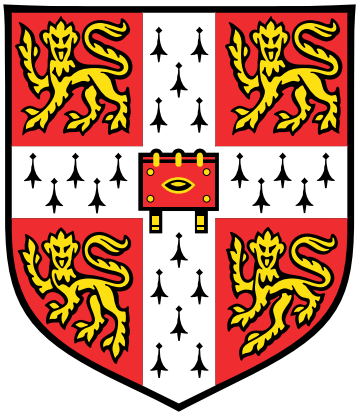

Matthew Anderson

Department of Physics
University of Cambridge

This dissertation is submitted for the degree of
Doctor of Philosophy

Darwin College

November 2020

Declaration

I hereby declare that except where specific reference is made to the work of others, the contents of this dissertation are original and have not been submitted in whole or in part for consideration for any other degree or qualification in this, or any other university. This dissertation is my own work and contains nothing which is the outcome of work done in collaboration with others, except as specified in the text and Acknowledgements. This dissertation contains fewer than 60,000 words including appendices, bibliography, footnotes, tables and equations and has fewer than 150 figures.

Matthew Anderson
November 2020

A Quantum Light Source for Quantum Information Applications in the Telecom *C*-Band

Matthew Anderson

Abstract

Semiconductor quantum dot (QD) quantum light sources have long been established as suitable candidates for many quantum information applications, due to the on-demand emission of highly pure and highly indistinguishable single and entangled photons. A key factor in the development of this technology is the operation over the standard telecommunication optical fibre network infrastructure, where the minimum absorption wavelength window is centred on the telecom *C*-band (1530 – 1565 nm).

Initial experiments in this work demonstrated single-photon emission of a QD light source emitting directly in the telecom C-band, under both continuous wave (CW) and 1-GHz pulsed excitation regimes. The QDs were further characterised in terms of fine-structure splitting (FSS) and coherence time, in order to determine their suitability for quantum entanglement and interference-based applications.

Long coherence times were observed in the majority of the QDs considered, allowing the demonstration of Hong-Ou-Mandel-type two-photon interference of subsequently emitted photons under CW excitation. The post-selected interference visibility was found to be limited by only the detector resolution and single-photon purity. A further demonstration of high-visibility interference under the same limitations was then made using QD photons and dissimilar photons from a laser, forming the basis of a fibre-based quantum relay.

Working further towards a quantum relay, polarisation-entangled photon pairs in the telecom *C*-band were then generated using the radiative cascade of the biexciton, where a record high fidelity to the Φ^+ Bell state was observed under both CW and 1-GHz pulsed excitation regimes. While an anomalous effect of the FSS was observed in a majority of the studied QDs, a further characterisation of the FSS in terms of the QD polarisation eigenstates confirmed the emission of entangled photon pairs from such an anomalous-splitting QD.

Finally, the work of this thesis was combined to demonstrate a proof-of-principle quantum relay using a QD light source in the telecom *C*-band. The relay was operated first under CW excitation where polarisation encoded laser input qubits were used and high-fidelity quantum teleportation was observed. In an effort to demonstrate a more technologically relevant application, the quantum relay was subsequently operated at 1 GHz in order to demonstrate the teleportation of initially time-bin encoded laser input qubits. A high mean teleportation fidelity was again observed, demonstrating the potential of this telecom *C*-band QD quantum light source in the future of long-distance quantum information applications.

Acknowledgements

There are many people to whom I owe a great deal.

First and foremost, I would like to thank Dr. Tina Müller of Toshiba Research Europe Ltd (TREL), for her continued support and guidance throughout this work. It has been a pleasure to work with you on the quantum relay project, you have taught me a lot and I have no doubt you will continue to produce many more exciting results.

I would also like to pay a special thanks to Dr. Mark Stevenson, also of TREL, whose depth of knowledge and experience has taught me a great deal and has led to many interesting discussions, while steering our experiments in the right direction.

To my supervisors, Dr. Andrew Shields of TREL and Prof. David Ritchie of the University of Cambridge, I would like to thank you for providing me with this opportunity and the overall support of this research.

I also owe thanks to Dr. Jan Huwer, Dr. Joanna Skiba-Szymanska and Dr. Martin Ward of TREL, for their consistent support and knowledge throughout this project, and for always being ready to provide help.

To my fellow PhD students at Toshiba both past and present, I thank you all for four years of making working in the lab a truly enjoyable experience, and four years of great memories, interesting conversations, and valuable friendships outside of it.

And of course, I would be nowhere without the continued love and support of my family, who have taken me on my word that I actually have been doing something interesting all this time. To Mum and Dad, you have made this possible, and a simple thank you will never be enough.

List of Publications

Parts of this thesis have or will appear in the following publications and conference contributions.

Article

Anderson, M., Muller, T., Skiba-Szymanska, J., Krysa, A.B., Huwer, J., Stevenson, R.M., Heffernan, J., Ritchie, D.A. and Shields, A.J. *Coherence in single photon emission from droplet epitaxy and Stranski-Kranstanow quantum dots in the telecom C-band.* Submitted for publication (2020)

Anderson, M., Muller, T., Skiba-Szymanska, J., Krysa, A.B., Huwer, J., Stevenson, R.M., Heffernan, J., Ritchie, D.A. and Shields, A.J. *Gigahertz-Clocked Teleportation of Time-Bin Qubits with a Quantum Dot in the Telecommunication C Band.* Physical Review Applied, **13**(5) 054052 (2020).

Anderson, M., Muller, T., Huwer, J., Skiba-Szymanska, J., Krysa, A.B., Stevenson, R.M., Heffernan, J., Ritchie, D.A. and Shields, A.J., (2020). *Quantum teleportation using highly coherent emission from telecom C-band quantum dots.* npj Quantum Information, **6**(1) 1-7 (2020).

Muller, T., Skiba-Szymanska, J., Krysa, A.B., Huwer, J., Felle, **Anderson, M.**, M., Stevenson, R.M., Heffernan, J., Ritchie, D.A. and Shields, A.J. *A quantum light-emitting diode for the standard telecom window around 1,550 nm.* Nature communications, **9**(1) 1-6 (2018)

Conference contributions

Anderson, M., Muller, T., Skiba-Szymanska, J., Krysa, A.B., Huwer, J., Stevenson, R.M., Heffernan, J., Ritchie, D.A. and Shields, A.J. *Quantum teleportation using highly coherent emission from telecom C-band quantum dots.* 7th International Workshop on Engineering of Quantum Emitter Properties, Berlin 11-13th December, 2019 (Poster presentation).

Anderson, M., Muller, T., Skiba-Szymanska, J., Krysa, A.B., Huwer, J., Stevenson, R.M., Heffernan, J., Ritchie, D.A. and Shields, A.J. *A quantum light-emitting diode for the standard telecom window around 1,550 nm.* SPIE Photonics West 2019, San Francisco (Conference presentation).

Table of contents

Nomenclature

Acronyms / Abbreviations

(P)BS	(Polarising) Beamsplitter
BSM	Bell-state measurement
C-band	Conventional band (1530-1565 nm)
CHSH	Clauser-Horne-Shimony-Holt
CW	Continuous wave
DE	Droplet-epitaxy
DM	Dichroic mirror
DVA	Digital variable attenuator
EL	Electroluminescence
EOM	Electro-optic modulator
FC	Fibre coupler
FM	Faraday mirror
FS	Fibre stretcher
FSS	Fine-structure splitting
FTS	Fourier-transform spectroscopy
GaAs	Gallium Arsenide
HBT	Hanbury-Brown and Twiss
HOM	Hong-Ou-Mandel
HWP	Half-wave plate

InAs Indium Arsenide

InP Indium Phosphide

LP Linear polariser

MI Michelson interferometer

NA Numerical aperture

O-band Original band (1260-1360 nm)

ODL Optical delay line

(E)PC (Electronic) Polarisation controller

(μ)PL (micro-) Photoluminescence

LED Light-emitting diode

QD Quantum dot

QKD Quantum key distribution

QWP Quarter-wave plate

RSA Rivest–Shamir–Adleman

SK Stranski-Krastanow

SM Single-mode

SNR Signal-to-noise ratio

SNSPD Superconducting nanowire single-photon detector

SPDC Spontaneous Parametric Down Conversion

TG Transmission grating

TPI Two-photon interference

TTTR Time-tagged time-resolved

TU Transcoder unit

(X)X Neutral (bi)exciton

(X)$X^{-/+/*}$ Charged (bi)exciton (with charge (-e, +e or unknown [*])

ZPL Zero-phonon line

Chapter 1

Introduction

Society has seen a rapid increase in integration with information technology over the last decade. What led to the marvel of people being able to connect and share information from all corners of the globe has also led to more pressing issues of data privacy and security. Particularly in recent years, there has been an increasing presence of social media and large information technology corporations which have access to an unprecedented amount of personal data. The large volumes of sensitive information being transferred and stored in remote sites on a daily basis, in addition to the ongoing efforts in fighting the ever advancing sophistication of cybercrime, make the question of security in data communications more relevant now than ever before.

Today, the cryptographic protocols used to ensure the transmission and storage of such data are secure enough to allow peace of mind when it comes to questions of such security. These protocols are typically centred around the exchange of long strings of binary digits (1s and 0s), or bits, which form a key. This key is then used to encrypt and decrypt information to be transmitted. Usually, the sender, Alice, and the receiver, Bob, agree on the key through communication over a private channel. The encrypted information is then sent over a public channel. Currently, if an eavesdropper, Eve, attempts to intercept and glean information they are unable to do so. These schemes are mainly implemented using the RSA protocol [1], which is based around the idea of generating complex private and public keys where the security is guaranteed by the mathematical complexity of the keys generated [2]. In particular, the schemes use the fact that the factorisation of large prime numbers is exponential with the number of digits involved [3], so the strengthening of the security can be done to an arbitrary degree by simply increasing the length of the key.

However, as technology moves forward, the invention of the quantum computer [4] has the potential to invalidate such protocols. The application of quantum mechanics to the factorisation of large numbers resulted in the development of the famous Shor's algorithm [5] in 1994, which demonstrated that a quantum computer would be able to break such classical security protocols in polynomial time [6]. By utilising the encoding of physical information onto a quantum state, problems such as the factorisation of prime numbers can be solved with an exponential speed up in

computation time. Whilst such technology is still in very early development, it has highlighted the need for truly guaranteed security.

1.1 Quantum Information

Quantum information is the representation of physical information using quantum systems that obey the laws of quantum mechanics. This allows for quantum information processing which, much like classical information processing, can be used in order to complete computational tasks [5, 7, 8], cryptographic protocols [9], or secure data transmission [10]. However, there are a few central features of a quantum information that are crucially different. The first is the fact that an arbitrary unknown quantum state cannot be cloned, the so-called No-Cloning Theorem [11], which has many implications in quantum computing and cryptography. The second, is that quantum mechanics is typically formulated as a probabilistic theory under the Copenhagen interpretation. As such, the most likely outcome of a measurement is described by a probability distribution. Lastly, information is encoded in a more complex way in quantum states, using the principle of superposition explained below. Using these features of quantum information to perform such tasks is what allows the superior performance to that of the classical counterpart.

1.1.1 Qubits

A large part of the advantage of using quantum states is the way in which information can be encoded. A classical system made up of bits, or states corresponding to 'on' $|1\rangle$ and 'off' $|0\rangle$ means that information can only be encoded in one state or the other. In the framework of quantum information, photons are often used for transmitting data and classical bits can be represented by two orthogonal polarisations of light, such as $|H\rangle$ and $|V\rangle$ corresponding the horizontal and vertical linear polarisations.

A quantum bit or 'qubit' however has a key difference. It can not only represent a $|H\rangle$ or a $|V\rangle$, but instead a whole two-dimensional space in which the bit exists in a superposition of these states. This principle of superposition is a fundamental property of a quantum state. In general, such a quantum state can be expressed as

$$|\psi\rangle = \alpha\,|H\rangle + \beta\,|V\rangle\,; |\alpha|^2 + |\beta|^2 = 1, \tag{1.1}$$

where α and β can be any complex number and $|\alpha|^2$,$|\beta|^2$ are the probability amplitudes for the photon being in a given state. This form of the qubit is suitably normalised such that it can be conveniently represented as a vector mapping out a sphere in two-dimensional space, the so-called Bloch sphere for a general two-level quantum state or Poincaré sphere in the case of polarisation of light, as depicted in Figure 1.1. In this representation the qubit can be parametrised in terms of polar and azimuthal angles describing the position on the surface of the sphere.

$$|\psi\rangle = \cos\frac{\theta}{2}\,|H\rangle + e^{i\phi}\sin\frac{\theta}{2}\,|V\rangle\,. \tag{1.2}$$

For specific angles on the Poincaré sphere corresponding to the equatorial poles, the following states can further be defined

$$|D/A\rangle = \frac{1}{\sqrt{2}}(|H\rangle \pm |V\rangle) \quad |R/L\rangle = \frac{1}{\sqrt{2}}(|H\rangle \pm i|V\rangle), \tag{1.3}$$

which are the diagonal/anti-diagonal linear and right/left circular polarisations, respectively. Thus, in general, transformations performed on the photon correspond to rotations of the quantum state on the Poincaré sphere.

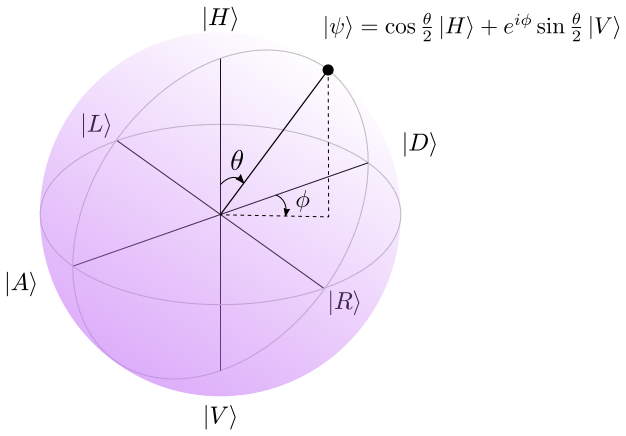

Figure 1.1: Poincaré sphere representation of a qubit. Vector states corresponding to qubits are points on the surface of the sphere. Points sitting at the poles of the sphere represent the orthogonal basis states. Any arbitrary state can be made from a linear combination of these.

By considering the case for multiple qubits, such as a register size of N=2, the real power of quantum computing can be seen. An arbitrary superposition with all basis combinations results in the state

$$|\psi\rangle = \alpha|HH\rangle + \beta|HV\rangle + \gamma|VH\rangle + \delta|VV\rangle, \tag{1.4}$$

where now all of the $2^N = 4$ possible combinations can be encoded using the same state, compared to only one of the possible states stored by classical bits. For increasing N, the dimension of the vector space spanned by the qubit grows as 2^N and so each additional qubit added to the register roughly doubles the computational power, allowing a relatively small number of qubits to compete and eventually surpass classical computational power [12]. Additionally, the power of a quantum computer compared to the classical counterpart was shown in the area of quantum simulation by Feynman [4]. The amount of memory resources required for a classical computer in applications such as quantum chemistry and the simulation of molecules also roughly doubles for each additional qubit, rapidly leaving the realms of what can be solved classically [13].

1.1.2 Quantum Entanglement and Teleportation

Revisiting the two-qubit register and considering the creation of a state through the principle of superposition such that

$$|\psi\rangle_{AB} = \frac{1}{\sqrt{2}}\left(|H\rangle_A|H\rangle_B + |V\rangle_A|V\rangle_B\right), \tag{1.5}$$

where the subscripts A and B denote that the photon belongs to subsystems A and B, respectively, demonstrates an interesting feature. That is that this state cannot be factorised into a product of the two system states such that

$$|\psi\rangle_A \otimes |\psi\rangle_B \neq |\psi\rangle_{AB} = \frac{1}{\sqrt{2}}\left(|H\rangle_A|H\rangle_B + |V\rangle_A|V\rangle_B\right). \tag{1.6}$$

Such states are known as *entangled* states. No information about one qubit can be determined without collapsing the wavefunction of the state and revealing information about the second in a perfectly correlated manner, even for arbitrary separations between the subsystems. In particular, the state above is maximally entangled and is one of four so-called Bell-states named after John Bell [14]

$$\begin{aligned} |\Phi^{\pm}\rangle_{AB} &= \frac{1}{\sqrt{2}}\left(|H\rangle_A|H\rangle_B \pm |V\rangle_A|V\rangle_B\right), \\ |\Psi^{\pm}\rangle_{AB} &= \frac{1}{\sqrt{2}}\left(|H\rangle_A|V\rangle_B \pm |V\rangle_A|H\rangle_B\right). \end{aligned} \tag{1.7}$$

The unusual behaviour of such states led Einstein, Podolski and Rosen to conclude that the theory of quantum mechanics was fundamentally incomplete, requiring hidden variables which pre-determine the measurement outcome in order to explain the "spooky action action at a distance" [15]. Later, Bell demonstrated that such theories of hidden variables were not compatible with perfect correlations expected from such states [14]. The Clauser-Horne-Shimony-Holt (CHSH) inequality [16] is one form of a test which has been frequently used to experimentally test Bell's theorem, demonstrating non-classical correlations inexplicable by hidden variables. Indeed, there have been many experimental violations of the Bell test [17–19], including recent demonstrations with much stricter loophole-free conditions [20, 21]

Quantum entanglement together with the No-Cloning Theorem can be used to introduce the basic quantum teleportation protocol. To see how this works, consider the schematic in Figure 1.2. An input qubit $|\psi\rangle_A = \alpha|H\rangle_A + \beta|V\rangle_A$ of system A and one photon of a shared state $|\Phi^+\rangle_{AB} = \frac{1}{\sqrt{2}}(|H\rangle_A|H\rangle_B - |V\rangle_A|V\rangle_B)$ between system A and B interfere on a beamsplitter. The three photon state can now be written as

$$|\psi\rangle_A \otimes |\Phi^+\rangle_{AB} = (\alpha|H\rangle_A + \beta|V\rangle_A) \otimes \frac{1}{\sqrt{2}}(|H\rangle_A|H\rangle_B - |V\rangle_A|V\rangle_B) \tag{1.8}$$

$$\begin{aligned} &= \frac{1}{2}[|\Phi^+\rangle_A(\alpha|H\rangle_B + \beta|V\rangle_B) + |\Phi^-\rangle_A(\alpha|H\rangle_B - \beta|V\rangle_B) \\ &+ |\Psi^+\rangle_A(\alpha|V\rangle_B + \beta|H\rangle_B) + |\Psi^-\rangle_A(\alpha|V\rangle_B - \beta|H\rangle_B)], \end{aligned} \tag{1.9}$$

where in the last line, the states of A have been written in terms of the four Bell states for this basis. When performing a Bell-state measurement (BSM) on the two-photon state at system A, the output photon in system B can then be related to the input photon as

$$\begin{aligned} |\psi\rangle_B^{\Phi^+} &= \sigma_0 |\psi\rangle_A, \\ |\psi\rangle_B^{\Psi^+} &= \sigma_x |\psi\rangle_A, \\ |\psi\rangle_B^{\Psi^-} &= \sigma_y |\psi\rangle_A, \\ |\psi\rangle_B^{\Phi^-} &= \sigma_z |\psi\rangle_A, \end{aligned} \tag{1.10}$$

by the unitary transformations

$$\sigma_0 = \begin{pmatrix} 1 & 0 \\ 0 & 1 \end{pmatrix} \quad \sigma_x = \begin{pmatrix} 0 & 1 \\ 1 & 0 \end{pmatrix} \quad \sigma_y = \begin{pmatrix} 0 & 1 \\ -1 & 0 \end{pmatrix} \quad \sigma_z = \begin{pmatrix} 1 & 0 \\ 0 & -1 \end{pmatrix}. \tag{1.11}$$

It becomes immediately apparent that that measurement after interference at the beamsplitter collapses the wavefunction to the corresponding B state superposition, depending on the measurement made. Upon obtaining information of the measurement made, all that remains to regain the initial state is the corresponding unitary transformation on the output state, which is communicated over a classical channel. With the type of scheme here it is possible to deterministically teleport any input state using a complete BSM, which is able to distinguish all four Bell states. In practice this requires the use of non-linear optics [22], in order to reach unity probability of successful teleportation, which can reduce the efficiency of the scheme through the losses induced by this process. Using only linear optics however, it is possible to unambiguously determine $|\Psi^{\pm}\rangle$ states, reducing the probability of success to 0.5 instead. This type of operation is a fundamental resource in quantum information and allows for complete security in data transmission when used in for communication applications.

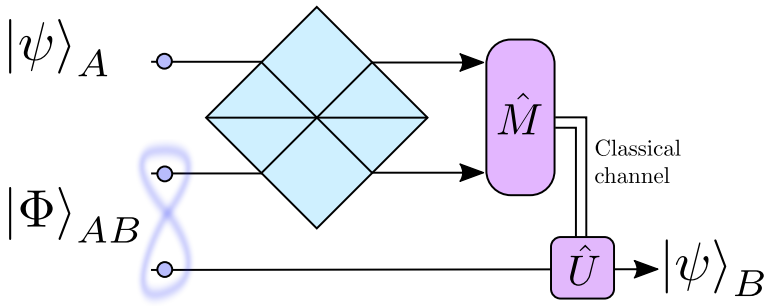

Figure 1.2: General teleportation protocol circuit. Teleportation of a qubit using entangled Bell states. System A prepares an input qubit while system B prepares an entangled Bell state. One photon from system B is interfered with the photon from system A to form a three-photon state. A Bell-state measurement heralds the teleportation of the input qubit, where a subsequent unitary operation can be performed on the photon in system B to recover the exact input state.

1.2 Quantum Cryptography

The use of quantum phenomena to boost the security of information sparked the next generation of cryptographic protocols; quantum cryptography [9]. The most widely implemented and developed scheme in utilising such properties has been in Quantum Key Distribution (QKD). The guarantee that no state can be cloned and the knowledge that measurement of the state of the system disturbs the system is enough to reveal the presence of an eavesdropper on the channel.

1.2.1 Quantum Key Distribution

In QKD, two parties Alice and Bob are able to generate a secret shared key over a public quantum communication channel, which can subsequently be used to encrypt and decrypt information sent over a classical communication channel.

The first protocol, proposed in 1984 by Bennet and Brassard [23] and termed BB84, implements this idea by using a pair of conjugate polarisation bases of light. As illustrated in Figure 1.3, Alice sends random photons over a public channel in one of four states, for example in $|H\rangle$,$|V\rangle$,$|D\rangle$, and $|A\rangle$ for linear and diagonal polarisation bases. Bob measures these states in the same two bases, but at random as well. Upon completion, they can publicly exchange information regarding the measurement bases they used. This reveals no information, but allows Alice and Bob to discard those bits of information where their bases were not the same.

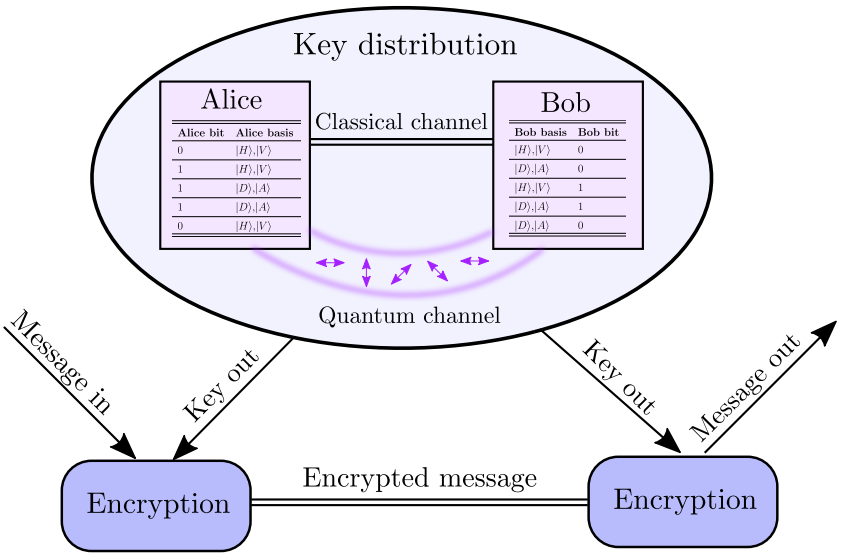

Figure 1.3: BB84 quantum key distribution protocol.

In principle, the data transferred is completely secure, since any attempt to disturb the system and glean information will result in detectable measurement error and so reveal the presence of the attacker, at which point Alice and Bob can simply stop transmitting.

Typical implementation of such protocols uses weak coherent laser pulses [9], which have been shown to be less secure than pure single-photon sources [24]. More recent protocols circumvent this requirement and have been used instead of a true single-photon source with some success, and the benefit of easy experimental implementation [25]. In principle, such operation of weak coherent sources is just as secure as a true single-photon source, but instead sacrifices performance. However, for true security and to be able to extend the transmission range, quantum relays [26] and quantum repeaters [27] must be implemented and the use of a real single-photon source now becomes mandatory [28].

There exist several candidates that offer the possibility for ideal single-photon quantum light sources, such as atoms/ions [29], molecules [30] and Nitrogen-Vacancy centres in diamond [31]. In this thesis, the focus will be on the long-established alternative semiconductor QDs [32] for these quantum information applications.

1.2.2 Long-Distance Fibre Transmission of Qubits

Although the No-Cloning Theorem allows for the operating principles of QKD, since no state can be measured without introducing an error, it also fundamentally limits the distance to which keys can be exchanged due to the fact there can be no signal amplification. For long-haul fibre transmission, the distance can be maximised by operating in the minimum absorption wavelength window of optical fibre, centred on the telecom *C*-band (1530 – 1565 nm), as well as the zero-dispersion window centred on the telecom *O*-band (1260 - 1360 nm). At these wavelengths, the loss is typically 0.2 dB/km and 0.35 dB/km, respectively. When compared to the typical operating wavelength of many single-photon sources around the visible and near infrared, up to around 900 nm, where the loss is typically >1 dB/km, the gain in transmission approaches a factor of ~ 1000 over distances of tens of kilometres, around the size of a metropolitan network, as shown in Figure 1.4.

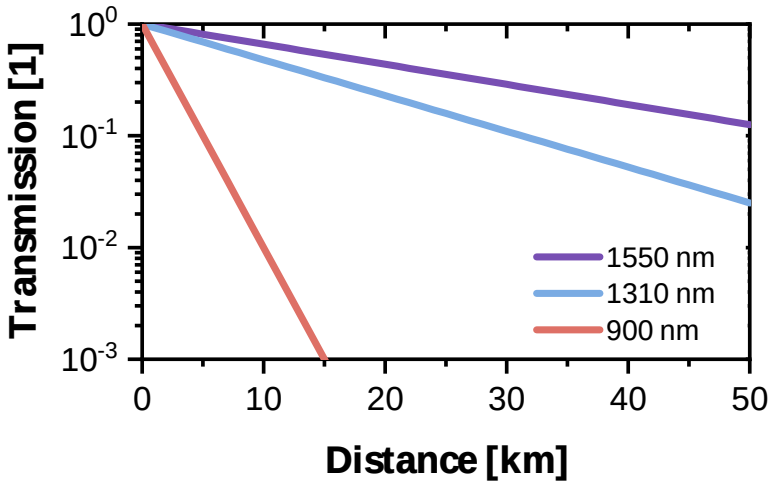

Figure 1.4: Long-distance fibre transmission.

This enables longer distances to be reached due to the lower photon losses suffered in transmission. Additionally, since classical communications operate at these wavelengths, there is the added benefit of an existing fibre infrastructure which can be adopted. Therefore, typical fibre-based QKD systems tend to operate at these wavelengths, motivating the requirement for a quantum light source in this transmission band.

1.2.3 Quantum Relay

The implementation of a large scale quantum network would involve data transmission across large distances and between multiple nodes, where information is processed and redistributed [10]. This would involve the development and implementation of quantum relays and repeaters that allow for data to be swapped across nodes without loss of security. Currently, QKD networks operate with an alternative solution, using so-called "trusted-nodes", as illustrated in Figure 1.5. In such nodes, the keys are decrypted and subsequently re-encrypted using a new quantum state. However, there is an assumption of the security of the node which means that such a scheme is never truly guaranteed to be secure.

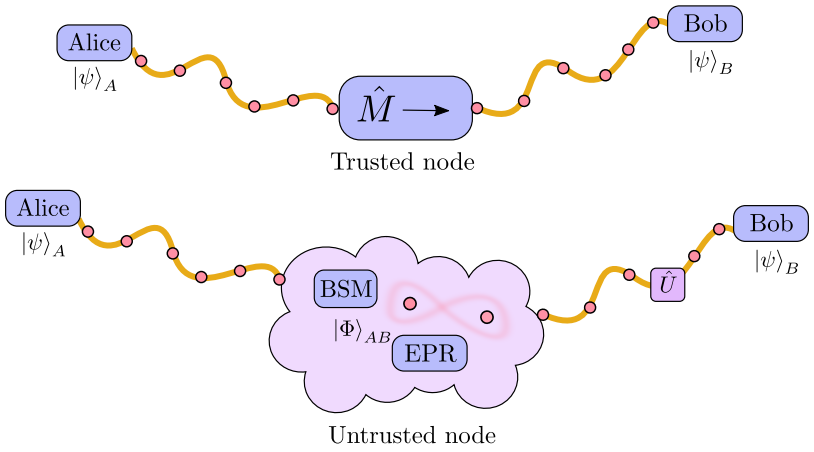

Figure 1.5: Quantum relay for enhancing the security of a QKD link through the use of an untrusted node. Security can be guaranteed through the use of quantum teleportation to map the encoded state from Alice onto the photon at Bob.

A quantum relay, on the other hand, could enhance the security of such a link by removing the need for the intermediate node to be trusted, using the principle of quantum teleportation. Furthermore, with such a scheme it would be possible to also increase the distance of the network link, due to the scaling of the signal-to-noise ratio (SNR) as a function of distance [26]. Such an application naturally requires the operation of an entangled quantum light source compatible with a telecom fibre network, such that the existing infrastructure can be adopted. While quantum relays and many other quantum technologies have been demonstrated using shorter wavelength single-photon sources, no system other than QDs has yet to be been shown to work in the telecom C-band. The work of this thesis therefore aims to bridge this crucial gap in the development of fibre-based quantum technologies.

1.3 Thesis Overview

This thesis describes the work in the development of a quantum light source operating at the minimum absorption wavelength window of optical fibre, centred on the telecom *C*-band (1530 – 1565 nm), making it suitable for transmission over the standard telecommunication optical fibre network infrastructure for future quantum information applications. The final goal is the demonstration of quantum teleportation of telecom *C*-band laser qubits, enabling such a platform to interface with current QKD systems.

After the introduction of the basic concepts in quantum information here, Chapter 2 gives a further overview of the photon number statistics for sources used in quantum information, as well as introducing the concept of two-photon interference (TPI), a fundamental resource required for quantum teleportation. The basic properties of semiconductor QDs, the source of choice for the work described here, will further be introduced forming the basis of all experimental work undertaken.

Chapter 3 then describes the experimental techniques used throughout this thesis in detail, including the use of various methods of spectroscopy for characterising fundamental properties in the emission from QDs.

In Chapter 4, a characterisation of the relatively new platform of InAs/InP QDs is carried out. The first task is to understand their emission characteristics and internal dynamics, which are determined from coherence time and correlation measurements. This allows for an assessment of the suitability of these sources for quantum interference and entanglement measurements, which are crucial for a quantum relay. The single-photon nature of the emission is characterised under continuous-wave (CW) operation and 1-GHz pulsed operation, alongside the coherence properties.

Using the results displayed in Chapter 4, the work in Chapter 5 describes the two-photon interference measurements made using this source. Firstly, the interference of subsequently emitted photons is demonstrated. Following that, the interference of photons with dissimilar statistics is performed, that is, light from a laser and the QD. The ability to perform interference is crucial for many quantum network applications and, in particular, lies at the core of a quantum relay.

Chapter 6 describes the characterisation of the entangled photon pairs, the next step towards a quantum relay. Again, this characterisation is performed for CW operation and under 1 GHz pulsed excitation, where both regimes are found to produce record high entanglement fidelities. An unusual property of the QD fine structure is also explored in this chapter, which probes a more fundamental feature of the entangled photon-pair emission.

Finally, Chapter 7 describes the combination of the work in the thesis to demonstrate for the first time a quantum relay in telecom *C*-band using a QD source. The quantum relay is operated under CW and 1 GHz pulsed excitation regimes, where first the teleportation proceeds with polarisation encoded input qubits, followed by a proof-of-principle demonstration using time-bin encoded input qubits.

Chapter 2

Semiconductor Quantum Dots as Quantum Light Sources

In this chapter, a basic introduction to the background of quantum light sources and applications will be given. The necessary background theory surrounding the use of semiconductor QDs for such applications will also be considered, including a review of the growth methods used in producing such structures. In particular, the techniques used to push emission into the telecom *C*-band will be introduced.

2.1 Single-Photon Quantum Light Sources

First, it is necessary to look at the photon statistics as a way to distinguish quantum light sources from classical laser light, by considering how such sources exhibit distinct quantum features when looking at their photon correlations. The autocorrelation as well as quantum interference effects when such sources are made to interfere on a beamsplitter will also be considered.

2.1.1 Photon Statistics

A pure single-photon source is of great interest for quantum information processing applications. An ideal source would have emission of a single-photon with unity probability in response to an external trigger [33]. A widely used alternative of a true single photon source is an approximation using a weak coherent laser pulse. The limitations of this approximation can be seen by considering the Fock state expansion of the coherent state in terms of the photon number n [34]

$$|\alpha\rangle = e^{-\frac{1}{2}|\alpha|^2} \sum_{n=0}^{\infty} \frac{\alpha^n}{\sqrt{n!}} |n\rangle \,, \tag{2.1}$$

where $\mu = \langle\alpha|\,\hat{n}\,|\alpha\rangle = |\alpha|^2$ is the mean photon number. The fluctuation of this field follows a characteristic Poisson distribution where the probability of having n photons is

$$P_n = |\langle n|\alpha\rangle|^2 = e^{-\mu}\frac{\mu^n}{n!}. \tag{2.2}$$

This distribution is plotted in Figure 2.1 for different values of μ. Immediately, it can been seen that such sources are inappropriate for the desired applications as there is a significant multi-photon probability, even for highly attenuated sources [33]. For QKD experiments, decoy-state protocols [35] using weak coherent pulses can address the security concerns of the multi-photon emission. However, running the sources with low enough μ to make this effective limits the efficiency of the source. For a true single-photon source, such limitations do not exist as in principle it is possible to generate one single photon for each excitation pulse.

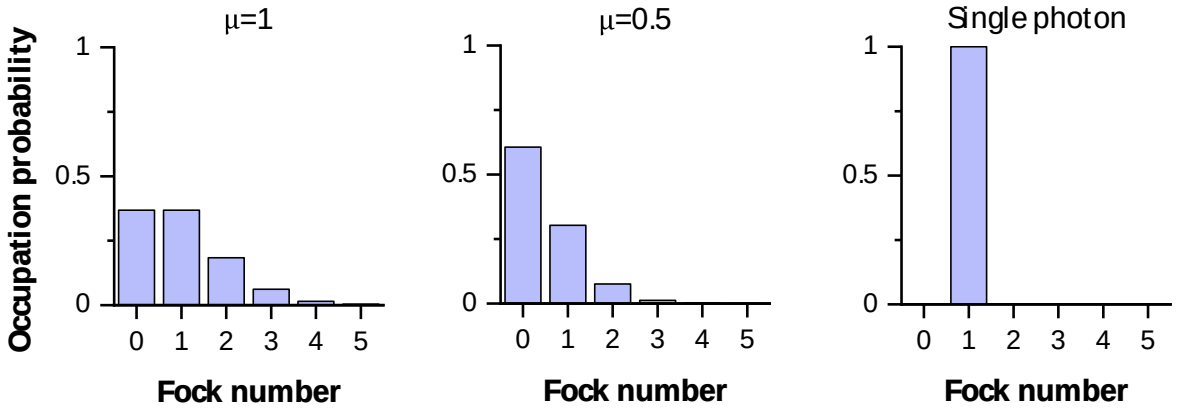

Figure 2.1: Photon statistics for average photon number per pulse $\mu = 1$ (**left**), $\mu = 0.5$ (**centre**) and for a pure single photon state (**right**). Due to the Poissonian nature of the coherent states, a small multi-photon probability always remains for decreasing mean photons per pulse.

Another approximation of a true single photon source can be constructed through the generation of photon pairs, for example using Spontaneous Parametric Down Conversion (SPDC). One photon is used to herald the presence of the other, improving the SNR issue created by the low-efficiency coherent pulses, since now the detectors are only switched on with the arrival of a triggering photon. However, these sources also display the typical Poissonian photon-number distribution, due to the random nature of the non-linear crystal pumping process [33].

While currently it is possible to circumvent the requirements of single photon sources in QKD using weak coherent pulses and decoy state QKD [35–38], the requirement to develop high purity and efficient true single photons sources is still essential for the development of quantum technologies [38]. Solid-state quantum light sources have the potential to offer near-perfect single-photon sources [39], and have demonstrated many proof-of-principles applications in quantum technologies such as BB84 QKD [40], entangled-based QKD [41], quantum teleportation [42], entangled swapping [43, 44] and Boson-sampling [45].

2.1.2 Second-Order Correlations

The statistics characterising photon sources can be determined through second-order field correlations which determine the probability of detecting photon at time $t+\tau$, conditional on the detection of a photon at time t [46]. Classically, the form of this second-order coherence function is given by

$$g^{(2)}(\tau) = \frac{\langle I(t)I(t+\tau)\rangle}{\langle I(t)\rangle\langle I(t+\tau)\rangle} = \frac{\langle I(t)I(t+\tau)\rangle}{\langle I(t)\rangle^2} \tag{2.3}$$

where $I(t)$ is the time-dependent intensity of the source under characterisation, and it is assumed that the source emission is time-invariant such that emission at t and $t+\tau$ are uncorrelated. This quantity can be accessed experimentally through a Hanbury-Brown Twiss (HBT) interferometer [47], shown schematically in Figure 2.2a. Incoming light is incident on a balanced beamsplitter, followed by detectors at each of the output modes. The detection time of one photon on the first detector constitutes the 'start' of the measurement and the arrival time of a subsequent photon on the second detector signals the 'stop'. A correlation between photon detection events is then made with the relative time delay.

While equation 2.3 is suitable for describing classical continuous-wave (CW) sources, such as laser light, a quantum mechanical interpretation is required to describe the statistics of quantum light sources, where the probability of emitting one photon is not independent on emission of the previous photon. This can be done through expressing Equation 2.3 in terms of photon creation and annihilation operators such that

$$g^{(2)}(\tau) = \frac{\langle \hat{a}^\dagger(t)\hat{a}^\dagger(t+\tau)\hat{a}(t+\tau)\hat{a}(t)\rangle}{\langle \hat{a}^\dagger(t)\hat{a}(t)\rangle} = \frac{\langle \hat{n}(t)\hat{n}(t+\tau)\rangle}{\langle \hat{n}(t)\rangle^2} \tag{2.4}$$

where $\hat{n} = \hat{a}^\dagger\hat{a}$ is the number operator. For an ideal n photon Fock state, this results in

$$g^{(2)}(0) = \frac{n(n-1)}{n^2}. \tag{2.5}$$

Thus, a single-photon source is determined by a $g^{(2)}(0) < 0.5$. For the case of a simple two-level quantum emitter, emission of a single photon results from radiative decay of an excited state after excitation from the ground. In this case, the $g^{(2)}(\tau)$ can be determined by considering the populations of the n_1, n_2 of the ground and excited state, respectively, with $n_1 + n_2 = 1$. As detection of a photon at time t puts the system in the ground state, $g^{(2)}(\tau)$ can be obtained from the solution of the rate equations

$$\frac{dn_1}{dt} = -\frac{n_1}{\tau_{exc}} + \frac{n_2}{\tau_r} \tag{2.6}$$

$$\frac{dn_2}{dt} = \frac{n_1}{\tau_{exc}} - \frac{n_2}{\tau_r} \tag{2.7}$$

where τ_{exc} and τ_r are the excitation and decay times, respectively, with the initial conditions $\{n_1 = 1, n_2 = 0\}$, such that

$$g^{(2)}(\tau) = \frac{(n_2(\tau)|n_2(0) = 0)}{n_2(\infty)} \tag{2.8}$$

$$= 1 - e^{-|\tau|/\tau_d} \tag{2.9}$$

where $\tau_d = \frac{1}{\tau_r} + \frac{1}{\tau_{exc}}$ and τ has been replaced with $|\tau|$ due to the symmetry $g^{(2)}(\tau) = g^{(2)}(-\tau)$ of the correlation function for this case. The comparison of the correlation function for such a single-photon source and a traditional coherent source can be seen in Figure 2.2b, where the difference in the photon statistics is immediately apparent. A quantum light source is said to be *anti-bunched* due to having $g^{(2)}(0) < 1$, and the photon statistics describing this non-classical light are said to be *sub-Poissonian*.

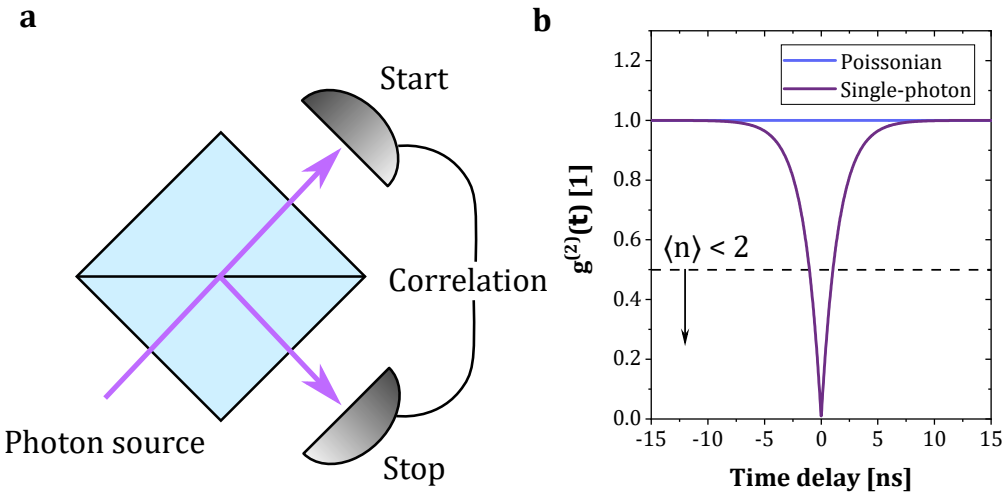

Figure 2.2: Hanbury-Brown and Twiss measurement of photon statistics. **a** Experimental concept for the measurement of photon statistics. **b** Second-order correlations for different photon statistics. A coherent source, dominated by Poissonian statistics, results in a flat line of value 1 corresponding to the equal probability of detecting one photon after another. A single-photon source on the other hand follows sub-Poissonian statistics, thus, there is a vanishing probability for detecting two photons at the same time.

2.1.3 Two-Photon Interference

The quantum interference of two single photons at a beamsplitter is one of the most fundamental operations in quantum information processing and is central to quantum computing, where it forms the basis of quantum logic in optical circuits in schemes such as those posed by Knill *et al.* [48], Gottesman & Chuang [49] and Nielsen & Chuang [50], and also quantum communication where it forms the basis of creating multi-photon states required for heralding the teleportation of photons [51] central to establishing a quantum relay [52], performing entanglement swapping [44] or even all-photonic quantum repeater schemes [53–55].

When two photons are incident on a 50:50 beamsplitter, they are either reflected or transmitted and so undergo a unitary transformation $\hat{U}_{BS}$. If the photons are indistinguishable in all degrees of freedom, there is no way to distinguish the process that led to one photon leaving in each output mode and so the probability amplitudes interfere destructively. The effect of this, originally demonstrated by Hong, Ou and Mandel [56] and subsequently named the Hong-Ou-Mandel (HOM) effect, is a bunching of the photons in either one of the output ports. Figure 2.3 depicts the concept of this interference in terms of the probability amplitudes for reflection and transmission for the four cases of the paths in which each photon can take when $|r|^2 = |t|^2 = \frac{1}{2}$. As shown, for the case of both reflections $p_{11} = -\frac{1}{2}$ and for both transmissions $p_{11} = \frac{1}{2}$, resulting in the vanishing probability to find one photon in each output port when adding the amplitudes before considering the outcome, as done for bosonic particles [57].

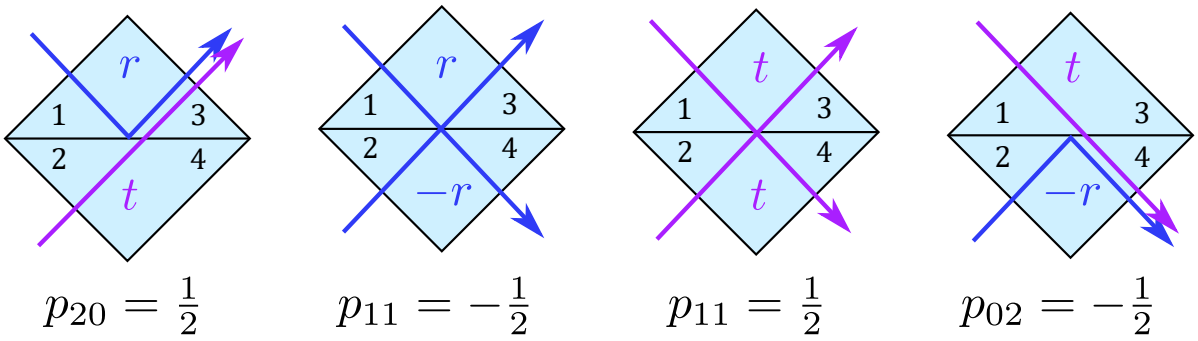

Figure 2.3: Interference of two single photons incident on a perfect 50:50 beamsplitter. The probability amplitudes for the photons exiting via each port of the beamsplitter is shown for the four possible cases when $|r|^2 = |t|^2 = \frac{1}{2}$.

This effect can been seen by also considering the action of the beamsplitter on the photons in terms of the bosonic field operators $\hat{a}_i$ for the input (modes 1 and 2) and output (modes 3 and 4) ports respectively. The input state for a state with one photon in each mode is given by

$$|\Psi_{in}\rangle = |1\rangle_1 |1\rangle_2 \tag{2.10}$$

$$= \hat{a}_1^\dagger \hat{a}_2^\dagger |0\rangle, \tag{2.11}$$

where $\hat{a}_i^\dagger$ refers to the creation operator for a photon in port i of the beamsplitter. The unitary operator $\hat{U}_{BS}$ is given by

$$\hat{U}_{BS} = \begin{pmatrix} \sqrt{\eta} & -\sqrt{1-\eta} \\ \sqrt{1-\eta} & \sqrt{\eta} \end{pmatrix}, \tag{2.12}$$

where η is the transmission through the beamsplitter corresponding to the more familiar unitary rotation $\sqrt{\eta} = \cos\theta$ and $\sqrt{1-\eta} = \sin\theta$. For symmetric and lossless 50:50 splitting $\eta = 1/2$. The input modes then transform as

$$\hat{a}_1^\dagger = \tfrac{1}{\sqrt{2}}\left(\hat{a}_3^\dagger + \hat{a}_4^\dagger\right) \qquad \hat{a}_2^\dagger = \tfrac{1}{\sqrt{2}}\left(\hat{a}_3^\dagger - \hat{a}_4^\dagger\right), \tag{2.13}$$

whereupon substitution of the operators in the input state in order to apply the transform results in the output state

$$|\Psi_{out}\rangle = \frac{1}{\sqrt{2}}\left(\hat{a}_3^\dagger + \hat{a}_4^\dagger\right)\frac{1}{\sqrt{2}}\left(\hat{a}_3^\dagger - \hat{a}_4^\dagger\right)|0\rangle \tag{2.14}$$

$$= \frac{1}{2}\left(\hat{a}_3^\dagger\hat{a}_3^\dagger + \hat{a}_3^\dagger\hat{a}_4^\dagger - \hat{a}_4^\dagger\hat{a}_3^\dagger - \hat{a}_4^\dagger\hat{a}_4^\dagger\right)|0\rangle \tag{2.15}$$

$$= \frac{1}{\sqrt{2}}\left(|2\rangle_3|0\rangle_4 + |0\rangle_3|2\rangle_4\right), \tag{2.16}$$

wherein the second to last line the Bose commutation $[\hat{a}_i^\dagger, \hat{a}_j^\dagger] = \delta_{ij}$ means that these possibilities cancel, leaving only the terms corresponding to two photons in either output port, demonstrating the peculiar bunching effect.

For the case of distinguishable photons, this is no longer the case, as the reflection and transmission resulting in one photon in each output has a distinct probability amplitude. This leaves a probability to observe one photon leaving the beamsplitter, due to now being able to distinguish which path it took. The indistinguishability of a photon source is of significant importance for the development of quantum network resources. Characterisation of the indistinguishability of a source can be performed by examining the interference visibility, which relies on the overlap of the input modes at the beamsplitter.

2.2 Semiconductor Quantum Dots

Semiconductor QDs [58, 59] are three-dimensional nanostructures where the spatial confinement of charge carriers becomes comparable to the de Broglie wavelength [60]. Such confinement results in a quantisation of the energy levels, and has earned them the title of 'artificial atoms' [61] due to the striking similarities of real atomic systems.

The QDs themselves are composed of a lower band gap material within a higher band gap material [59] where these band offsets are the source of the confining potential. Electrons excited out of the valence band to the conduction band leave holes behind. These carrier pairs subsequently form quasi-particles through their mutual Coulomb attraction, so-called excitons, and can be captured by the QD, where they can radiatively recombine through the emission of a photon. Figure 2.4 shows an example of such a QD band structure with an InAs QD surrounded by InP, creating a particle-in-a-box type confinement potential along the growth axis of the QD (where the spatial confinement here is typically much smaller than the lateral confinement). Following the language of atomic physics, the s and the p excited states of the electron and hole in such a potential have been labelled, and in this example, lead to a recombination energy of ~ 0.8 eV. Other typical QD materials include InAs/GaAs or AlGaAs/GaAs, where emission is typically around ~ 1.2 – 1.4 eV and ~ 1.6 eV, respectively. In this simple picture, the population of the QD with an exciton (excited state) and the empty QD (ground state) is an ideal two-level system, forming the basis for semiconductor quantum light sources [32].

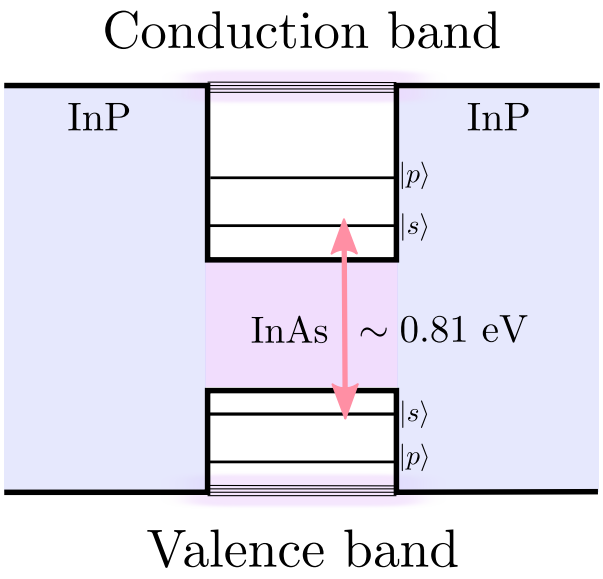

Figure 2.4: Band structure of a QD. The low band gap material (InAs) is grown in between two higher band gap material layers (InP). The band offset creates a 3D confinement on the scale of nanometres. Discrete energy levels exist in the QD, resulting in atom-like emission.

2.2.1 Carrier Excitation

There are multiple excitation schemes for generating carriers and driving the QD emission. The most common excitation is optical pumping with laser energy above the bulk material band gap. This above-band excitation, shown schematically in Figure 2.5, generates carriers in the higher band gap material. These carriers are captured by the QD and relax via phonon scattering (on timescales < 100 ps)[33, 62] to the ground state. When this relaxation is not short compared to the radiative lifetime of the exciton, there is an additional jitter in emission due to the delay [33, 63], which reduces the quality of the source. The experimental advantage is that the excitation and emission spectrum are easily filtered. As these nano-structures can be incorporated into light emitting diodes (LEDs) [64–66], current injection can also be used to electrically pump the QD emission. This works in a similar fashion to the above-band excitation, in that carriers are generated in the doped regions of the diode before relaxation and capture by the QD.

For higher control over electron-hole injection [67], quasi-resonant excitation of the excited p-shell state of the QD can be used. In this scheme, a higher purity of single-photon emission can also be observed due to a lower probability of generating carriers in the continuum states [68]. The most desirable scheme for applications relying on optimal single-photon properties, however, is the resonant excitation of the QD s-shell [33]. In this regime, there is no additional relaxation leading to highly-pure and indistinguishable photons [33]. The drawback here is that the excitation wavelength is the same as the emission wavelength, requiring filtering of ~ 50% of the photons in an experimental setup using polarisation filtering to reject the laser. However, there have been interesting recent developments in the case of resonant excitation working to remove the filtering restrictions [69]. It is also possible to perform resonant excitation of the biexciton, which relies on a two-photon absorption process [70, 71], resulting in highly-pure and indistinguishable photon pairs [72].

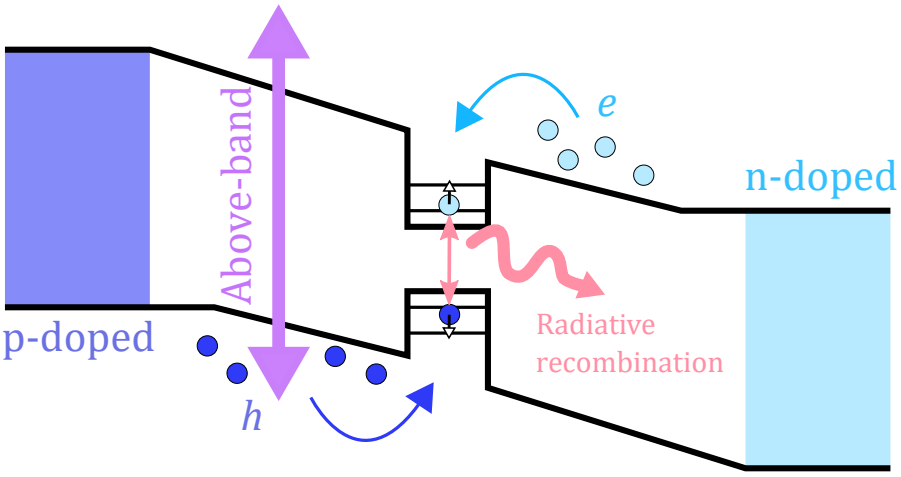

Figure 2.5: Carrier excitation in single QDs. Optical excitation using an above-band laser energy creates electrons and holes in the bulk semiconductor. Subsequent capture of electron-hole pairs in the QD form quasi-particles, which can then relax through radiative recombination.

2.2.2 Charge Configurations

In order to gain insight into the mechanisms for non-classical light generation in QDs, first consider the excitonic configurations and energy structure. Figure 2.6 shows the most common charge configurations found in typical QDs. The neutral exciton (X) and biexciton (XX) consist of one and two electron-hole pairs, respectively. The addition of an extra electron or hole results in the formation of the negatively (X^-) and positively (X^+) charged excitons. Further configurations exist with lower relative intensities corresponding to states with more electron-hole pairs, or additional excess carriers [73, 74]. Populations of such highly charged configurations are sensitive to doping conditions or electrostatic potential, the latter being controllable in charge-tunable structures [75, 73].

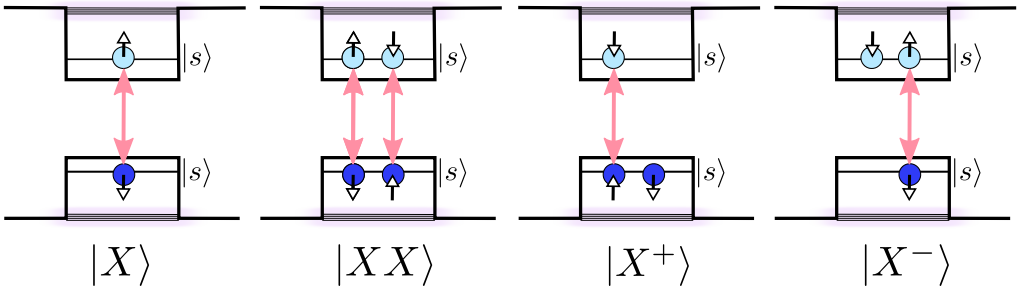

Figure 2.6: Charge configurations in single QDs. Different configurations of trapped electrons and holes leads to emission of different transitions. The neutral exciton (X), neutral biexciton (XX), negatively (X^-) and positively (X^+) charged excitons form the most common configurations.

Unless directly pumping a specific transition, a QD usually displays several emission lines, as shown by a typical spectrum in Figure 2.7, relating to these different charge configurations that can be present. Transitions can tentatively be labelled by considering the relative probability of injecting electron-hole pairs, and will be discussed further in Section 4.2.

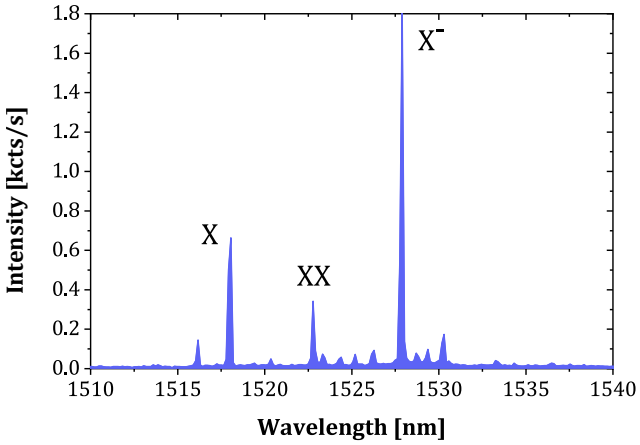

Figure 2.7: Sample spectrum of an optically excited QD. The main transitions typically seen in these types of QDs, corresponding to the different charge configurations, have been labelled where possible.

2.2.3 Entangled Photon-Pair Generation

The generation of entangled photons from semiconductor QDs was first demonstrated by Stevenson *et al.* [76] and Akopian *et al.* [77], where the principle of polarisation entanglement here relies on the radiative cascade of the $|XX\rangle$ state to the $|X\rangle$, and the ground state $|G\rangle$. Due to the Pauli-exclusion principle, the $|XX\rangle$ s-state is comprised of a spin-up and a spin-down electron. Since the radiative recombination with a hole of each is equally probable, the cascaded emission results in a pair of polarisation-correlated photons, with a well-defined phase. However, in reality the situation is more complicated due to the electron-hole exchange interaction, which modifies the fine structure of the X.

At zero magnetic field the X fine structure is a result of the electron-hole exchange interaction which couples the spins [78]. The z-direction is taken as the quantisation axis in the QD structure. The electron has spin $S_{e,z} = \pm 1/2$ and the heavy hole (due to the splitting of the light-hole/heavy-hole states, the light hole is generally neglected [78]) has spin $J_{h,z} = \pm 3/2$. Thus, total angular momentum $M = J_{h,z} + S_{e,z}$ results in the projections $M = \pm 1, \pm 2$. The $M = \pm 1$ states give rise to optically allowed transitions, or 'bright' excitons, while the $M = \pm 2$ states are forbidden and optically 'dark'. The general form of this interaction using these states as the basis can be expressed as [78]

$$H_{\text{exchange}} = \frac{1}{2}\begin{pmatrix} \Delta & S & 0 & 0 \\ S & \Delta & 0 & 0 \\ 0 & 0 & -\Delta & S_d \\ 0 & 0 & S_d & -\Delta \end{pmatrix}, \tag{2.17}$$

where Δ, S, S_d refer to the energy splitting of the bright and dark states, the bright state components and the dark state components respectively. For rotationally symmetric QDs, $S = S_d = 0$ and the bright states are eigenstates [78], separated from the dark states by Δ. Figure 2.8 shows the energy structure of this. Due to the conservation of momentum, the radiative decay from the XX will result in polarisation entangled photon pairs. For the symmetric case of only the isotropic exchange interaction, decay to the $|\pm 1\rangle$ states will result in circularly polarised photon pairs with the two-photon state

$$|\psi\rangle = \frac{1}{\sqrt{2}}(|R_{XX}L_X\rangle + |L_{XX}R_X\rangle). \tag{2.18}$$

For asymmetric QDs characterised by the anisotropic interaction, as is the case for the majority of QDs due to growth conditions, the hybridisation of the angular momentum eigenstates results in linearly polarised photon pairs with an additional time-dependent phase due to the energy difference. In this case, the two-photon state becomes [79, 80]

$$|\psi\rangle = \frac{1}{\sqrt{2}}(|H_{XX}H_X\rangle + e^{\frac{iS\tau}{\hbar}}|V_{XX}V_X\rangle). \tag{2.19}$$

The splitting of the bright states, termed the fine-structure splitting (FSS), S, now plays an important role in the emission dynamics of entangled photon pairs. As the FSS increases beyond the natural linewidth, the which-way path information of the photon cascade is revealed, leading to an eventual loss of the entanglement fidelity. However, even in the presence of large FSS, it is still possible to observe entangled photon emission by only considering time scales small enough such that only small phase shifts are caused by the time-dependent phase term. However, this leads to a requirement on detector resolution for measuring the entanglement, as now the time-varying phase needs to be resolved in order to avoid the effective averaging out of the signal, resulting in classically correlated photon pairs, which correspond to a statistical mixture.

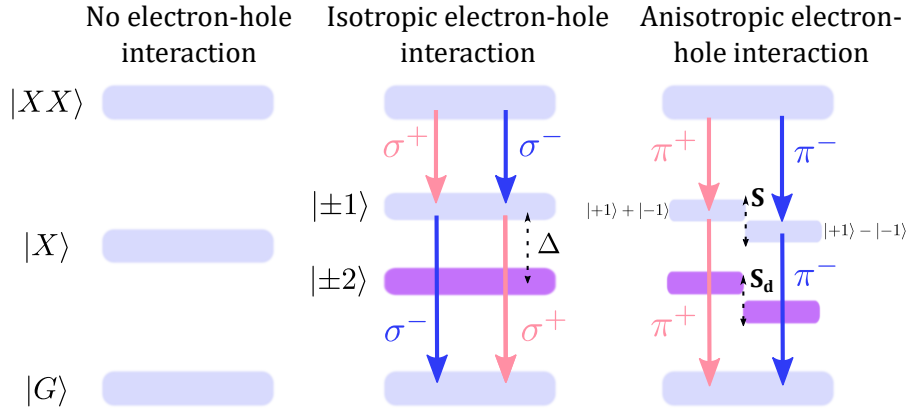

Figure 2.8: Fine structure of the biexciton cascade. Electron-hole interactions create energy splitting into $M = \pm 2$ optically dark states and $M = \pm 1$ optically bright states. Radiative decay results in entangled circularly polarised emission. The effect of crystal symmetry on this interaction causes a mixing of the states resulting in linearly polarised entangled photon pair emission.

2.2.4 Formation of Self-Assembled Quantum Dots

Semiconductor QDs are typically grown epitaxially by deposition of material onto a crystalline substrate. The most common growth method is Stranski-Krastanow (SK), which has dominated the growth of InAs/GaAs structures [33, 32]. This growth process relies on the lattice mismatch of the two semiconductor materials. As the QD material is deposited on the substrate in atomically thin layers, the grown material adopts the lattice constant of the substrate initially, but accumulates strain as each additional layer is deposited [80]. The group III and V material flux is supplied at the same time and forms a two-dimensional 'wetting layer' as the strained layers grow. This wetting layer also provides carriers with an additional density of states. When some critical strain is reached, relaxation into small islands becomes energetically favourable. Figure 2.9a shows a schematic of this process. As the strain is intrinsically connected to the formation of the QD, the structural symmetry is also related to that of the substrate. Typically, this results in highly asymmetric QDs or dashes [81]. However, it is possible to grow highly symmetric structures using this technique, such as those observed in the growth of QDS emitting around ~ 885 nm, where there is an inversion of the wavefunction

symmetry [82]. This makes it possible to observe entangled-photon pairs, albeit with a wavelength unsuitable for transmission in conventional fibre.

For this application, it is possible to add further material such that a second critical thickness is reached. This results in the growth of larger QDs, which naturally increases the wavelength of the emission due to the lower confining potential, and can push this wavelength towards telecommunications bands [83, 84]. Other methods based on strain-driven growth used to reach such wavelength regions include the addition of metamorphic buffer layers, which act as strain-relaxing layers in order to help the formation of long wavelength emitting QDs [85]. There has also been a recent demonstration of the formation of QDs emitting in the telecom *C*-band with very high symmetry, with FSS values of ~ 2 μeV on average [86]. Here, the QDs were grown by Molecular Beam Epitaxy using a ripening technique [87], whereby the cooling time after deposition of the InAs layer on an InP substrate is controlled in order to realise the high symmetry, long wavelength emitters.

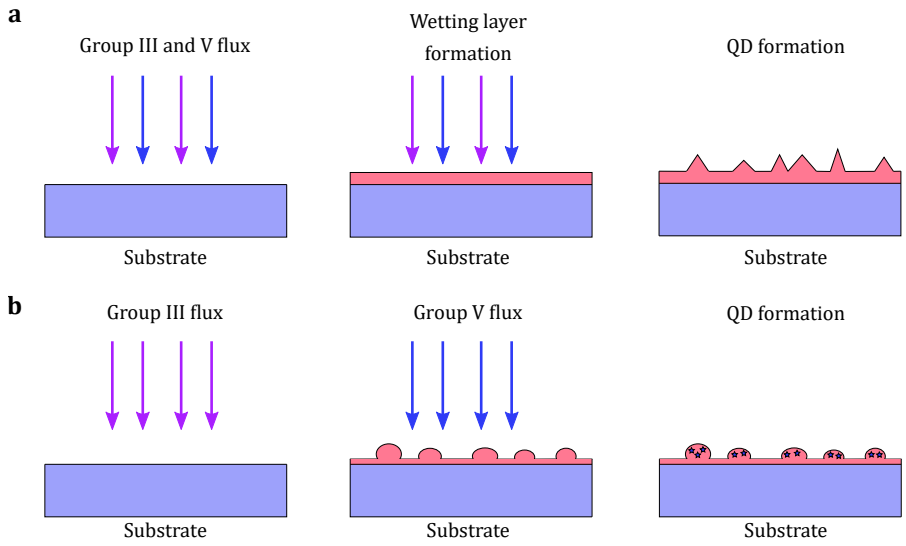

Figure 2.9: Growth-modes for self-assembled QDs. a SK growth of QD. Flux of the group III and V material is deposited in layers onto of the crystal substrate. As the strained layers build, formation of QD islands becomes favourable. **b** Droplet-Epitaxy QD growth. Group III flux is deposited as liquid droplets on the surface of the crystal substrate. This is later reacted with a flux of group V material which causes crystallisation and formation of QD structures. In the absence of a strain inducing wetting layer, the droplet QDs remain highly symmetric.

An alternative method of QD growth which does not rely on lattice strain layers is Droplet-Epitaxy (DE) [88], and is the method used for the growth of the QDs considered in this work. In this method, the group III material is deposited at lower comparative temperatures as liquid droplets on the surface of the crystal. A flux of group V material is then applied in order to react and crystallise the droplets. Figure 2.9b shows a schematic of this. By doing this, the formation of a wetting layer is avoided, only a 'quasi-wetting layer' exists where the droplets lattice match to the substrate. With no strain-driven growth, it is possible to reach much higher QD symmetries, demonstrated by [89, 90], which is crucial for entangled light emission [91, 92].

2.2.5 InP Material System

Another method to push the emission of a QD light source into the telecom *C*-band around 1.55 μm is to swap the host material GaAs for InP [87, 93–96]. Most systems looking to reach this band have relied on the InAs/GaAs QD material system [85]. However, the wavelength capabilities here are limited due to strain mismatch between the QD layer (InAs) and the substrate layer (GaAs). Swapping the host material to the InP material system is an effective method to overcome this problem as the lattice mismatch is on the order of 3%, as opposed to the 7% in GaAs [97]. This reduction redshifts the fundamental exciton energies on the order of ~ 200 meV compared to GaAs, to around 0.8 eV.

2.2.6 Sample

The samples used for this work were grown by collaborator Dr. Andrey Krysa at the University of Sheffield EPSRC National Epitaxy Facility, using Metalorganic Vapour Phase Epitaxy (MOVPE) [98]. The structure is similar to that used in a recent demonstration of an entangled-LED [99], and is shown in Figure 2.10. It consists of a 20-repeat n-doped distributed Bragg reflector (DBR) grown on the (001) surface on an InP substrate. These DBR pairs are made from ~ 112 nm $(A_{0.3}Ga_{0.7})_{0.48}In_{0.52}As$ and ~ 123 nm InP and allow for greater light collection efficiency from the top of the device. Following this, there is a 3/4-λ intrinsic InP layer, where metallic In droplets are deposited. These droplets are then crystallised under an AsH_3 flow before a 5/4-λ intrinsic InP layer. Finally, a 3-repeat p-doped DBR is grown to form an asymmetric 2-λ weak planar cavity for a small enhancement of the photon extraction efficiency.

Devices were fabricated from these samples at the University of Cambridge by Toshiba Research Laboratory colleague Dr. Joanna Skiba-Szymanska, where standard photolithography was used to define the mesas and device patterns. The mesas were wet-etched down to the n-doped layer. The doped layers were then contacted by evaporation of ~ 150 nm of AuGeNi for the n-type, and ~ 20 nm of Cr followed by ~ 100 nm Au for the p-type, for application of an electric field or electrical excitation.

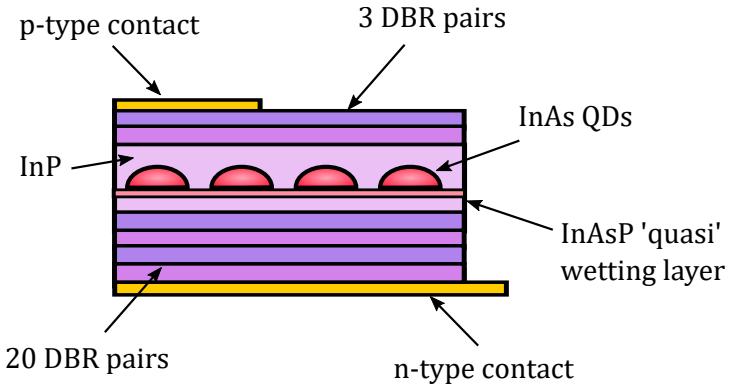

Figure 2.10: Sample device structure.

Chapter 3

Experimental Methods

This chapter presents the main experimental methods and techniques used throughout the course of this project. The basic spectroscopic and time-resolved methods used for characterising single QD properties are presented alongside details of the analysis employed to extract information on the key parameters defining the QD performance, which were critical in the selection of QDs for the experiments detailed in Chapters 5, 6 and 7.

3.1 Single Quantum Dot Spectroscopy

Standard spectroscopic methods were employed to access single QDs and characterise their suitability. The superior optical quality of QDs, however, can only be accessed when the thermal energy is low enough such that the confinement in all three dimensions becomes comparable to the de Broglie wavelength [3]

$$\lambda_{DB} \propto \frac{h}{\sqrt{2m^* k_B T}}, \tag{3.1}$$

where h is Plank's constant, m^* is the effective particle mass, k_B is Boltzmann's constant and T is the absolute temperature. In this regime, the density of states forms a discrete series of delta-function peaks with well-separated energies, resulting in the well-known atom-like energy structure. When the thermal energy is higher, confinement is no longer comparable and so the density of states broadens, allowing coupling of optical phonons and escape of bound charges, thus reducing optical quality.

For this reason, all experiments were conducted with the QDs held at cryogenic temperatures of ~8-44 K using a liquid Helium-cooled cryostat. The main experimental setup for performing single QD spectroscopy can be seen in Figure 3.1. It consists of a confocal microscope mounted atop a cryostat where the QD sample is housed. After insertion into the cryostat, the QD position was accurately controlled using an XYZ piezo-electric nanopositioner, while a small heating wire wrapped around the mounting stage of the sample was used to finely adjust the temperature of the device through application of a small current. The temperature was stabilised to the designated value using a standard PID temperature controller for both the cryostat and the heater stage.

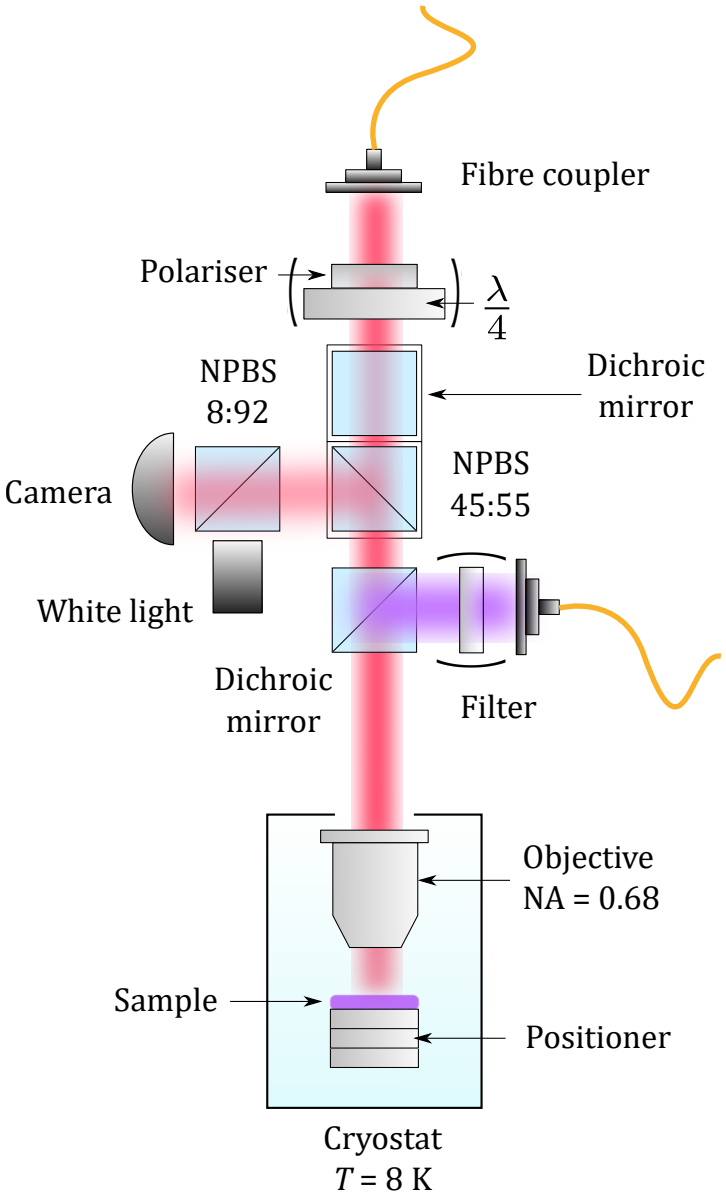

Figure 3.1: Photoluminescence spectroscopy setup. A standard microscope in the confocal setup is used to collect and fibre couple emission from QDs optically excited by a laser. The sample is held at temperatures of 8-44 K in a liquid-Helium cool vapour cryostat. An optional rotation mount housing a quarter-wave plate and a fixed linear polariser can be inserted to allow for polarisation-resolved spectroscopy.

3.1.1 Photoluminescence

Photoluminescence (PL) spectroscopy was used to measure the spectrum of light emitted from the QD after optical excitation. A standard confocal microscope, shown in Figure 3.1, with the QD positioned at the focal spot of an NA = 0.68 objective lens was used to couple light into a standard telecom single-mode (SM) fibre. Due to the size (~1 μm^2) of the focal spot and the 8.2 μm core of the collection fibre, it was routinely possible to collection emission from single QDs, provided the

density of QDs in the wafer was low enough. As such, the term micro PL, or μPL, is often used to describe such spectroscopy. Once coupled to the fibre, light from the QDs was sent to a 600 g/mm spectrometer and spectra were recorded using a liquid-nitrogen cooled InGaAs detector, sensitive to wavelengths of up to 1600 nm.

Optical excitation was performed using either a longpass dichroic mirror (above-band excitation) or 8:92 pellicle beamsplitter (below-band excitation) to reflect the laser light down into the objective. The differences in excitation schemes are discussed below. In most cases, an additional filter was used after the laser fibre coupler in order to clean up the exciting laser light. This was particularly necessary when using a below-band excitation laser of 1310 nm. In the collection path of the microscope, an optional 45:55 pellicle beamsplitter was used to direct light from the sample to a InGaAs camera for imaging. Here, an optional white-light source was sometimes used for imaging, requiring an additional 8:92 pellicle beamsplitter. An additional dichroic mirror (pellicle) perpendicular to the first was also used in most cases to compensate for any polarising effects of the first mirror (pellicle), as this is essential when performing any entanglement-based measurement. Optionally, there was also a rotation mount housing a quarter-wave plate (QWP) followed by a fixed linear polariser (LP) used in the FSS measurements detailed in Section 3.1.3.

Excitation schemes

As discussed in Section 2.2.1, there are multiple excitation methods for creating carriers in the QD which result in radiative transitions. Here, the cases of above and below-band non-resonant excitation are the predominate focus. For the case of above-band, a continuous-wave (CW) or pulsed 785-nm diode laser was used. This was generally the scheme used for initial characterisations of the QDs, however, it was later determined that using a below-band laser at 1310 nm improved the relative intensity of the the X and XX with respect to the X^- compared to 785-nm excitation. An example of this can be seen in Figure 3.2, which compares the normalised spectra of a QD when excited at the X saturation power with 785 nm and 1310 nm. The integrated intensity across the X and X^- is 0.0256 and 0.0278 for 785 nm, compared with 0.0282 and 0.0189 for 1310 nm, showing a redistribution of the intensity towards the neutral transitions. This can further be seen by the reduction of intensity in what is speculated to be the XX^- lines at a longer wavelength than the X^-. This effect can be explained by the below-band excitation creating more equal numbers of electrons and holes which are subsequently captured by the QD, as opposed to the above-band scheme and stronger n-type doping creating an excess of electrons. Given the relative ease of using this type of excitation and the benefit of greater intensity from the neutral lines, below-band excitation was used for the main experiments presented in Chapters 5, 6 and 7, unless otherwise stated.

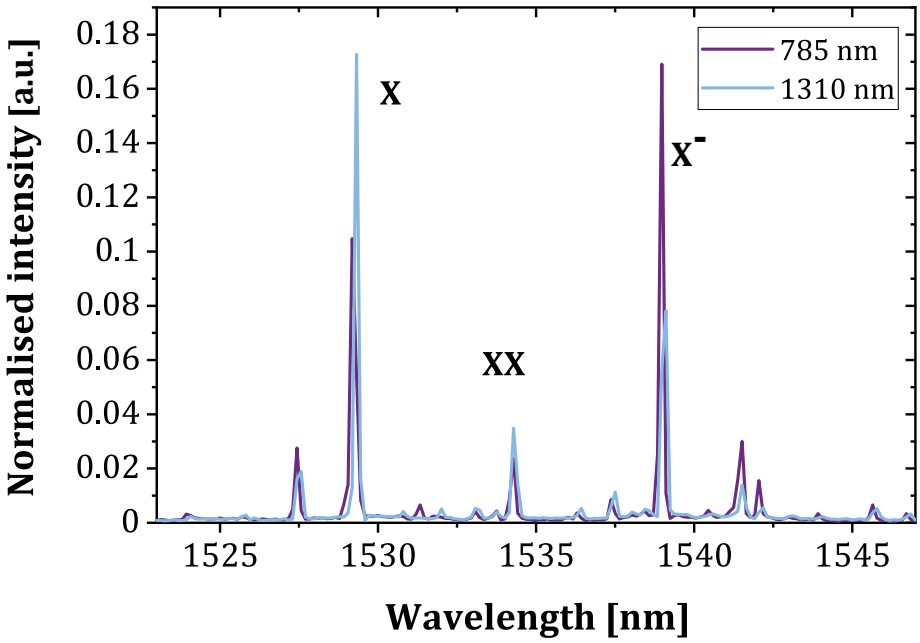

Figure 3.2: Below-band excitation. Spectra of a QD optically excited at the *X* saturation power for 785 nm and 1310 nm. The integrated intensities show that there is a redistribution from the negatively charged states towards the neutral and positively charged states.

3.1.2 Electroluminescence

The sample structure presented in Section 2.2.6 showed that this wafer was grown with the intent of creating a diode, such as those used in previous measurements of this lab [52, 64–66, 100, 101]. This was indeed one of the original goals for the project, as the goal for developing an electrically-driven single-photon source is of natural interest given the reduced experimental complexity [102, 103], especially with high-speed pulsed driving schemes [104–106], the possibility to also operate in a high temperature regime [107–109] and with development of such sources at telecom-wavelengths [110, 111].

As the QDs are grown in the intrinsic region of a p-i-n diode structure, applying a bias voltage across the device can be used to bring the diode into flat-band operation. This allows current to flow and carriers to excite the QD. This method of excitation is therefore referred to as electroluminescence (EL). For the device used in this project, EL was in fact limited in use to temperatures of above ~ 40 K, due to issues of p-type doping causing holes to freeze out at lower temperatures. This was supported by the relatively large p-p type contact resistance. This effect was also found previously in wafers grown with DE QDs on GaAs at shorter wavelengths [112–114]. It was also hypothesised that in this regime there could have be crystal defects or large nucleation sites, which were acting as charge traps preventing carriers from reaching the QD and providing non-radiative decay channels [115].

An attempt was made to improve the temperature of operation by increasing the amount of p-type doping in the top mirror. Figure 3.3 shows an example of QD emission from one such wafer

as a function of temperature. The overall temperature of operation was marginally improved, and reasonable emission could be found around 25 K. Cooling further, however, rapidly quenched the emission. As will be discussed in Section 4.4, the coherence time was strongly affected by temperature and, as a result, experiments were predominately carried out with optical excitation due to the lower temperature of operation and superior optical quality of the QD emission.

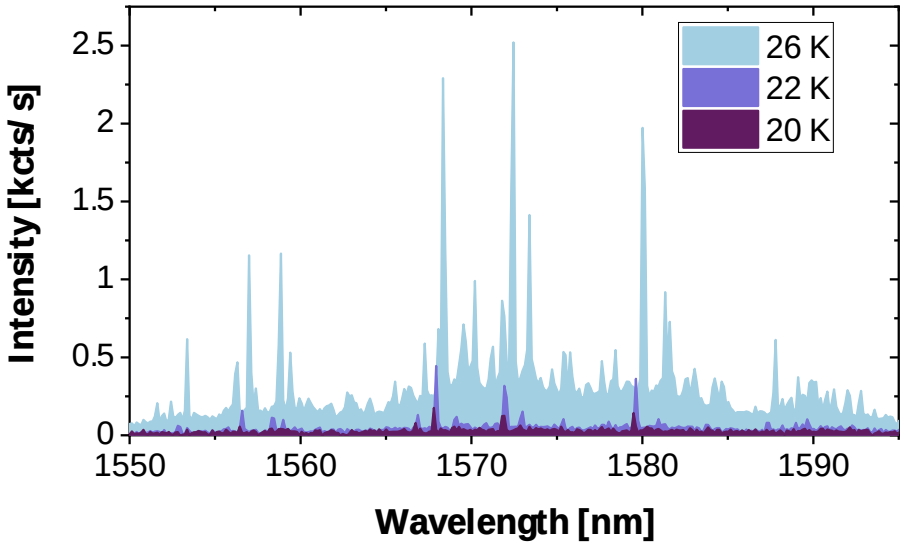

Figure 3.3: Quenching of electroluminescence. Spectra of part of wafer MR4195 showing the emission from QDs as a function of temperature for the same bias voltage of 1.75 V. The temperature of operation was lowered from MR4059 down to 26 K while retaining bright QD emission, however, cooling further caused a quench of the emission over a few Kelvin.

Application of a bias voltage was still, however, an important tool for some characterisation, such as the FSS study which could be performed at higher temperatures, and also to apply an electric field either in reverse or forward bias. The latter is a useful tool in some cases to improve the charge environment of the QD [116, 117].

3.1.3 Fine-Structure Splitting Characterisation

An important task in the characterisation of QDs to be used for entanglement based experiments is to quantify the FSS. As mentioned in Section 2.2.3, the FSS is the key parameter in determining the expected entanglement fidelity when using detectors with limited temporal resolution due to the phase evolution of the two-photon state. In order to resolve oscillations, the jitter of the detector needs to be smaller than a $\pi/2$ change in the phase, leading to a limit on the FSS of $S < h/4\tau_{Det}$. Since the resolution of the SNSPDs used throughout this project was never below ~ 90 ps, the limit imposed on the maximum usable FSS was ~ 12 μeV.

Polarisation-resolved spectroscopy is a convenient method to determine the FSS of neutral Xs and XXs, as the polarisation of the emitted photon correlates with its energy. A polarimeter, which

consists of a rotating QWP followed by fixed LP, can be used to determine this splitting through discrimination of the polarisation state of the light. If the input state of light is given in terms of Stokes parameters, the output intensity is then

$$\begin{pmatrix} I_0 \\ I_1 \\ I_2 \\ I_3 \end{pmatrix} = \vec{M(\chi)} \begin{pmatrix} I \\ Q \\ U \\ V \end{pmatrix}, \tag{3.2}$$

where I, Q, U and V denote the Stokes parameters defining the total intensity and the intensity of polarisation in the horizontal, diagonal and circular bases, respectively, $\vec{M(\chi)}$ is the Muller matrix defining the measurement of a QWP at an angle χ to a subsequent linear polariser [118], set to be aligned along the horizontal axis. The resulting measured intensity is then

$$I_0(\chi) = \frac{1}{2}(2I + Q + Q\cos(4\chi) + U\sin(4\chi) + 2V\sin(2\chi)). \tag{3.3}$$

This relates to the FSS, S, as the mean energy, $\langle E \rangle$, of the transition is the polarisation weighted average of the eigenstates $|X_H\rangle$ and $|X_V\rangle$ with energies $E_H = \langle E \rangle + S/2$ and $E_V = \langle E \rangle - S/2$, respectively. Thus, the energy measured by the spectrometer is then

$$E_0(\chi) = \frac{1}{2}\left(E_H \frac{I_0(\chi)}{I} + E_V \frac{\bar{I}_0(\chi)}{I}\right) \tag{3.4}$$

$$= \frac{1}{2}\left(2\langle E \rangle + \frac{SQ}{2I} + \frac{SQ\cos(4\chi)}{2I} + \frac{SU\sin(4\chi)}{2I} + \frac{SV\sin(2\chi)}{I}\right), \tag{3.5}$$

where $\bar{I}_0(\chi)$ is the intensity of the orthogonal polarisation corresponding to $\{Q, U, V\} \rightarrow -\{Q, U, V\}$, and S is then determined as the length of the polarised part of the energy Stokes vector

$$\vec{I} = \begin{pmatrix} 2\langle E \rangle \\ SQ \\ SU \\ SV \end{pmatrix}, \tag{3.6}$$

following the normalisation of $I^2 = Q^2 + U^2 + V^2 = 1$. This method is a reformulation of that which has been detailed in the previous work of this lab [90] and is robust against fixed birefringence in the system, such as that introduced by semi-polarising optical components or optical fibre.

The added benefit of expressing the problem in this way is that we can use frequency analysis on Equation 3.4 to directly determine the Stokes parameters in terms of the magnitude of the 0χ, 2χ and 4χ frequency components by performing a Fourier Transform, allowing an essentially fitting free reconstruction of the measured polarimeter data. Analysing the data in this way is further robust to

effects such as beam-steering in the intensity as this only introduces 1χ components, as long as the measurement is taken over a full rotation of the QWP.

By measuring spectra of the QD as a function of χ, $E_0(\chi)$ can be calculated. As the resolution of the spectrometer grating used here is ~ 89 μeV, Gaussian fitting routines are required in order to accurately determine the central energy of the transition, with a resolution of approximately 2 μeV. A Fast Fourier Transform (FFT) is then performed on the data in order to extract the relevant frequency components from which the polarimeter curve can be reconstructed. Figure 3.4 shows an example of such a measurement for the X and XX where the deviation in energy $E_0(\chi) - \langle E \rangle$ alongside the reconstructed polarimeter curves detailed in Equation 3.4 have been plotted. Immediately, it can be seen that the reconstructed curves describe the data almost exactly, and are essentially the same as those determined by the fitting methods used in [90]. From Figure 3.4, it is also noted that the measured state is elliptical in splitting polarisation with respect to the lab frame; however, the E_{XX} and E_X remain perfectly anti-correlated in energy corresponding to the emission of co-polarised photon-pairs, as expected from the radiative cascade system with eigenstates $\{|X_H\rangle, |X_V\rangle\}$. The determined $S = 18.2 \pm 2.2$ μeV, where the error has been calculated by a Monte-Carlo approach from the variance of the fitted central energies. Unfortunately, for the purposes of entanglement, this QD is unsuitable due to its large FSS and serves only as an example here.

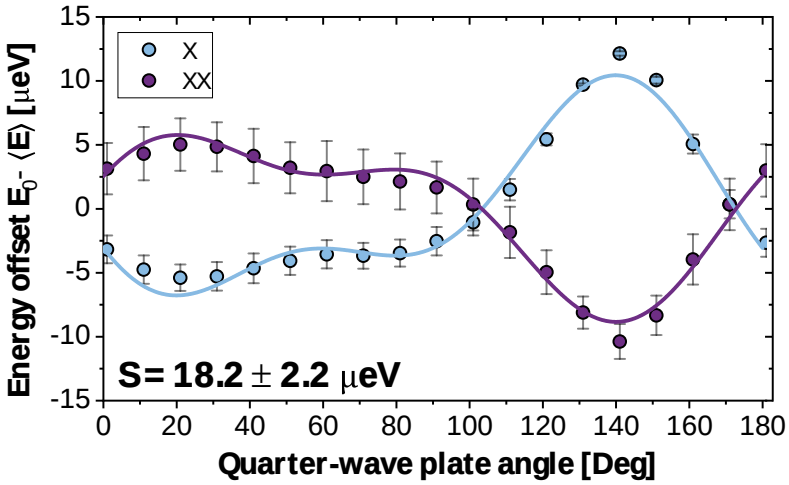

Figure 3.4: Fine-structure splitting measurement of the X and XX lines from an example QD. μPL spectra were measured for a range of QWP angles and the central energy of the lines were determined from Gaussian fits to the spectra. Reconstruction of the polarimeter curve according to Equation 3.4 then requires no further fitting procedures and allows S to be obtained directly.

A characterisation of the fine-structure splitting on the device M10 of the sample wafer MR4059 was then performed using electrical injection at a temperature of 44 K. The device was operated under a bias of 1.9 V, chosen to be somewhat above the QD emission turn on of around 1.5-1.6 V in order to have reasonable intensity and improve on the SNR for the subsequent spectral analysis. In this

regime, the emission is expected to be similar to that under optical excitation using an above-band laser with a power close to the X saturation.

Statistics were gathered from 90 QDs distributed across the single mesa. A scatter plot of the X recombination energy and the FSS alongside the marginal distributions can be seen in Figure 3.5, where a mean FSS of 27.1 ± 1.1 μeV and standard deviation of 13.4 μeV was found. This value is a factor ~ 1.5 lower than the previously reported average from samples grown by this method [90]. This could suggest that there has been an improvement in growth for this sample leading to more symmetrical QDs, such as the reduction of strain-driven mixing in the InAsP 'quasi' wetting layer during QD formation. The mean X recombination from the measurements is 0.814 eV, corresponding to $\lambda = 1523$ nm, which is somewhat below the centre of the expected planar-cavity mode for this sample ($\sim\lambda = 1535$ nm). This could be a result of the local growth conditions for this particular section of the wafer and contributes to some of the challenges in finding candidate QDs for the experiments presented later, due to the requirements of QD intensity in two and three-photon measurements. It is further noted that there is no correlation between the X recombination energy and the measured FSS within the cavity mode for this sample.

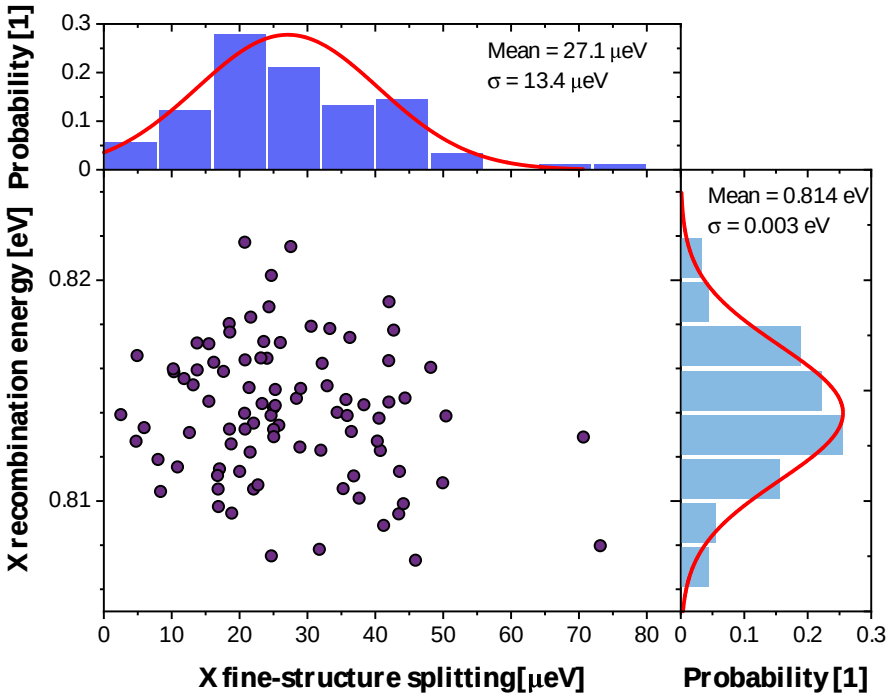

Figure 3.5: Fine-structure splitting statistics for the neutral exciton. Scatter plot of the measured FSS and the X recombination energy for 90 QDs. The mean of the fitted distribution (red curves) determines a mean of 27.1 ± 1.1 μeV. The mean X recombination from the measurements is 0.814 eV, which is somewhat below the peak of the expected cavity mode for this sample, suggesting that most QDs would lose significant enhancement from the cavity when cooling further below 44 K for optical measurements.

3.2 Time-Resolved Spectroscopy

Many experiments using QDs require probing the dynamics of the emission. This is achieved by performing time-resolved measurements using fast single-photon detectors and fast correlation electronics to time tag photon detection events relative to a syncronisation, or sync, clock. Histograms of the number of detected photons can then be acquired for the relative time delay between the sync and detection events. In this work, superconducting nanowire single-photon detectors (SNSPDs) with efficiencies ranging from 48−65%, and timing resolutions of 90−125 ps were used. Due to a range of technical problems, detectors were frequency replaced and therefore vary between experiments throughout this work. The relevant timing resolutions, or jitter, will be stated for each experiment. Time-correlation electronics enable photon time-tagging with a resolution of down to 1 ps, which was performed using a PicoQuant HydraHarp for all measurements.

In order to measure time-resolved emission from the QD, the light from the correct wavelength of interest must be filtered before being sent to the detectors. To achieve this, a free-space transmission grating is used for all time-resolved data acquisition. The transmission grating allows the QD transitions to be spatially separated and fibre-coupled with a transmission bandwidth of ~ 0.5 nm and coupling efficiencies of typically >65%. After fibre coupling, the light can then be sent to any of the fibre-based experimental setups or directly to the detectors. With this setup, it is then possible to perform time-resolved measurements. An example of such measurement can be seen in Figure 3.6, where the radiative decay time, τ_r, of the X can be determined from the time-resolved intensity following excitation by a pulsed laser, where the laser trigger is used as the sync clock to begin coincidence counting events. By fitting the decay to a bi-exponential, the radiative lifetime (given by the fast-decay) was determined to be $\tau_F = 1.77 \pm 0.01$ ns (slow component $\tau_S = 17.8 \pm 2.9$ ns), which was found to be fairly typical of QDs in this sample, as discussed later in Section 4.3.

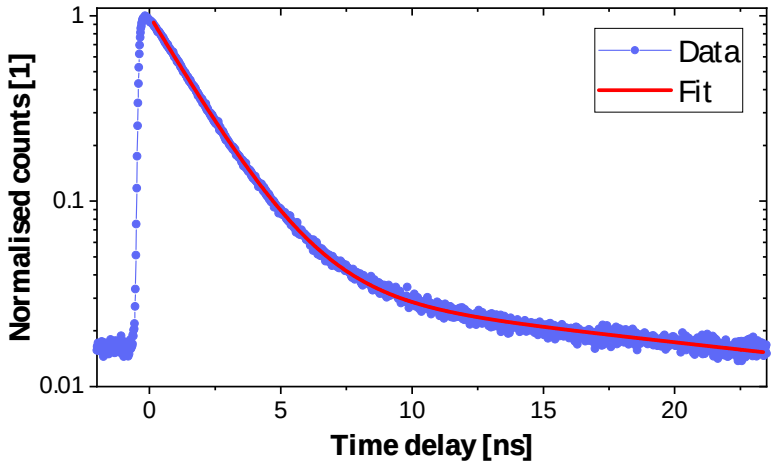

Figure 3.6: Time-resolved spectroscopy. Time-resolved intensity of the emission from an X, optically excited with a pulsed 785 nm laser with a repetition period of 40 MHz. The radiative lifetime was determined to be $\tau_r = 1.77 \pm 0.01$ ns using a bi-exponential fit to the data.

3.2.1 Second-Order Correlations

As discussed in Section 2.1.2, intensity autocorrelation measurements using a HBT setup are critical for characterising the photon statistics of a light source. The experimental implementation of the HBT measurement is shown in Figure 3.7, where emission from the QD is sent through the transmission grating before coupling back into a balanced fibre beamsplitter. The 'start'-'stop' measurement can then be made with the correlator, where histograms of events with the relative time delay are built. For more complex experiments involving raw photon time tagging, the correlator can be operated in time-tagged time-resolved (TTTR) mode, where the time of each photon detection event is recorded relative to a sync event.

Not only do such measurements allow for characterisation of the single-photon performance of a QD when operated in histogram mode, but also form the basis of all two-photon measurements, such as TPI discussed in Chapter 5 and entanglement discussed in Chapter 6. Cross-correlations between different transitions in the QD can also be performed to further characterise the QD emission dynamics, such as those discussed in Chapter 4. The operation in TTTR mode for time tagging is useful in order to build three-photon coincidence events, such as those required for measuring teleportation, as discussed in Chapter 7.

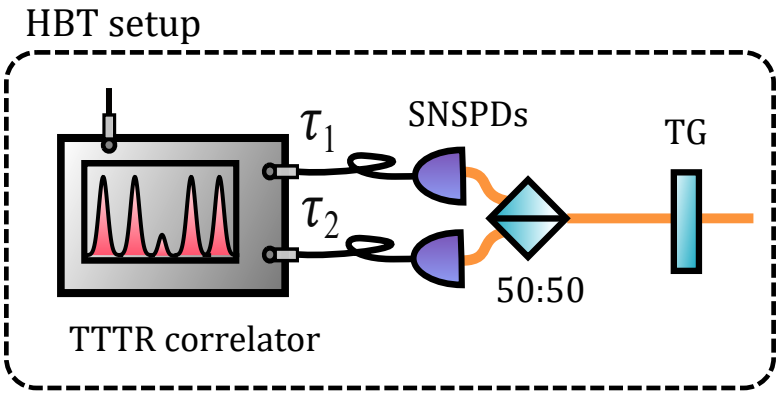

Figure 3.7: Experimental setup of the Hanbury-Brown Twiss autocorrelation measurement. Emission from the microscope is sent to a free-space transmission grating (TG) to spatially separate and couple individual transitions. After the TG, the light is sent through balanced fibre beamsplitter before detection on the SNSPDs. Correlation electronics are used to build histograms of detection events with relative time delay $\Delta\tau = \tau_2 - \tau_2$.

3.3 Flexible Pulsed Excitation Scheme

As one of the aims of this project was to operate the photon-source at high repetition rates to match those used by operational QKD protocols [119, 120], the implementation of an excitation scheme to facilitate this was required. Traditional laboratory pulsed lasers used for optical excitation are generally limited to repetition rates of around 80 MHz and below, whereas for the experiments described here, the desired operating frequency was 1 GHz. In order to reach such high repetition rates, a flexible scheme based on an electro-optic modulator (EOM) was used to carve out pulses of independently tunable width and frequency from a CW laser.

The scheme used, and built by colleague Dr. Tina Müller, is outlined in Figure 3.8, where a 1310-nm fibre-coupled laser was aligned to the transmission axis of a 20-GHz bandwidth EOM using a polarisation controller (PC) for intensity modulation. A pulse generator was used to define narrow (FWHM down to 100 ps) excitation pulses through the application of a radio-frequency (RF) signal (up to 3.3 GHz) to the EOM. An offset bias voltage was applied with active feedback routine (written by Dr. Müller) based on the voltage of a photo-diode (PD), in order to maintain > 20 dB suppression of the laser between the excitation pulses. The output pulses from the EOM were then directed to another PC before the digital variable attenuator (DVA) used to control the excitation power. Emission from the QD was then collected using the standard microscope described in Section 3.1.1. With this setup, a high level of control of the excitation conditions for various frequencies could be achieved. An example of such pulses can be seen in Figure 3.9, where the time-resolved intensity of the excitation laser was measured relative to the pulse-generator clock, for a frequency of $f = 1.07$ GHz. The frequency is slightly above that of the desired value of 1 GHz, as this was found to be optimal in terms of simultaneously achieving the narrowest pulses with highest contrast. The resulting width of the excitation pulses was ~ 160 ps. This configuration was used for all GHz-clocked experiments in Chapters 4, 6 and 7.

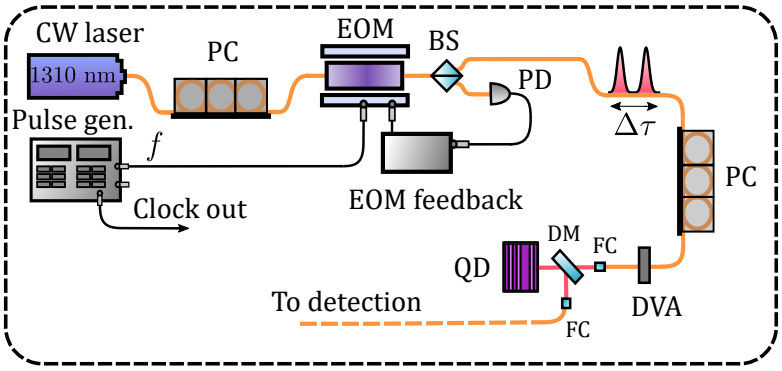

Figure 3.8: Flexible excitation pulse scheme. A 1310-nm CW laser is modulated by an EOM with active voltage stabilization in order to create flexible excitation pulses. The GHz-clocked emission is collected from the QD and sent to the detection system for subsequent measurement. PC, polarization controller; EOM, electro-optic modulator; BS, beam splitter; PD, photodiode; DM, dichroic mirror; FC, fiber coupler; DVA, digital variable attenuator.

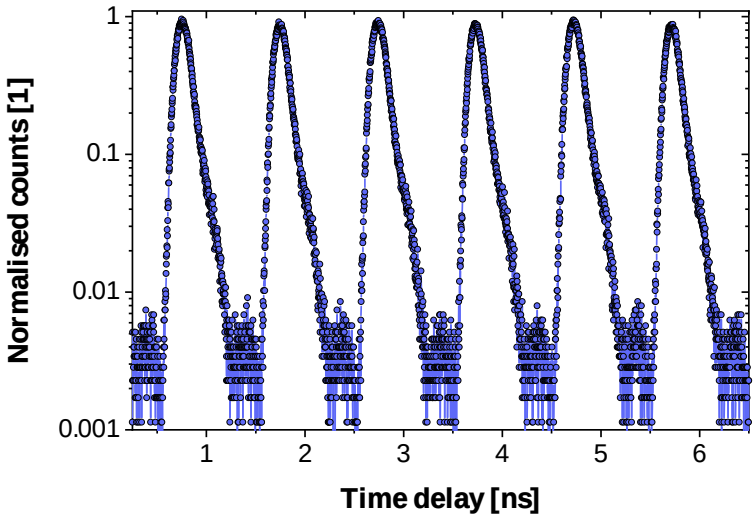

Figure 3.9: Time-resolved measurement of GHz-clocked excitation pulses. Generation of excitation pulses at f = 1.07 GHz with a width of ~ 160 ps and a suppression of 2.5 orders of magnitude, using the setup described above.

3.4 Fourier-Transform Spectroscopy

As discussed in Section 1.2.3, quantum teleportation and other applications in LOQC utilise interference of single-photon wave packets [48]. Being able to characterise the coherence in the emission of a source is thus of great importance in order to determine not only the temporal width of the photon wave packet, but also to determine the shape of the temporal modefunction, as this too contributes to the inference at the beamsplitter.

For a QD, spontaneous emission from radiative transitions results in a frequency distribution related to the natural linewidth $\Delta\omega$. Due to the energy-time uncertainty this leads to a characteristic temporal width of the photon wave packet, or coherence time, $T_2 \propto 1/\Delta\omega$. In the presence of additional dephasing processes from the semiconductor environment, the state is no longer fully coherent and becomes mixed with an incoherent part [58], leading to a coherence time

$$\frac{1}{T_2} = \frac{1}{2T_1} + \frac{1}{T_2^*}, \tag{3.7}$$

where T_1 and T_2^* define the radiative lifetime and the pure dephasing time, respectively. The dephasing reduces the coherence time of the photon and, additionally, has the potential to change the resulting profile, depending on the type of process present. Since the temporal fluctuations in phase and broadening of the frequency spectrum are manifestations of the same physical effects resulting from the dephasing processes, the Wiener-Kintchine Theorem tells us that the frequency spectrum $\tilde{I}(\omega)$ is related to the first-order temporal coherence function, $g^{(1)}(\tau)$, via the Fourier transform [58]

$$\tilde{I}(\omega) = \frac{1}{\sqrt{2\pi}} \int_{-\infty}^{\infty} g^{(1)}(\tau) e^{i\omega\tau} d\tau, \tag{3.8}$$

where $g^{(1)}(\tau)$ is defined by the correlation of the electric field operators for the single-photon mode [46]

$$g^{(1)}(\tau) = \frac{\langle \hat{E}^-(t)\hat{E}^+(t+\tau)\rangle}{\langle \hat{E}(t)\rangle^2}, \tag{3.9}$$

and is therefore related to the temporal modefunction, $\xi_j(t)$, defining the single-photon wave packet by [121]

$$\begin{aligned} \hat{E}_j^+(t) &= \xi_j(t)\hat{a}_j \\ \hat{E}_j^-(t) &= \xi_j^*(t)\hat{a}_j^\dagger, \end{aligned} \tag{3.10}$$

where $\hat{a}_j$ ($\hat{a}_j^\dagger$) is the photon annihilation (creation) operator for mode j.

This allows information about the spectral features to be inferred directly from measurements in the time domain. Such a technique, known as Fourier-transform Spectroscopy (FTS) [122–124], is a very powerful tool in single-photon spectroscopy, as characterisation of narrow linewidth emitters in the spectral domain can be experimentally challenging, typically relying on the use of highly lossy Fabry-Perot etalons. Conversely, measurements of the temporal coherence function $g^{(1)}(\tau)$ can be made directly with very high precision using a Michelson Interferometer (MI), where single-photon

interference fringes can be measured according to the output intensity

$$I(\tau) = I_0 \left[1 + |g^{(1)}(\tau)| \cos\left(\frac{E_0 \tau}{\hbar} + \phi(\tau) \right) \right], \tag{3.11}$$

where I_0 is the input intensity. The interference visibility can then be calculated as

$$V(\tau) = \frac{I_{max} - I_{min}}{I_{max} + I_{min}} = |g^{(1)}(\tau)|, \tag{3.12}$$

where I_{max} (I_{min}) correspond to the cases of constructive (destructive) interference. Thus, by measuring fringes for several values of the coarse delay and calculating $V(\tau)$, one can access $|g^{(1)}(\tau)|$ which directly determines T_2, the shape of the $\tilde{I}(\omega)$ in the frequency domain and thus the characteristic dephasing processes affecting the emitter. The coherence time is calculated from $|g^{(1)}(\tau)|$ using [125]

$$T_2 = \int_{-\infty}^{\infty} |g^{(1)}(\tau)|^2 d\tau. \tag{3.13}$$

3.4.1 Temporal Mode Function of the Neutral Exciton

As the focus of experiments in this project work is towards teleportation using the entangled photon-pairs from the XX-X cascade, the coherence properties of these lines are the main interest, since they will be used for the interference discussed in Chapter 5. For this reason, characterisation of coherence times will also predominantly focus on these neutral lines. As discussed in Section 2.2.3, the presence of the anisotropic exchange interaction results in the FSS between the degenerate levels of the X, resulting in a linearly polarised doublet. Assuming for now that the transition is dominated by homogeneous broadening as a result of fast-relaxation processes such as those caused by carrier relaxation in above-band excitation, the frequency spectrum of the X will then comprise a pair of Lorentzian functions of the form

$$\tilde{I}(\omega) = \frac{\Gamma}{2\pi} \frac{m}{(\omega + \omega_0)^2 + \Gamma^2/4} + \frac{\Gamma}{2\pi} \frac{(1-m)}{(\omega - \omega_0)^2 + \Gamma^2/4} \tag{3.14}$$

where m defines the relative intensity of the doublet, Γ is the frequency linewidth and ω_0 is the frequency splitting. Here, the linewidth Γ is taken to be the same for each transition, however, in general this may not be true [126]. The relative intensity m is used to account for any difference in detection probability corresponding to polarising elements of the detection system. The first-order coherence function is then simply

$$g^{(1)}(\tau) = e^{-\frac{1}{2}(2i\omega_0 + \Gamma)\tau} \left(-e^{2i\omega_0 \tau} (-1 + m) + m \right) \tag{3.15}$$

from which the visibility can be determined as

$$V(\tau) = e^{-\frac{\tau}{T_2}} \sqrt{-2(m-1)m\cos(S\tau/\hbar) + 2(m-1)m + 1} \tag{3.16}$$

where the coherence time, T_2, and the energy splitting, S, are defined as

$$T_2 = \frac{2}{\Gamma} \tag{3.17}$$

$$\frac{S}{\hbar} = 2\omega_0 \tag{3.18}$$

and Equation 3.16 fulfils the condition of Equation 3.11. A simulation of the expected output for such a state is shown in Figure 3.10 for $T_2 = 2$ ns, $S = 2$ μeV and for different values of the relative intensity m, showing the effect of moving from a perfectly balanced doublet into a single transition.

The unpolarised emission is chosen for measurement as it allows all the intensity from the QD to be sent into the interferometer. Since the loss of the MI was approximately 50%, this was helpful for increasing the SNR. Additionally, the measurement of the beating effect from the doublet provides an independent and high-resolution method to determine the FSS, as the curve can be sampled in the time-domain with a resolution set by the step-size of the optical delay line (ODL). This can be particularly useful for characterising smaller FSS values, provided the length of the ODL is sufficient to resolve the beat.

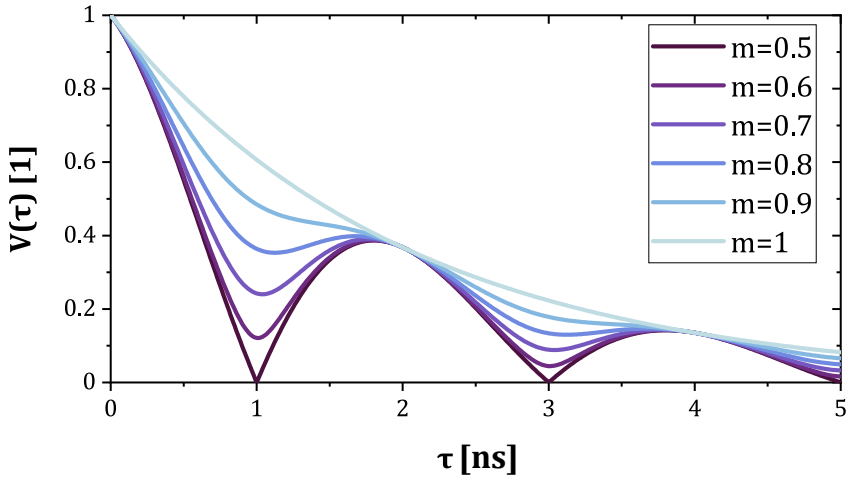

Figure 3.10: Simulated visbility function for an X doublet.

3.4.2 Single-Photon Interference Measurement

For characterising single-photon interference, a MI was used to determine the coherence time T_2 of the emission from single QDs. For this purpose, an all-fibre MI was constructed using standard SM telecom wavelength components. Figure 3.11 shows the implementation of this. A 50:50 beamsplitter was used to split the incoming light between the two arms. An ODL in one arm allowed the time delay between the two arms to be varied coarsely, while a piezo-actuated fibre-stretcher (FS) in the other arm allowed the length between the two arms to be varied with sub wavelength resolution. In both arms, a Faraday mirror (FM) was used to reflect the light back onto the 50:50 beamsplitter.

The output intensity was then sent to either the spectrometer for multi-line analysis, or towards a transmission grating for detection using SNSPDs. The use of the FM ensured that any rotations to the state caused by the fibre while in transmission in one direction were subsequently reversed upon transmission back down the same path. This was found to work with great success provided the MI was relatively well-isolated from fast thermal fluctuations, which was achieved simply by housing the interferometer in a polystyrene box. Experimentally, the fine-delay in the interferometer was scanned through the application of a bias voltage to the FS, for each coarse position set on the ODL. The inset of Figure 3.11 displays an example of such interference fringes for a scan range of 0.5-1.5 V, where multiple wavelengths can be seen, thus allowing accurate sinusoidal fits to the data.

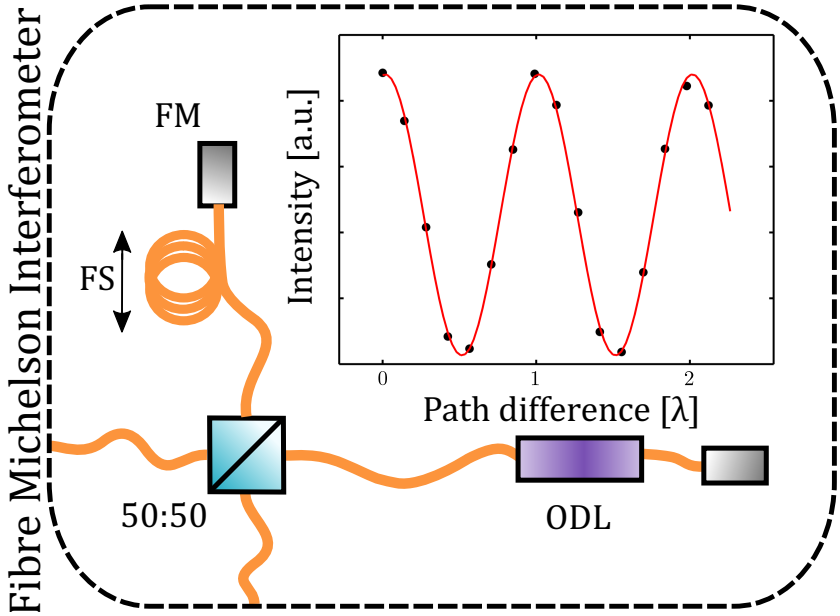

Figure 3.11: Fibre-based Michelson interferometer for single-photon interference measurements. All standard telecom fibre components are used in the construction. Input light is incident on a 50:50 beamsplitter and sent down two arms of the interferometer. In one arm, an ODL use used to set the coarse delay position, before being reflected using a FM. In the other arm, the voltage of a piezo-actuated FS is scanned to measure single-photon interference fringes in the output intensity.

An example measurement of an X can be seen in Figure 3.12, where the calculated interference contrast is plotted over a range of ~ 500 ps for a QD optically excited at the X saturation power. The data has been fitted using the Equation 3.16, where $T_2 = 309 \pm 15$ ps, $S = 17.8 \pm 0.2$ μeV and $m = 0$. The upper panel shows the corresponding interferogram for the measurement, where it is possible to see the interference decay for all major transition in the QD. The right panel shows a time-integrated spectrum close to the zero-delay, where the shaded area denotes the region of integration. The main panel inset shows two examples of the integrated intensity of the X for high and low visibility, where additional care has been taken to integrate over a region wider than the spectral resolution, as to not artificially increase the coherence time through spectral filtering [122]. The QD used for this

measurement is the same as that shown in Figure 3.4 for the FSS measurement, and shows a perfect agreement with the value for the FSS. This measurement was best described with $m = 0$, highlighting that there were no significant polarisation effects.

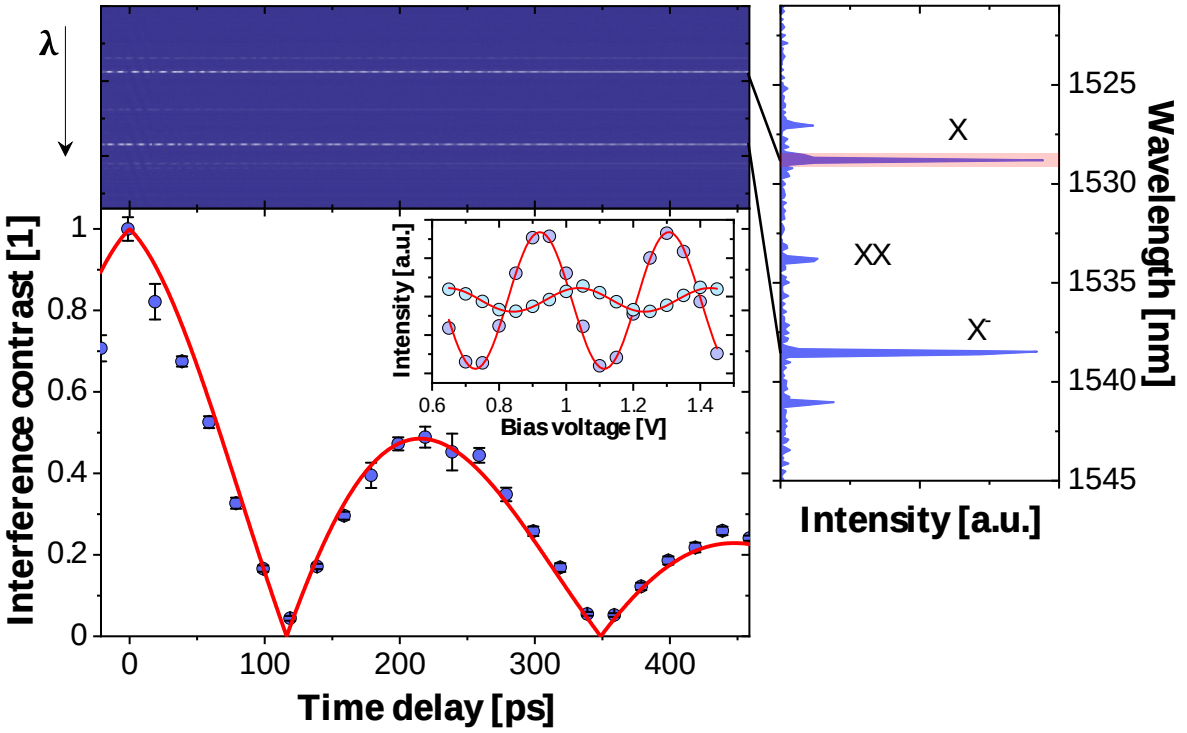

Figure 3.12: Measurement of single-photon interference using all-fibre MI. Fitted interference visibility as a function of coarse delay steps for a QD optically excited at the X saturation power. Solid (red) line is a fit to the data according to Equation 3.16, where $T_2 = 309 \pm 15$ ps, $S = 17.8 \pm 0.2$ μeV and $m = 0$. Upper panel displays the raw interferogram of the measurement, and the right panel displays a time-integrated spectrum of the QD, where the shaded region denotes the area integrated for the visibility calculation. Main panel inset displays two examples at zero delay and ~ 120 ps of interference fringes for high and low visibility.

Chapter 4

Characterisation of Single-Photon Emission from InAs/InP Quantum Dots

In this chapter, a thorough characterisation of the InAs/InP QDs emitting near the telecom *C*-band is performed. The emission from the QDs is characterised both spectrally, in order to determine the main spectral features and the coherence properties, and through time-resolved measurement, in order to determine the single-photon level and emission dynamics of the emitters. These measurements provide an understanding of the internal dynamics of the emitters and are used in order to determine suitable QDs for performing interference and entanglement measurements, the prerequisites for quantum teleportation.

4.1 Introduction

The development of QD quantum light sources emitting directly into the telecom *C*-band is crucial for applications in efficient long-distance fibre quantum networks due to the minimum loss in transmission at these wavelengths. As discussed in Section 2.2.5, most systems currently looking to reach this band have relied on strain relaxing growth methods using the InAs/GaAs QD material system [85], where single-photon emission has been demonstrated [127–129]. An alternative method to reach these wavelengths, and the approach adopted in this work, is to swap the host material for InP [93, 94, 96], where there have also been successful demonstrations of single-photon emission [87, 95, 130–132]. However, there is to date a lack of a promising single-photon sources in this band which simultaneously offer high photon count rates, high entanglement fidelity and high photon indistinguishability, such as to enable quantum information applications.

Building on the previous success in this lab with InAs QDs emitting at telecom wavelengths [83, 84, 99, 133, 134], a characterisation of InAs QDs grown on an InP will be performed in order to understand the emission dynamics of these QDs. Firstly, power and temperature-dependant spectroscopy will be considered to determine the different excitonic complexes, followed by time-resolved spectroscopy to analyse the single-photon performance and the internal QD dynamics. The chapter will then

conclude with a study of the coherence times, in order to characterise the suitability for interference-based applications.

4.2 Photoluminescence Spectroscopy

As discussed in Section 3.1.1, photoluminescence spectroscopy was used to perform measurements in the spectral domain of the QDs. Optical excitation of the QD using a non-resonant laser creates electrons and holes in the bulk InP matrix, which are captured by the QD with picosecond relaxation times. Since the decay time of the QD transitions is on the order of nanoseconds, and the acquisition of a spectrum is on the order of seconds, the measured spectrum consists of the sum of the many charge configurations reached within this time. As such, many transitions from each of the charge complexes discussed in Section 2.2.2 can be seen in a typical spectrum. These spectra, therefore, show numerous lines originating from a single QD. It is possible to use excitation power, temperature and polarisation-dependent measurements to assign the main spectral features to the different excitonic complexes, in order to characterise and further understand some of the relevant emission dynamics from these QDs. This type of basic characterisation is an essential first step in the unambiguous identification of the neutral X and XX, which form the basis of all experiments in this work. Additionally, such understanding is necessary for this relatively new platform, where little research has been conducted previously, in order to guide future improvements to the growth conditions or doping profiles, for instance.

4.2.1 Power Dependence

To begin, an excitation power dependence in the PL intensity was measured using a CW above-band laser at 785 nm at $T = 12$ K, in order to classify the single excitonic states from the multi-excitonic states. Due to the population dynamics of the QD, it is expected that the probability to capture an electron-hole pair, for excitation powers below saturation, is Poissonian [135, 136]. A typical power-dependent spectrum is shown in Figure 4.1a, where initial estimates of the spectral assignments have been labelled. The respective integrated intensities of these spectral features is shown in Figure 4.1b.

As can be seen for three of the five major transitions, there is an approximately linear dependence on the excitation power corresponding to a single excitonic state. This is confirmed by a linear fit (on a log-log scale) to what is suspected to be the neutral X at this point, showing a gradient of ~ 0.88. The remaining two lines show a somewhat increased gradient in the excitation power dependence. However, in contrast to the expected quadratic dependence on excitation power, the gradient is determined to be only super-linear with a value of ~ 1.35. The increased gradient thus determines such states to be multi-excitonic or potentially higher-lying charged states, such as a doubly charged exciton, where the additional charge carrier occupies the p-state [73]. This dependence of the PL intensity with above-band optical excitation was found to be consistent across many QDs in the sample investigated. From the measured gradients, in addition to the polarisation dependence of the

FSS as discussed in Section 3.1.3, it was possible to clearly determine the neutral X and XX states. While this was sufficient to proceed for the experiments considered here, it is interesting to examine the other spectral features in order to develop a greater understanding of the QD dynamics.

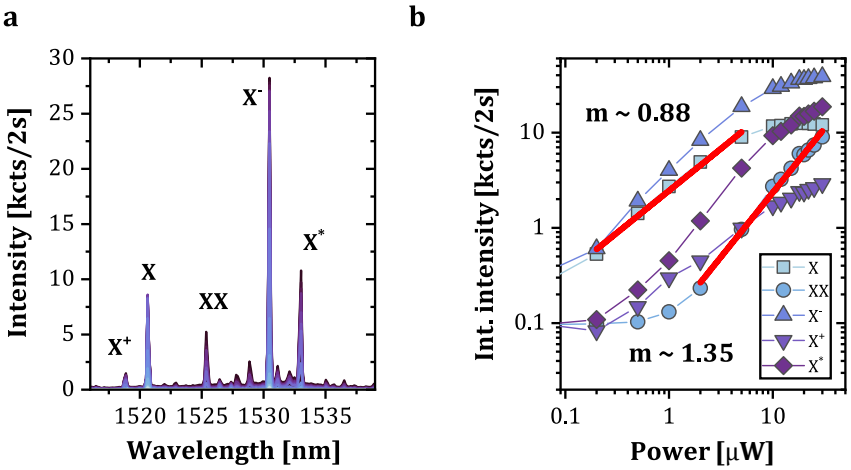

Figure 4.1: Power dependence of an optically excited QD. a Power-dependent spectrum under optical excitation with 785 nm light at $T = 12$ K. **b** Integrated intensity of the main transitions from **a**. Linear fits (on a log-log scale) to the data (red-lines) shows gradients of ~ 0.88 – 1.35 for all transitions.

In addition to the consistency of the gradients of the PL intensity as a function of excitation power for the five major spectral features, the relative intensities and relative recombination energy of these features was also found to be remarkably consistent across the majority of QDs in the sample. While the average recombination energies shifted due to size variations of the QDs, the relative energies of the transitions with respect to the X remained consistent. The distinctive pattern in the energy distribution of the transitions can be seen in Figure 4.2, where the binding energy of each line has been plotted relative to the X. This data was taken from the FSS study in Section 3.1.3, however, the distinctive pattern remained similar for lower temperatures, with a shift in relative intensities.

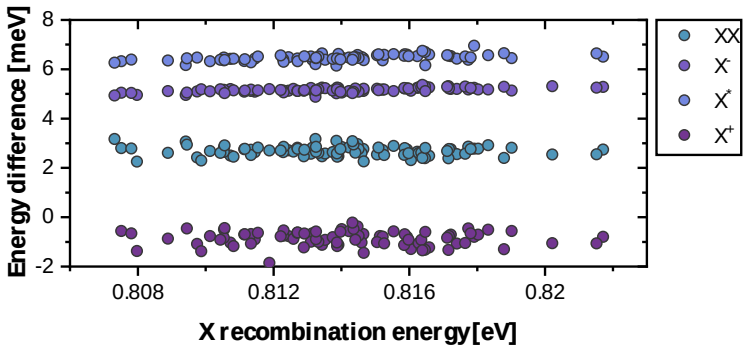

Figure 4.2: Relative recombination energies of main QD transitions. Energy of the main transitions relative to the neutral X for a sample of 90 QDs under EL at $T = 40$ K. The spectra of each QD displayed a consistent pattern in energies, as shown for nearly all QDs measured. No trend is seen as a function of X recombination energy, for the range considered here.

This distinctive distribution of the recombination energies suggests that the formation and morphology of the QDs in this sample was similar, resulting in similar confinement potentials and energy structure. From this, the additional transitions are tentatively assigned as in Figure 4.1a, by consideration of the energetic ordering, whereby due to the Coulomb interaction and the relative mass of the electron and the heavy hole, the X^- (X^+) is found at lower (higher) energy than the X [75, 137–139]. The XX is found to be in the binding regime with a mean binding energy of $\Delta E_B = 2.69 \pm 0.19$ meV. The assignment of the X^* corresponds to an indeterminate charged state, with the possibility of it being a charged biexciton XX^- or a doubly negatively charged exciton X^{2-}. The assignment of the singly charged states is supported by the excitation power dependence, in addition to the absence of a fine-structure [73]. It is further supported from the doping profile of the structure [99], the large p-p contact resistance discussed in Section 3.1.2, and the increased overall intensity in the lower energy side of the spectrum, suggesting an asymmetry of electron and hole capture rates and an overall tendency for the QD to be negatively charged. It should also be noted that while doping profile and asymmetric capture rates of electrons and holes could explain the overall negative spectrum, it was recently demonstrated that the lack of a wetting layer could result in highly negatively charged complexes in smaller QDs emitting near 960 nm [140]. However, the structure investigated in this work comprised of a pronounced Coulomb blockade, whereby electrons could be added one by one through the application of a gate voltage, which is not the case here.

4.2.2 Temperature Dependence

The operating temperature of a QD source requires a compromise between technical convenience and optimal environment afforded by very low operating temperatures. At higher temperatures above liquid He temperature, increased interaction with phonons are a dominant source of dephasing and reduction in the optical quality of QD emission [141–143]. On the other hand, it is more technically feasible to operate such sources at higher temperatures, in order to reduce the complexity of the experimental apparatus, resulting in the possibility of more compact systems [144, 145]. Operation of a single-photon source at liquid-nitrogen temperatures in the telecom C-band has already been demonstrated with GaAs-based QDs [128], as well as entangled photon pairs in InP-based devices [99]. Such a high temperature operation would be a desirable situation moving forward, especially when looking towards field deployment applications [134] using portable systems [145]. Since similar QDs to those used here have already been used in a demonstration of single and entangled photon emission at elevated temperatures (up to ~ 77 K), consideration of the suitability of such an operation for interference-based applications will be made in Section 4.4. However, the characterisation of the QD as a function of temperature is used here to first assist in the assignment of the main spectral features.

The PL characterisation above was performed at cryogenic temperatures of $T = 12$ K, where only very low-energy phonons up to $k_B T \sim 1$ meV are available to interact with the QD states, resulting in sharp features from the zero-phonon line (ZPL) [141]. Figure 4.3a shows an example of a spectrum

for the same QD excited optically at $T = 45$ K, where the phonon-induced broadening is immediately apparent. Another feature, is the increased relative intensity of the X^+ transition with respect to the X^- and X^*. Indeed, by examining the normalised intensity as a function of temperature, as shown by Figure 4.3b, it can be seen that there is a shift in the relative intensity from the X^- to the X^+ for increasing temperature. This supports the previous assignment of the charge complexes, due to the consistency with the increased availability of holes for higher temperatures, corresponding well with the onset of EL under a positive bias at such temperatures. The characteristic redshift in the X-energy is also seen for increasing operating temperatures, relating to the change in the bandgap energy. In addition to this, there is a rapid broadening of the ZPL as a result of phonon-assisted relaxation, and also emission into the phonon sidebands corresponding to the coupling of the exciton to acoustic phonon states [146]. While it is possible to filter out these sidebands, the observed broadening of the ZPL for increasing temperature will naturally reduce the coherence in the emission, and will be explored in Section 4.4 to determine the suitability for higher temperature experiments.

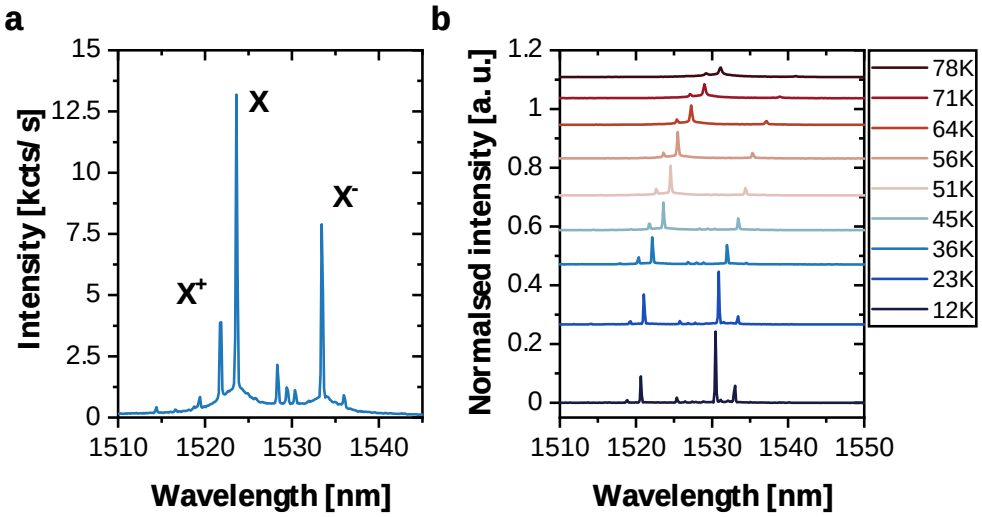

Figure 4.3: Temperature dependence of the QD spectrum. **a** Spectrum of a QD under optical excitation with 785 nm light at $T = 45$ K. Higher temperatures result in the coupling of optical phonons leading to an increase in the linewidth of the QD ZPL transitions, in addition to the appearance of phonon side-bands. **b** Temperature-dependent normalised spectra for excitation powers below the X saturation. The increasing temperature leads to a redistribution of the charge configurations within the QD, as seen by the change in the relative intensity of the negative and positive charged excitons

4.3 Single-Photon Emission Dynamics

The single-photon nature of the QD light source is of particular importance when looking towards quantum information applications. As discussed in Section 2.1.1, the quantum nature of the emission from QDs can be characterised by determining the degree to which the light is anti-bunched. In this section, a basic characterisation of the single-photon properties of a QD emitting near the telecom C-band is performed using above-band excitation at 785 nm.

4.3.1 Second-Order Intensity Correlations

The HBT correlation for the X is shown in Figure 4.4, under excitation at P_{Sat} (left) and $P_{Sat}/4$ (right). Following the anti-bunching dip at short time delays $|\tau| > 0$, the correlations show a small bunching. This corresponds to an increased probability for detection of another X photon at short times after fast re-excitation or population from a long-lived shelving state. The width of the dip is narrower than expected for the radiative lifetime of this QD, corresponding to re-excitation of the X. The most important feature to note is the relatively smooth dip that is almost Gaussian in shape, for both excitation powers. This deviates strongly from the expected exponential dip shown in Figure 2.2 for an ideal two-level system, indicating the presence of multiple energy levels involved in the single-photon emissions dynamics. This is, in part, seen by the fact the emission spectrum displays five prominent spectral transitions, with a host of much smaller ones, and can also be related to the excitation scheme used. Since carriers are excited in the bulk InP, there are multiple relaxation channels available when populating the QD. Therefore, each energy state involved in the process adds to the emission dynamics. For lower power, the bunching time increases and remains coupled, indicating a slower population and longer population time of the intermediate shelving states.

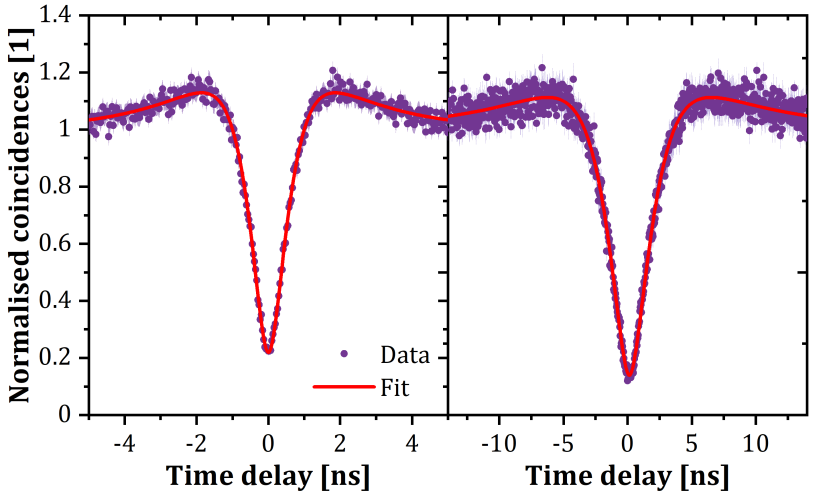

Figure 4.4: HBT autocorrelation under 785-nm excitation. (**Left**) High power excitation at P_{Sat}. A fit to the data (solid line) reveals a raw (deconvolved) $g^{(2)}(0) = 0.22 \pm 0.01$ (0.21 ± 0.01). (**Right**) Low power excitation at $P_{Sat}/4$. A fit to the data (solid line) reveals a raw (deconvolved) $g^{(2)}(0) = 0.15 \pm 0.02$ (0.14 ± 0.02).

To describe the main features of the data, a 10-level rate equation model based on the work in [147] is constructed and numerically solved. The model includes the main QD transitions seen in the spectra, in addition to the individual charge states, such that there are the levels $\{g, e, h, X, X^+, X^-, 2e, X^{2-}, XX, XX^-\}$. To account for the above-band excitation, the population dynamics are defined solely by the timescales c_e and c_h, the electron and hole capture times, respectively. The capture of a bound exciton such as in the model of [148] is decoupled here. The radiative decays are set to be those determined from time-resolved measurements for the X ($\tau_X = 1.77$ ns), XX ($\tau_{XX} = 0.35$ ns), and the charged lines are set equally to the measured value of the X^- ($\tau_{X^-} = 1.6$ ns), which is merely an approximation here. The radiative transitions of the XX^- and the X^{2-} in the first case are set to be instantaneous and have little effect on the emission dynamics when considering only the X (as determined by large fitting errors).

By solving the system of equations for the populations, the second-order autocorrelation functions are then defined as in Section 2.1.2 by [149]

$$g^{(2)}_{\mathrm{QD}}(\tau) = \frac{(n_i(\tau)|n_i(0) = 0)}{n_i(\infty)} \tag{4.1}$$

where n_i is the population of the state i and the initial conditions are determined by the system being in the state resulting after excitonic recombination from the state considered. For the X, the conditions simply start from the ground state being populated due to the previous detection of an X photon. To account for the contributions of uncorrelated light and the detector dark counts (typically $< 1\%$ of the count rate at saturation power), the correlation function is corrected according to

$$g^{(2)}_{\mathrm{HBT}}(\tau) = \frac{g^{(2)}_{\mathrm{QD}}(\tau) + 2\beta + \beta^2}{(1+\beta)^2} \tag{4.2}$$

where β is the fraction of uncorrelated light, which leads to an increase in the $g^{(2)}(0)$ and reduces the single-photon purity of the source. Equation 4.2 is then convolved with the Gaussian detector response with a timing resolution of $\Delta\tau_{\mathrm{Det}} = 125$ ps for these measurements. Using this model results in an excellent agreement with the experimental data for the X in both power regimes, as shown by the solid red lines in Figure 4.4. For the measurement at P_{Sat}, the fitted electron and hole capture times were $c_e = 1.07 \pm 0.08$ ns and $c_h = 1.16 \pm 0.06$ ns, respectively. The slightly faster capture time for the electron suggests again that the holes are limited in supply leading to a more negatively charged QD, on average. A fitted background contribution of $\beta = 0.12 \pm 0.01$ results in a deconvolved $g^{(2)}(0) = 0.21 \pm 0.01$, which is far below the threshold of 0.5 to demonstrate single-photon emission. This value is relatively high when compared to some other values of telecom C-band QD sources [68]; however, these QDs were quasi-resonantly excited using the QD p-shell. The values obtained here are still comparable to other InAs/InP-based systems at this wavelength [81]. For the measurement at $P_{\mathrm{Sat}}/4$, the fitted electron and hole capture times $c_e = 3.86 \pm 0.10$ ns and $c_h = 4.44 \pm 0.08$ ns, respectively, are much longer due to the low excitation power. The difference between the electron and hole capture times is more pronounced for the lower excitation power, indicating that the holes become

the limit in the X emission. This leads to longer bunching times as a result of the time spent in the intermediate electron state, as shown in Figure 4.4. The fitted background here is $\beta = 0.08 \pm 0.01$ leading to a $g^{(2)}(0) = 0.14 \pm 0.02$, which is lower as expected. This is due to the lower excitation power reducing the amount of background light coming from the semiconductor environment, since at high power the X intensity becomes saturated and the background intensity increases linearly. Note that the detector response here has little effect on the measured $g^{(2)}(0)$ due to the wide nature of the dip around the zero delay and, therefore, the deconvolved curves are not displayed. In this regard, the model has given a fairly accurate estimation of the emission dynamics and single-photon level, since it accurately describes the shape of the correlation function under both powers considered.

4.3.2 Multilevel Dynamics

After using the multilevel rate equation model to some degree of success in describing the X emission dynamics, it is interesting to further consider some of the other levels involved. For this, a series of cross correlations were recorded by Toshiba Research Laboratory colleague Dr. Tina Müller, with the QD excited at P_{Sat}. The results of these can be seen in Figure 4.5, where each correlation considered has been labelled and the model discussed previously has been evaluated using the parameters derived from the previous fits.

The main focus in these cross correlations was to examine relations between the X and the charged complexes X^-, X^+ and the indeterminate X^*. Here, it was found that describing this transition using the X^{2-} population gave the most accurate picture. Indeed, excellent agreement was found qualitatively for the dynamics of the negatively charged transitions when assuming radiative lifetimes $\tau_{XX^-} = 0.5$ ns and $\tau_{X^{2-}} = 1.2$ ns, which were determined manually through iterative adjustments to obtain reasonable agreement, and were not fitted. This is evidenced in particular by the excellent fit to the X^- autocorrelation, where only the background contribution was fitted and all other parameters were fixed to those determined from the X fit. The X^- autocorrelation is not only well described by the model, but also displays a better single-photon character than the X, with a raw (deconvolved) $g^{(2)}(0) = 0.09 \pm 0.02 (0.08 \pm 0.02)$. The lack of bunching features leads to a more familiar two-level appearance. However, the round dip is still present here indicating again the high relaxation dynamics involved in the X^- emission. In terms of applications requiring only single-photon emission such as QKD [24], the brighter emission of the X^- coupled with the higher single-photon purity could be a promising route for further investigation, particularly when looking towards resonant excitation schemes to further improve the single-photon purity.

Considering the X^--X correlation, the small bunching after detection of an X^- photon relates to the capture of time of a hole in the e state, leading to a small increase in the probability to detect a subsequent X. The lack of any bunching features on the X^*-X correlation shows that there is no significant coupling between the states. The slightly faster rise time for negative delay corresponds to a faster capture time of multiple electrons and a hole from the ground state versus the capture time of multiple holes after emission of a X^*. The increased probability for detection of a X^- following

detection of an X^* corresponds to a fast capture time of a hole from a double electron state. Further evidence to suggest X^* may originate from doubly-charged complex could also be seen from the XX-X^* correlation, where there are no bunching features indicative of indirect cascades. In such a model, there would be a small level of bunching present between the XX and an XX^- state, relating to the capture time of a single hole following emission of an XX^-. Instead, there is a longer refill time for the X^* following detection of an XX, and no increased probability for detection of an X^* prior to the detection of an XX.

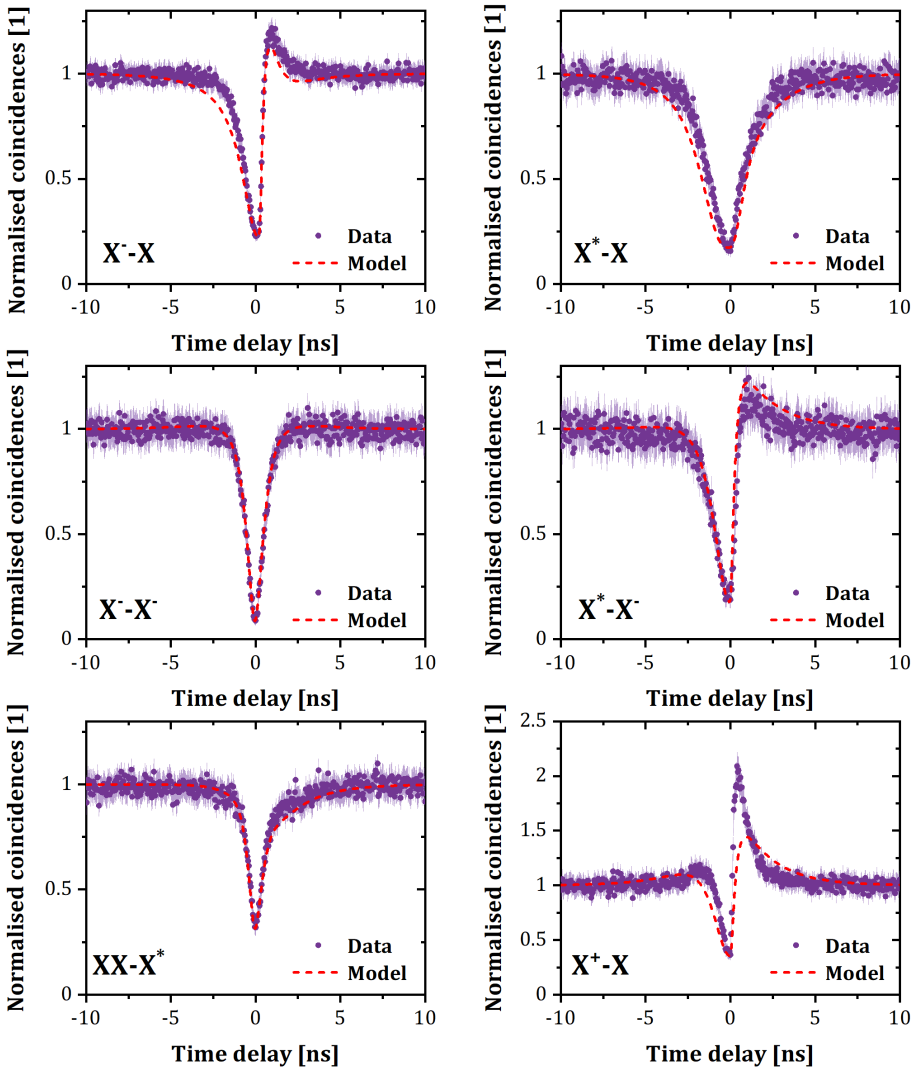

Figure 4.5: HBT cross correlations under 785-nm excitation. Cross-correlations taken between various different transitions of the QD, focused mainly on the longer wavelength transitions and the X. Each correlation was defined using the fitted electron and hole capture rates from the X autocorrelation, with assumed radiative lifetimes $\tau_{XX^-} = 0.5$ ns and $\tau_{X^{2-}} = 1.2$ ns.

Finally, it is noted that this model, while able to describe some of the features observed, does not hold a complete picture of the dynamics from this QD. While there is decent qualitative agreement, some details involving the XX and X^+ emission are not captured, as evidenced by the X^+-X correlation. Some of the main features are still present, including the increased probability for detection of an X after detection of an X^+, as a result of the fast electron capture time. This serves to highlight the rich dynamics involved in the emission of the QD when excited non-resonantly. Naturally, resonant excitation schemes would not only reduce the complexity of the QD population, but also lead to cleaner and more pure emission from the QD [68].

4.3.3 GHz-Clocked Single-Photon Emission

The development of a single-photon source compatible with state of the art QKD systems is critical for the generation of high-speed, unconditionally secure key rates [24, 150]. It has the potential to yield an advantage over commonly used weak coherent state sources and decoy state implementations [35] of QKD when the operation of such a device becomes feasible [151]. In this section, the work towards realising such a high-speed single-photon source in the telecom C-band will be introduced and further characterised in terms of the single-photon level with respect to the operating frequency of typical pulsed single-photons sources based on QDs [152, 153].

In order to characterise this source under high frequency excitation and demonstrate that the single-photon nature persists, the flexible pulsed excitation scheme introduced in Section 3.3 was used to excite the QD selected for the laser-QD interference (Section 5.4), entanglement (Chapter 6) and the teleportation experiment (Chapter 7). As discussed, for these later measurements 1310 nm excitation was used. The characterisation is summarised in Figure 4.6, where comparison of the time-resolved intensity for a lower, typical excitation frequency of $f = 100$ MHz, and a higher $f = 1$ GHz frequency is shown in Figure 4.6a. The lifetime measurements show typical behaviour for both the X and the XX. For the XX, there is a sharp turn on corresponding to the rise time of the electrical trigger and the fast population of the XX state, then similar relatively short radiative lifetimes of 272 ± 2 ps and 262 ± 6 ps at 100 MHz and 1 GHz, respectively. For the X, a slower rise time due to the population filling effects is seen, along with a much longer radiative lifetime of 1.56 ± 0.01 ns at both repetition rates. This leads to well-separated pulses in the QD emission at 100 MHz, however, for the GHz-excitation rate common for many QKD protocols [154, 155], the time period becomes comparable to the radiative lifetime. Consequently, a significant reduction of the on-off contrast in the emission of the X, to around 12%, is seen and a similar but reduced effect for the XX is seen, going down to 69%.

It is reasonable to expect that this overlap of radiative decay cycles will affect the single-photon nature of the emission under high frequency excitation. Looking at the intensity autocorrelations of the X using a HBT setup with the correlator in histogram mode, as was utilised previously, the expected pulse signature is found when driving at 100 MHz, as shown in Figure 4.6b, where the finite intensity for the zero-delay pulse is mainly due to re-excitation effects. For excitation at 1 GHz,

however, a strong CW emission signature is seen, including large bunching around the zero-delay dip. When comparing the excitation at 100 MHz and 1 GHz, the single-photon purity is comparable. The measured $g^{(2)}(0)$ values of 0.14 ± 0.01 and 0.09 ± 0.05 for excitation at 100 MHz and 1 GHz, respectively, were determined by fits to the experimental data. In both cases, the $g^{(2)}(0)$ is far below the 0.5 threshold required to prove predominantly single-photon emission, thus confirming that the single-photon nature is preserved under high frequency excitation. The model for the 100-MHz data includes the effects from both a shelving state (increased probability for time delays $> |\tau_0|$) and re-excitation (a small volcano-like feature around the zero delay [156]). For the 1.07-GHz measurement, a standard three-level CW model with background correction was sufficient to describe the data [157].

In order to fully characterise the emission dynamics for the X at 1 GHz, it is interesting to consider how the correlation looks for each excitation cycle, given the relatively long radiative lifetime. To recover the pulsed signature of the single-photon emission, the arrival times of both X photons in the HBT setup are measured with respect to the laser excitation clock in a TTTR mode correlation. The result of this measurement can be seen in Figure 4.6c. Along the diagonal, corresponding to zero-delay coincidences of both X detectors, there is an absence of photons within the same 0.935×0.935 ns square, determined by the 1.07-GHz repetition rate. An increase in the normalised coincidences is seen for the excitation cycles immediately preceding, and following, the zero-delay cycle, corresponding to the bunching seen in the histogram measurement in Figure 4.6b. In a histogram correlation, the correlator effectively sums all events along the $\tau_1 = \tau_2$ line, corresponding to simultaneous detection times. The dotted data points in Figure 4.6d show the effect of performing such a summation on the TTTR data in Figure 4.6c. As can be seen, the observed CW-like signature is reconstructed fully, and serves to highlight that this is purely an artifact of this type of measurement. The added benefit is, of course, the extra information gained on the pulsed nature of the emission. By performing a pulse-wise summation of the coincidences, a $g^{(2)}(0) = 0.33 \pm 0.01$ for the zero-delay pulse is determined. While this is naturally higher than the histogram mode measurement due to the much larger integration window, it still clearly shows that there is a lack of multi-photon events within one entire excitation and emission period. Naturally, it would be more desirable to have a fully 'on-demand' single-photon source with such repetition rates and reduced multi-photon events within the entire cycle. Such a source in itself could be useful for single-photon QKD [151, 158–161], and could be realised through radiative lifetime enhancement through cavity coupling [130]. However, as shown in this section, despite non-resonant excitation and the long radiative lifetime of this QD, it is still possible to generate single-photon emission clocked at 1 GHz from InAs/InP QD sources emitting near the telecom C-band.

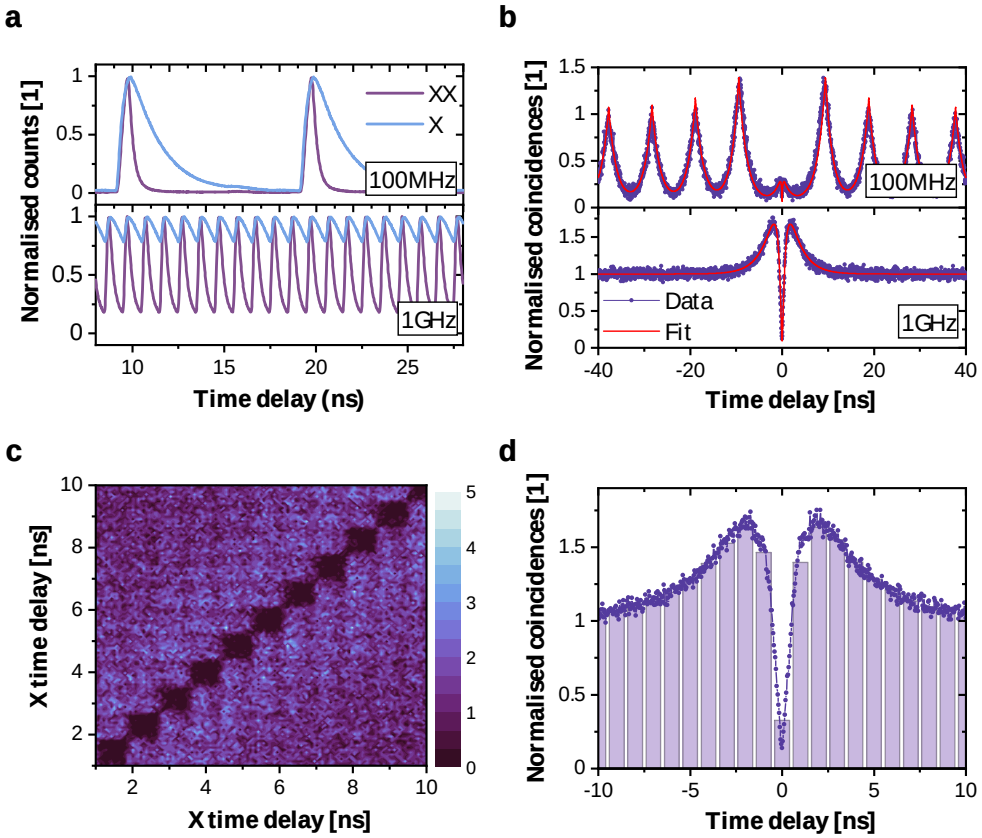

Figure 4.6: GHz-clocked single photon emission. **a** Time-resolved intensity of the X and the XX emission lines at a repetition frequency of 100 MHz (top) and 1.07 GHz (bottom). **b** Second-order intensity correlations of the X for 100-MHz (top) and 1.07-GHz (bottom) excitation frequencies. The solid lines show fits to the data. **c** Second-order correlation of each X photon, measured with respect to the excitation laser clock. The colour bar denotes normalized coincidences. **d** Reconstructed histogram from the measurement in **c**, obtained by summation over the $\tau_1 = \tau_2$ times for simultaneous detections, showing the observed CW-like signature in **b**. Bars denote normalised coincidences calculated for each excitation period.

4.4 Dephasing of Droplet Epitaxy Quantum Dots

An intrinsic problem in semiconductor QDs that limits their utility for interference-based experiments is the pure dephasing from the interaction with the environment, resulting in emission of photons away from the Fourier limit. A fluctuating charge environment in the vicinity of the QD is seen as the main contribution towards this [116]. As previously mentioned, carriers are generated in the bulk material and diffuse into the QD before recombination. However, imperfections and defects in the crystal lattice can trap holes and electrons. These trapped charges will shift the emission energy of the QD due to the quantum-confined Stark effect [116]. Fluctuation of this charge environment leads to a time-varying modulation of the emission, that obeys a Gaussian random process behaviour as depicted by Figure 4.7.

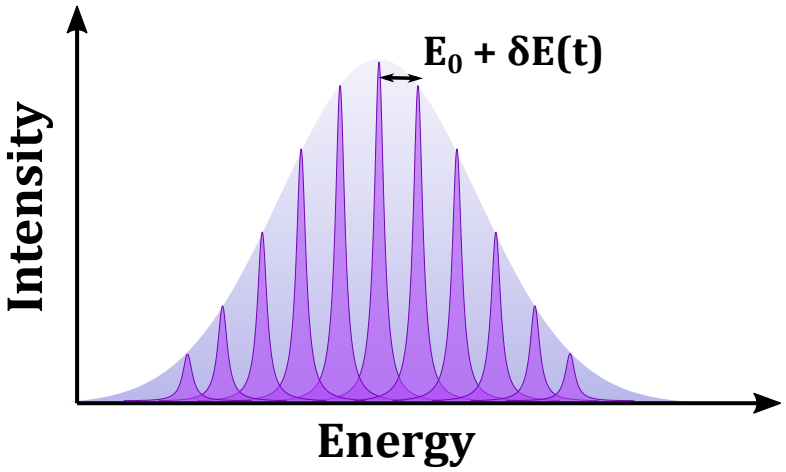

Figure 4.7: Spectral wandering in the emission of a QD. Nearby charge traps in the vicinity of the QD lead to a time-varying shift in the emission energy through the quantum-confined Stark effect. Due to the random nature of this process, the emission energy of the QD is weighted by a Gaussian frequency distribution.

An increase in the modulation of the emission can be caused by many factors, such as increasing the excitation laser power to generate more carriers [116, 162] or by increasing the temperature [163]. Creating more carriers in the continuum states causes increasing fluctuations in the charge environment as new configurations are explored. This leads to a faster spectral modulation of the emission line. A theory to model this in terms of the spectral fluctuation has been developed by [116], and applied to various QD systems [162–164] with great success. A stochastic theory of relaxation coupled to a fluctuating reservoir can be used to derive a form of the interference contrast decay [116]

$$V(\tau) = \mathrm{Exp}\left[-\frac{\Sigma^2\tau_c^2}{\hbar^2}\left(\mathrm{Exp}\left(-\frac{\tau}{\tau_c}\right)+\frac{\tau}{\tau_c}-1\right)\right] \tag{4.3}$$

where Σ and τ_c are the emission modulation amplitude and correlation time (describing the timescale to explore different charge configurations), respectively. The parameter $\frac{\Sigma\tau_c}{\hbar}$ is used to discriminate the level of dephasing in the system. This results either in an exponential with decay time $T_2 = \frac{\hbar^2}{\Sigma^2\tau_c}$

for $\frac{\Sigma\tau_c}{\hbar} \ll 1$, the fast modulation limit, or a Gaussian with FWHM $2\sqrt{2\ln 2}\Sigma$ for $\frac{\Sigma\tau_c}{\hbar} \gg 1$, the slow modulation limit. One can model the transition from fast to slow modulation by varying a single parameter $\frac{\Sigma\tau_c}{\hbar}$.

In this section, the dephasing mechanisms present in these DE QDs are probed through measurement of the coherence time using a MI. As discussed in Section 3.4, measurement of the temporal lineshape in this way can offer information about the dephasing mechanisms present. For fast (slow) modulation timescales, the type of dephasing is considered to be a homogeneous (inhomogenous) broadening of the natural linewidth of the emitter. In terms of FTS, it is simply modelled by a Gaussian weighting of the Lorentzian frequency spectrum, resulting in a Voigt profile [125]. In the time domain, this is simply calculated by the product of the individual Fourier-transforms, such that

$$V(\tau) = \tilde{L}(t) \times \tilde{G}(t) \tag{4.4}$$

$$= \mathrm{Exp}\left[-\frac{|\tau|}{\tau_L} - \frac{\pi}{2}\left(\frac{\tau}{\tau_G}\right)^2\right] \tag{4.5}$$

where $\tilde{L}(t)$ and $\tilde{G}(t)$ are the Fourier-transforms of the Lorentzian and Gaussian emission spectrum, respectively, and τ_L and τ_G refer to the characteristic Lorentzian and Gaussian decay times. The level of spectral modulation, or inhomogeneous broadening, is thus characterised by the presence of a Gaussian component in the decay of the interference contrast. Analogous to the above, Equation 4.4 results in an exponential decay with $T_2 = \tau_L$ for $\tau_L << \tau_G$, a Gaussian decay with $T_2 = \frac{\tau_G}{\sqrt{\pi}}$ for $\tau_L >> \tau_G$, and a time-domain Voigt profile for $\tau_L \sim \tau_G$, with the coherence time T_2 calculated using Equation 3.13.

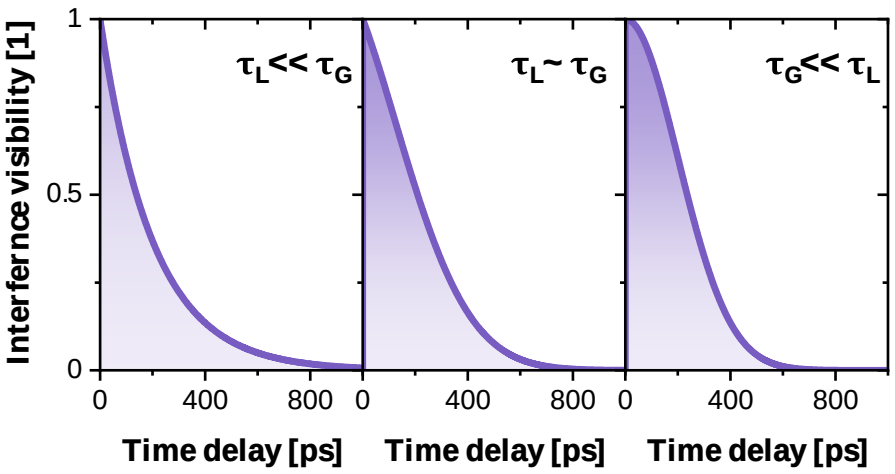

Figure 4.8: Interference contrast for increasing spectral wandering. For $\tau_L << \tau_G$, the decay profile is exponential. As the Gaussian dephasing becomes stronger, the decay follows a time-domain Voigt profile where $\tau_L \sim \tau_G$ before finally following a completely Gaussian decay for $\tau_G << \tau_L$.

4.4.1 Excitation Power Dependence of the Coherence Time

The characterisation of the coherence time begins by considering the excitation power-induced broadening of the ZPL. Particularly in non-resonant excitation schemes, the effect of increasing excitation power is to increase the carrier density in the semiconductor material. This naturally leads to an increasing interaction of the QD with the environment, which also introduces additional dephasing, for example, through the Stark effect as discussed above. However, an increase in the carrier density also results in higher PL intensity, which is beneficial in multi-photon experiments since they scale well with detection count rate. Therefore, being able to determine optimal operating conditions in terms of excitation power is an important first step towards TPI measurements.

This section presents an excitation power-dependent study of the coherence times of a QD that was found to display suitable brightness for two-photon measurements, with detected photon count rates of ~ 300 kcounts/s under above-band excitation at saturation. Figure 4.9a displays the results of this, where the coherence time of the X (blue) and the integrated intensity (purple) is plotted as a function of the excitation laser power. At the X saturation power, where the emission is the brightest, the coherence time is determined to be $T_2 = 299 \pm 9$ ps, which is more than sufficient to demonstrate post-selected interference with the detectors used here. Indeed, when comparing to the lifetime (shown in Figure 3.6 for this QD) of $T_1 = 1.77 \pm 0.01$ ns, the ratio $T_2/2T_1 = 0.085 \pm 0.003$ is determined. This value demonstrates an unprecedented level of coherence in such QDs emitting in the telecom C-band, being a factor of four larger than GaAs-based counterparts for similar excitation powers [165]. This poses a question of whether the InP-based system results in a reduction of the pure dephasing due to the different growth techniques for achieving emission in the C-band, or whether the investigated diode structure here was beneficial for producing a calmer charge environment for the QDs, despite the fact that the measurements here were conducted under an electrically open configuration. Such an investigation was outside of the scope of this thesis, but would be interesting in order to determine optimal structures for telecom C-band quantum light sources.

For low excitation powers, the coherence time increases, as expected, up to a remarkable $T_2 = 1058 \pm 134$ ps for $0.03P_{\mathrm{Sat}}$, corresponding to $T_2/2T_1 = 0.298 \pm 0.038$. While the intensity here is only ~ 10% of the saturation value, this demonstrates a potential for photonic engineering of the structure in order to improve extraction efficiency enabling the use of lower excitation powers, as well as, again, the potential of resonant excitation schemes in order to obtain photons much closer to the transform limit [166]. It is surprising that the emission remains reasonably coherent up to saturation given the excitation scheme, where a high level of dephasing is expected. This could be the result of the growth scheme used here, since QDs grown by DE nominally form without a wetting layer [90]. The wetting layer typically seen in the SK growth of QDs is essentially a charge reservoir for carriers to relax into the QD; therefore, removal or reduction of such a layer could potentially reduce the charge noise.

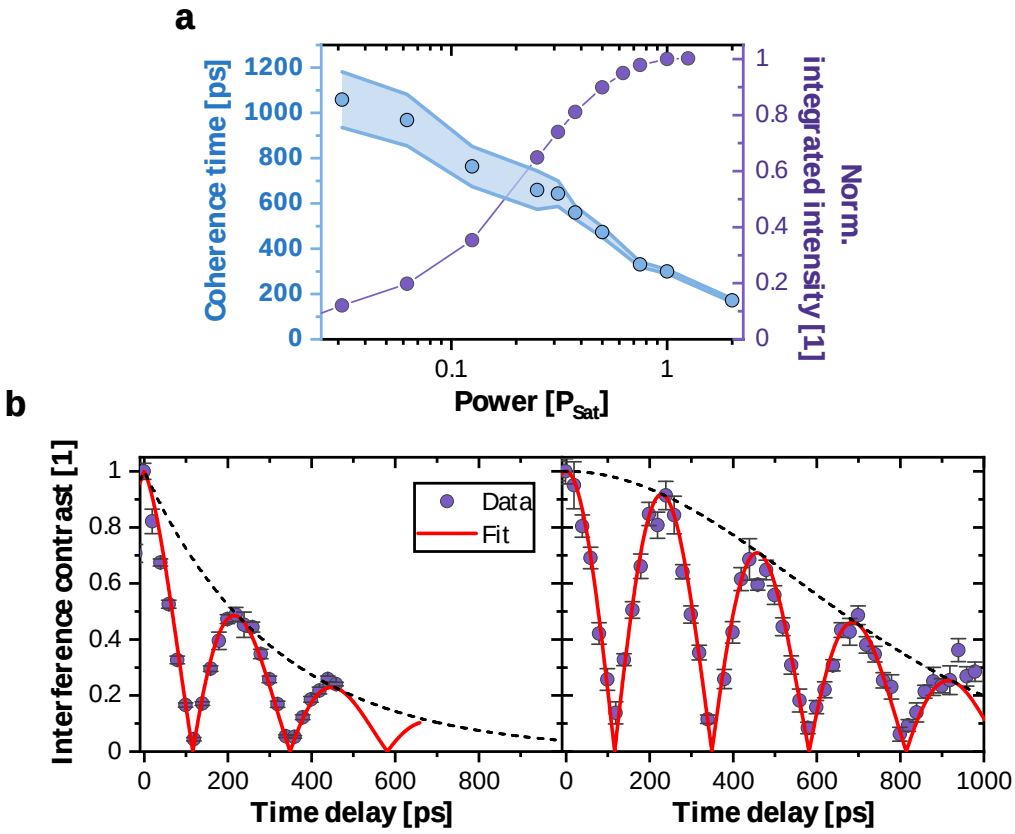

Figure 4.9: Excitation power-dependent coherence time. a Excitation power dependence of the coherence time (blue) and of the normalised integrated intensity (purple), for a QD optically excited at $T = 8$ K. Shaded areas denote error on the fitted coherence time. **b** (Left) Visibility decay using an extended ODL when exciting at P_{Sat}, displaying a largely exponential decay. (Right) Corresponding measurement for the low excitation power of $0.03P_{\mathrm{Sat}}$, displaying a largely Gaussian decay.

The power dependence in Figure 4.9a was measured using an ODL with a limited delay range in terms of the measured coherence times, as shown in Figure 4.10, and additionally revealed Lorentzian lineshapes for all powers. This is surprising, as it suggests homogeneous broadening was the dominant source of dephasing even for low powers, where a much calmer environment leading to slow modulation timescales is expected. Later, a longer ODL was implemented into the MI in order to more accurately determine the coherence time, given the unexpected long decay times. This ODL was used to verify the previous measurement, and the results for two example powers, P_{Sat} and $0.03P_{\mathrm{Sat}}$, are shown in the left and right panels of Figure 4.9b, respectively. When exciting at P_{Sat}, the fitted lineshape remained Lorentzian with $T_2 = 309 \pm 16$ ps, agreeing well with the previous measurement within the experimental error. However, when exciting at $0.03P_{\mathrm{Sat}}$, the longer accessible delays revealed instead a Gaussian decay with $T_2 = 986 \pm 19$ ps, indicating that for low excitation power, the inhomogeneous broadening in fact becomes the limiting source of dephasing. Again, the value determined here agrees well within the experimental error to the previous measurement. It is also

possible to fit this visibility decay with a time-domain Voigt profile, in order to evaluate estimates of the Lorentzian and Gaussian decay times. The fitted curve (not shown) is largely similar to the fitted curve for the Gaussian decay, and indeed reveals $\tau_L = 2318 \pm 509$ ps and $\tau_G = 1274 \pm 95$ ps resulting in a $T_2 = 927 \pm 171$ ps, where, again, the fitted coherence time is within error of that determined in the previous measurement. Such long Lorentzian decay times are promising when considering the potential resonant excitation schemes, which reduce the effect of charge noise in the vicinity of the QD [117].

The observation under non-resonant excitation of relatively long coherence times persisting up to the maximum brightness of the X, with respect to both the detector resolution ($\sim 90-120$ ps) and the emitter lifetime, demonstrated that this source was viable for performing TPI under CW excitation. Therefore, the QD used here will be subsequently used for performing HOM interference, discussed in the next chapter.

4.4.2 Temperature Dependence of the Coherence Time

In addition to increasing excitation power, temperature also plays a role in the dynamics of the QD emission. As mentioned in Section 4.2.2, a high operating temperature could be beneficial for certain applications and so it is interesting to determine whether coherent emission persists for elevated temperatures. The coherence time of the ZPL can easily be determined by integration over the region excluding the phonon sidebands in the MI measurement. Figure 4.10a displays the visibility decay for the QD shown in Section 4.2.2, at a temperature of $T = 8$ K for an excitation power P_{Sat}, for the two major transitions X and X^-. Fits to the experimental data, as shown by the solid line, reveal a Lorentzian profile for the X and a corresponding coherence time of $T_2 = 430 \pm 13$ ps. The X^- displays a Voigt profile with Lorentzian and Gaussian decay times $\tau_L = 604 \pm 31$ and $\tau_G = 564 \pm 26$, respectively, corresponding to a coherence time of $T_2 = 340 \pm 18$ ps.

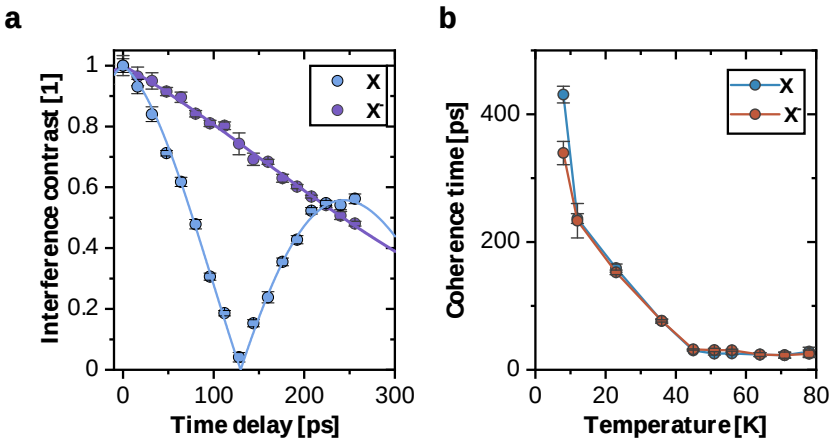

Figure 4.10: Temperature dependent coherence time. **a** Visibility decay at $T = 8$ K for an excitation power P_{Sat} for the X and X^-. Solid lines are fits to the experimental data. **b** Temperature dependence of the coherence times when exciting at P_{Sat}. A rapid decay of the coherence time for increasing temperature is observed.

A temperature dependence of the coherence time for this QD is shown in Figure 4.10b, where a rapid decay with increasing temperature for both transitions is observed, as expected from the onset of phonon-induced broadening. The decay profiles remain exponential for all temperatures up to $T = 50$ K for the X, which supports the fast relaxation timescale of the phonon-induced broadening being the main source of dephasing for high temperatures. Above $T = 50$ K, the coherence time becomes largely saturated to ~ 25 ps; and due to the fast decay, it is difficult to accurately determine the exact lineshape. For the X^-, the Voigt profile rapidly reduces to an exponential decay at around $T = 20$ K, indicating again that the homogeneous broadening from carrier-phonon interactions becomes the main source of dephasing.

Furthermore, as the temperature approaches the turn on for EL at = 45 K, the coherence times measured using EL (not shown) agree well with those shown here for above-band optical excitation. As $T_2 = 30 \pm 1$ ps at this temperature is much shorter than the resolution of the detectors used here, electrical operation of this source for the demanding experiments discussed in Chapters 5 and 7 is infeasible. Therefore, as the main focus of the work here is to demonstrate primarily interference-based applications of this new InAs/InP telecom C-band source, the low temperature regime where the most coherent emission is observed will be the operating temperature for the remainder of the experiments considered.

4.4.3 Comparison to Stranski-Krastanow Quantum Dots

In the last step of characterising the coherence in the emission of the DE-grown QDs used here, it is interesting to make a comparison to similar QDs grown by the more conventional method; SK. As DE QDs are formed with only a 'quasi' wetting-layer [90], as mentioned above, it is hypothesised that this could lead to a reduced charge reservoir near the QDs [140]. It is also hypothesised that the more symmetric growth of DE QDs leading to altered strain environments and less strain-related charge defect sites, which are both potential sources of noise, could also act to improve the coherence of the emitted photons. In order to determine the relevant impact of these differences, statistics on coherence times from both types of QDs were gathered and compared in terms of the absolute values, relevant for the CW interference considered in Chapter 5, as well as in terms of the transform limit, relevant for a more general metric of the coherence. The measured temporal lineshape is also considered, in order to provide insight as to the main sources of dephasing in each system.

The comparison begins by considering the statistics of the radiative lifetimes in each system. A survey of QD lifetimes was recorded by Toshiba Research Laboratory colleague Dr. Tina Müller and a summary of the data extracted by the preceding analysis is shown in Table 4.1. The data was analysed by fitting exponential decay curves to the X and X^-, and bi-exponential decay curves to the XX, where the fast decay was taken to be the radiative lifetime. The absence of a second slower decay for the X is in contrast to the measurement in Figure 3.6, which suggested the presence of a dark non-radiative state [167]. However, the average lifetime measured was consistent. Indeed, for the measurements recorded here, a repetition rate of 80 MHz was used, which is faster than the 40 MHz

rate used previously. Given the slow additional timescale and weak effect, the requirement of only a single exponential to describe the data is likely a result of this. The presence of an additional decay time in the XX is surprising due to the absence of a fine structure in the XX energy level, which in the X case can lead to coupling to the dark X states via spin relaxation. Since the fast timescale here is consistent with the QD measured in Section 4.3.3 (where a single exponential was used to describe the decay under 1310-nm excitation), the longer component could potentially be due to spectral pollution adding additional timescales to the time-resolved intensity [167]. In all cases, the initial period was excluded from the fits in order to remove the soft rise time due to filling effects from the non-resonant excitation scheme and multi-excitonic relaxation [168], where it was noted that such effects were particularly pronounced in the SK sample.

	DE QDs		SK QDs	
	Mean [ns]	σ [ns]	Mean [ns]	σ [ns]
τ_X	2.00	0.26	1.63	0.3
τ_{X^-}	1.61	0.24	*	*
τ_{XX}	0.33	0.05	0.58	*
τ_{X^*}	*	*	1.61	0.48

Table 4.1: Average radiative lifetime of DE and SK QDs.

For the DE system, it was possible to reliably determine mean values for the X, X^- and XX due to the repeating spectral signature discussed in Section 4.2. For the SK system, it was possible to determine X and some X^* by a combination of power-dependent and polarisation-dependent spectroscopy. On the whole, the emission of a XX transition with sufficient signal to resolve energy correlation was not seen, and is therefore neglected for the following discussion. In both cases, the mean X lifetime is comparable to other InP-based QDs emitting at 1.55 μm [132, 131], while the DE is somewhat longer in comparison to the SK. The radiative lifetimes are longer than the shorter wavelength GaAs-based QDs, despite being roughly similar in size [90]. This is due to the fact that recombination depends on the frequency dispersion of the photonic density of states [125], in addition to potential non-radiative decay channels. The large difference between the X and the XX decay times for the DE system, on average $\tau_X/\tau_{XX} \approx 6$, is much larger than the theoretical ratio of $\tau_X/\tau_{XX} = 2$ by considering the case of ideal decay channels of the XX and the X, and even larger than the limit of $\tau_X/\tau_{XX} = 4$ in the strong confinement regime [169]. This, in turn, suggest the presence of coupling to dark states, where the exciton instead decays via spin relaxation, therefore increasing the average lifetime observed experimentally [136]. It could also explain the relatively high probability for exciting the XX, seen by the super-linear dependence of the intensity on the excitation power (as opposed to the quadratic dependence expected), due to the fact that there is an increased time spent after relaxation of the XX before the following emission of an X. Therefore, only the capture of another electron-hole pair is required. While there is currently no explanation for such a large difference, it is possible to have

asymmetric Purcell enhancements, which have been shown to selectively enhance transitions more into the resonance, even for weak planar cavities [170]. The quality factor (defined by $Q = \omega_c/\Delta\omega$ where ω_c and $\Delta\omega$ correspond to the central cavity frequency and the width of the cavity resonance) of the weak planar cavity in [170] was in fact much larger than in the sample studied here ($Q \sim 50$ [90]). This allowed for selective tuning due to the narrower cavity resonance in addition achieving some Purcell enhancement. However, since here the observed effect also persists for QDs not on the edge of the cavity mode, this is unlikely to be a possible cause. Interestingly, it has recently been proposed that such a large asymmetry in the XX and X radiative lifetimes leads to an increase in the TPI visibility under resonant excitation of the cascaded system [171], due to the effective reduction and the timing jitter in the X emission from a faster XX decay. However, as mentioned previously, the proposal here considered the integrated zero-delay pulse of a resonant two-photon excitation of the XX, which differs from the non-resonant and post-selection considered in Chapter 5. Furthermore, such a large difference in the decay times has also been proposed for the creation of time-bin entangled photons pairs using, again, a resonant preparation of the XX state, this time through population from the metastable dark X state [172].

With the average lifetime dynamics for each system determined, it is now possible to consider the average coherence time and proximity to the transform limit. In order to do this, statistics of the coherence time of 18 QDs in the DE sample and 14 QDs in the SK sample were measured. To maintain consistency, each QD was excited at the X saturation power P_{Sat}. The X was determined as in Section 4.2, using power and polarisation-dependent measurements. Figure 4.11a (b) displays a histogram of the results of this for the X (X^-/X^*) for each system, where similar mean values (μ) and standard deviations (σ) are seen between the neutral and charged lines, with the charged lines being slightly higher in both cases. The mean values of the DE sample are ~ 3 times larger than the SK sample. More importantly, the average value $\mu = 45$ ps of the X is far below the detection resolution, and would significantly impact the measurable TPI in SK QDs under CW excitation. While it is possible to find QDs approaching the required threshold here, $\sigma = 27$ ps shows that this is unlikely in the majority of QDs in the sample (2%), making it realistically infeasible. Even for the charged lines, the probability to find such a QD is still only 15%. On the contrary, $\mu = 150$ ps and $\sigma = 71$ ps for the DE X shows that it is routinely possible to find QDs meeting the detection resolution criteria, with 75% being above 100 ps, increasing to 86% for the X^-. While such comparisons of the raw coherence time were necessary for the practical considerations of measuring TPI under CW excitation, the difference in radiative lifetimes needs to be taken into account in order to access the difference in the pure dephasing of each system.

The mean lifetime and mean coherence time allows for a fairer comparison of the coherence in each system to be made using the transform limit to determine the relative levels of dephasing. A summary of this can be seen in Table 4.2, which also includes the XX of the DE system, alongside the top of the axes in Figures 4.11a and b. From the table, it is clear that despite the shorter lifetime of the SK QDs, the much shorter coherence time results in the DE system being a factor of 2.7 closer to the transform limit. For the charged lines, this increases up to a factor of 3.8 of DE compared

to SK, and is even a factor of 1.9 larger than the DE X. Furthermore, from Table 4.2, it is apparent the the XX in the DE system offers the largest coherence in its emission, which can be seen from the reduced interaction from the charge environment due to the relatively short lifetime. However, the raw coherence, times together with the much lower intensity, meant that using the XX for two and three-photon experiments would have been realistically infeasible due to the much longer acquisition times and lower SNR.

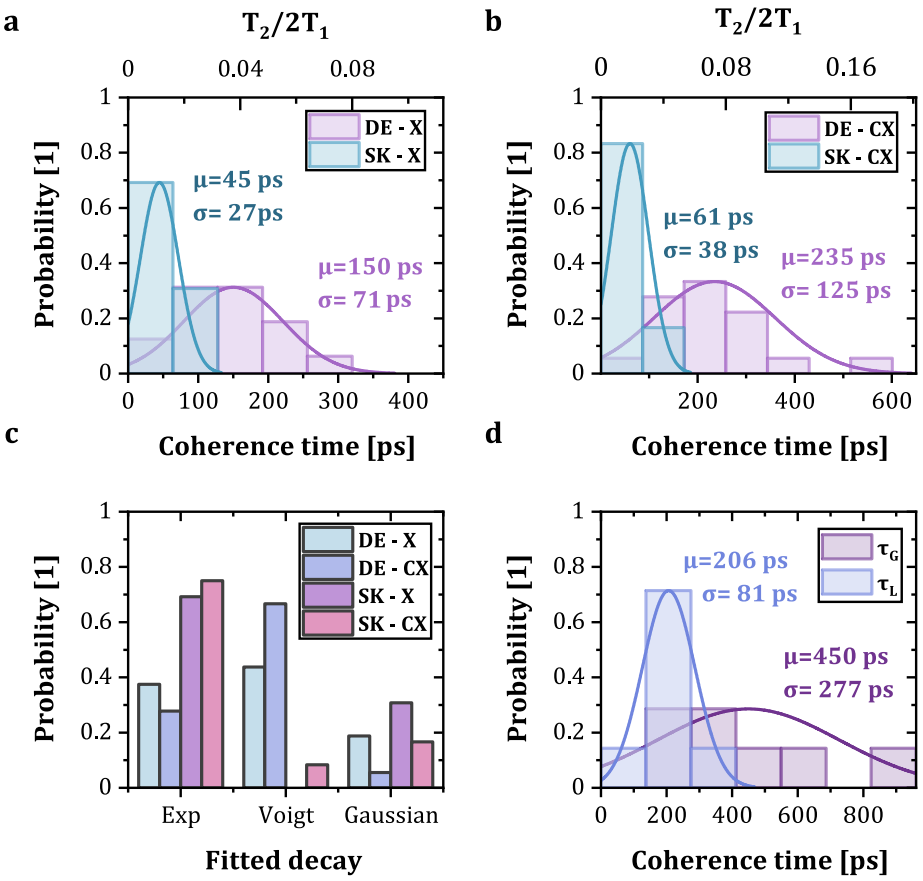

Figure 4.11: Coherence time statistics of SK and DE QDs. **a** Histogram of the coherence times of the X for both SK and DE QDs, excited non-resonantly at P_{Sat}. **b** Same as **a** but the for the X^- (X^*) of the DE (SK) QDs. **c** Histogram of the fitted lineshapes in each system. **d** Histogram of the average Lorentzian and Gaussian decay times when considering the Voigt profile fits for the X.

As previously discussed, the characteristic timescale of the dephasing processes determine the resulting shape of the decay. For fast processes, typically associated with phonon interactions or electronic coupling to a charge bath, the decay is expected to be exponential. However, for slower processes, typically associated with spectral wandering due to nearby charge trap close to the QD, a Gaussian decay is expected. When these processes have comparable timescales, a Voigt profile with Lorentzian and Gaussian components is expected. For further insight into the physical dephasing

mechanisms present in each system, a comparison of the fitted decay profile is made in Figure 4.11c. For both the neutral and charged lines, a similar pattern is observed between the SK and DE systems, where the majority of DE transitions follow a Voigt decay profile. The SK QDs, however, exhibit almost entirely exponential decays. In both cases, a small number of Gaussian decays are observed consistent with a large energy modulation from a nearby impurity site [173]. This suggests that the dephasing in the SK sample is almost entirely in the fast-modulation limit. By considering the time-domain Voigt profiles of the X, the Lorentzian and Gaussian components can be extracted in order to compare the relative timescales of the fast processes. Figure 4.11d shows histograms of the result. The determined mean $\bar{\tau}_L = 206$ ps shows that fast dephasing processes are ~ 5 times weaker for DE QDs. Consequently, this allows the presence of a slow Gaussian component to be resolved, with a mean of $\bar{\tau}_G = 450$ ps. Due to the low temperature and non-resonant excitation scheme, charge noise is suspected to be the main source of dephasing in each system [117]. This suggests that the wetting layer present in the SK QDs could in fact be the source of the much faster relaxation. Therefore, the calmer environment of the DE QDs leads to much slower processes, which results in an overall reduction in pure dephasing for the DE QDs. Together with the previously demonstrated lower average FSS [88, 90], this makes DE QDs a much more feasible and desirable source for future entanglement and interference-based quantum information applications.

	DE QDs		SK QDs	
	Mean [ps]	σ[ps]	Mean [ps]	σ [ps]
$T_2/2T_1$ X	0.038	0.018	0.014	0.008
$T_2/2T_1$ CX	0.0730	0.039	0.019	0.012
$T_2/2T_1$ XX	0.159	0.048	*	*

Table 4.2: Average Fourier-transform limit of DE and SK QDs.

4.5 Summary

In this chapter, the basic spectral and time-resolved characterisation of DE QDs emitting in the telecom *C*-band was performed. Such characterisation is vital in order to determine the suitability for use in quantum interference-based applications, in addition to determining the set of optimal parameters for such measurements. Using spectral analysis, several of the charge complexes could be determined in the QD emission signatures, which, in turn, displayed very consistent behaviour across the sample. It was further found that the main transitions displayed highly non-classical photon statistics under both non-resonant CW and 1-GHz pulsed excitation, with strong evidence of multi-level dynamics, probably resulting from the excitation scheme used.

A subsequent analysis of the coherence in the emission revealed unprecedented coherence times for the DE QDs, comparable to state of the art GaAs-based systems under comparable excitation conditions. A strong limit was found on the coherence for elevated temperatures where non-resonant electrical excitation would be possible. Development of the sample structure to enable lower operating temperature under electrical excitation in order to access the longer coherence times could be one potential avenue for future work, towards the development of remote systems where experimental complexity is undesirable. This avenue could also consider the use of recently demonstrated 'on-chip' pumping schemes [134, 174], where carriers excited into the quantum well surrounding the QD recombine to quasi-resonantly excite QDs in a nearby mesa. Such structures have enabled fully electrically tunable and excited emission of a QD source in the telecom *O*-band [134]. The opposite direction, that is to work towards resonant excitation schemes, would also be an interesting area for future work. In this regime, not only is the single-photon purity greatly enhanced, but also the pure dephasing is reduced significantly, such that transform-limited emission is possible [166, 175]. This would enable highly indistinguishable and pure telecom *C*-band single photons, a suitable candidate for integration with silicon integrated photonics [176, 177].

Chapter 5

Two-Photon Interference

In this chapter, the HOM-type interference of a single-photon source in the telecom *C*-band will be considered in order to quantify the degree of indistinguishability between subsequently emitted photons. An extension of the model for interfering wave packets will be made to consider the case of interference of unpolarised doublets, as this is an important consideration when using such imperfect QDs (non-zero FSS) for teleportation experiments. Finally, a more 'real-world' scenario will be considered; namely, the interference of photons with different photon statistics. This final experiment will form the basis of the desired quantum relay, detailed in Chapter 7.

5.1 Introduction

As discussed in Section 2.1.3, two-photon interference between single photons is a fundamental element in many quantum information processing and communication applications. It is therefore not surprising that much work has gone into interfering photons using various sources since the first demonstration of HOM interference [56]. Such demonstrations have included; interference of photons emitted from separate atoms [178], remotely trapped ions [179] and molecules [180], as well as interference of spatially-separated sources at telecommunications wavelengths using SPDC sources [181]. Recent demonstrations have further shown interference with sources emitting at even longer wavelengths, in the mid-infrared region ($\sim 2\ \mu$m) [182], where it has been suggested such sources offer an alternative route forward in both free-space QKD, as well as on-chip quantum information processing [183].

Semiconductor QDs have also been shown to be promising candidates since the first demonstrations of HOM interference [63, 184], where work in this field has continued with great success demonstrating high indistinguishability for single-photon [39, 185, 175, 186, 187] and entangled pair-photon sources [72, 188–190]. While many of these schemes utilise QD sources emitting below 1 μm, there has also been recent success in demonstrating HOM interference at telecommunications wavelengths using QD sources, both by the frequency conversion of short wavelength QDs using non-linear processes [191], and also by QDs emitting natively at these wavelengths [84, 165, 192].

In the standard HOM-type interference of photon pulses, the interference visibility, v_{HOM}, is determined by the overlap of the temporal mode function, and is necessarily determined then by [193]

$$v_{\mathrm{HOM}} = \frac{T_2}{2T_1}, \tag{5.1}$$

such that perfect visibility will be seen for Fourier limited photons, i.e. the photons are phase coherent with those emitted at any time during the pulse and can interfere perfectly. The act of dephasing is to make the photons emitted at separate times distinguishable, therefore reducing this value.

However, it is possible to post-select photons for non-Fourier limited pulses interfering on timescales shorter than T_2 [164], in addition to CW sources used primarily in this work, in order to filter out the events where the photons were indistinguishable. This is not necessarily such a problem for certain applications. For example, when considering a typical quantum key distribution protocol, photon detection events are gated with a certain frequency and a certain width, in order to reduce the noise from detecting dark counts outside of the expected signal region [194]. However, this naturally comes at the cost of significantly reducing the effective brightness of slow sources[195] as now only a small fraction of the photons are considered for short timescales and the photons arriving outside of the gate are rejected. In order to mitigate this, it is desirable to have long T_2 times such that the gate width can be chosen to be long enough to optimise the signal against the dark counts, enabling subsequent quantum information processing. In this regime, the important consideration is then maximising the number of post-selected photons interfering within a given gate width which is determined by the detector resolution, as in addition to losing photons, the contrast of the interference is lowered. This is something which is particularly important when utilising TPI to perform quantum teleportation, as described in Chapter 7.

Consequently, for the following work, the constraint of maximising Equation 5.1 then relaxes to instead maximising T_2 with respect to the detector resolution $\Delta\tau_{\mathrm{det}}$ [164], such that the high visibility interference events can be detected on short timescales. Indeed, as shown in Chapter 4, the coherence times of a majority of the QDs in this sample fulfil this criterion and thus we expect to see high contrast TPI.

5.2 Modelling Two-Photon Interference

In order to understand precisely the processes occurring during TPI with our source, an extension to the concepts of TPI introduced in Section 2.1.3 for photons incident on a balanced beamsplitter will be made using the standard wave packet analysis developed by Legero *et al.* [121, 196], and later extended by Patel *et al.* [197]. This theory will allow for the description of more realistic photon sources by introducing considerations for the deviations away from perfectly ideal and indistinguishable photons, such as the mismatch of frequency or arrival time at the beamsplitter. As such, it can be used to describe a CW source of QD photons interfering at a balanced beamsplitter. Figure 5.1 describes this scenario, where two single QD photon wave packets are incident on ports 1 and 2 of a balanced beamsplitter, before a coincidence detection of photons in output modes 3 and 4 is made

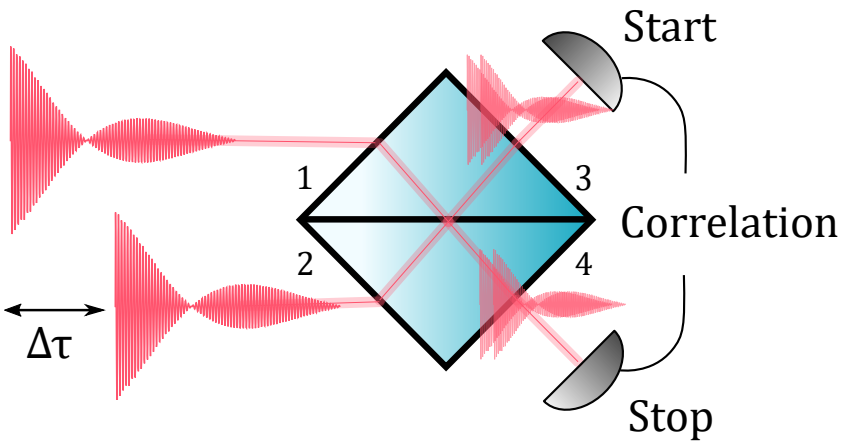

Figure 5.1: Hong-Ou-Mandel interference of real single-photon wave packets. Single photons incident at each input port of a balanced beamsplitter result in a coalescence on either output port. Detection in a 'start'-'stop' configuration reveals a dip in the probability resulting from the interfering wave packets.

By considering the transformation given by Equation 2.12 on the electric field operators

$$\begin{cases} \hat{E}_1^+(t) = \xi_1(t)\hat{a}_1, \\ \hat{E}_2^+(t) = \xi_2(t)\hat{a}_2, \end{cases} \tag{5.2}$$

where $\xi_i(t)$ denote the temporal mode functions as before, evaluation of the output operators allows the joint probability of detecting photons in output mode 3 at time t and mode 4 at time $t+\tau$, based on the condition of a single photon on each input, to be determined as

$$\begin{aligned} P^{||}_{joint}(t, t+\tau, \Delta\tau) &= |\langle 1_1 1_2| \hat{E}_3^-(t)\hat{E}_4^-(t+\tau)\hat{E}_4^+(t+\tau)\hat{E}_3^+(t)|1_1 1_2\rangle|^2 \\ &= \frac{1}{4}|\xi_1(t+\tau-\Delta\tau)\xi_2(t) - \xi_1(t-\Delta\tau)\xi_2(t+\tau)|^2, \end{aligned} \tag{5.3}$$

for indistinguishable photons, where the timescale $\Delta\tau$ has been introduced here to account for the difference in arrival time at the beamsplitter between the first and the second photon, due to the CW excitation scheme where emission of photons occurs at random times. For distinguishable photons, the joint probability is similarly determined as

$$\begin{aligned} P^{\perp}_{joint}(t, t+\tau, \Delta\tau) &= |\langle 1_1 1_2| \hat{E}_3^-(t)\hat{E}_4^-(t+\tau)\hat{E}_4^+(t+\tau)\hat{E}_3^+(t)|1_1 1_2\rangle|^2 \\ &= \frac{1}{4}|\xi_1(t+\tau-\Delta\tau)\xi_2(t)|^2 + |\xi_1(t-\Delta\tau)\xi_2(t+\tau)|^2. \end{aligned} \tag{5.4}$$

The mode functions $\xi_j(t)$ of the QDs are determined straightforwardly from the temporal wave packet given by the Fourier-transform of the emission spectrum, as detailed in Equation 3.8. For the case of a single Lorentzian, the normalised mode function is a one-sided exponential

$$\xi_j(t) = \begin{cases} \sqrt{\frac{2}{T_{2,j}}} e^{-t/T_{2,j} - i(\bar{\omega}-\Delta\omega/2)t}, & t \geq 0 \\ 0, & \text{otherwise} \end{cases} \tag{5.5}$$

$$\xi_i(t) = \begin{cases} \sqrt{\frac{2}{T_{2,i}}} e^{-t/T_{2,i} - i(\bar{\omega}+\Delta\omega/2)t}, & t \geq 0 \\ 0, & \text{otherwise} \end{cases} \tag{5.6}$$

where $\Delta\omega = \omega_i - \omega_j$ and $\bar{\omega}$ is the average frequency. Integration of Equation 5.3 over times t and $\Delta\tau$ results in the probability based on the relative detection times τ of the photons, averaged over all possible emission and detection times. Inserting Equation 5.5 into Equation 5.3 and performing the integration yields

$$\begin{aligned} P_{HOM}(\tau) &= \int_{-\infty}^{\infty}\int_{-\infty}^{\infty} P^{||}_{joint}(t, t+\tau, \Delta\tau, \Delta\omega)\mathrm{d}t\mathrm{d}\Delta\tau \\ &= \frac{1}{2}\left(1 - e^{-\tau\left(\frac{1}{T_{2,j}}+\frac{1}{T_{2,i}}\right)}\cos(\Delta\omega\tau)\right), \end{aligned} \tag{5.7}$$

whereupon setting $T_{2,j} = T_{2,i} = T_2$ and $\Delta\omega = 0$ for interference of photons from the same emitter reduces to the well-known result

$$P_{HOM}(\tau) = \frac{1}{2}\left(1 - e^{-2\tau/T_2}\right). \tag{5.8}$$

Again, the importance of the coherence time T_2 which defines width of the resulting dip in coincidence probability is noted. So far, this model only takes into account the homogeneously-broadened Lorentzian lineshape, characterised by the exponential wave packet. To account for the inhomogeneously-broadened component, the probability $P^{||}_{joint}(t, t+\tau, \Delta\tau, \Delta\omega)$ can additionally be weighted by a Gaussian probability distribution

$$G(\delta\omega) = \frac{1}{\sqrt{2\pi}\sigma} e^{-\delta\omega^2/2\sigma^2}, \tag{5.9}$$

such that now the joint probability is described by

$$P^{||}_{joint}(t,t+\tau,\Delta\tau,\delta\omega) = \int_{-\infty}^{\infty} G(\delta\omega) P^{||}_{joint}(t,t+\tau,\Delta\tau,\Delta\omega+\delta\omega)\mathrm{d}\delta\omega. \tag{5.10}$$

This can be evaluated to give

$$P_{HOM}(\tau) = \frac{1}{2}\left(1 - e^{-2\tau/\tau_L - \pi\tau^2/2\tau_G^2}\right), \tag{5.11}$$

where now τ_L has replaced T_2 as the Lorentzian component of the coherence time and $\tau_G = \sqrt{\pi}/\sigma$ is the Gaussian component, representing the homogeneous and inhomogeneous contributions, respectively.

In the experiment discussed below, the measurement of co- and cross-polarised $g^{(2)}(\tau)$ will be used to access the visibility of interference, which depends on the probability $P_{HOM}(\tau)$. For the cross-polarised case, the measured correlation is

$$g^{(2)}_{\perp}(\tau) = \frac{1}{2}g^{(2)}(\tau) + \frac{1}{4}\left(g^{(2)}(\tau+\Delta\tau) + g^{(2)}(\tau-\Delta\tau)\right), \tag{5.12}$$

where $\Delta\tau$ is the delay between photons determined by the interferometer. The first term describes the single-photon nature of the emitter and the resulting probability of emitting multiple photons that simultaneously travel down the same arm of the interferometer. The second and third terms account for the probability of emitting multiple photons which travel down different arms of the interferometer. For the co-polarised case, the above equation is modified by the probability $P_{HOM}(\tau)$ to give

$$g^{(2)}_{||}(\tau) = \frac{1}{2}g^{(2)}(\tau) + \frac{1}{4}\left(g^{(2)}(\tau+\Delta\tau) + g^{(2)}(\tau-\Delta\tau)\right)\left(1 - e^{-2|\tau|/T_2 - \pi\tau^2/2\tau_G^2}\right), \tag{5.13}$$

where only the terms referring to the presence of two photons in the interferometer are modified. The resulting visibility of interference is then defined as

$$V_{HOM}(\tau) = 1 - \frac{g^{(2)}_{||}(\tau)}{g^{(2)}_{\perp}(\tau)}. \tag{5.14}$$

5.3 Indistinguishable Photons from the Neutral Exciton

In Section 3.4, the single-photon interference of the neutral X was described by considering the Fourier transform of a double Lorentzian emission spectrum, resulting in a beating of the single-photon wave packet, as determined by the first-order coherence function $g^{(1)}(\tau)$. While a quantum mechanical description based on creation and annihilation operators was used to describe the wave packet, the same result could be obtained by considering a purely classical scenario and would not require the consideration of the single-photon nature of the emission.

Here, an extension of this concept to the case of two-photon interference will be considered. The system can be modelled analogously to that described in the previous section, with now the temporal mode function describing the superposition X state defined from $g^{(1)}(\tau)$ as

$$\xi_j(t) = \begin{cases} Ae^{-\frac{t}{T_2}-\frac{1}{2}i(\Delta\omega+2\omega_0)\tau}\left(m - e^{i\Delta\omega\tau}(m-1)\right), & t \geq 0 \\ 0, & \text{otherwise} \end{cases} \tag{5.15}$$

where $\Delta\omega$ is the frequency splitting corresponding to the FSS, m is the relative intensity of the Lorentzian doublet as before and A is a normalisation constant such that $\int_{-\infty}^{\infty}|\xi_j(t)|^2 \mathrm{dt} = 1$. Progressing through the same steps as previously results in tedious algebra, but can be evaluated analytically with lengthy expressions.

To demonstrate the effect of the double Lorentzian shape of the single-photons at each input port of the beamsplitter, a comparison of the expected correlations for co- and cross-polarised photons, as well as the visibility, is made to the case where each port receives a single Lorentzian photon with a frequency mismatch. Figure 5.2 shows the simulated correlations (top) and visibility (bottom) for the cases of interfering frequency mismatched single-Lorentzian emitters (left) and perfectly unpolarised ($m = 0.5$) double-Lorentzian emitters with a FSS and equal central frequency (right). As can be seen, the form of the visibility still has the expected beating behaviour resulting from the different frequency components, however, the shape is different to the case of separate photons with a frequency mismatch, as a result of the difference in the temporal mode functions.

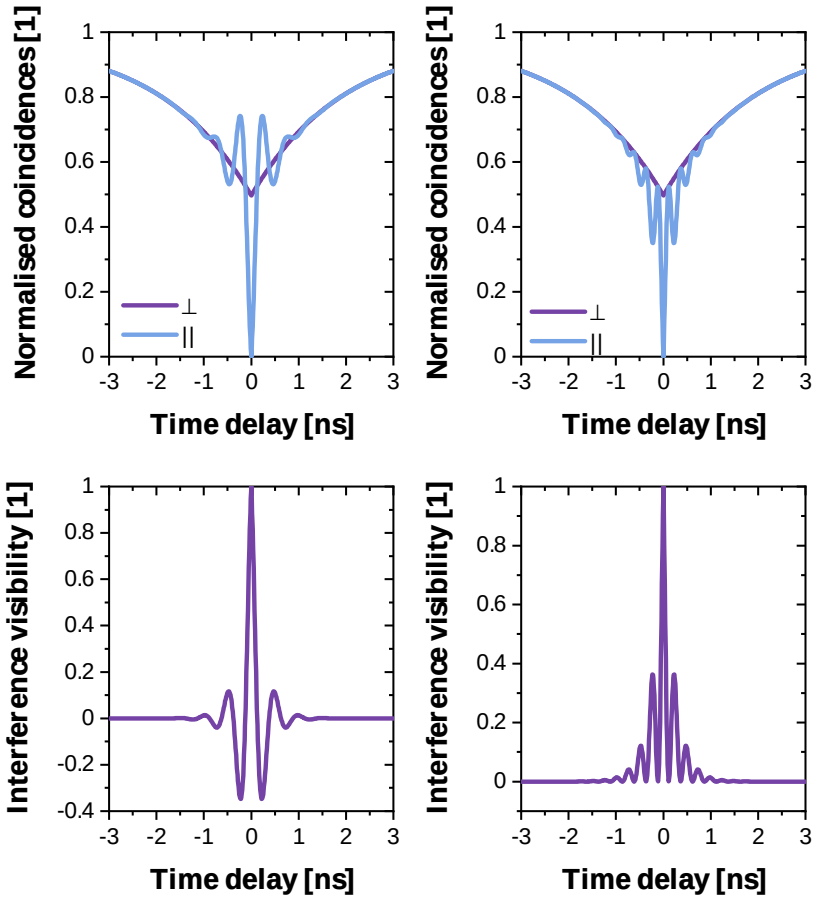

Figure 5.2: Simulated correlations for the HOM interference of single-photons. (**Top**) Simulated correlations for co- and cross-polarisations for the cases of single Lorentzian wave packets with mismatched frequency $\Delta\omega = 4$ GHz (left) or double Lorentzian wave packets with the same frequency difference (right). (**Bottom**) Corresponding interference visibility for the correlations in the top row.

5.3.1 Experimental Setup

In order to determine the visibility of interference, an all-fibre HOM-style interferometer was constructed. Figure 5.3 shows a schematic of the experimental implementation. Photons from the X transmission grating were coupled to a 50:50 beamsplitter. Each arm was then sent through an electronic polarisation controller (EPC), used to align the polarisation bases. In one arm, there was an additional fibre delay set to be longer than the radiative lifetime of the X, such that photons from different excitation cycles were then incident on the subsequent interfering beamsplitter. In addition to the fibre delay, an optical switch (OS) was placed in one arm for calibration. On one output mode of the interfering beamsplitter, a further 99:1 splitter was used to direct 1% of the light towards a polarising beamsplitter (PBS), used for calibration of the EPCs. In order to calibrate the polarisation bases of the detectors, and thus the polarisation of the photons interfering at the beamsplitter, a polarised reference laser was sent through the setup. First, the optical switch was used to switch out

one arm of the interferometer. A minimisation routine was then used to adjust the voltages of the EPC for the light in the remaining arm, in order to minimise the count rate of one of the detectors. This then defined the cross-polarised detection. Minimisation was then performed for the opposite detector, in order to define the co-polarised base. At this point, the optical switch was used to insert the second arm back in, before the minimisation of the same detector in order to align the second EPC to the co-polarised detection. The measurement was then performed by recording second-order correlations for the co- and cross-polarised detection bases, set by changing the voltages of the EPCs.

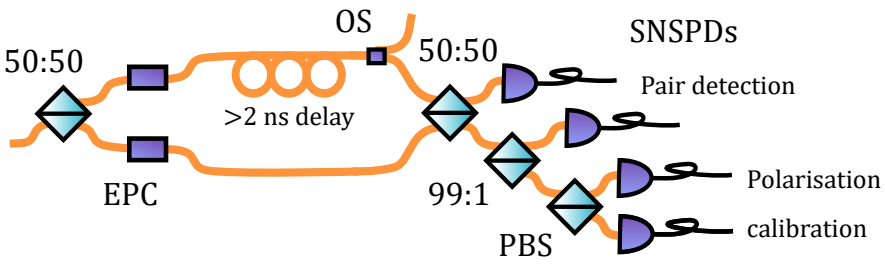

Figure 5.3: Experimental setup of the two-photon interference with a delayed single photon. Photons are split by a 50:50 coupler where then a delay in one arm allows interference with a subsequently-emitted photon at a second 50:50 coupler. A 99:1 coupler is used in order to separate some light for polarisation calibration using a reference laser. EPCs are used to control the polarisation of each arm of the interferometer.

5.3.2 Results

In the experiment presented in this section, the QD from the coherence time power-dependent study in Section 4.4 was used. However, in order to increase the intensity for these two-photon measurements, 1310 nm excitation was used, as discussed in Section 3.1.1. The QD emission under this type of excitation will first be characterised before proceeding with the TPI results. Figure 5.3.2a shows the power dependence of the emission from the most significant lines in the spectra. Fits to the data (solid lines) reveal gradients of $M \sim 1$ for all transitions, including the XX. This is surprising, and suggests that the excitation is not limited by the probability of capturing one electron-hole pair, as seen for excitation at 785 nm. Given that the X^- remains largely dominant in intensity, and that there is an overall shift of the emission towards the neutral lines, this behaviour could be the result of a limited hole capture rate.

Figure 5.3.2b shows some corresponding power-dependent coherence times measured for this QD under 1310 nm excitation. The points in black have been determined from fits to the normal exponential beating function, introduced in Section 3.4. As can be seen, the high-power values correspond to those shown in Figure 4.9 under 785 nm excitation, especially at the X saturation power where $T_2 = 319 \pm 6$ ps. However, upon decreasing the power, the coherence time does not increase to the same extent, and seemingly becomes limited to ~ 500 ps. Given the below-band nature of the excitation, this is surprising as it is expected to reduce the broadening resulting from the carrier capture and relaxation processes. In order to examine this further, fits were made using a beating time-domain Voigt function. Values for the extracted Lorentzian and Gaussian components

are displayed in Figure 5.3.2b for the powers where the fitting routine was able to converge. For the saturation power, the coherence time is largely defined by a Lorentzian component of 445 ± 68 ps and Gaussian component of 606 ± 106 ps. For the lower power measurements, the Lorentzian time increases significantly as expected (albeit with large error as a result of the difficulty of fitting the lineshape); however, the Gaussian component becomes faster and is the limiting component in the coherence time. This suggests that the inhomogeneous broadening for this QD under below-band excitation is in fact worse than under above-band excitation. This could potentially be the result of a charge screening process whereby charge traps in the vicinity of the QD are saturated under 785 nm due to the abundance of carriers [162, 195].

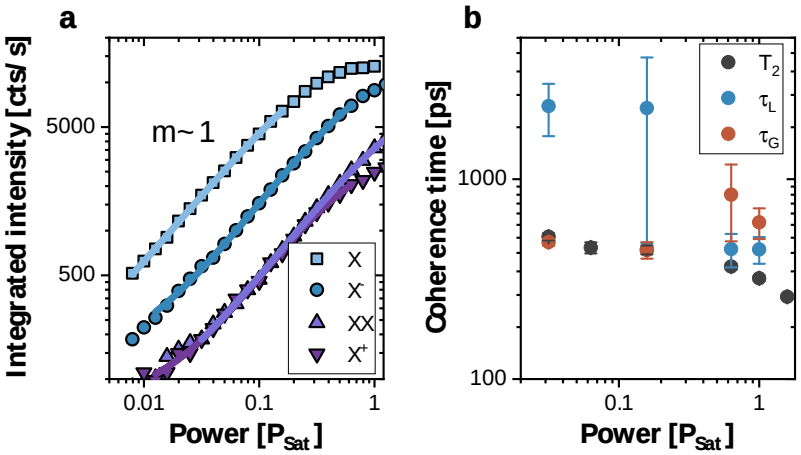

Figure 5.4: Emission intensity and coherence times for 1310 nm excitation. **a** Integrated intensity as a function of excitation power, relative to the X saturation power. Solid lines display fits to a saturation function, with all major lines fitting with a gradient of $M \sim 1$. **b** Coherence times for the same power range. Where possible, fits of the Lorentzian and Gaussian components of the Voigt profile are also shown. The coherence times near P_{sat} are similar to those measured under excitation with 785 nm light; however, for decreasing power, the coherence becomes limited by a significant Gaussian contribution.

Figure 5.5 shows the corresponding X HBT measurements for this QD under excitation with 1310 nm at P_{Sat} (a) and $P_{Sat}/5$ (b). In both cases, the correlations show a much stronger bunching following the anti-bunching dip for short time delays $|\tau| > 0$, when compared to the respective measurements under excitation with 785-nm light. The width of the dip is also much narrower at P_{Sat}, corresponding to a faster excitation rate of the X. For lower power, the bunching time increases significantly, indicating a slower excitation and longer decay time of the intermediate shelving state. The data can be described again using the 10-level rate equation model introduced in Section 4.3, with the additional decoupling of the higher order negatively charged XX^- and X^{-2} states carried out by setting the respective radiative decay times to be much faster than any other timescale. Additionally, an electron-hole pair capture time is introduced, to account for the change of excitation. This results in excellent fits to the experimental data, as shown by the solid lines in Figure 5.5. For excitation at P_{Sat}, the fitted electron, hole and exciton capture times are 0.99 ± 0.01 ns, 1.50 ± 0.01 ns and 2.27 ± 0.06 ns, respectively. The difference of the electron and hole capture times again highlights the

increased likelihood of capturing an electron, resulting in the large dominance of the X^- emission. The longer capture time of the electron-hole pair suggests that with this excitation scheme, the emission of the neutral lines are limited by the capture of holes. For the lower power measurement, the fitted electron, hole and exciton capture times are 3.96 ± 0.03 ns, 6.58 ± 0.04 ns and 6.78 ± 0.09 ns, respectively. An even larger difference in the electron and hole capture times suggest further that in the low power regime, holes capture is limited leading to a long bunching time, corresponding to the time spent in the electron state after emission of an X^- photon. The fitted background contributions are $\beta = 0.020 \pm 0.007$ and $\beta = 0.017 \pm 0.005$ corresponding to a deconvolved $g^{(2)}(0) = 0.04 \pm 0.01$ and $g^{(2)}(0) = 0.03 \pm 0.01$ for the high and low powers, respectively, as shown by the dashed grey lines in Figure 5.5.

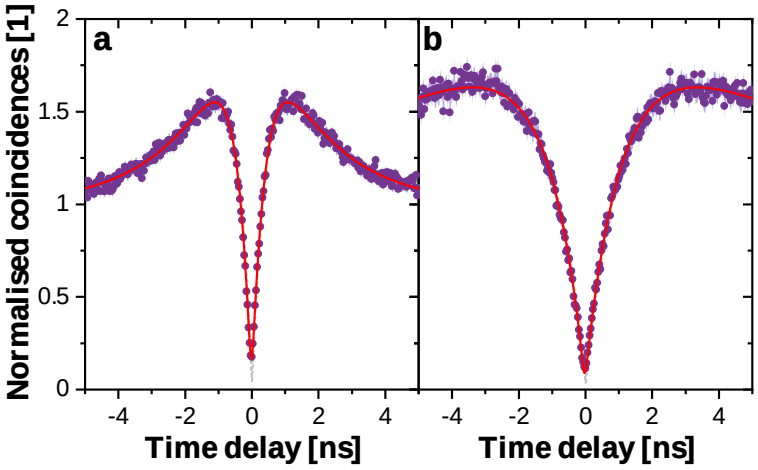

Figure 5.5: HBT autocorrelation under 1310 nm excitation. a High power excitation at P_{Sat}. A fit to the data (solid line) reveals a raw (deconvolved) $g^{(2)}(0) = 0.17 \pm 0.01$ (0.04 ± 0.01). **b** Low power excitation at $0.2P_{Sat}$. A fit to the data (solid line) reveals a raw (deconvolved) $g^{(2)}(0) = 0.11 \pm 0.01$ (0.03 ± 0.01)

Having characterised emission from the QD under this type of excitation, the results of the TPI will now be presented. For the case of excitation at P_{Sat}, the resulting correlations for co- and cross-polarised photons arriving at the interfering beamsplitter with a delay of 6.25 ns are shown in Figure 5.6a. As expected from the simulations shown in Figure 5.2, the correlation dip for the cross-polarised case extends down towards 0.5, where in this case it is not limited by the detector resolution, as shown by the deconvolution of the detector response in the dashed grey line. Instead, it is limited mainly by the bunching of the delayed photons, given that the delay is close to the bunching time. A fit to the data (solid lines) using Equation 5.12 with the same rate equation model as for Figure 5.5a yields excellent agreement with the experimental data. The correlation dip for the co-polarised case extends down towards 0 as expected, and is limited largely by the detector response time, shown by the dashed grey lines. In addition to this, the correlation displays a small oscillation resulting from the different frequency components of the X interfering. A fit to the data using Equation 5.13, with the exception of P_{HOM} calculated using the X doublet wave packet, reveals

excellent agreement with the experimental data. The FSS =17 μeV and the polarisation $m = 0.5$ were fixed during the fit and $\tau_G = 608$ ps the Gaussian component of the coherence time was also fixed to the value determined from coherence time measurements. The free-fitting parameter was $\tau_L = 540 \pm 41$ ps, corresponding to the Lorentzian component of the coherence time. This time agrees well with the Lorentzian timescale from the MI measurement at this power, and results in a coherence time $T_2 = 334$ ps of a time-domain Voigt profile.

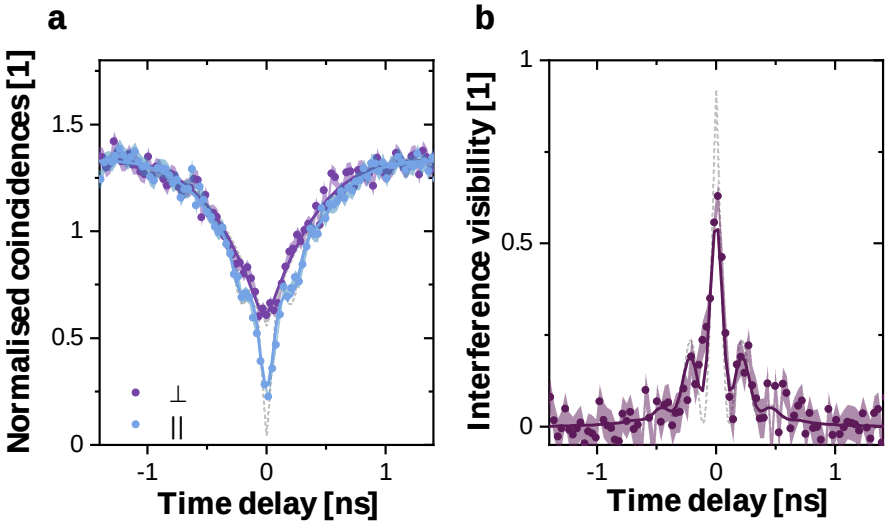

Figure 5.6: High power HOM interference. a Co- and cross-polarised correlations. Solid lines represent fits to the data using parameters determined from the autocorrelation. **b** Corresponding interference visibility displaying a maximum of $62.9 \pm 3.6\%$. Solid line fit is determined directly from the fits of the correlations. Post-selection bin size is 32 ps.

Figure 5.6b shows the calculated interference visibility for the correlations shown in Figure 5.6a, alongside the calculated fit, using Equation 5.14. Furthermore, the data shows excellent agreement with the fit directly calculated from the fits to the correlations. A maximum raw visibility of $62.9 \pm 3.6\%$ is achieved for a post-selected bin size of 32 ps. The effect of the Gaussian component is seen in the visibility for long time delays where the oscillations die off rapidly. However, given that the coherence time is too short to allow the beating oscillations to be seen fully, these effects are more difficult to distinguish. A deconvolution of the data reveals a maximum achievable visibility of 91%, as a result of the multi-photon contributions to the $g^{(2)}(0)$.

For the case of excitation at $P_{Sat}/5$, the resulting correlations for co- and cross-polarised photons arriving at the interfering beamsplitter with a delay of 6.25 ns are shown in Figure 5.7a. As before, the cross-polarised correlation is not limited by the detector response but instead by the bunching of photons in the shoulders of the $g^{(2)}(\tau)$. For the co-polarised correlation, the detector response significantly affects the measured coincidence dip. A deconvolution with the detector response reveals that the dip extends down to 0.01 ± 0.01, where the background contribution is determined to be $\beta = 0.0034 \pm 0.0057$. The much longer Lorentzian time reveals large beats resulting from the FSS. A

fit to the data using the same values of the FSS and m reveal $\tau_L = 1.18 \pm 0.03$ ns and $\tau_G = 0.589 \pm 0.06$. These values agree well with those determined from the MI measurement, and result in a coherence time $T_2 = 440 \pm 45$ ps of a Voigt profile.

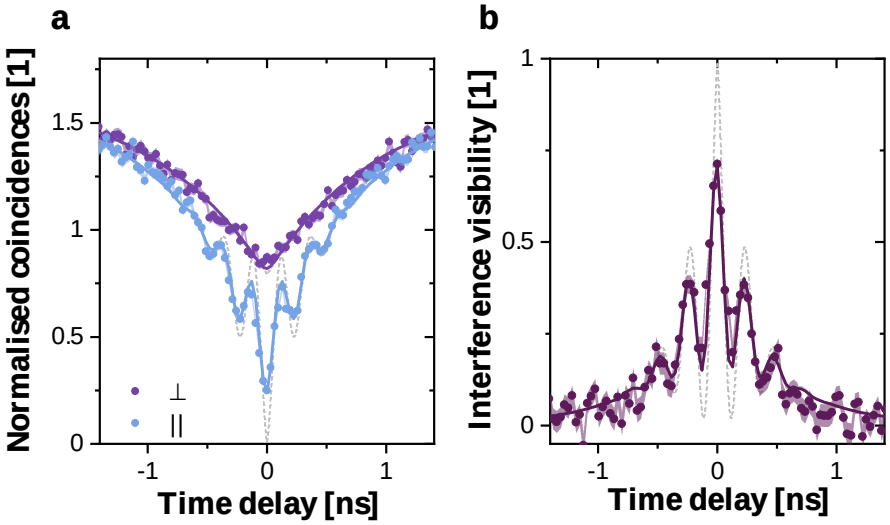

Figure 5.7: Low power HOM interference. **a** Co- and cross-polarised correlations. Solid lines represent fits to the data using parameters determined from the autocorrelation. **b** Corresponding interference visibility displaying a maximum of $73.1 \pm 1.6\%$. Solid line fit is determined directly from the fits of the correlations. Post-selection bin size is 32 ps.

Figure 5.7b shows the calculated interference visibility for the correlations shown in Figure 5.7a, alongside the calculated fit. A maximum raw visibility of $71.3 \pm 1.6\%$ is found, extending to $98.6 \pm 1.6\%$ upon deconvolution of the data, limited only by a small background contribution to the correlations. The agreement of the Lorentzian and Gaussian components to the coherence time support the conclusions drawn from the MI data in that for excitation at 1310 nm, decreasing excitation power leads to a coherence time limited by the inhomogeneous broadening. Similar effects have been seen in nanowires QDs which displayed the longest coherence times at saturation power as a result of the defect trap saturation for higher powers [195], and suggest the effect seen here could also be related to an absence of charge trap saturation for low powers. The MI data for excitation at 785 nm conversely suggests that as the coherence time remains longer for lower powers with a predominantly Lorentzian lineshape, the contribution of the inhomogeneous broadening does not become the limiting factor. Given the excess carriers generated in the QD environment under this type of excitation and the corresponding dynamics of the HBT correlations for the two excitation wavelengths, this seems like a reasonable conclusion. It is further noted that this was not a general effect seen for the QDs, suggesting further the contribution of the local environment to the coherence in the emission of the QD.

5.4 Interference with a Weak Coherent State

While the characterisation of the degree of mutual indistinguishability of a photon source yields information on the coherence properties of the emitter, it is unlikely in practice that such a setup using delayed single-photons from the same emitter would be used for long-distance quantum communications. For schemes such as a quantum relay, where the entangled photon-pair source may be separated physically over tens of kilometres from the input qubit, the case of interference of photons from separate sources becomes crucial.

More ideally, such schemes would be implemented using single-photon sources, this can be circumvented in the short term by looking to implement these schemes using a laser input source, and is favourable even due to the fact that QKD systems operate with weak coherent pulses. This, of course, requires being able to interfere photons of different photon statistics, something that was first demonstrated by Bennet *et al.* [198]. This concept was extended to include the interference laser and QD photons originating from the $XX-X$ cascade, allowing the teleportation of laser qubits using an electrically operated device [52, 42]. Later, this was extended further to the telecommunications wavelength using QD sources by Felle *et al.* [83], which again subsequently resulted in the teleportation of telecom *O*-band laser qubits [199].

This section presents a further development to this area by using the relatively new InAs/InP QD source in the telecom *C*-band to perform interference for the first time with a laser qubit of the form

$$|L\rangle = \cos\left(\frac{\theta}{2}\right)|H_L\rangle + e^{i\varphi}\sin\left(\frac{\theta}{2}\right)|V_L\rangle\,, \tag{5.16}$$

where θ, φ characterise the polarisation state on the Poincaré sphere, a crucial first step in working towards the teleportation of *C*-band laser qubits suitable for the enhancement of long-distance QKD networks.

5.4.1 Experimental Setup

A schematic of the two-photon interference (TPI) measurement is shown in Figure 5.8. In contrast to the HOM interference, a 99:1 beamsplitter was used in order to make efficient use of the QD photons, as the laser intensity could be set arbitrarily. A further 50:50 beamsplitter was then used in order to perform correlation measurements. The polarisation bases of the detectors was again set by using EPC and was calibrated using the 1% output of the interfering beamsplitter, with minimisation routines used as in the previous section. In contrast to the HOM interference, a more standard approach sending the QD photons through a LP orientated to select one linear polarisation was used in order to remove the effect of the beating from the FSS, instead allowing a focus on the energy overlap of the laser and QD photons. An overlapping routine was carried out periodically throughout the measurement using an OS after the interfering beamsplitter. The OS could be used to sequentially direct laser or QD photons towards a grating spectrometer with 1200 g/mm. A series of spectra was then fitted using a Gaussian function to extract the central energy of the emission. A feedback routine

was employed to minimise the difference in energy between the laser and the QD to below 2 μeV by controlling the energy of the laser. The intensity ratio between the laser and QD photons was also controlled periodically throughout the measurement using a digital variable attenuator (DVA), with a tolerence set to be 1% of the time-integrated average intensity.

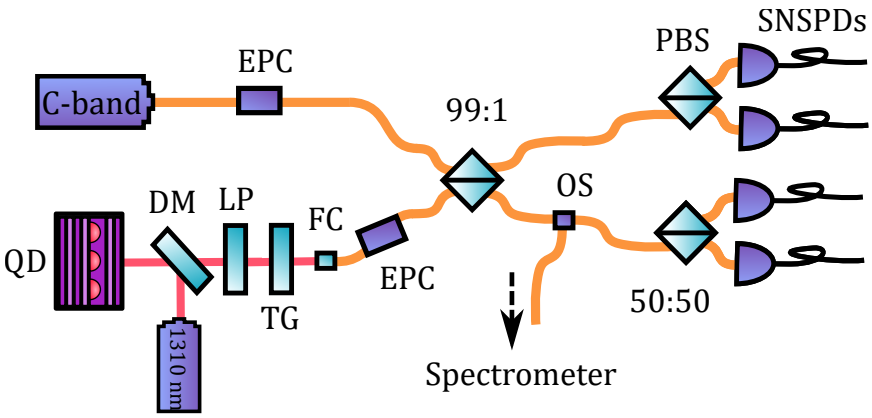

Figure 5.8: Two-photon interference with a weak coherent state. A tunable CW laser is used to generate a weak coherent state in the telecom *C*-band to interfere with a QD photon on a 99:1 unbalanced beamsplitter. On the QD 99% port, correlation measurements are performed to analyse the two-photon state using a standard HBT setup and SNSPDs. The QD 1% port is used for polarisation calibration. An optical switch (OS) allows for periodic frequency matching of the laser and QD photons.

When the laser and dot photons are distinguishable (due to their orthogonal polarisation), a dip at zero delay is expected in the correlation, due to the single-photon nature of the QD photons superimposed on the laser-QD and laser-laser background. When the input photons are indistinguishable and identical in all degrees of freedom (corresponding to the co-polarised case), a bunching at zero delay is expected due to two-photon interference superimposed on the dip, reflecting the higher probability for measuring the two-photon state at the beamsplitter. The form of the expected correlations can be described by a modified version of the two-photon correlation function for dissimilar photon sources presented by Bennett et al. [83, 198], which takes into account the differences of this experimental setup. The form of the correlation function is

$$g^{(2)}(\tau) = 1 + \frac{2\eta\alpha^2\left(e^{-|\tau|/T_2}\cos\left(\Delta E_L\tau/\hbar\right)\cos^2\phi\right) + \eta^2\left(g^{(2)}_{QD}(\tau) - 1\right)}{\left(\eta + \alpha^2 + \beta\right)^2}, \tag{5.17}$$

where η is the dot intensity, α^2 is the laser intensity, β is the uncorrelated background contribution, ΔE_L is the detuning between QD and laser photon, and ϕ gives the polarisation difference between the two photons ($\phi = 0$ and $\phi = \pi/2$ for co-and cross-polarised photons, respectively). The interference visibility can be calculated from the contrast of the co-and cross-polarised correlation measurements as

$$V(\tau) = \frac{g^{(2)}_{||}(\tau)}{g^{(2)}_{\perp}(\tau)} - 1, \tag{5.18}$$

with the correlation functions for co- and cross-polarised photons defined from Equation 5.17.

For perfect emitters with $g^{(2)}(0) = 0$ and no additional background, the post-selected interference visibility is defined by the relative intensity of the laser and QD photons at the beamsplitter. Together with the QD intensity, which is strongly correlated with the coherence time of its emission, this provides a parameter space by controlling both this ratio and the QD intensity. Two cases of experimental condition are considered in this chapter. The first consideration is the realistic conditions for maximising the two-photon coincidence rates, corresponding to the QD being excited at P_{Sat} and the QD/laser intensity ratio $\eta/\alpha^2 = 1$. The second consideration is a more idealistic case, where the QD is excited at $P_{Sat}/20$ to maximise the coherence time and $\eta/\alpha^2 = 2.5$ to maximise the visibility.

5.4.2 Results

Due to the large FSS of the QD used in the previous section, there would be a significant problem measuring entanglement, since the detector resolution would wash out such fast oscillations, resulting in a low entanglement fidelity. Therefore, it would have been infeasible to use in a quantum teleportation experiment, where not only are the interfering QD photons left unpolarised, but, crucially, a high entanglement fidelity is required. For this reason, another QD was selected for this experiment which will subsequently be used for the teleportation detailed in Chapter 7. As shown in Figure 4.11, coherence times exceeding 150 ps when exciting at P_{Sat} are found in ~ 80% of the QDs in this sample. This allows the FSS and source intensity to be the main focus of QD selection. Eventually, a QD with a FSS of 5.7 ± 0.2 μeV, one of the lowest found in this sample, was selected for the subsequent measurements. Autocorrelation measurements of this QD for the two powers P_{Sat} and $P_{Sat}/20$ are shown in Figure 5.9a and Figure 5.9b, respectively. Here, it is found that a simplified four-level model for the autocorrelation function is enough to capture the relevant QD dynamics stemming from additional population processes [157]. This fitting function has the form

$$g^{(2)}(\tau) = 1 - (1 + A + B)e^{-|\tau|/\tau_1} + Ae^{-|\tau|/\tau_2} + Be^{-|\tau|/\tau_3}, \tag{5.19}$$

where A and B denote coupling strengths to the additional levels, τ_1 is a timescale which depends on the radiative lifetime and the pumping rate and τ_2, τ_3 are the timescales of the additional decay processes. For low powers $B \to 0$ and this model reduces to a more standard three-level model. The background contribution and detector response is taken into account using the same method as described in Section 4.3 and a jitter of 90 ps is again used.

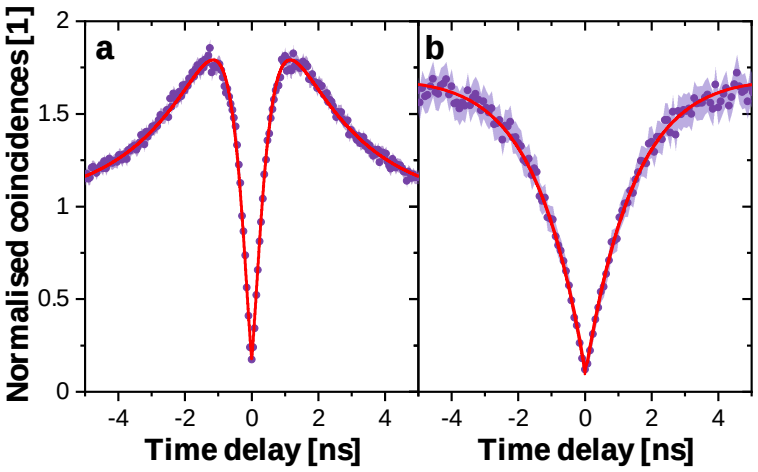

Figure 5.9: HBT autocorrelation of the QD used for TPI. a High power excitation at P_{Sat}. A fit to the data (solid line) reveals a $g^{(2)}(0) = 0.177$. **b** Low power excitation at $P_{Sat}/20$. A fit to the data (solid line) reveals a $g^{(2)}(0) = 0.095$.

From the fit a $g^{(2)}(0) = 0.177$ is determined from a $\beta = 0.10 \pm 0.02$ at P_{Sat}, with $A = 1.97 \pm 0.08$, $B = 1.96 \pm 1.33$, $\tau_1 = 0.36 \pm 0.03$ ns, $\tau_2 = 2.18 \pm 0.03$ ns and $\tau_3 = 0.19 \pm 0.05$ ns. The relatively high background in this case differs from the previous section, and is seemingly not a consequence of the detector response. Instead, it may be the result of uncorrelated emission from the semiconductor environment. For the lower power measurement, a $g^{(2)}(0) = 0.095$ is determined from a $\beta = 0.05 \pm 0.01$, with $A = 0.90 \pm 0.01$, $B = 0$, $\tau_1 = 1.53 \pm 0.02$ ns, $\tau_2 = 40.80 \pm 0.02$ ns. The lower value of β corresponds well with a power-dependent background emission, and $\tau_1 = 1.53$ ns corresponds well with the fitted radiative lifetime of this QD, which was determined to be $T_1 = 1.58 \pm 0.01$ ns from an independent lifetime measurement. The reduction of both coupling strengths and increase in the bunching time for lower power suggest similar dynamics as those described by the full rate equation model for the previous QD, with the faster electron capture rate and limited hole/exciton capture rate causing a long-lived electron shelving state after emission of an X^- photon. For the high power measurement, the additional timescale τ_3 is most likely related to the fast decay of the XX, again corresponding well with the decoupling of $B = 0$ for the lower power measurement.

The resulting correlations of the TPI measurement for the QD excited at P_{Sat} and intensity ratio $\eta/\alpha^2 = 1$ are shown in Figure 5.10a, where the the dip of the cross-polarised correlation extends down to just below 0.8, as a result of the relatively high laser-laser and QD-laser contributions. A small bunching peak around $\tau = 0$ can be seen for the co-polarised correlation, resulting from the increased probability of two photons entering the 50:50 beamsplitter. Solid lines are fits to the data using the parameters determined from the autocorrelation measurement and the experimentally-determined average intensities. Good agreement is found for the cross-polarised case. For the co-polarised case, additional fitting parameters are included to determine the coherence time $T_2 = 294 \pm 9$ ps and the energy detuning $\Delta E = 1.9 \pm 0.1$ μeV. This value for the coherence time agrees well with the value of $T_2 = 262 \pm 19$ ps determined from the MI. Figure 5.10b shows the corresponding interference

visibility where the fit is determined directly from the fits of the co- and cross-polarised correlations. A maximum raw visibility of $56.5 \pm 1.1\%$ is found out of a possible maximum theoretical value of 66.67% for this intensity ratio. This result constitutes 85% of the maximum obtainable value, limited only by the background contribution.

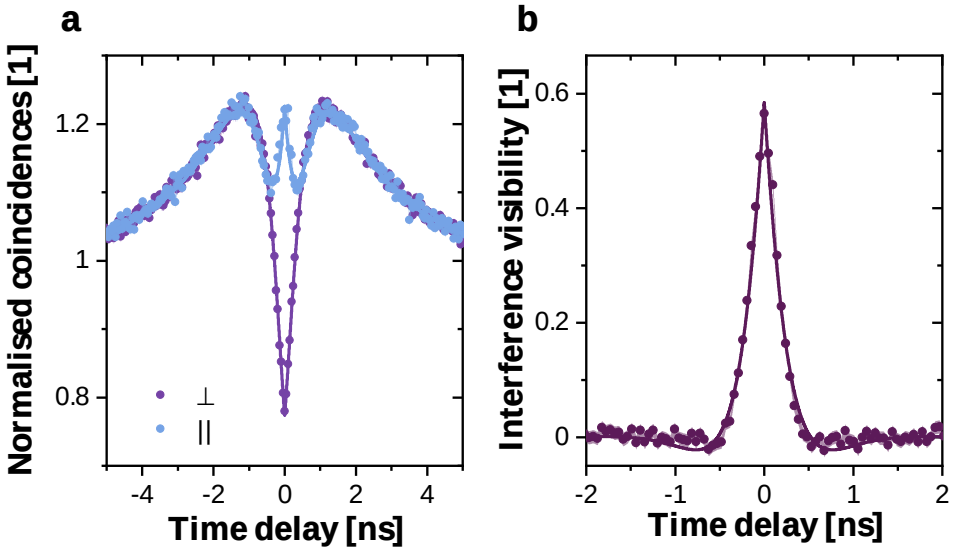

Figure 5.10: High power TPI with a weak coherent state. a Co- and cross-polarised correlations for $\eta/\alpha^2 = 1$. A small bunching peak is seen on the co-polarised correlation corresponding to the increased probability for detecting two photons entering the beamsplitter. Solid lines represent fits to the data using parameters determined from the autocorrelation. **b** Corresponding interference probability displaying a maximum visibility of $56.5 \pm 1.1\%$ and a coherence time of $T_2 = 294 \pm 9$, as a result of the measurement conditions. Solid line fit is determined directly from the fits of the correlations. Post-selection bin size is 48 ps.

The corresponding measurement for $P_{Sat}/20$ and $\eta/\alpha^2 = 2.5$ is shown in Figure 5.11. The dip of the cross-polarised correlation extends further down towards 0 due to the reduced laser-laser contributions, while the width of the co-polarised correlation peak, and hence the visibility peak, is much wider, corresponding to the increased coherence time. The raw visibility at $\tau = 0$ is found to be $72.8 \pm 2.7\%$, where the theoretical maximum is 80% for this intensity ratio, and so this result constitutes 91% of the maximum achievable value limited only by the background contribution. From the fits, a coherence of $T_2 = 471 \pm 29$ and detuning of $\Delta E = 1.5 \pm 0.1$ μeV is determined, corresponding well with the measured values using the MI and the accuracy of the energy-overlapping routine.

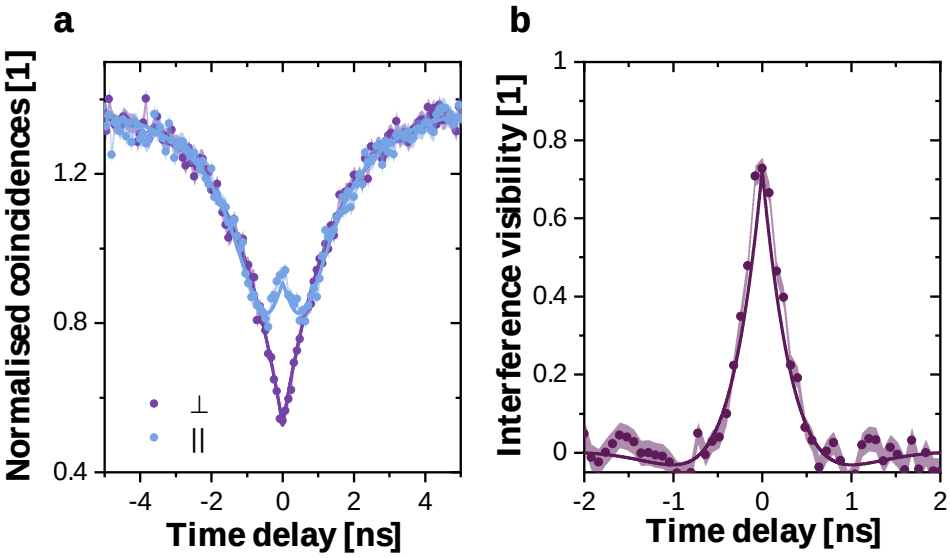

Figure 5.11: Low power TPI with a weak coherent state. a Co- and cross-polarised correlations for $\eta/\alpha^2 = 2.5$. The dip of the cross-polarised correlation extends further towards 0 as a result of the reduced laser-laser contribution. Solid lines represent fits to the data using parameters determined from the autocorrelation. **b** Corresponding interference probability displaying both a higher maximum visibility of $72.8 \pm 2.7\%$ and longer coherence time of $T_2 = 471 \pm 29$, as a result of the measurement conditions. Solid line fit is determined directly from the fits of the correlations. Post-selection bin size is 80 ps.

5.5 Summary

The work in this chapter first considered the HOM-type interference of superposition-state single photons from the neural X. The model describing interference of photon wave packets was extended to consider the beating mode function of these neutral transitions. Interference was carried out for high and low power regimes, exploring the level of achievable mutual indistinguishability. High post-selected visibilities were achieved despite the non-resonant excitation, and the values of the homogeneous and inhomogeneous components of the coherence time compared well with the corresponding MI measurements.

The second part of this section considered the first key element of the teleportation protocol for the teleportation of laser qubits; the TPI with a weak coherent state. Interference was performed again in two power regimes, exploring the parameter space and the limitations on the interference visibility for this type of emitter. It was found that the visibility was mainly limited by background contributions in both experimental conditions considered. The success in demonstrating non-classical interference with laser photons will be used directly in Chapter 7, when looking at the teleportation of such qubits.

Future work in this area would naturally concentrate on the reduction of the pure dephasing processes limiting the mutual indistinguishability of these photon sources, allowing future experiments involving remote single-photon emitters. In the first step, this could be achieved by utilising resonant excitation schemes in order to remove dephasing associated with carrier relaxation processes [165, 166, 171, 200]. Additionally, enhancement of the radiative lifetime of the QD by incorporation into a cavity, such as those recently demonstrated [189, 190, 201], would improve the overall source brightness, indistinguishability and efficiency. For the experiments involving laser photon interference, reduction of the pure dephasing and emitter lifetime would naturally reduce the time-gate restriction, allowing wider gates to be used.

Chapter 6

Entangled Photon Pairs in the Telecom C-Band

In this chapter, the entangled pair photon properties resulting from the $XX-X$ cascade will be considered, the next crucial element for performing quantum teleportation. A basic model for describing the polarisation-resolved correlations will be considered, as well as the full description of the two-photon density matrix for a general entangled state.

6.1 Introduction

Since the first demonstrations of entanglement using QD sources [76, 202, 77], there has been much work in the field towards realising ideal entangled photon-pair sources, consisting of transform-limited on-demand emission from fully symmetric QDs. There has been research focusing on the removal of temporal filtering [203], using a combination of excitation schemes [72, 204], the growth of more symmetric QDs to reduce the FSS [90, 188, 205], as well as work which focused on developing electrically-driven entangled photon-pair sources [66, 99, 19, 206, 207]. Again, much of this has been carried out with QDs emitting at wavelengths below 1 μm. However, there have been recent demonstrations from QDs emitting in the telecommunications bands [99, 133, 134, 208, 209], which are more desirable for application involving quantum cryptography [210], where the transmission through fibre is much more practical for long-distance communication links.

Here, the entangled photon-pair generation from QDs emitting near the telecom C-band will be considered under CW optical excitation and under excitation at 1 GHz, which is a requirement for developing a relay compatible with existing QKD infrastructure.

6.2 Modelling Entanglement from the Biexciton Cascade

In order to develop a qualitative understanding of the entanglement dynamics in the QD, a simple model will be introduced. As discussed in Section 2.2.3, entangled photon-pairs are generated in QDs through the radiative cascade of the XX-X decay, resulting in the two-photon state which has the form

$$|\psi\rangle = \frac{1}{\sqrt{2}}\left(|H_{XX}H_X\rangle + e^{iS\tau/\hbar}|V_{XX}V_X\rangle\right), \tag{6.1}$$

where the time-dependent phase is due to the FSS of the intermediate X state. This causes the polarisation to evolve over time after the measurement of a XX photon in any basis other than the QD eigenbasis. For $\tau = 0$, the expected state is simply the maximally-entangled Bell state $|\Phi^+\rangle$.

The density operator $\rho = |\psi\rangle\langle\psi|$ can be used to fully describe the two-photon state and the resulting dynamics of the emission from the QD. A simple model to describe the entangled photon emission from the QD, based on the solutions to a system of multi-level rate equations, is reproduced here from [206]. In its simplest form, the system includes the XX, the correlated exciton X_C, the uncorrelated exciton X_U and the ground state G. Detection of a XX photon places the system in the initial coherent exciton state. The time-dependent solutions to this system can then be used to describe the ideal time-dependent intensity and polarisation of the two-photon state as

$$\rho(\tau, S) = \frac{1}{2}\left(\rho_e(\tau, S)X_C(\tau) + \rho_m X_U(\tau)\right) \tag{6.2}$$

where ρ_e is the density operator for the entangled state given by Equation 6.1 and ρ_m is the density operator for mixed light given by the normalised identity matrix $I_4/4$. For the negative time delays, the same model is used to determine the the population of the XX after emission of an X, i.e. the ground state is initially populated. The benefit of utilising such a system to describe the entangled photon emission is that the system of rate equations can be easily extended to incorporate more intricate QD dynamics, if necessary. The most significant concept to note here is that for describing the entanglement, it is required to subdivide the X level in order to capture the relevant correlations with the previously detected XX photon.

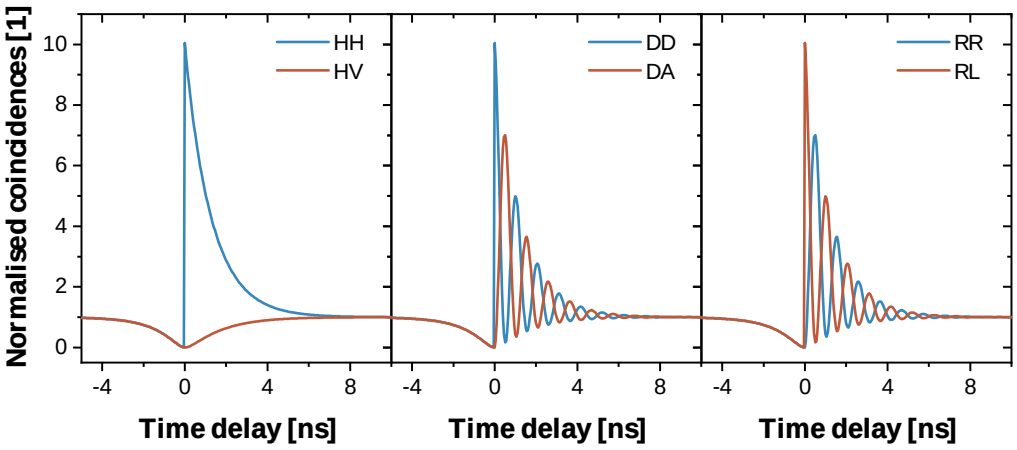

Figure 6.1: Simulated correlations for the polarisation-resolved $XX-X$ cascade in three complementary bases on the Poincaré sphere. Parameters used correspond to radiative lifetimes of $\tau_x = 1.5$ ns, $\tau_{xx} = 0.3$ ns and a FSS of $S = 6\hbar\,\mu$eV, excited at an e-h pump time $\tau_p = 12$ ns

The resulting correlations describing the measurement of an X photon after previous detection of an XX photon are then determined straightforwardly by projection of the density matrix $\rho(\tau, S)$ into the relevant polarisation detection basis. Figure 6.1 shows the result of such a simulation for the simple model discussed above. The parameters used correspond to a QD with a radiative lifetime of $\tau_x = 1.5$ ns, $\tau_{xx} = 0.3$ ns and a FSS of $S = 6\hbar\,\mu$eV, excited at an e-h pump time $\tau_p = 12$ ns. As, expected, the measurement in the QD eigenbasis results in static correlations, where there is a significant probability of measuring co-polarised photon pairs. Measurement of the state in the superposition bases reveals time-dependent oscillations at the frequency corresponding to the FSS.

6.3 Characterising Entanglement

In order to characterise entanglement, polarisation-resolved correlations are required in order to determine the correlation coefficient

$$E_{\alpha,\beta} = \langle \alpha\beta | \rho | \alpha\beta \rangle + \langle \alpha'\beta' | \rho | \alpha'\beta' \rangle - \langle \alpha\beta' | \rho | \alpha\beta' \rangle - \langle \alpha'\beta | \rho | \alpha'\beta \rangle , \tag{6.3}$$

where α and β denote the polarisation of the XX and X and the prime denotes orthogonal polarisation. For the unpolarised sources used here, the correlation coefficient can be determined directly from the polarised correlations $g^{(2)}_{\alpha\beta}(\tau)$ and $g^{(2)}_{\alpha\beta'}(\tau)$ as [211]

$$E_{\alpha\beta}(\tau) = \frac{g^{(2)}_{\alpha\beta}(\tau) - g^{(2)}_{\alpha\beta'}(\tau)}{g^{(2)}_{\alpha\beta}(\tau) + g^{(2)}_{\alpha\beta'}(\tau)}. \tag{6.4}$$

By considering the elements of the density matrix describing the entangled state and the relations to the correlation coefficients in three complementary bases, it can be shown that the fidelity to the Bell state $|\Phi^+\rangle$ is given by [58, 211]

$$f^+ = \langle \Phi^+ | \rho | \Phi^+ \rangle \tag{6.5}$$

$$= \left(\rho_{11} + \rho_{44}\right)/2 + \mathrm{Re}\{\rho_{14}\} \tag{6.6}$$

$$= \left(1 + E_{HV} + E_{DA} - E_{RL}\right)/4, \tag{6.7}$$

where E_{HV}, E_{DA}, E_{RL} refer to the correlation coefficient in the rectilinear, diagonal and circular bases, respectively. From the form of Equation 6.6, it can be seen that it is exactly the off-diagonal terms of the density matrix which allow the measurement of $f^+ > 0.5$ and thus the discrimination of the entangled state. It is the correlation coefficients E_{DA}, E_{RL} in the QD superposition basis which contribute to these off-diagonal terms. Therefore, the number of measurements required to determine the fidelity to the expected Bell state is significantly reduced to just three basis combinations, instead of the nine required to determine the full density matrix. The labelling of the basis here refers to the eigenbasis of the QD, and so measurements are performed in the QD basis, which can be determined by using a LP to select either the H or V component, from which all other polarisation states are defined.

The top panel of Figure 6.2 shows the resulting correlation coefficients for the simulated QD correlations shown in Figure 6.1, determined using Equation 6.4. Due to the nature of the QD state, the correlation coefficient is positive for measurement in the linear bases and negative in the circular basis. Evaluation of the fidelity using Equation 6.7 shows the expected oscillatory behaviour of the QD state with respect to the maximally entangled Bell state.

Along with the fidelity to the expected entangled state, the Bell parameter provides another metric for quantifying the non-classicality of the observed correlations. In the CHSH inequality form [16], the Bell parameter in three orthogonal planes of the Poincaré sphere can be related to the elements

of the density matrix, and therefore the correlation coefficients as [58]

$$S_{rd} = \sqrt{2}\,(E_{HV} - E_{DA}) \leq 2, \tag{6.8}$$

$$S_{dc} = \sqrt{2}\,(E_{DA} - E_{RL}) \leq 2, \tag{6.9}$$

$$S_{rc} = \sqrt{2}\,(E_{HV} - E_{RL}) \leq 2. \tag{6.10}$$

where S_{rd}, S_{dc} and S_{rc} are the Bell parameters in the rectilinear-diagonal, diagonal-circular and rectilinear-circular planes of the Poincaré sphere, respectively. Violation of these inequalities then serves to demonstrate that the observed correlations cannot be produced classically by way of local hidden variables and require an entangled state. Again, it can be seen that only measurements of three correlation coefficients are required in order to quantify the Bell parameter in three orthogonal planes of the Poincaré sphere.

6.3.1 Time-Evolving Entanglement

While the above formalism describes the required measurements to determine the fidelity to the static Bell state for delays $\tau = 0$, the actual form of the entangled state from the QD evolves over time according to Equation 6.1. The above concept can be extended, and has been by Ward *et al.* [208], to include the time-evolving dynamics. Following the supplementary note of [208], the time-evolving fidelity can again be expressed by considering the two-photon density matrix as

$$f^{+}(\tau) = \langle \psi(\tau) | \rho | \psi(\tau) \rangle \tag{6.11}$$

$$= \frac{1}{4}\left[1 + E_{HV} + (E_{DA} - E_{RL})\cos\left(\frac{S\tau}{\hbar}\right) + (E_{LD,RA} - E_{LA,RD})\sin\left(\frac{S\tau}{\hbar}\right)\right] \tag{6.12}$$

where $E_{LD,RA}$, $E_{RD,LA}$ correspond to the correlation coefficients in two elliptical polarisation basis on the $\{DLAR\}$ plane of the Poincaré sphere, bisecting the $L-A$ and $L-D$ states, respectively. This extends the number of measurements required to characterise the time-evolving entangled light emission from the QD to just five bases.

By combining all of the above, a simulation of the expected correlation coefficients can be seen in the top panel of Figure 6.2. The same behaviour from the correlations is seen, where now the correlation coefficient of the superposition basis states oscillates with a period defined by the FSS, and the initial phase is determined by the respective measurements basis, such that each basis is $\pi/2$ out of phase with the next.

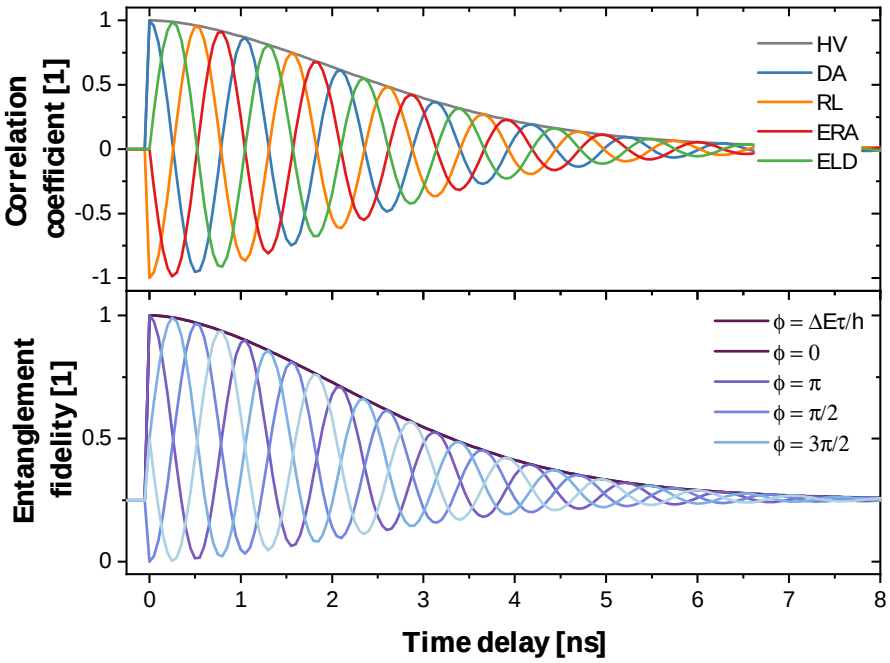

Figure 6.2: Simulated time-evolving entanglement. (**Top**) Correlation coefficients for the polarisation-resolved $XX-X$ cascade in 5 bases on the Poincaré sphere. (**Bottom**) Resulting fidelity to the static and time-evolving states. For $\phi = 0$, the fidelity is to the Bell state $|\Phi^+\rangle$.

The simulated fidelity to various maximally entangled Bell states, determined by the phase of Equation 6.12, can be seen in the bottom panel of Figure 6.2. For the static phases, the entanglement fidelity oscillates in time as expected, with $\phi = 0$ corresponding to the fidelity to the Bell state $|\Phi^+\rangle$. However, with the time-dependant phase $\phi = S\tau/\hbar$, the fidelity no longer oscillates and becomes static following the envelope of the oscillations, corresponding to the fidelity to the time-evolving entangled state given by Equation 6.1.

6.3.2 Experimental Setup

A schematic of the experimental setup used for characterising the entangled photon-pair properties is shown in Figure 6.3. The QD was excited using a 1310 nm laser. The PL was collected using a pair (not shown) of pellicle beasmsplitters in order to remove polarising effects of the optical elements. The light was then directed towards a TG where the XX and X emission was filtered, spatially separated and coupled back into fibre. EPCs were used in order to define the polarisation basis before detection using a PBS and SNSPDs with timing jitter ~ 90 ps. The measurement bases were calibrated using a polarised reference laser aligned to the QD eigenbasis, after selection of one of the linear components using LP. Once in the QD basis, a HWP and QWP were then used to put the reference laser in the superposition bases of the QD. A minimisation of the laser count rate on the detectors was performed as in the TPI calibration in Chapter 5, and the voltages of the EPCs saved.

Time-correlated spectroscopy was performed using the XX photons as the start and the X photons as the stop. Co- and cross-polarised correlations in polarisation bases P and Q were then measured in this way, cycling through the polarisation bases every 30 minutes to ensure similar experimental conditions between measurements.

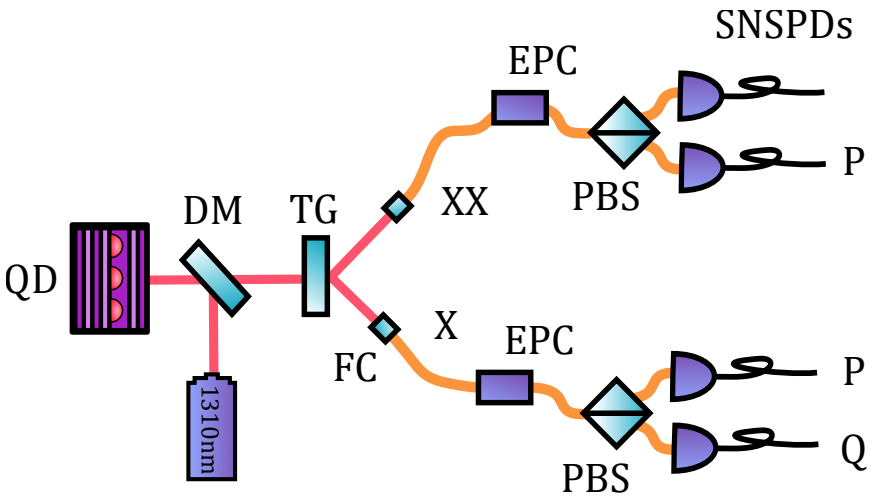

Figure 6.3: Experimental setup for measuring entanglement. Light from the QD is collected and directed towards a TG to spatially separate and spectrally filter the X and XX emission. After the TG, the light is coupled into SM fibre where it is then sent through an EPC, before detection using a PBS and SNSPDs.

6.3.3 Results

The second-order polarisation-resolved correlation measurements for the five required bases are shown in Figure 6.4. Most of the correlations show the expected behaviour when comparing qualitatively to the simulations. For the correlations in the HV basis, small oscillations suggest a detection misalignment of the XX and X, away from the QD eigenstates. This could be the result of the projection and alignment of the reference laser to the linear QD state. The slightly high probability of detecting a V polarised X could be the result of this misalignment; however, it must also be noted that spin-scattering [206, 211–213] of the QD could also lead to this increased probability, leading further to a reduction of the correlation coefficient. For the well-aligned bases, the increase in the base envelope of the oscillations could be as a result of the QD dynamics, which display a small bunching following the anti-bunching dip for short time delays away from $\tau = 0$, indicating the presence of re-excitation [214]. It can also be seen that there is an increased probability for detection of cross-polarised photons in the circular basis, when compared to all other correlations. Such effects have been seen previously for QDs with low FSS in the presence of a fluctuating nuclear magnetic-field, where the eigenstates are closer to the circular basis, due to the effect of an increase in the circular component of the FSS [206].

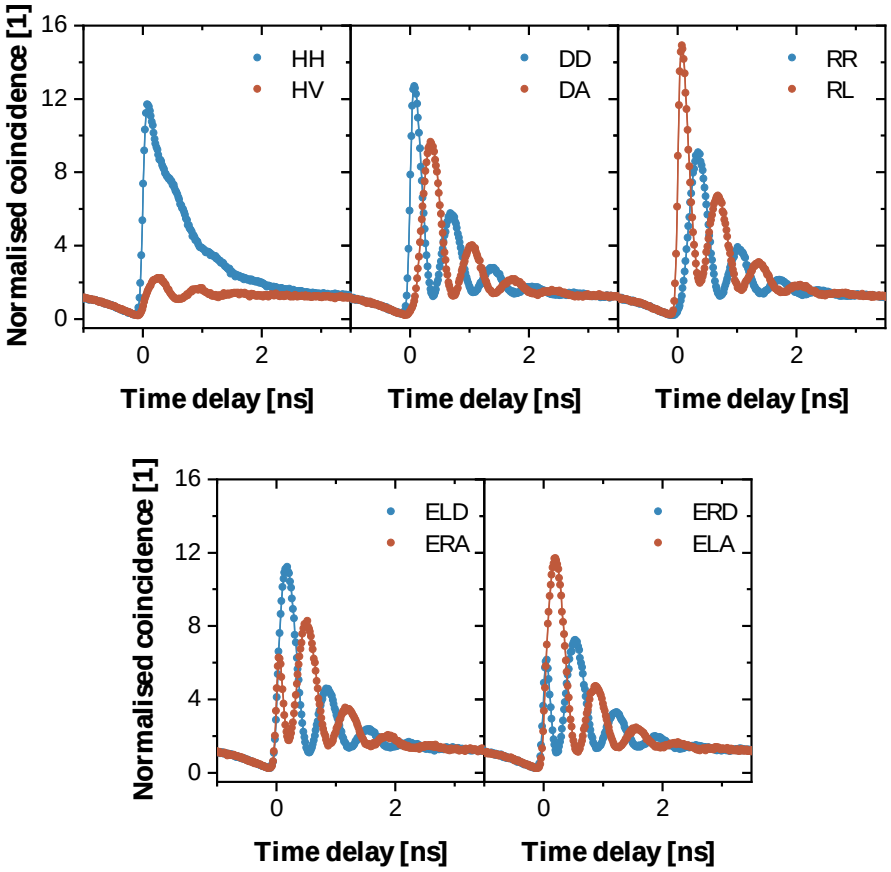

Figure 6.4: Measured polarisation-resolved second-order correlations. Each basis measurement consists of a simultaneously measured co- (blue) and cross-polarised (orange) correlation. Measurements in the superposition basis reveal strong oscillations of the two-photon state with a period of 713 ps, as expected from a FSS of $S = 5.8$ μeV. A slight oscillation in the HV basis indicates a potential misalignment of the detection basis. The data was recorded with a timing resolution of 16 ps and binned into 32 ps in post-processing. Shaded area (visible as lines) denote error calculated from counting statistics.

The correlation coefficients calculated for each basis can be seen in the top panel of Figure 6.5. Again, the data qualitatively follows the expected behaviour from the simulations; however, the effect of the misalignment is seen more clearly. The correlation coefficient oscillates in the HV basis, with the other bases each following the envelope. From the phase of the correlation coefficients, it appears that only the $E_{LD,RA}$ suffers from a small misalignment in phase, with all others following the expected pattern. The unusual feature of this is that the negative envelope does not follow such an oscillation, as would typically be expected from a simple rotation of the detection basis. The correlation coefficients reach maximum values of $E_{HV} = 0.83 \pm 0.01$, $E_{DA} = 0.90 \pm 0.01$ and $E_{RL} = -0.90 \pm 0.01$ at $\tau = 0$.

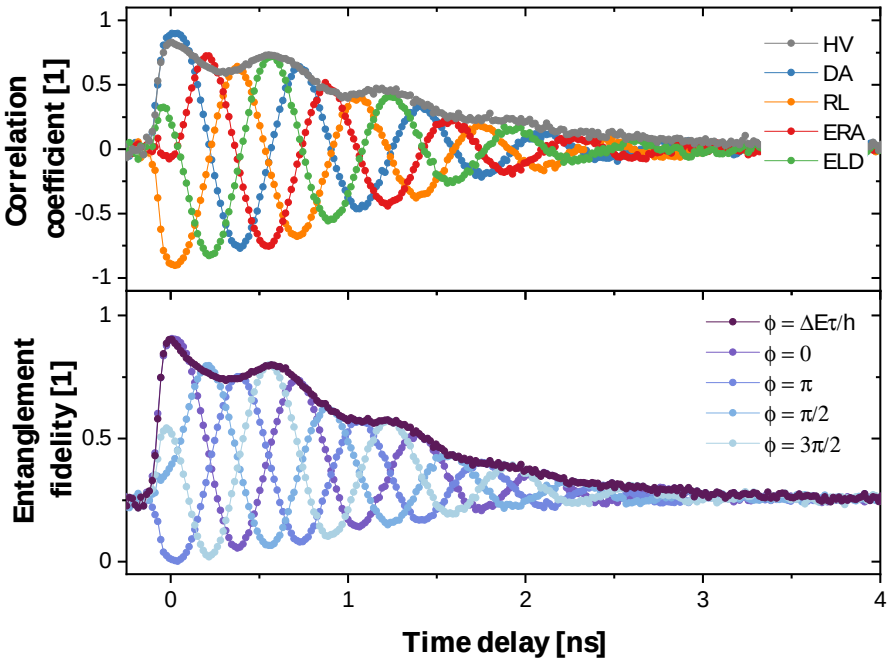

Figure 6.5: Measured time-evolving entanglement. (**Top**) Correlation coefficients for the polarisation-resolved $XX-X$ cascade in five bases on the Poincaré sphere. (**Bottom**) Resulting fidelity to the static and time-evolving states. For $\phi = 0$, the fidelity is to the Bell state $|\Phi^+\rangle$. The phase of the correlation coefficients indicate good alignment of the detection bases, with a slight offset in the *ELD* basis. The presence of an oscillation on the *HV* basis, with the oscillation in the envelope of the other correlation coefficients, however, indicates a potential misalignment.

The bottom panel of Figure 6.5 shows the calculated fidelities to the various entangled states, as discussed above. The behaviour follows closely that of the correlation coefficient, with now the fidelity to the time-evolving state being the envelope of the fidelity to the static entangled states. For the time-evolving state and the $|\Phi^+\rangle$ Bell state, the fidelity reaches a maximum of $f^+ = 0.91 \pm 0.01$ at $\tau = 0$, and constitutes the highest recorded entanglement fidelity of a QD source operating near the Telecom *C*-band. At this excitation power, the entanglement persists for approximately 1.5 ns, before dropping below the value of 0.5, corresponding to classical correlations. A counts-weighted average over the period in which the entanglement fidelity to the time-evolving state remains greater than 0.5 results in $\tilde{f}^+ = 0.72 \pm 0.01$, implying that entanglement would be observed with a gate-period close to the radiative lifetime of the X in the absence of a FSS. Such a result is encouraging motivation for the development of FSS erasure methods [215, 216]. However, in such a scheme the operation of the source under pulsed excitation would be much more desirable in order to reduce strong re-excitation degrading the entanglement fidelity over longer times.

Finally, the Bell parameters can be calculated according to Equation 6.8, and are found to be $S_{rd} = 2.44 \pm 0.02$, $S_{dc} = 2.54 \pm 0.03$ and $S_{rc} = 2.44 \pm 0.02$ for the three orthogonal planes of the Poincaré sphere, with all values violating the classical threshold of two, thus confirming the large degree of entanglement in the two-photon state.

6.4 Anomalous Fine-Structure Splitting

The deviation away from the expected time-evolving entanglement fidelity can be explained by the fact that the polarisation basis of the X and XX are not perfectly aligned as discussed. However, an alternate explanation is that the X and XX do not share a common eigenbasis. That is to say, they do not emit in a co- or cross-polarisation basis. This effect has been seen in the FSS measurements of many QDs in this sample, where here, the effect manifests as a deviation away from the anti-correlation in energy of the expected $\{|H\rangle, |V\rangle\}$ basis. Figure 6.6 shows an example measurement of such a QD with an anomalous FSS, determined from a QWP measurement of the FSS, as described in Section 3.1.3. The spectrum, displayed in Figure 6.6a, shows the typical ordering of the transitions seen in QDs in this sample, where the X, XX and X^- have been labelled. Figure 6.6b shows the corresponding measurement of the FSS. As can be seen at the onset, there is a small amount of energy correlation, suggesting that the polarisation of the emitted photons are not well-correlated in the usual linear basis. Another feature of QDs with such anomalous splitting of the X and XX is the presence of a splitting in the charged X lines, as shown in Figure 6.6c, being most noticeable in the X^- transition where the signal is strong enough to resolve small splitting.

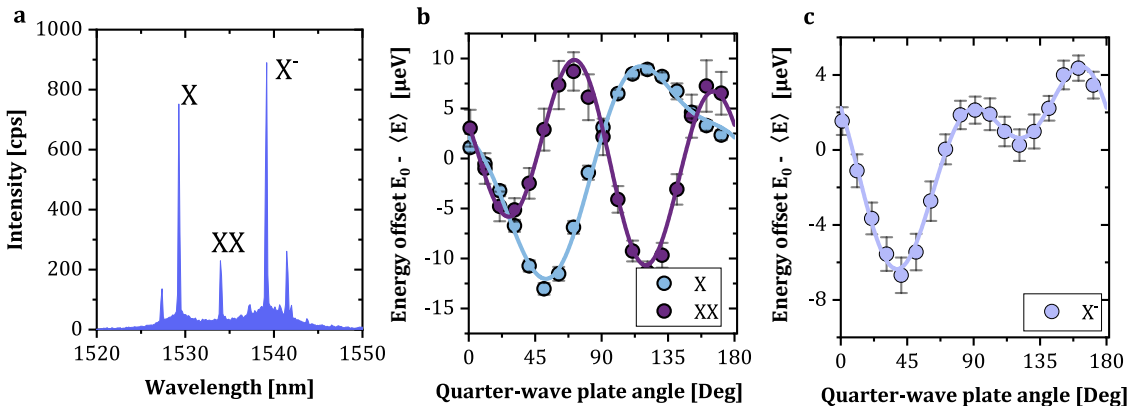

Figure 6.6: Anomalous fine-structure splitting in a QD. a Spectra of a QD measured under EL at $T = 44$ K, with the typical transitions of the X, XX and X^- labelled. **b** FSS measurement and reconstructed curve of the X and XX, showing a typical anomalous splitting, where there is a deviation away from the expected anti-correlation for co-polarised photon-pairs. **c** Same measurement but for the X^-, which should typically have zero splitting.

In general, this effect is prevalent across QDs in this sample and causes a problem when looking to perform entanglement measurements. Calibrating the detection basis is no longer possible in the straightforward manner using the linearly polarised eigenstates to determine the reference frame for the polarisation calibration. This effect was particularly prevalent when performing excitation at 1 GHz on the QD, discussed in the following section. A further deviation of the states away from the linear basis was seen under pulsed optical excitation for this QD.

Currently, no theory exists to explain this new phenomenon. Consequently, the rest of this chapter develops a framework to provide insight into possible origins, along with a method to recover entanglement from these QDs in order to perform the quantum teleportation at 1 GH, discussed in Chapter 7.

6.4.1 Free-Eigenstate Model

The presence of a splitting on the charged exciton indicates the presence of a magnetic field in the vicinity of the QD [217, 78, 218–220]. Given that a significant proportion of the QDs measured on the sample display both simultaneous anomalous splitting and a splitting of the charged line, it seems reasonable that this is the result of the same effect. One explanation for such an effect is the presence of a nuclear magnetic field [206, 221, 222], which modifies the eigenstates of the XX and X to a general non-orthogonal set, in addition to lifting the degeneracy of the charged exciton triplet and singlet.

The model presented below offers an explanation in terms of such an internal magnetic field; however, an equivalent external magnetic field that is required to demonstrate such an effect seen in Figure 6.6c needs to be large, on the order of ~ 1 T. This is much larger than the typical fields generated by nuclear magnetic interactions [222]. There is no obvious origin of such a large internal field and so the model presented below is somewhat implausible. Therefore, it is likely that there is a better explanation that has not been considered, something that would be an interesting area for future research.

Returning to the exchange interaction picture of the eigenstates of the X introduced in Section 2.2.3, and considering only the part referring to the bright exciton, the effect of a normally orientated magnetic field on the fine-structure is [217, 78]

$$H = \frac{1}{2}\begin{pmatrix} \Delta & S \\ S & \Delta \end{pmatrix} + \frac{\mu_0 B}{2}\begin{pmatrix} g_z & 0 \\ 0 & -g_z \end{pmatrix}, \tag{6.13}$$

using the angular momentum basis $M = |\pm 1\rangle$, corresponding to the polarisations $\{|R\rangle, |L\rangle\}$, where B is the magnetic field strength and g_z is the electron g-factor in the normal direction. By subtracting the dark X splitting energy Δ and rotating to the $\{|H\rangle, |V\rangle\}$ basis, the Hamiltonian for the bright X energy splitting can be written as [206]

$$H = \frac{1}{2}\begin{pmatrix} S_r & -iS_c \\ iS_c & -S_r \end{pmatrix}, \tag{6.14}$$

where S_r and S_c refer to the splitting in the rectilinear and circular bases, respectively. Here the component S_c is now proportional to the strength of a normally orientated magnetic field and the total splitting is given by $S = \sqrt{S_r^2 + S_c^2}$. The effect of this for a fluctuating nuclear magnetic field has been detailed in [206], and results in a modification of the polarisation eigenstates to a general elliptical eigenbasis, as shown schematically in Figure 6.7. For the normal case of no magnetic

field interaction, the eigenstates of the XX and X are parallel with emission of linear co-polarised photon pairs. With increasing magnetic field strength, the eigenstates of the XX and X transition to non-orthogonal states given by [206]

$$|P_{XX}\rangle = \alpha|H_{XX}\rangle - i\beta|V_{XX}\rangle \qquad |P_X\rangle = \alpha|H_X\rangle - i\beta|V_X\rangle, \tag{6.15}$$

$$|Q_{XX}\rangle = \alpha|V_{XX}\rangle - i\beta|H_{XX}\rangle \qquad |Q_X\rangle = \alpha|V_X\rangle - i\beta|H_X\rangle, \tag{6.16}$$

where $\alpha^2 + \beta^2 = 1$ and $\beta/\alpha = S_c/(S_r + S)$, with emission of elliptically polarised photon pairs. The two-photon state is now

$$|\Psi\rangle = \frac{1}{\sqrt{2}}\left(|P_{XX}\rangle|P_X\rangle + e^{iS\tau/\hbar}|Q_{XX}\rangle|Q_X\rangle\right), \tag{6.17}$$

and still results in emission of polarisation entangled photon pairs. At $\tau = 0$, the entangled state is still the expected Bell state $|\Phi^+\rangle$, when expressed in the QD basis.

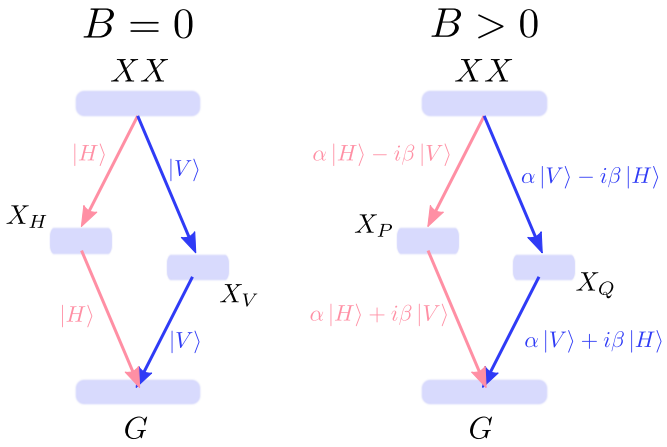

Figure 6.7: Modification of the polarisation eigenstates under a normally orientated magnetic field. At zero-field, the energy structure resultant from the exchange interaction remains the same and the mixing of the $M = |\pm 1\rangle$ eigenstates results in the linearly polarised eigenbasis $\{|H\rangle, |V\rangle\}$. With the application of a magnetic field in the normal direction, the eigenstates are modified resulting in an elliptically polarised non-orthogonal basis.

With no magnetic field $S_c \to 0$ and the states are the same as those in Equation 2.19. For increasing S_c, the states become elliptically polarised before eventually tending towards the circular basis states

$$|\Psi\rangle = \frac{1}{\sqrt{2}}\left(|R_{XX}\rangle|L_X\rangle + e^{iS\tau/\hbar}|L_{XX}\rangle|R_X\rangle\right). \tag{6.18}$$

The expected effect of a QWP measurement can be simulated by calculating

$$E(\chi) = \frac{\mathrm{Tr}\{\rho_i M(\chi)^\dagger H(S_r, S_c) M(\chi)\}}{\mathrm{Tr}\{\rho_i M(\chi)^\dagger \rho_i M(\chi)\}}, \tag{6.19}$$

where $M(\chi)$ denotes the matrix operator for the measurement and ρ_i is the density matrix determined as an equal mixture of the eigenvectors of $H(S_r, S_c)$, corresponding to an unpolarised source. The splitting energy is opposite for the X and XX corresponding to $S_X = -S_{XX}$, and is taken into account by setting $H_X = -H_{XX}$. Figure 6.8 shows the result of this effect on the FSS measurement for the X and XX. As can be seen for increasing S_c, the states move from anti-correlated (co-polarised) for $S_c = 0$ to become partially correlated (elliptically polarised), to finally completely correlated (cross-polarised).

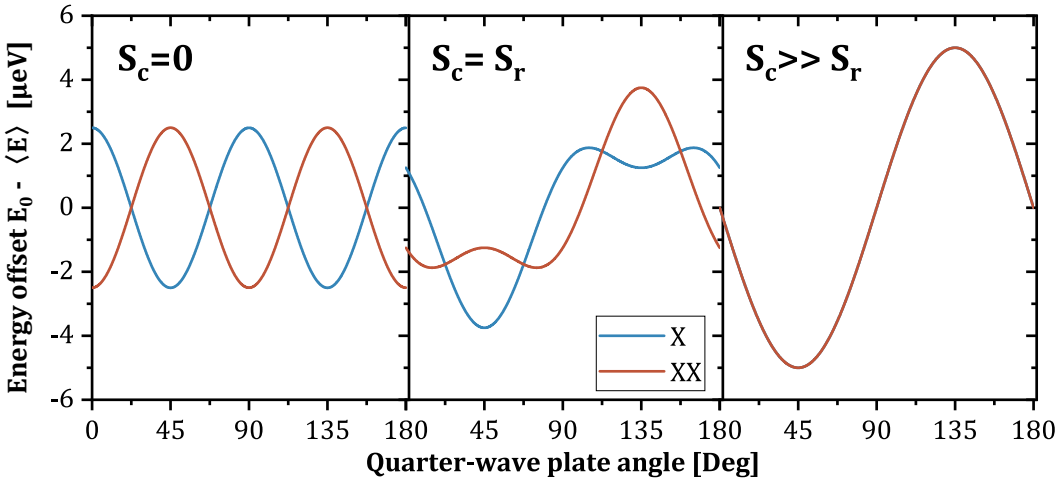

Figure 6.8: Simulated FSS measurement of the X and XX for increasing magnetic field strength $\propto S_c$. (**Left**) Resulting eigenstates in a QWP measurement for $S_c = 0$ where there is no modification. The states remain perfectly linear with only the $4f$ component. (**Centre**) Modification for a component of $S_c \sim S_r$, where the eigenstates are now elliptically polarised, with both $2f$ and $4f$ components. (**Right**) For large S_c the states tend towards circularly polarised eigenstates and the $2f$ component dominates.

The corresponding density matrix is then parametrised by the linear and circular components of the total splitting and calculated as before

$$\rho(\tau, S_r, S_c) = \frac{1}{2}\left(\rho_e(\tau, S_r, S_c) X_C(\tau) + \rho_m X_U(\tau)\right). \tag{6.20}$$

Writing this matrix using the linear QD eigenbasis and performing the projections as before, corresponding to measurement in the different polarisation bases, the correlation coefficients and entanglement fidelity can be plotted to highlight the effect of measuring such a QD. Figure 6.9 shows a simulation of this for the same parameters as before, except now with $S_r = 3.4$ μeV and $S_c = 1.1$ μeV, a similar ratio to those determined for the QD used for the entanglement measurement described above. The overall result agrees qualitatively very well with the measured data. The oscillation of

the HV correlation coefficient enveloping all other oscillations, corresponding to the misaligned detection, is reproduced without any further assumptions on the detection bases. This indicates that with the measured data, the projection of the states onto the linear basis, and the subsequent alignment to this basis follow the form of state in Equation 6.17, where there is a small circular component to the splitting, indicating the presence of a small magnetic field felt by the QD.

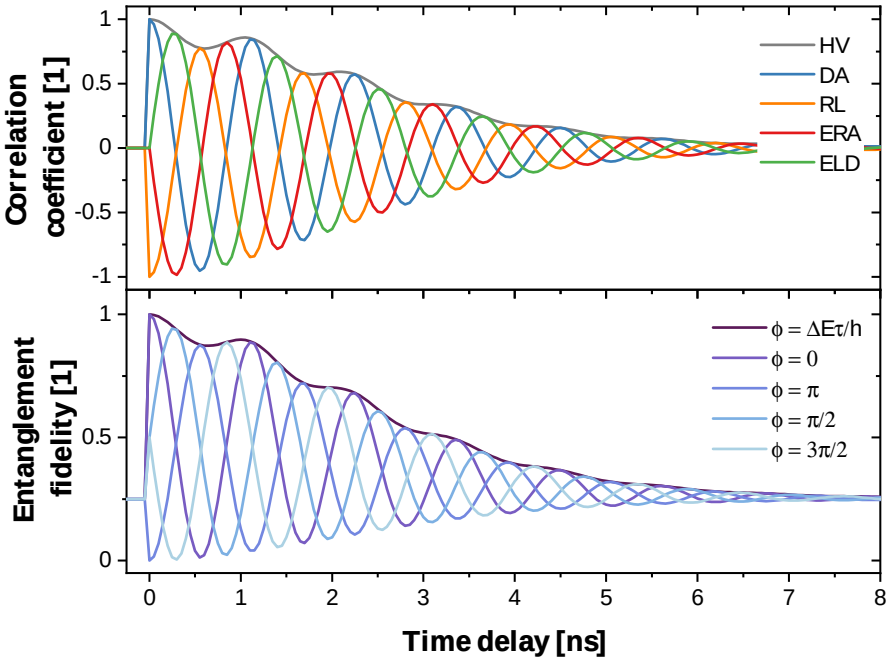

Figure 6.9: Simulated time-evolving entanglement in the presence of a small circular splitting S_c, projected against the linear basis. (**Top**) Correlation coefficients for the polarisation-resolved $XX-X$ cascade in five bases on the Poincarè sphere. (**Bottom**) Resulting fidelity to the static and time-evolving states. For $\phi = 0$, the fidelity is to the Bell state $|\Phi^+\rangle$. With the measurement basis projected against the expected linear basis, the oscillation of the envelope is recovered, qualitatively describing the effect seen in the data in Figure 6.5

6.4.2 Statistics of Anomalous Fine-Structure

To explore this effect further, data for 90 QD FSS measurements measured under EL at $T = 44$ K, the same measurements from Section 3.1.3, were analysed using the Fourier method to determine the linear and circular components of the splitting from the magnitudes of the 2χ and 4χ frequency components, as discussed in Section 3.1.3. However, this only determines the magnitudes of those components with respect to the lab measurement basis, which, in general, is not aligned to the axis of the QD. In order to correct for this rotation introduced by the optics of the measurement and the alignment of the QD with respect to the axis of the LP, the Stokes parameters for all 90 QD X and XX were determined and the corresponding states plotted on the Poincaré sphere.

For a normal QD, growth is preferentially elongated along the same crystal axis. Therefore, the collinear eigenstates tend to point along the crystal axis corresponding to the H and V linear

polarisations [82, 223]. Indeed, by looking at the statistics, the majority of QDs were found to have states lying within a plane, concentrated along an axis in the plane. By using the mean state to define the QD axis, a rotation Muller matrix was defined to map the lab frame to the QD frame, in order to transform the determined Stokes parameters.

Figure 6.10 shows the result of transforming all 90 QD X and XX states into the defined QD frame, using this method. The colour of the states represent the overlap of the X and XX, where the overlap has been calculated using the eigensates, and so co-polarised photons have an overlap of 1. For the Stokes parameters determined here, an X pointing along H will have a corresponding co-polarised XX pointing along V. From the plots it can be seen clearly that many QDs approximately emit in the linear bases, as expected. However, a significant number display eigenstates deviating away from the polar states, towards the circular basis, with the X and XX pointing now towards the same circular state, as described by the states in Equation 6.15. Again, this corresponds to the QD becoming elliptically polarised with non-collinear eigenstates. It is noted that while the eigenstates deviate way from the linear basis, the cascade still produces correlated photon pairs with orthogonal polarisation due to the conservation of spin. This coherent effect allows for the measurement of entanglement, despite the elliptical eigenbasis.

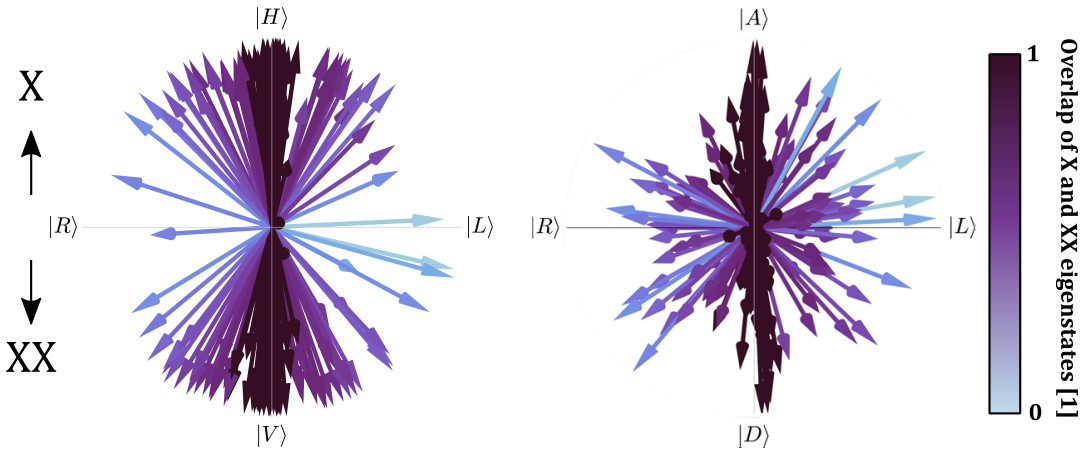

Figure 6.10: Measured states expressed in the frame of the QD. (**Left**) Side view and (**Right**) Top view of the determined X and XX states for 90 QDs in the frame of the QD, determined by rotation into the frame of the mean linear state. The colour of the states represent the overlap of the X and XX, where the overlap has been calculated using the eigensates, and so co-polarised photons have an overlap of 1.

After rotation into the QD frame, the linear S_r and circular S_c components of the splitting then correspond to that of the QD. Figure 6.11a plots the calculated circular component of the X and X^- splitting against the corresponding magnitude of the X^- splitting for each QD. For splitting below approximately 4 μeV, the data is relatively noisy merely due to the error of extracting parameters for low FSS. However, the trend is clear with higher X^- splitting correlating with the circular component of the X splitting. It also highlights that the charged line FSS is dominated by a circular component following the $y = x$ line near perfectly, again, as expected for a charged line in a magnetic field.

Figure 6.11b shows the statistics of the circular component within this sample for the neutral, positively and negatively charged Xs, showing that there is a ~ 40% probability of finding such an anomalous splitting dot, characterised by the presence of a significant component of splitting in the circular basis. The distribution can be described by a normal distribution with a width $\sigma \sim 8\ \mu$eV for all Xs.

Finally, in Figure 6.11c, the fraction of the circular component is plotted against the infidelity of the X/XX, defined as

$$\gamma = 1 - \langle XX(S_r, S_c) | X(S_r, S_c) \rangle \tag{6.21}$$

where $|XX(S_r, S_c)\rangle$ and $|X(S_r, S_c)\rangle$ are determined from the solutions to the Hamiltonian in Equation 6.14, constituting the general eigenbasis states as a function of the circular component, which is proportional to the strength of the field [206]. Once more, the data here agrees well with this description. For $\gamma \to 1$, the fraction of the circular component becomes large, and the states tend towards the cross-polarised circular basis. For $\gamma = 0$, the X and XX states have no circular component and the states remain in the linear QD basis, as expected.

Overall, this seems to align well with the fact that a QD with anomalous splitting appears to be as a result of potentially a local magnetic field, or some interaction which manifests as the introduction a circular component to the splitting or splitting of the charged line. In contrast to the nuclear magnetic reaction, however, this local magnetic field does not average to zero over the duration of a measurement [206].

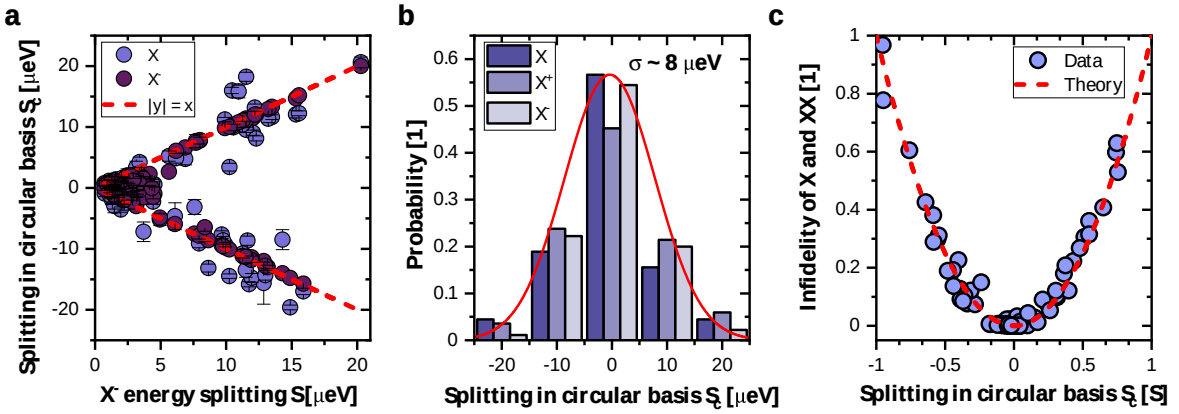

Figure 6.11: Statistics of the anomalous fine-structure effect seen in our sample. **a** Splitting of the circular component of the FSS for X^+, X and X^- plotted against the total splitting X^- line for 90 different QDs. The red dashed line denotes a linear function with unit gradient, showing that the splitting of the charged complexes are dominated by the circular component of the splitting. The line also shows that the circular components all increase roughly linearly with the increasing X^- splitting, corresponding to a stronger local magnetic field. **b** Statistical distribution of the circular component of the FSS for the X, XX and X^-. The data is well described by a Normal distribution with mean 0 and $\sigma \sim 8\mu eV$. **c** Infidelity of the X and XX states plotted against the fraction of circular splitting. The dashed line corresponds to the calculated behaviour, assuming states of the form of those resulting from a magnetic field interaction.

As a demonstration of how the anomalous splitting is determined in the QD frame from an experimental measurement, a calculation of some example curves from determined Stokes parameters using the general Hamiltonian in Equation 6.14 and calculating the energy using Equation 6.19 is shown in Figure 6.6. This example serves to highlight the difference between a normal QD measurement compared to a QD with a dominant circular component, as measured in the lab. The data for the lab measurement of a QD with $\gamma = 0.01$ shows the expected anti-correlation, but with some elliptical polarisation state (left panel). When looking in the QD frame, the expected linear polarisation state is recovered, with the expected 4χ frequency. For a QD with $\gamma = 0.43$ corresponding to a circular fraction of ~ 50%, the lab frame displays some arbitrary polarisations for the X and the XX, with no real visible correlations (center panel). In the QD frame, however, the recovered state demonstrates more clearly the anomalous eigenstate behaviour, with the partial correlation and symmetry of the state. Lastly, a QD with a dominant circular fraction and $\gamma = 0.97$ (right panel) results in a state that is almost perfectly correlated in energy, as expected. Similarly to the case of the dominant linear splitting, the state shows some elliptical polarisation in the lab frame. In the QD frame, however, the circular state is recovered with the expected 2χ frequency.

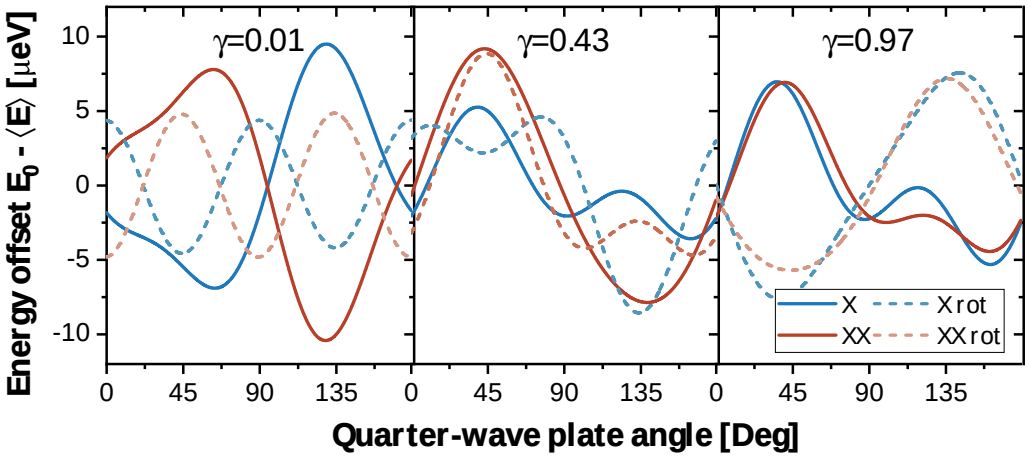

Figure 6.12: Simulated polarimeter curves rotated to the QD frame based on measured parameters. (**Left**) Measurement in the lab frame (solid lines) and QD frame (dotted lines), for a QD with an infidelity of $\gamma = 0.01$, corresponding a QD with linear eigenstates. (**Center**) Parameters for a QD with $\gamma = 0.43$, corresponding to an approximately equal fraction of linear and circular components. (**Right**) Parameters for a QD with $\gamma = 0.97$, corresponding a QD with highly circular eigenstates. The lab frame rotation is discussed in the main text.

6.4.3 Power Dependence Under Optical Excitation

As a final investigation into the anomalous behaviour of these QDs, a power dependence of the splitting was measured under optical excitation with 785-nm light at $T = 8$ K. The data was analysed as previously discussed and the rotation was applied in order to extract the parameters in the QD frame. Figure 6.13a shows the result of this for the X transition. For excitation at the X saturation power P_{Sat}, the QD displays a dominant linear splitting. Increasing the power further to approximately

$2P_{\text{Sat}}$ results not only in an increase of the total splitting, but also an introduction of a significant circular component which modifies the eigenstates of the QD. Similar behaviour is observed in the splitting of the X^-, shown in Figure 6.13b, where initially there is close to no splitting, within the error of the measurement. With an excitation power of $2P_{\text{Sat}}$, a large splitting is measured with an almost entirely circular component. Increasing the power further results in a relaxation and a return of the splitting close to the original values. The total splitting of the X^- increases by approximately twice that of X; however, the circular components increase by similar values. Figure 6.13c shows the calculated infidelity, as discussed in the previous section, after rotation into the QD frame. The infidelity, as expected, starts close to 0, before rising to 0.41 at $2P_{\text{Sat}}$, coincident with the introduction of the circular component in the splitting.

The situation is investigated further by considering whether or not there is any strong influence of the FSS on the coherence time. As shown in Section 3.4, the FSS can be conveniently extracted from the beating period in a MI coherence time measurement. Figure 6.13d shows the measured total splitting obtained from the fits of the temporal coherence profile of the X and X^-, on the same dot as above. Despite the apparent offset in the extracted splitting compared to the spectral measurements, the same trend is seen and the difference in total splitting of a factor ~ 2 between high and low excitation powers is also consistent. For the extracted coherence times, shown in Figure 6.13e, there appears to be no strong effect. A small drop in both the coherence time of the X and the X^- is seen around the turn on of the anomalous splitting effect, followed by a short stabilisation before the expected reduction for increasing excitations powers. However, given the size of the effect and the overall trend following the expected reduction for increasing power, it is difficult to conclusively remark on any facet apart from that the QD remains largely coherent (above 100ps) for significantly high excitation powers. It is also noted that the fitted temporal profiles all remained Lorentzian in shape, suggesting that the inhomogeneous broadening was not the dominant source of dephasing here.

Lastly, the extracted states from the spectral FSS measurements for the X and the XX are displayed Figure 6.13f in the frame of the QD, using the same rotation as determined in the previous section. As can be seen, the states show the same pattern as the ensemble measurements shown in Figure 6.10 for an increasing component of circular splitting, this time as a result of the increasing excitation power.

The features seen here for this QD under increasing excitation power agree well with the ensemble measurements discussed in the previous section. Interestingly, the QD studied here for the power dependence already showed a large component of circular splitting from the statistics study, conducted at a temperature of $T = 44$ K under EL. This further suggests that the anomalous splitting is a result of a persistent local effect, possibly a coupling to a nearby impurity or defect site, such that a change in the electric field/population of nearby trapping sites results in a change in the coupling to the QD, and hence the modification of the QD eigenstates.

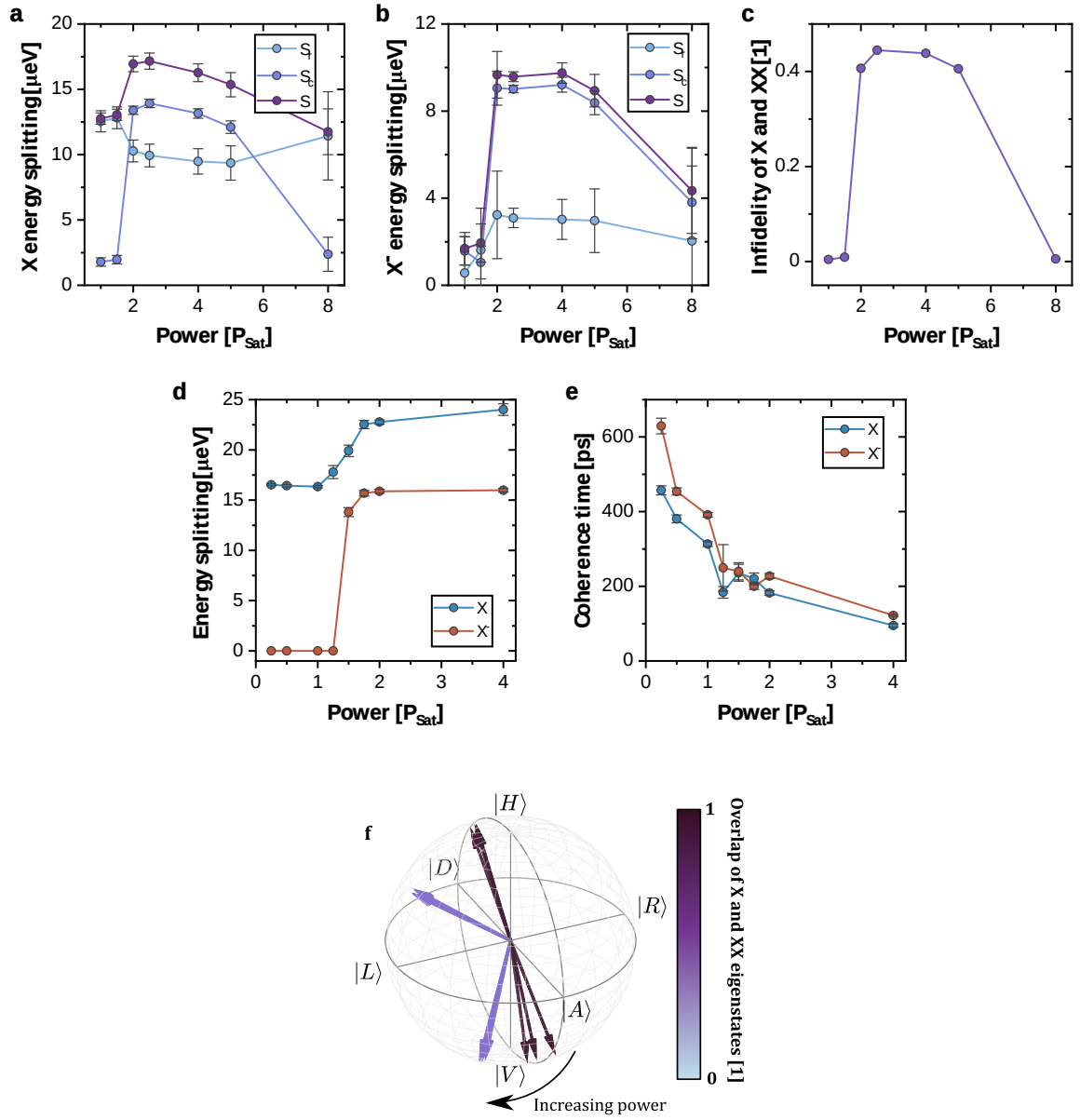

Figure 6.13: Power dependence of the anomalous fine structure effect under optical excitation. **a** Total splitting S, as well as the circular S_c and linear S_r components, extracted from the FSS measurements for the X as a function of excitation power. **b** Same as **a** but for the corresponding X^-. **c** Infidelity of the X and XX states. **d** Total splitting extracted from fits of the temporal profile. **e** Coherence times of the X and X^- extracted from fits to the temporal profiles. **f** Resulting X and XX states in the QD frame for increasing excitation power. A similar behaviour to the ensemble measurements is seen for powers with a large component of circular splitting. The colour of the states represent the overlap of the X and XX, where the overlap has been calculated using the eigensates, and so co-polarised photons have an overlap of 1.

6.5 GHz-Clocked Generation of Entangled Photon Pairs

Given that the previous results demonstrated that, in general, the QDs in this sample tend to have non-ideal eigenstates for performing entanglement, it was decided to explore an alternative form of measurement for the entanglement fidelity for the measurement at 1GHz. The most direct candidate, which is basis independent, is the full measurement of the two-photon density matrix. By measuring the full density matrix, not only can the fidelity be determined, but, additionally, it provides an independent means of determining the QD eigenstates, as a rotation of the density matrix to the eigenbasis can be performed. From this, the single-photon density matrices ρ_{XX} and ρ_X can be determined under certain assumptions on the eigenvectors, as will be discussed in the duration of this chapter.

It was decided to use this method primarily due to an observed change in the behaviour of the eigenstates as a function of time throughout this project, where the phase between the X and XX was seen to change. The result of this was that determination of the QD detection basis was nearly impossible using the methods described in Section 6.3.2. Therefore, a more direct measurement was required in order to compute the correct basis for the QD, as to allow for subsequent calibration of the states for teleportation in Chapter 7, under pulsed excitation. The change in behaviour observed when moving from CW excitation to pulsed excitation could be as a result of the peak power per pulse being much higher than the average power under CW excitation.

6.5.1 Determination of the QD Basis Using the Density Matrix

In order to determine the single photon states $|XX\rangle$ and $|X\rangle$ from the two-photon density matrix $\hat{\rho}$, an assumption is made about the form of the measured density matrix $\hat{\rho}'$ such that

$$\hat{\rho}' \propto k_e\hat{\rho}_e + k_c\hat{\rho}_c + k_m\hat{\rho}_m, \tag{6.22}$$

where $\hat{\rho}_e$, $\hat{\rho}_c$ and $\hat{\rho}_m$ are the density matrices for the entangled state, a classically correlated mixture and a completely uncorrelated mixture with k_e, k_c and k_m being the respective fractions of each component such that $k_e + k_c + k_m = 1$. The form of the entangled state is assumed to be the Bell state $|\Phi^+\rangle$ corresponding to emission from the QD at $\tau = 0$. The classical contribution here is assumed to be

$$\hat{\rho}_c = \frac{1}{2}\left(|HH\rangle\langle HH| + |VV\rangle\langle VV|\right), \tag{6.23}$$

and the mixed component is $I_4/4$, corresponding to a complete mixture. Such an assumption is justified, due to the fact that finite temporal resolution acts to wash out correlations in the superposition basis, adding instead a classically correlated component of $|HH\rangle$ and $|VV\rangle$ photons, and the presence of uncorrelated background photons add to a completely mixed fraction.

Since any density matrix can be written as a sum over pure states $|\psi_i\rangle$

$$\hat{\rho} = \sum_i p_i |\psi_i\rangle \langle\psi_i| , \tag{6.24}$$

where p_i is the probability to measure state $|\psi_i\rangle$, the measured density matrix can then be expressed as a sum over Bell states as

$$\begin{aligned} \hat{\rho}' = &(k_e + k_c/2 + k_m/4) |\Phi^+\rangle \langle\Phi^+| + (k_c/2 + k_m/4) |\Phi^-\rangle \langle\Phi^-| \\ &+ (k_m/4) |\Psi^+\rangle \langle\Psi^+| + (k_m/4) |\Psi^-\rangle \langle\Psi^-| . \end{aligned} \tag{6.25}$$

From inspection, it is obvious that a measured state with a small contribution of classical correlations will result in the leading eigenvalues $\lambda_{\Phi^+} > \lambda_{\Phi^-}$ of the eigenvectors $|\Phi^+\rangle$ and $|\Phi^-\rangle$ after diagonalisation of the measured density matrix $\hat{\rho}'$. The leading eigenvectors can therefore be used to define the two-photon density matrices $\hat{\rho}_{HH}$ and $\hat{\rho}_{VV}$, from which it is then simple to trace out either photon in order to determine the single photon states $\hat{\rho}_{XX,H}$, $\hat{\rho}_{X,H}$ and $\hat{\rho}_{XX,V}$, $\hat{\rho}_{X,V}$.

This process is highlighted in Figure 6.14a, where a simulation of a density matrix with $k_e = 0.85$, $k_c = 0.1$ and $k_m = 0.05$ is measured in a rotated frame with respect to the QD Bell state. This matrix bears a close resemblance to the expected Bell state; however, there are non-zero elements in the imaginary part of the matrix as a result of the rotated detection introducing a phase. The eigenvalues from diagonalising the matrix are $\lambda_1 = 0.9125 > \lambda_2 = 0.0625 > \lambda_3 = 0.0125 = \lambda_4 = 0.0125$, as expected. The above procedure is then used in order to define a change of basis matrix to express the rotated density matrix in the QD basis. Upon application of the change of basis matrix, the density matrix in the frame of the QD is restored, as shown in Figure 6.14b, and more closely resembles the $|\Phi^+\rangle$ state. The state determined is then shown in Figure 6.14c, in the frame of the measurement. With the states determined in this way, it is then simple to calculate the required wave plate angles in order to move from the measured basis to the QD basis. This is the crucial step in preparation for the pulsed teleportation experiment discussed in Chapter 7, where the input laser qubit is calibrated in the frame of the QD basis.

In order to proceed, a detection basis in the lab frame was used to perform the measurement of the required correlations for determining each element of the density matrix. The detection basis was calibrated using the same methods described previously. The resulting correlations were then analysed to compute each of the necessary correlation coefficients $E_{\alpha\beta}$. The density matrix was determined using the method described in [58, 224], based on the measurement of the correlation coefficient in nine bases E_{rr}, E_{dd}, E_{cc}, E_{rd}, E_{rc}, E_{dc}, E_{dr}, E_{cr} and E_{cd}, under the assumption of no polarising effects.

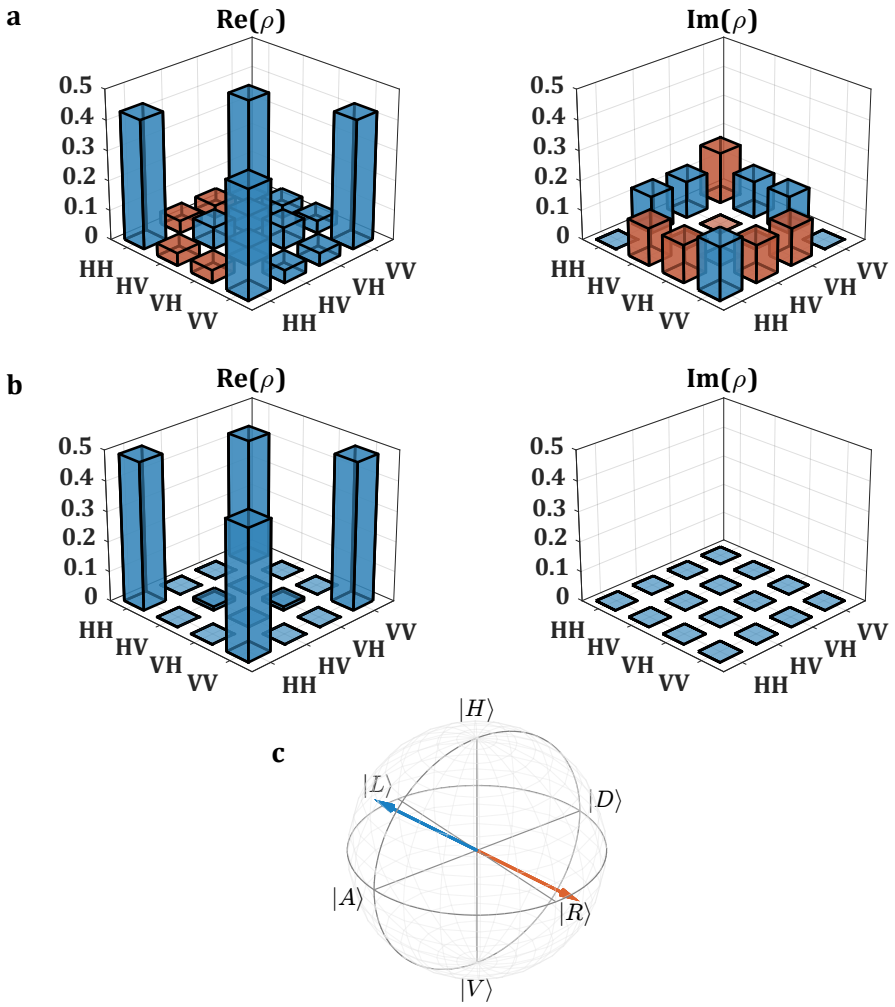

Figure 6.14: Simulated density matrix measured in a rotated frame. a Real (left) and imaginary (right) parts of the simulated two-photon density matrix, measured in an arbitrary reference frame. Red bars denote negative values. **b** Real (left) and imaginary (right) parts of the simulated two-photon density matrix after making a change of basis into the QD frame, using calculated eigenvectors of the rotated reference frame measurement. In this basis, the strong resemblance to the Bell $|\Phi^+\rangle$ state is recovered. **c** Recovered states of the QD with respect to the measurement basis.

Figure 6.15a shows the real (left) and imaginary (right) parts of the resulting density matrix when measured in this lab reference basis. There is a strong resemblance to the expected Bell state. However, as in the simulation, there are non-zero imaginary components resulting from the rotated detection basis. In this form, it is already suitable to determine the fidelity to a maximally entangled state by simply calculating the leading eigenvalue. In this case, the eigenvalues are found to be $\lambda_1 = 0.873 > \lambda_2 = 0.138 > \lambda_3 = 0.006 > \lambda_4 = -0.018$, and thus confirm the presence of an entangled two-photon state. The negative eigenvalue here shows that due to the measurement error, the resulting density matrix is non-physical, since all eigenvalues of a density matrix represent probabilities and the density matrix itself should be Hermitian and positive semi-definite. As the component is small

here, the treatment shall proceed in this first case by ignoring this, and will be analysed later through fitting using a maximum-likelihood estimation [225].

The above procedure is carried out and the result after rotation into the QD frame is shown in Figure 6.16b, where the resemblance to the expected Bell state is even more apparent. In this basis, the fidelity to the $|\Phi^+\rangle$ Bell state is exactly the leading eigenvalue λ_1, as expected. The resulting states with respect to the measurement basis are shown in Figure 6.15c, where, surprisingly, there is no significant difference between the XX and the X.

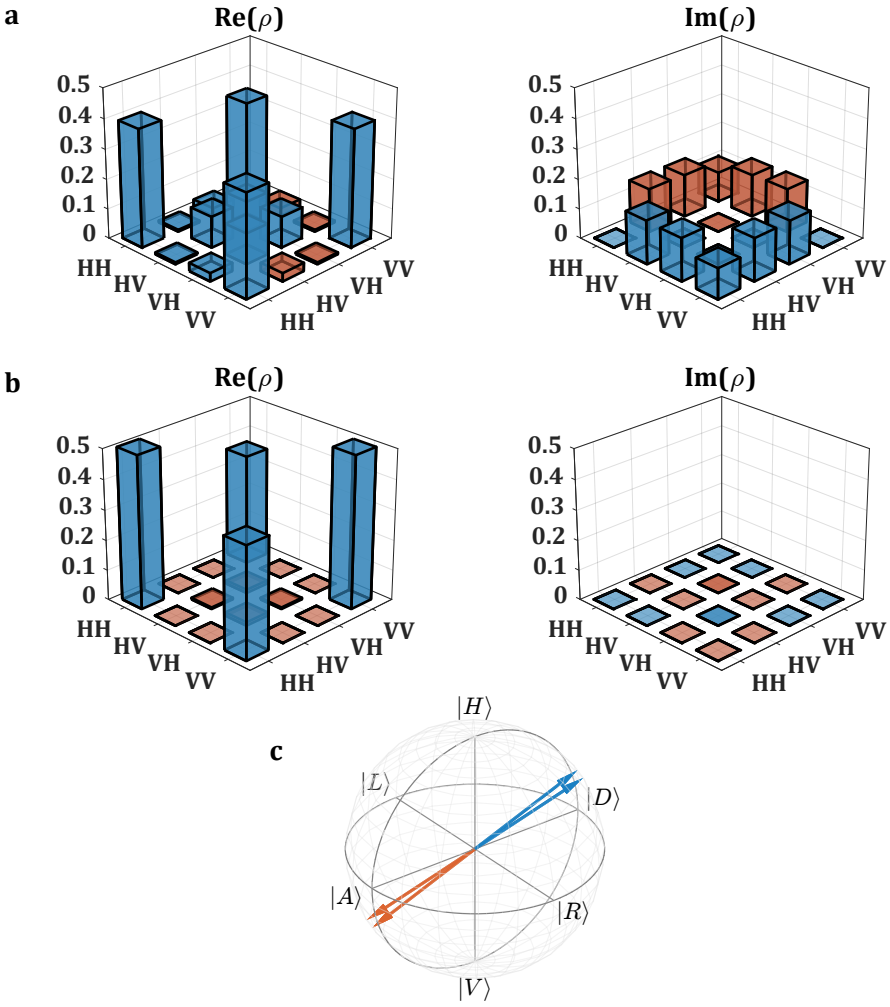

Figure 6.15: QD density matrix measured in a rotated frame. **a** Real (left) and imaginary (right) parts of the QD two-photon density matrix, measured in an arbitrary reference frame. Red bars denote negative values. **b** Real (left) and imaginary (right) parts of the QD two-photon density matrix after making a change of basis into the QD frame, using calculated eigenvectors of the rotated reference frame measurement. In this basis, the strong resemblance to the Bell $|\Phi^+\rangle$ state is recovered. **c** Recovered states of the QD with respect to the measurement basis.

6.5.2 Two-Photon Density Matrix for GHz-Clocked Entangled Photon Pairs

With the basis for measuring the QD determined from the previous measurement, a further measurement of the density matrix was made in order to test the accuracy of this method. By calculating the projections of the complementary bases from the previously determined states, familiar correlations in the QD bases were recovered. The resulting density matrix expressed in the QD basis can be seen in Figure 6.16a, where the strong resemblance to the $|\Phi^+\rangle$ Bell state is recovered immediately. In this case, the eigenvalues are found to be $\lambda_1 = 0.878 > \lambda_2 = 0.098 > \lambda_3 = 0.033 > \lambda_4 = -0.009$ and, thus, confirm the presence of an entangled two-photon state.

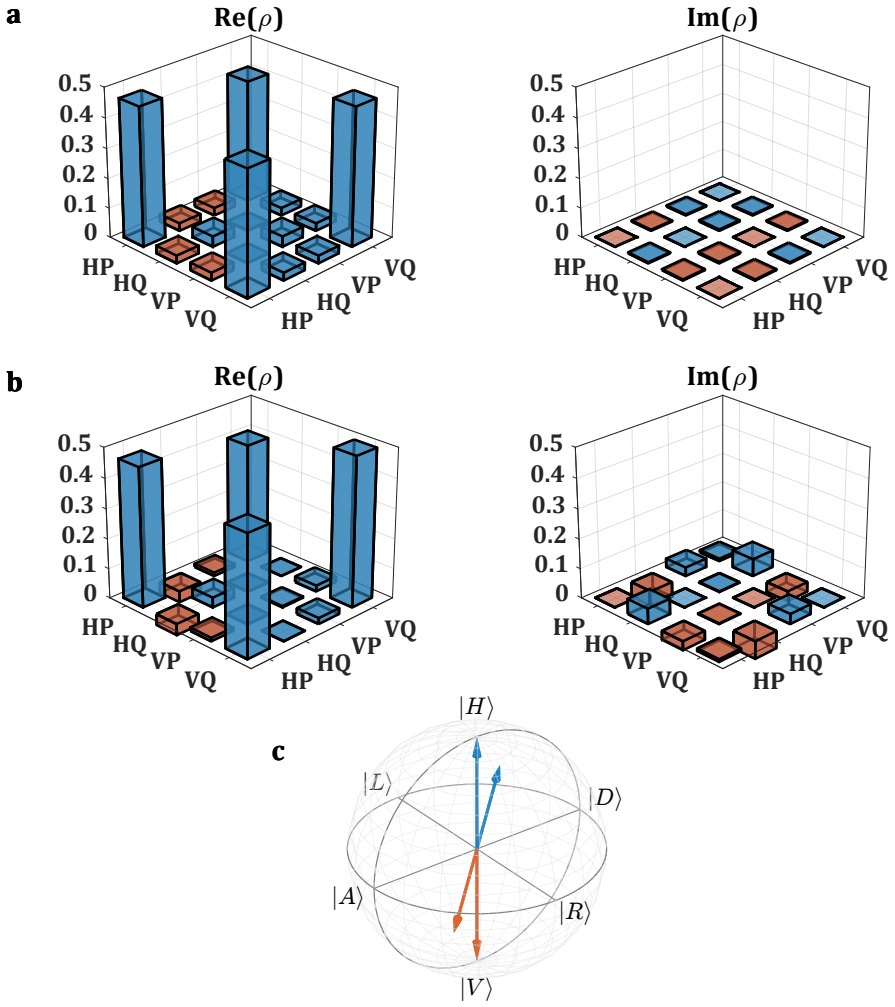

Figure 6.16: QD density matrix measured in QD basis. **a** The real (left) and imaginary (right) parts of the two-photon density matrix, reconstructed using a time window of 96 ps, under pulsed optical excitation clocked at 1.07 GHz, measured in the QD basis. Red bars denote negative values. **b** The real (left) and imaginary (right) parts of the fitted two-photon density matrix, determined by a maximum-likelihood estimation based on the measurement in **a**. **c** Recovered states of the QD with respect to the measurement basis.

Again, the presence of a small negative eigenvalue highlights the impact of the measurement on the density matrix. As mentioned before, using a maximum-likelihood estimation [225] based on errors propagated from the counting statistics, allows the experimental data to be fitted to the form of a physical density matrix. Figure 6.16b shows the result of this fitting procedure on the measured density matrix. The differences to the measured data in Figure 6.16a are very small, with only a small redistribution of the elements, the most noticeable being between the HP and VQ elements, which is suggestive of a small amount of polarisation imbalance in some of the optics of the experimental setup. This was expected due to the flaws in the assumption of no polarising terms when constructing the density matrix from the correlation coefficients [58]. After the fitting, the determined eigenvalues are $\lambda_1 = 0.893 > \lambda_2 = 0.093 > \lambda_3 = 0.014 > \lambda_4 = 0.000$, and are in satisfactory agreement with the values determined from the raw data.

Interestingly, the infidelity of the states is $\gamma = 0.049$ between the $|HV\rangle$ and $|PQ\rangle$ states, respectively, as shown by Figure 6.16c and corresponds to a fraction of circular splitting of 0.22. This seems to suggest that the previous measurement may have determined the projection of the linear state, such as that measured under CW excitation. This is probably as a result of the assumption on the form of the classically correlated state, as for a QD with basis states $\{P,Q\}$, the expected classical correlations would in fact be between polarisations $|PP\rangle$ and $|QQ\rangle$.

The states determined here and the corresponding wave-plate angles used for aligning to them, including the superposition basis projections, were saved for the pulsed teleportation experiment in Chapter 7 where they would be crucial for setting the basis of the Bell measurement and the input laser qubit polarisation.

Finally, after full measurement of the QD density matrix in the QD basis and fitting, the fidelity to the Bell state $|\Phi^+\rangle$, as well as the fidelity to a maximally entangled state, was extracted for multiple time windows in 96 ps bins. The result can be seen in the top panel of Figure 6.17, where again the familiar oscillation as a function of time for the Bell state is recovered. The fidelity to a maximally entangled state, or the leading eigenvalue, follows a similar time-dependence as the fidelity to the time-evolving state in Equation 6.12, again highlighting the fact that the QD emits entangled photon-pairs for all times. At $\tau = 0$, the fidelity to the Bell state $|\Phi^+\rangle$ is found to be 0.88 ± 0.01, where the error has been determined from a Monte-Carlo approach, based on the errors propagated from the counting statistics. Similar to before, for a gate width corresponding to one excitation period when clocked at 1.07 GHz, a counts-weighted fidelity average of 0.81 ± 0.004 to a maximally entangled state is determined, with a detected entangled-pair rate of 32 ± 0.2 pairs per second into this gate. This improvement of the average fidelity is due to the reduction of re-excitation under the pulsed optical excitation, and is also apparent from the increase in the decay time of the two-photon state, when comparing to the measurement under CW excitation. The entangled-pair rate is expected to increase significantly with further improvements to the photonic structure [189, 190].

In addition, the measurement of the density matrix allows the concurrence of the state to be determined, which is defined by [226]

$$C = \max\{0, \lambda_1 - \lambda_2 - \lambda_3 - \lambda_4\}, \tag{6.26}$$

where here λ_i are the eigenvalues in decreasing order of the Hermitian matrix $R = \sqrt{\sqrt{\rho}\tilde{\rho}\sqrt{\rho}}$ and $\tilde{\rho} = (\sigma_y \otimes \sigma_y)\rho^*(\sigma_y \otimes \sigma_y)$ is the spin-flipped complex conjugate density matrix. This metric, which scales from 0 (separable state) to 1 (maximally entangled state), is usually used to describe the amount of entanglement present between qubits in mixed states. Such a metric allows for evaluation of the degree of the entanglement present in the system and comparison between fundamentally different systems. The concurrence has been evaluated here for multiple times and the result can be seen in the bottom panel of Figure 6.17, where the maximum is determined to be $C = 0.80 \pm 0.01$. The concurrence drops to 0 approximately in line with the fidelity dropping to 0.5, indicating the state is no longer entangled. This serves to highlight the consistency of these metrics in determining the level of entanglement present in the emitted photon pairs.

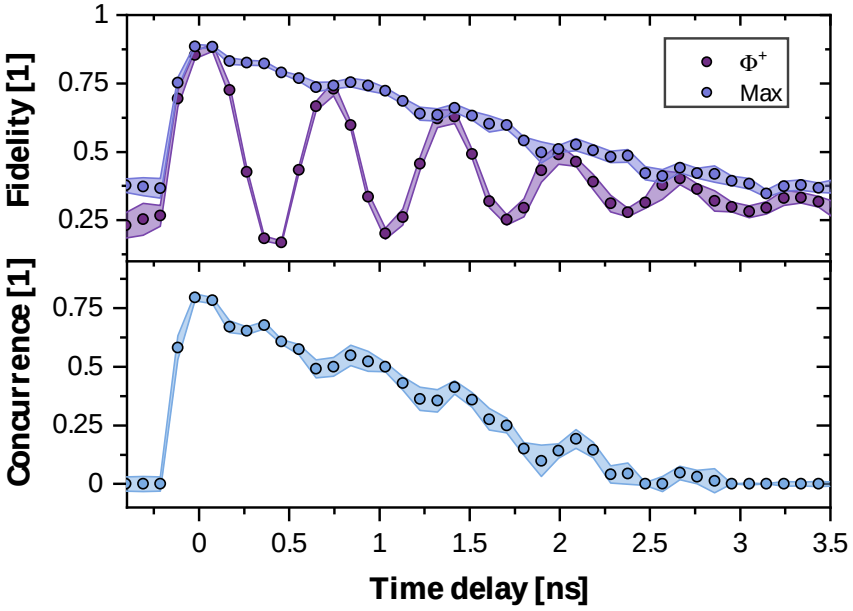

Figure 6.17: Time-dependent entanglement metrics for the QD density matrix. **(Top)** Entanglement fidelity of the fitted density matrix to the static Bell state $|\Phi^+\rangle$ and to a maximally entangled state, for reconstruction windows of 96 ps. **(Bottom)** Concurrence of the fitted density matrix evaluated for the same times. The fidelity and concurrence metrics agree with the decay of the entangled state, approaching classical values around the same time. Shaded areas denote error.

6.6 Summary

The work in this chapter considered the entangled photon-pair generation of QDs emitting near the telecommunications *C*-band, under both CW and pulsed optical excitation.

In the first section, a model for the entanglement dynamics based on a combination of the expected two-photon density matrix and the emission dynamics of the QD was considered, reproduced from [208, 206]. Subsequent measurement of the correlation coefficient in five complementary bases revealed a post-selected maximum entanglement fidelity of 0.90 ± 0.01 and a counts-weighted average fidelity of 0.72 ± 0.01 to the expected Bell state, constituting a record-high measurement for this type of solid-state quantum emitter. A violation of the Bell parameter was also measured in three orthogonal planes of the Poincaré sphere.

In the following secton, an unusual feature of the FSS found in a large number these QDs was investigated by considering an ensemble of 90 FSS measurements. The statistics gathered from this data strongly correlated with the proposed model, which detailed the modification of the FSS and the photon polarisation resulting from a magnetic-field type interaction, developed in [206]. The main features seen in the data and the model were in agreement; however, a full explanation and detail of the observed behaviour would be an interesting subject for further investigation. The optical excitation power dependence was found to be in agreement with the proposed model, suggesting further the attribution of the effect to be from a local origin.

Due to the anomalous behaviour of the FSS under pulsed optical excitation, a method was introduced to recover the QD eigenstates from the measurement of the two-photon density matrix. After determination of the QD basis using this method, the full QD density matrix was demonstrated through measurement in this basis, and was found to bear strong resemblance to the expected Bell state, with a maximum fidelity of 0.88 ± 0.01. Furthermore, the concurrence of the measured density matrix was found to be 0.80 ± 0.01, in agreement with the high entanglement fidelity.

Future work in this area would be to operate the system under resonant two-photon excitation, in order to increase the entanglement fidelity and single-photon purity of the emitted photons [72]. Such a scheme would also naturally enhance the coherence properties of the emitted photons, further increasing the utility for interference based applications such as teleportation [42, 227] or entanglement swapping [43]. Additionally, an overall enhancement of the efficiency of the system, through engineering of the photonic structure in order to reduce the radiative lifetime and improve the collection efficiency, would allow for a higher rate of detection events, critical for deployed fibre applications [133, 134]. Such improvements could be made through the use of recently developed circular Bragg gratings [189, 190], where development towards telecommunications O-band wavelengths has already been considered [228].

Chapter 7

Quantum Teleportation of Telecom *C*-Band Qubits

In this chapter, the previous work of this thesis will be combined in the final experiments demonstrating the teleportation of telecom *C*-band qubits. Firstly, an experiment on the teleportation of polarisation-encoded laser photons under CW excitation will be considered, before extension of this scheme to involve pulsed operation and the teleportation of initially time-bin encoded laser photons. In the final part of this chapter, a proof-of-principle demonstration of the time-bin input, time-bin output teleportation under 1GHz clocked speeds will be shown, constituting the final project goal.

7.1 Introduction

As discussed in Section 1.2.3, quantum teleportation is an important tool towards the realisation of long-distance quantum communication. In a quantum relay scheme, such as the focus of this work, teleportation can be used to improve the SNR of the channel and thus improve the scaling of the transmission as a function of the channel length [26, 229], as well as enhancing the security of the channel through the removal of an intermediate trusted node. These features are appealing in the context of quantum cryptography and QKD, allowing key exchanges over greater distances.

Since the first demonstration of quantum teleportation [51], there has been much work in the area; such as realising full BSM protocols [22], demonstrations over long distances in free space [230], and using fibre [231, 229]. However, the factor that these demonstrations have in common is that they utilise photon-pair sources using SPDC, which is inherently probabilistic and suffers from Poissonian photon statistics, making such schemes less desirable for practical implementations.

This has prompted significant work in this area utilising QD sources [52, 101, 42], where the superior optical quality and potential to operate on-demand [72] offers a promising alternative for real-life applications of teleportation [227] and entanglement swapping [43]. Again, these demonstrations have in common that the operating wavelength was ~ 900 nm, where losses in fibre are ~ 2 dB/km, an order of magnitude higher than in the telecom *C*-band (0.2 dB/km), making such sources less

desirable for fibre-based applications. Recent work of this lab has been successful in demonstrating quantum teleportation utilising QDs emitting in the telecom *O*-band [**?**].

In the following work, these previous developments will be extended further to include the operation of a quantum relay near the most technologically important wavelength window for long-distance communication, the telecom *C*-band. While the operating principles of this experiment are the same as those that have been demonstrated previously, no QD sources have thus far been available to conduct this experiment in the technologically important wavelength region. Thus, the combination of the previously demonstrated indistinguishability (Chapter 5) and high entanglement fidelity (Chapter 6) are crucial for such a demonstration.

7.2 Teleportation of Telecom *C*-Band Polarisation Qubits

The experiment described in this section considers the operation of the quantum light source under CW excitation and the teleportation of a polarisation encoded telecom *C*-band laser qubit. As such, the work follows directly from the TPI between a quantum light source and a weak coherent input state, discussed in Section 5.4, and the CW entanglement measurement, discussed in Section 6.3.3.

7.2.1 Experimental Setup

The experimental implementation of the teleportation protocol is illustrated in Figure 7.1, where the naming convention of a typical quantum communication link is adopted. The sender, Alice, prepares a polarisation encoded qubit of the form of Equation 5.17, which is then sent onto the relay station, Charlie. At Charlie, a polarisation entangled photon-pair is generated. The X photon from the entangled two-photon state is interfered with the laser photon on a 99:1 coupler, similar to the TPI interference measurement discussed in Section 5.4. Following the interfering beamsplitter, a $|\Psi^+\rangle = \frac{1}{\sqrt{2}}(|HV\rangle + |VH\rangle)$ BSM measurement is performed by resolving H and V polarisations in the same arm of the output using a PBS with the detection basis aligned to the QD eigenbasis, in order to herald the teleportation to Bob, where the XX photon is sent. At Bob, another PBS is used to a perform polarisation resolved detection in basis PQ, in order to determine the output state polarisation.

In the experiment, the QD from Section 5.4 was also used for the teleportation presented here. The QD was excited at P_{Sat} with a CW laser at 1310 nm using a pellicle beamsplitter. As with the entanglement measurement, a second pellicle oriented orthogonal to the first is used in the collection arm, in order to compensate for the polarisation effects of the first. The emitted light was collected and sent towards a free-space transmission grating, where the X and XX photons were spectrally filtered and coupled back into fibre. At Alice, a commercial tunable C-band CW laser was used with a DVA and EPC to generate weak coherent input photons. The laser photons from Alice and the X photons from the QD, which were set to be equal intensity as in Section 5.4, were sent towards a fibre 99:1 beamsplitter, where on the 99% output port, an EPC (not shown) was used before the PBS. The EPC was used to calibrate the BSM detection basis of the SNSPDs at Charlie, in addition to setting the calibration basis for the EPC at Alice. The XX photons were sent towards a similar polarisation detection setup with a PBS and SNSPDs. As in Section 5.4, an optical switch following the interfering beamsplitter was used to periodically direct the laser and QD photons towards a spectrometer, where a minimisation routine was used to spectrally overlap the laser with the X photons with an accuracy of $\sim 2\mu$eV. In addition to the spectral overlap, the intensity was also periodically adjusted in order to maintain an average ratio of $\eta/\alpha^2 = 1$, to within 1%.

For the calibration, the same method described in Section 6.3.2 based on the linear projection of the QD eigenbasis was used, as no effects of an internal magnetic field was seen from the QD during the time of this CW measurement. This set the basis of the detectors at Charlie, thus allowing the laser photon input states to be calibrated to the QD basis. For the measurement, the EPC at Charlie

was then fixed to the QD HV basis, while the Alice and Bob EPCs were changed for each polarisation input state. The detectors used in this experiment had timing resolutions of ~ 90 ps for $D_V - D_H$ and ~ 100 ps for the $D_V - D_{P(Q)}$.

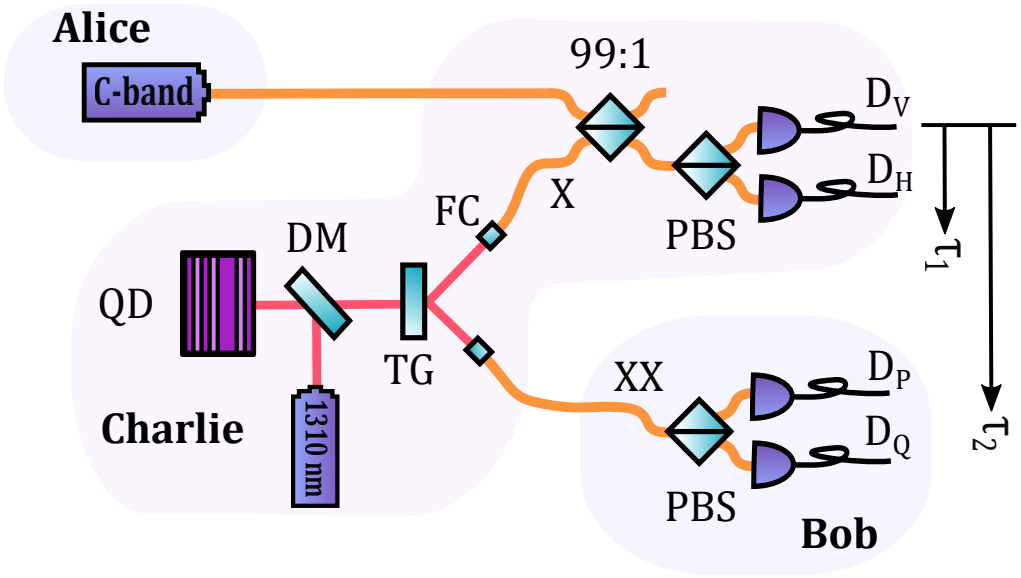

Figure 7.1: Quantum teleportation experimental setup. An input polarisation encoded laser qubit from Alice is interfered with an X photon at a 99:1 beamsplitter. At Charlie, a BSM is performed using a PBS and SNSPDs D_H and D_V. At Bob, a polarisation resolved correlation is used to analyse the output state in different polarisation bases, with SNSPDs D_P and D_Q

7.2.2 Characterising Teleportation

To characterise the teleportation, coincidences of photons were measured at Charlie and Bob in order to generate third-order correlation maps, $g^{(3)}_{HVP(Q)}(\tau_1,\tau_2)$, as a function of the time delays, $\tau_1 = \tau_{D_H} - \tau_{D_V}$ and $\tau_2 = \tau_{D_{P(Q)}} - \tau_{D_V}$, measured relative to the detection of a V polarised photon at time τ_{D_V}. A successful BSM at Charlie ($\tau_1 = 0$) heralds the teleportation which can then be correlated with the photon detection at Bob. By considering the form of a general input state from Equation 5.17 and the entangled two-photon state $|\psi\rangle$, the output state at Bob will then be mapped as

$$|\Psi_L\rangle = \cos\left(\frac{\theta}{2}\right)|H_L\rangle + e^{i\varphi}\sin\left(\frac{\theta}{2}\right)|V_L\rangle \rightarrow \tag{7.1}$$

$$|\Psi_{Bob}\rangle = \cos\left(\frac{\theta}{2}\right)|V_{XX}\rangle + e^{i(\varphi - S\tau_2/\hbar)}\sin\left(\frac{\theta}{2}\right)|H_{XX}\rangle\,, \tag{7.2}$$

constituting the σ_x transform as expected for this type of teleportation protocol [199]. Therefore, successful teleportation will follow this unitary transform, such that: $H \rightarrow V$, $V \rightarrow H$, $D \rightarrow D$, $A \rightarrow A$, $R \rightarrow L$, $L \rightarrow R$, up to the FSS phase in Equation 7.2 for the six input states distributed symmetrically on the Poincaré sphere considered here. The teleportation fidelity is then calculated as

$$f_P^T = \frac{g^{(3)}_{HVP}(\tau_1,\tau_2)}{g^{(3)}_{HVP}(\tau_1,\tau_2) + g^{(3)}_{HVQ}(\tau_1,\tau_2)} \tag{7.3}$$

where $g^{(3)}_{P(Q)}(\tau_1,\tau_2)$ is the third-order correlation function for Bob's photon detected in polarisation P(Q), and serves as a measure of the expected (unexpected) output polarisation compared to the input.

In the experiment, photon coincidences were measured using HydraHarp time correlation electronics running in TTTR mode, with detection of a V polarised photon forming the sync clock and beginning the time-tagging of subsequent detection events of H and $P(Q)$ polarised photons. The raw data was acquired with 8 ps resolution by cycling through each input state for durations of one hour, for a total acquisition time of approximately 170 hours. In post-processing, 2-D histograms were constructed according to the times of triple coincidence events (τ_1,τ_2), and the data was normalised to the values at times $|\tau_1,\tau_2| \rightarrow \infty$, in order to generate the third-order correlation maps $g^{(3)}_{HVP(Q)}(\tau_1,\tau_2)$.

7.2.3 Teleporting Logical States

The first case of input states considered were those matching the QD eigenbasis, and the basis in which the BSM was calibrated to. These states corresponding to $|H\rangle$ and $|V\rangle$ are referred to as the logical basis, and require no quantum interference, or even entanglement, in order to demonstrate teleportation. This is apparent from the input state being in the basis of the BSM. Therefore, when a H/V laser photon is present, a triple coincidence can only happen for V/H polarised QD photons, as a result of the polarisation-resolved detection. Thus, only statistical mixture $\rho_c = \frac{1}{2}(|H_{XX}H_X\rangle + |V_{XX}V_X\rangle)$ resulting in classical correlations, is required for this 'teleportation'.

The measured correlations for laser inputs $|\Psi_L\rangle = |H\rangle$ and $|\Psi_L\rangle = |V\rangle$ can be seen in Figures 7.2 and 7.3, respectively. For the case of a H-polarised input photon, the expected successful correlation is achieved when measuring a V-polarised XX photon $g^{(3)}_{VHV}(\tau_1,\tau_2)$, shown in Figure 7.2a. The temporal ordering is reversed along τ_2 in comparison to similar work [84, 101], due to the fact that the X is used for the trigger of detection events at the BSM, not the XX as in previous work. Thus, behaviour of interest is seen for $\tau_2 < 0$, which corresponds to detection events prior to the detection of the X. The main feature is a bright vertical stripe at times $\tau_2 < 0$ corresponding to the increased probability of detecting laser and XX photons, following the detection of an X photon at detector D_V. This happens uniformly for all τ_1 due to the laser photons always being present at the detector at D_H. In addition, the X-laser correlation seen along τ_1 reveals the familiar flat behaviour with the dip at $\tau_1 = 0$, corresponding to the single-photon nature of the X, and is seen as a dark horizontal strip. Along the $\tau_1 = \tau_2$ line corresponding to simultaneous detections of D_H and $D_{P(Q)}$, a faint dark stripe is seen for $g^{(3)}_{VHV}(\tau_1,\tau_2)$, which is a result of a misalignment in the BSM detection basis, away from the QD eigenbasis. Similarly to the misalignment in the HV detection basis introducing small oscillations in the HH and HV entanglement correlations, a small oscillation can be seen here for detections corresponding to a H-polarised X on D_H, correlating with a V-polarised XX on D_P. When measuring a V-polarised photon at Bob, the unexpected correlation $g^{(3)}_{VHH}(\tau_1,\tau_2)$ shown in Figure 7.2b has related features. The dark horizontal line along $\tau_1 = 0$ again corresponds to the single-photon nature of the X. Similar to before, the dark vertical stripe corresponds to detections of the XX-X cascade for all laser detection times. This time, however, there is a weak oscillation for $\tau_2 < 0$, due to the small misalignment of the BSM. More importantly, there is an absence of triple coincidences for $\tau_1 = 0$ and $\tau < 0$ as expected, indicating that no teleportation has taken place. The fact that no interference is required for this input state is seen also by the fact that the bright stripe in Figure 7.2a extends through the origin for time delays beyond the X coherence time. This is confirmed by calculating the fidelity $f^T_H(\tau_1,\tau_2)$, where there is a near-unity stripe along the vertical, as shown in Figure 7.2c, for all laser detection times. The maximum fidelity $f^T_H = 0.91 \pm 0.09$ is limited due to the non-unity degree of correlation in the HV basis, as shown by the entanglement results in Section 6.3.3. A further examination of the fidelity along the $\tau_1 = 0$ axis where general teleportation can succeed is shown in Figure 7.2c, which decays towards the uncorrelated threshold of 0.5, corresponding to the decay of the two-photon state.

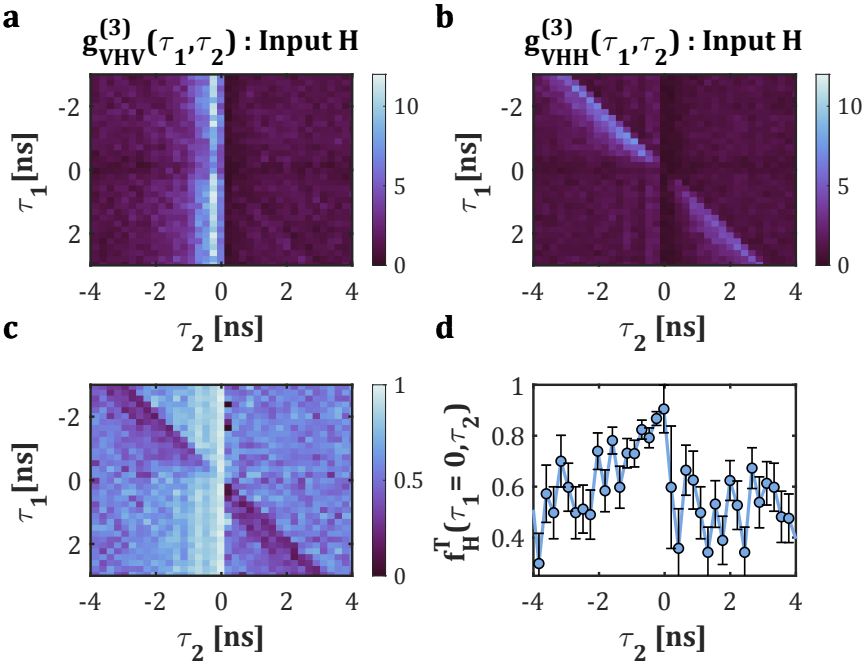

Figure 7.2: Teleportation of H polarised laser photons onto V polarised XX photons. **a** Third-order correlation $g^{(3)}_{HVV}(\tau_1,\tau_2)$. **b** Third-order correlation $g^{(3)}_{HVH}(\tau_1,\tau_2)$. **c** Corresponding teleportation fidelity $f^T_H(\tau_1,\tau_2)$. **d** Slice at $\tau_1 = 0$ along τ_2 of f^T_H. Data shown for a post-selection window size of $\Delta\tau_1$ x $\Delta\tau_2$ = 184 x 224 ps.

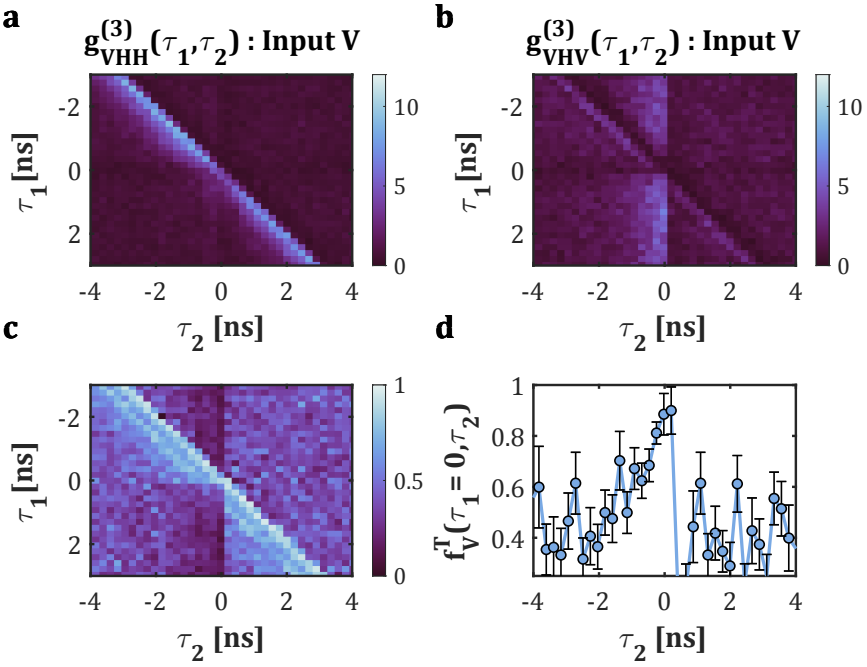

Figure 7.3: Teleportation of V polarised laser photons onto H polarised XX photons. **a** Third-order correlation $g^{(3)}_{HVH}(\tau_1,\tau_2)$. **b** Third-order correlation $g^{(3)}_{HVV}(\tau_1,\tau_2)$. **c** Corresponding teleportation fidelity $f^T_V(\tau_1,\tau_2)$. **d** Slice at $\tau_1 = 0$ along τ_2 of f^T_V. Data shown for a post-selection window size of $\Delta\tau_1$ x $\Delta\tau_2$ = 184 x 224 ps.

Re-excitation effects lead to additional features present in the correlations. Since the detection is triggered from the measurement of an X, the immediate re-excitation of the XX has no effect; therefore, only re-excitation of the X leads to additional features. The first case to consider is the emission of a correlated V-polarised X-XX pair followed by an uncorrelated H-polarised X. This leads to an increase in the triple coincidences in $g^{(3)}_{VHV}(\tau_1,\tau_2)$ for detections $\tau_1 > 0$ and $\tau_2 < 0$, such as can be seen to a small degree in Figure 7.2a. The other case to consider is the detection of an uncorrelated V-polarised X preceded by a correlated H-polarised pair as a result of the X being re-excited quickly following relaxation to the ground state, leading to an increase in triple coincidences in $g^{(3)}_{VHH}(\tau_1,\tau_2)$ for $\tau_1 < 0$, $\tau_2 < 0$ and $\tau_2 < \tau_1$, as seen in Figure 7.2b. A weaker feature of increased triple coincidences in $g^{(3)}_{VHH}(\tau_1,\tau_2)$ for $\tau_1 > 0$, $\tau_2 > 0$ and $\tau_2 < \tau_1$ corresponds to this case, but for a correlated pair following the uncorrelated detection at D_V, this time relating to the full excitation to the XX from the ground state after detection of an X.

For the V-polarised input photon, the expected successful correlation is when measuring a H-polarised XX photon $g^{(3)}_{VHH}(\tau_1,\tau_2)$, shown in Figure 7.3a, where the features are similar to the above. The distinct difference here, however, is that now the laser photons land on D_V, leading to the detection of correlated QD H-polarised photons along $\tau_1 = \tau_2$. The darker vertical stripe again corresponds to the small misalignment of the BSM detection basis. Similarly for the unexpected correlation $g^{(3)}_{VHV}(\tau_1,\tau_2)$, there is reduced triple coincidences, corresponding to the detections from re-excitation events as discussed above. Calculating the fidelity revels the near-unity diagonal stripe with a maximum $f_V^T = 0.89 \pm 0.08$, with the same decay seen along the $\tau_1 = 0$ axis.

7.2.4 Teleporting Superposition States

The next case of input states considered are the superposition states $|D\rangle/|A\rangle$ and $|R\rangle/|L\rangle$, corresponding to four states equally distributed on the equatorial plane of the Poincaré sphere. This section present the results for $|D\rangle$ and $|L\rangle$. This case is much more interesting, as now the output state critically relies on both the quantum interference of the QD and laser photons, and the quantum entanglement of the two-photon state. Figure 7.4a (b) shows the resulting three-photon coincidence maps when measuring the expected (unexpected) output polarisations at Bob. For the input state $|D\rangle$, the act of the σ_x transform is to map $|D\rangle \rightarrow |D\rangle$ and so, as anticipated, $g^{(3)}_{VHD}(\tau_1,\tau_2)$ shows a peak in triple coincidences for $\tau_1 = \tau_2 = 0$. This time, however, the small peak displays reduced triple coincidences for $|\tau_1| \gtrsim T_2$ along the τ_1 axis, as a result of the reduced probability for TPI to take place due to the coherence time of the X. In addition to the limit along τ_1 according to the X coherence time ($T_2 \sim 260$ ps), the nature of the time-evolving two-photon state has an effect along the τ_2 axis, where the same oscillatory behaviour as in the entanglement measurement is seen. Similar features to each case of the teleportation of logical states is also seen, due to the fact that the BSM now acts as a 50:50 splitter for the input state with both X and laser photons able to trigger triple detection events on D_V.

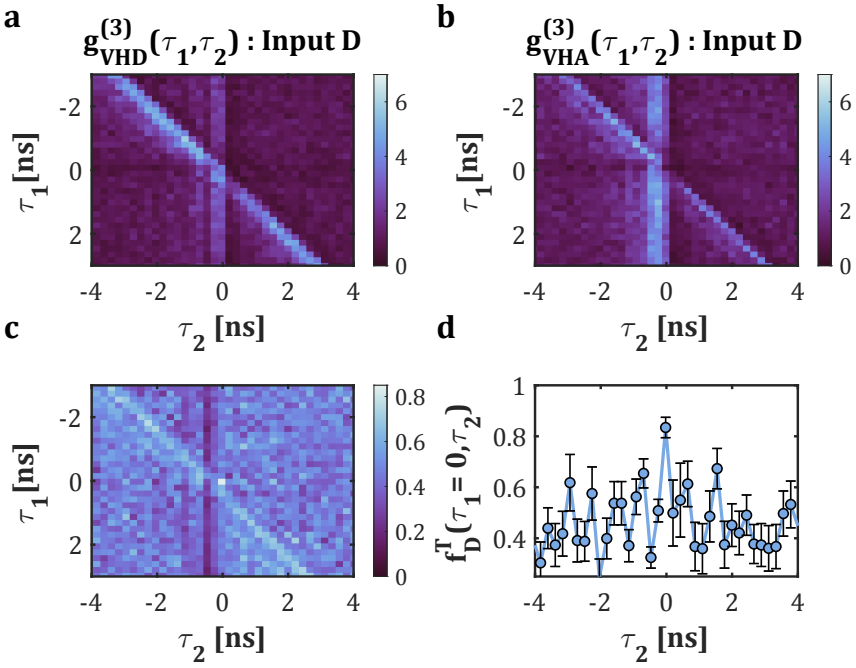

Figure 7.4: Teleportation of D polarised laser photons onto D polarised XX photons. **a** Third-order correlation $g^{(3)}_{HVD}(\tau_1,\tau_2)$. **b** Third-order correlation $g^{(3)}_{HVA}(\tau_1,\tau_2)$. **c** Corresponding teleportation fidelity $f^T_D(\tau_1,\tau_2)$. **d** Slice at $\tau_1 = 0$ along τ_2 of f^T_D. Data shown for a post-selection window size of $\Delta\tau_1$ x $\Delta\tau_2$ = 184 x 224 ps.

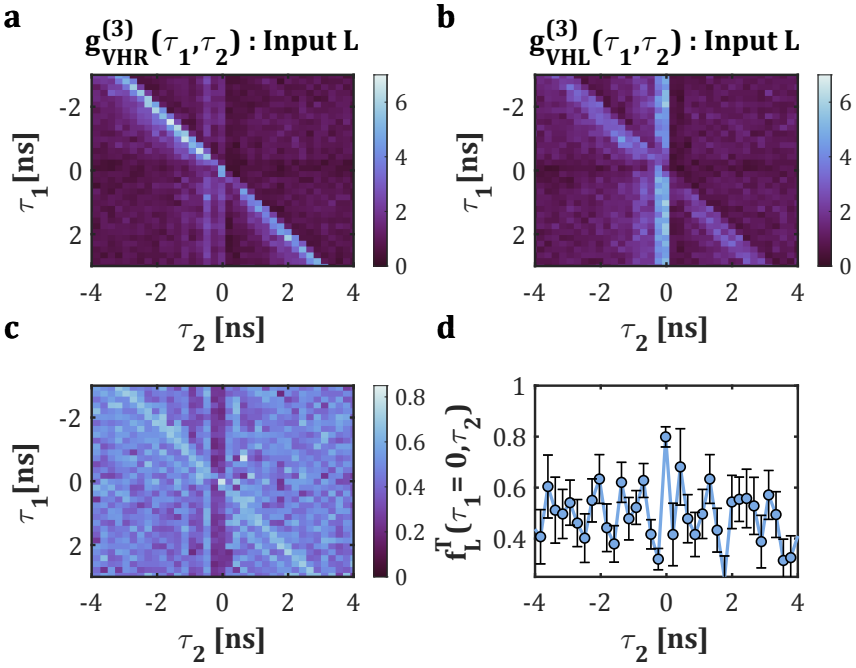

Figure 7.5: Teleportation of L polarised laser photons onto R polarised XX photons. **a** Third-order correlation $g^{(3)}_{HVL}(\tau_1,\tau_2)$. **b** Third-order correlation $g^{(3)}_{HVR}(\tau_1,\tau_2)$. **c** Corresponding teleportation fidelity $f^T_L(\tau_1,\tau_2)$. **d** Slice at $\tau_1 = 0$ along τ_2 of f^T_L. Data shown for a post-selection window size of $\Delta\tau_1$ x $\Delta\tau_2$ = 184 x 224 ps.

The similar oscillations can be seen along the τ_2 from the misalignment discussed above. For the unexpected output $g^{(3)}_{VHA}(\tau_1,\tau_2)$ when measuring A-polarised photons at Bob, the correlation shows a similar behaviour for all times away from $\tau_1 = \tau_2 = 0$, where, in this instance, there is a distinct absence of triple coincidences. This indicates that teleportation has taken place, and is shown more clearly by calculating the fidelity $f^T_D(\tau_1,\tau_2)$, which can be seen in Figure 7.4c. The single high-fidelity peak reaching a maximum $f^T_D = 0.83 \pm 0.04$ is a clear signature of the teleportation. A cut along the $\tau_1 = 0$ shows the situation more clearly for the evolving two-photon state, albeit with some additional noise hiding the oscillations due to the FSS. The coherence time and the FSS directly lead to a reduction of the fidelity for the superposition input states. The additional features seen in $f^T_D(\tau_1,\tau_2)$ are a consequence of the misalignment in the BSM as discussed. Ideally, it would be 0.5 for all times away from $\tau_1 = \tau_2 = 0$, revealing just a single peak. Teleportation is similar in the circular basis, as seen in Figure 7.5 for the case of an $|L\rangle$ input state, where this time the expected (unexpected) output state is found when measuring R (L)-polarised photons at Bob. At the origin, a maximum $f^T_L = 0.77 \pm 0.04$ is found, similar within error to the diagonal basis.

7.2.5 Results

While in principle only three linearly independent input states are required in order to verify non-classical teleportation, due to the fact that any state can be then made from a linear combination [232], teleportation of the other two states on the Poincaré sphere ($f^T_A = 0.88 \pm 0.04$ and $f^T_R = 0.80 \pm 0.04$) allows for a calculation of the six-state mean teleportation fidelity. This allows the general performance of the teleporter to be determined based only on the assumption of real, positive, linear combinations [42]. The resulting mean fidelity coincidence map $f^T_{\text{Mean}}(\tau_1,\tau_2)$ is displayed in Figure 7.6a. The data is shown for the post-selection bin sizes corresponding to the most statistically significant teleportation, defined by a quality factor [84]

$$\left(f^T_{\text{Mean}} - \frac{2}{3}\right)/\sigma_{\text{Mean}}, \tag{7.4}$$

where σ_{Mean} is the measured uncertainty in the mean teleportation fidelity. The factor of $\frac{2}{3}$ is the classical threshold for teleportation, and so measurement of a mean fidelity above this threshold serves to demonstrate quantum teleportation. Therefore, Equation 7.4 describes the number of standard deviations the measured teleportation fidelity is above the classical threshold. As can be seen, there is a familiar pattern with more clarity this time, due to the additional SNR gained from averaging all six results together. The point of highest fidelity is centred on $\tau_1 = \tau_2 = 0$, corresponding to the three-photon coincidence where the input polarisation state is mapped to the output photon at Bob, with a maximum mean fidelity of $83.6 \pm 2.2\%$ for a post-selection window size of $\Delta\tau_1$ x $\Delta\tau_2$ = 184 x 224 ps. This fidelity exceeds the classical threshold by 7.8 σ in this configuration, and constitutes the first demonstration of quantum teleportation in the telecom C-band using a QD quantum light source. Additionally, when thinking about the application of such a scheme for a real

quantum network, demonstration of the fidelity above the classical threshold alone is not enough. Such implementations require additional tolerances for error correction. For example, considering a six-state QKD protocol [233], the maximum mean teleportation fidelity is 5.1 σ above the limit of 0.724 imposed for secure implementations of the secret key sharing protocol [234].

The relevant features of interest can be examined further by taking cuts along each time axis. Figure 7.6b shows the cut along $\tau_2 = 0$, where the high-fidelity teleportation heralding TPI peak with width set by the X coherence time is seen. A small amount of residual detuning of the laser from the QD is present, accounting for the difference in the peak width from Figure 5.10 in the TPI measurement presented in Section 5.4. A similar cut along the $\tau_1 = 0$ axis, as shown in Figure 7.6c, displays oscillations in the fidelity resulting from the time-evolving nature of the two-photon state, where the period (728 ± 11 ps) corresponds to a FSS $S = 5.7 \pm 0.2$ μeV as expected. Finally, the maximum teleportation fidelity for each individual input state, along with the mean, is shown in Figure 7.6d, where each is above the classical threshold (shown by the dashed black line).

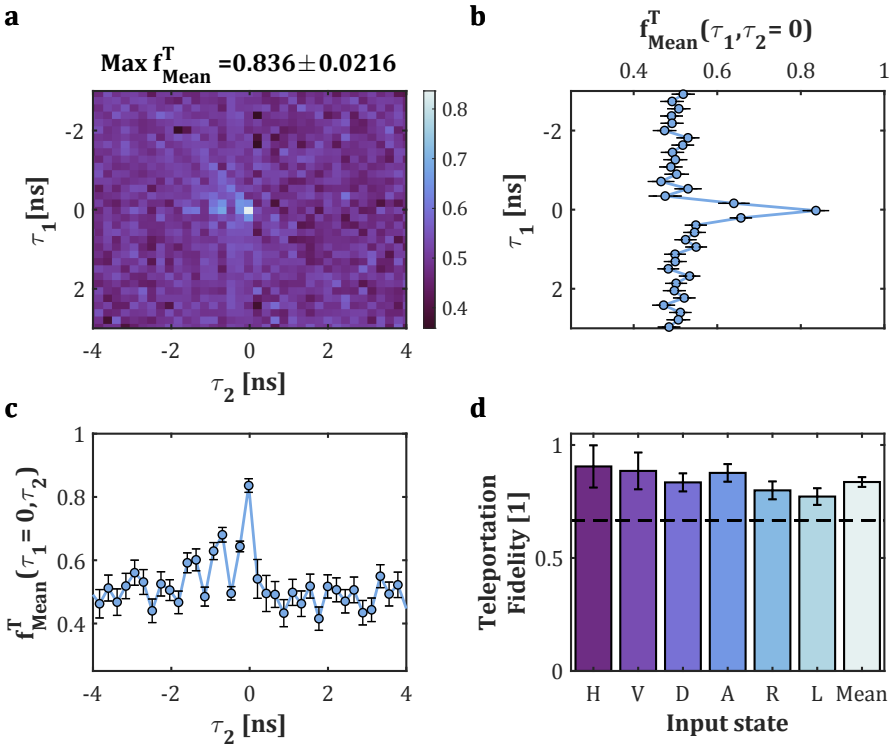

Figure 7.6: Six-state mean teleportation fidelity. **a** Mean teleportation fidelity map $f^T_{\text{Mean}}(\tau_1,\tau_2)$. **b** Slice at $\tau_2 = 0$ along τ_1 of $f^T_{\text{Mean}}(\tau_1,\tau_2)$. **c** Slice at $\tau_1 = 0$ along τ_2 of $f^T_{\text{Mean}}(\tau_1,\tau_2)$. **d** Individual maximum teleportation fidelities, where each one is above the classical threshold of $\frac{2}{3}$. Data shown for a post-selection window size of $\Delta\tau_1$ x $\Delta\tau_2$ = 184 x 224 ps.

There are several limitations restricting the performance of the teleportation. As the source is operated using the X saturation power in order to achieve the maximum photon count rate, this naturally leads to an increase in the $g^{(2)}(0)$ HBT value of the X. This imposes a limit, as discussed

in Section 5.4, on the achievable TPI visibility. The expected teleportation fidelity is consequently lowered as a result of fewer photons interfering at the 99:1 coupler and therefore leads to a higher proportion of incorrectly heralded photons measured at Bob. The $g^{(2)}(0)$ also poses a limit on the entanglement fidelity, since it leads to a higher number of photon pairs uncorrelated in polarisation. Better performance for low excitation power could be expected. However, the reduced brightness leads to much fewer three-photon coincidences, requiring significantly longer integration times while competing with non-zero detector counts to give a lower SNR, as well.

Post selection

As previously mentioned, temporal post-selection was used to gate the successful teleportation events for times close to $\tau_1 = \tau_2 = 0$. The temporal limitation along τ_1 is imposed by the interference visibility of the laser and QD photons, which is determined on a time-scale given by the X coherence time and the detector resolution. Therefore, a longer X coherence time would lead to more efficient teleportation by enabling a larger number of teleported photons within a gate. As with the entanglement measurement, the evolution of the quantum state due to the FSS with the detector resolution imposes a limit on the maximum window size along τ_2. By varying the window size for the post-selection, more photons can be teleported at the cost of a reduced teleportation fidelity. Reducing the window size can lead to even fewer teleported photons, but with a higher fidelity. The maximum teleportation fidelity here was found to be $88.4 \pm 4.0\%$, for an equivalent post-selection window size of 103 ps, 5.4 σ above the classical threshold. Additionally, as the main source of error here is due to the photon counting statistics (all errors quoted are propagated from this), the act of decreasing the post-selection bin size naturally increases the error, as fewer photons are taken into consideration. Consequently, while the fidelity increases, it becomes less statistically significant. Hence the motivation to adopt a bin size which optimises the quality of the teleportation versus the number of teleported photons or fidelity.

7.3 GHz-Clocked Teleportation of Telecom *C*-Band Time-Bin Qubits

In this final section of the thesis, a demonstration of a quantum relay run on-demand at GHz clock rates and teleporting time-bin qubits in the telecom C-band, suitable for integration with existing QKD systems, is made. While polarisation encoding is useful for free-space QKD implementations [159] or teleportation [230], it is less useful for fibre-based applications where polarisation drift in fibre needs to be actively compensated for [133]. A more desirable scheme is time-bin encoding, with which long-distance QKD systems operate, in order to increase the robustness of fibre transmission [235, 236]. Since QDs natively generate polarization-encoded single and entangled photons, a method to overcome this incompatibility is required. Some schemes based on weak pulsed excitation have demonstrated time-bin encoded single [237] and entangled photons [172, 238–240] directly from QDs. In the latter schemes for entangled photon pairs, the direct time-bin encoded entanglement generation from QDs has an advantage, in that larger FSS values can be acceptable [172]. However, it is unable to produce true on-demand entangled pairs without the addition of a metastable state [172, 238], in addition to the technical requirement of maintaining phase control between the early and late photons, relying on resonant two-photon excitation [239, 240]. An alternative approach is adopted for this measurement, based on the use of qubit transcoder units using asymmetric Mach-Zehnder interferometers to map polarisation-encoded photons to time-bin-encoded photons. Such a scheme can also be used to map polarisation-entangled photons to time-bin-entangled photons [241, 242].

The schematic for the chosen implementation of a quantum relay for time-bin encoded qubits is shown in Figure 7.7, where the input laser qubit is prepared at Alice and subsequently sent through a qubit transcoder (T1) in order to create a time-bin encoded input state. This state is sent onwards to the relay station Charlie, where a second phase-matched decoding interferometer is used to map the time-bin encoded state back into polarisation encoding for interfacing with the native polarisation-entangled QD photons. The teleportation then simply proceeds as discussed previously, where a BSM aligned to the QD eigenbasis is used to herald the teleportation of the input state to the XX photon. At this point, there are two possible options, which will be discussed in Section 7.3.2 and Section 7.3.3. Firstly, a polarisation resolved measurement can proceed at Bob as previously conducted, in order to verify that the time-bin mapping was correct and resulted in the expected outcomes. Secondly, and the case depicted in Figure 7.7, the output photon at Bob can then be sent through a third phase-matched transcoder in order to map the polarisation to a time-bin, before analysis of the output time-bin.

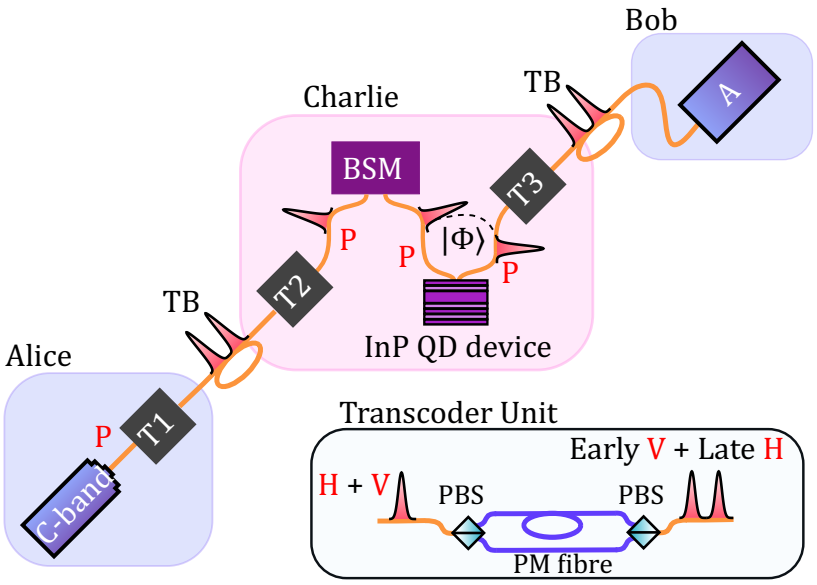

Figure 7.7: Teleportation of time-bin encoded laser qubits. Alice prepares a GHz-clocked time-bin encoded qubit using an interferometric transcoding unit. At the relay node, Charlie, another phase-stabilized transcoding unit converts the qubits back into polarization. The same teleportation protocol as previously demonstrated can then be used. After successful teleportation at Charlie, the photons can be transcoded back into time-bin encoding, before being sent on to a receiver, Bob. P, polarization qubit; TB, time-bin qubit; T1–T3,transcoder units; A, time-bin qubit analysis; BSM, Bell-state measurement.

7.3.1 Qubit Transcoder Units

In order to generate the time-bin input qubits at Alice, a similar setup to that described in Section 3.3 was used to create GHz-clocked pulses (FWHM 130 ps) from a tunable telecom C-band CW laser. Time-bin to polarisation interferometric transcoding units (TUs) were then constructed by Dr. Müller. The inset in Figure 7.7 shows the main operating principles of the TU. Polarisation qubits are incident on a PBS which splits the photons into H and V polarisations, aligned by a PC (not shown). In one arm, a fibre delay of ~ 5 ns is added in order to delay the H-polarised photons with respect to the V-polarised photons. The photons then recombined at a subsequent PBS, where the polarisations are split into early, e, and late, l, time-bins. In this way, the logical time-bin encoded states are created by the mappings $|V\rangle \rightarrow |e\rangle$ and $|H\rangle \rightarrow |l\rangle$. An example of such an early state $|e\rangle$ is shown in Figure 7.8a. Alignment of the input polarisation with the polarisation axis of the TU results in the generation of an $|e\rangle$ state from sending V-polarised weak coherent states. A phase can then be encoded between the early and the late pulses through the use of a fibre-stretcher in one arm to fine-tune the delay between the two arms, in order to create superposition-basis states. An exemplary state is shown in Figure 7.8b, for a state corresponding to approximately equal intensities in the output time-bins.

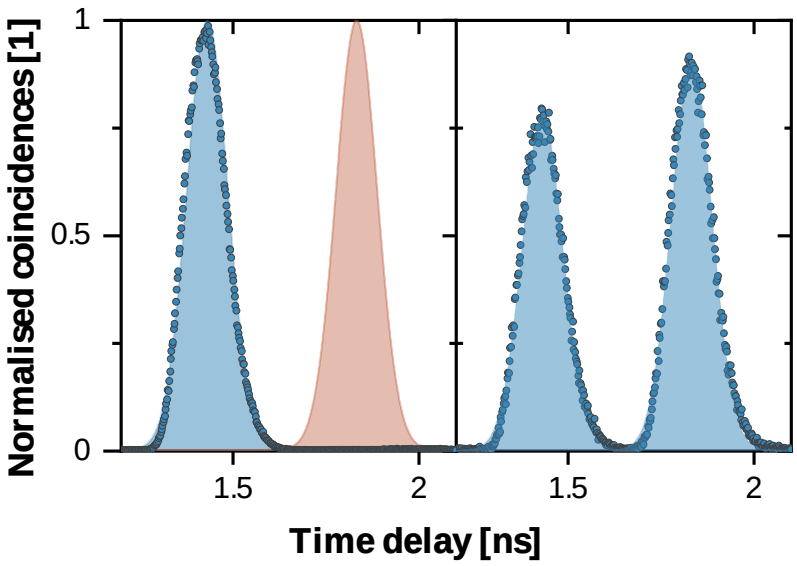

Figure 7.8: Time-bin encoded weak coherent states. Left Logical time-bin basis state $|e\rangle$, comprising of a photon in the early time-bin. **Right** Superposition time-bin basis state $\propto (|e\rangle + |l\rangle)$, with approximately equal intensity in the early and late time-bins.

To interface these qubits with the QD polarisation states at the relay station, a second phase-matched TU is then used to map the states back into polarisation, allowing the teleportation to proceed as discussed previously in Section 7.2. This is done by using an EPC in order to align the pulses into the correct arms of the interferometer, such that sending a V-polarised photon is mapped to an early time-bin, then subsequently mapped back to a V-polarised photon. The second TU is phase-stabilised using a feedback routine written by Dr. Müller to monitor the output polarisation of the second interferometer and adjust the delay between the two arms in order to keep it constant. When stabilised in this way, it is then possible to map a superposition state back into the corresponding superposition polarisation state. In the experiment, the calibration basis is set by the QD. As discussed in Section 6.5, when operating the QD under GHz-excitation rates, the anomalous FSS effect disrupted the eigenstates, making the method used in Section 7.2 no longer possible. The reference basis for this was therefore determined through the measurement of the density matrix, as discussed in Section 6.5. The saved alignment angles of the reference laser were then used to calibrate the detectors at Charlie to the QD basis states, from which all other calibrations were derived from.

7.3.2 Teleporting Time-Bin Input States

The teleportation of initially time-bin encoded input states proceeds by simply decoding the input photons back into polarisation, then analysing the output photon in polarisation. For the time-bin scheme to work, the QD source must naturally be operated under pulsed excitation. Therefore, the previous work in demonstrating the GHz-clocked single and entangled emission from the QD is used here when operating the relay under the same pulsed excitation scheme. The QD is excited using the flexible pulsed excitation scheme, with $f = 1.07$ GHz, as before. Figure 7.9 shows the resulting third-order correlation maps when sending the $|\Psi_L\rangle = |e\rangle$, which subsequently decodes into the $|V\rangle$ state at the relay station. The expected correlation in Figure 7.9a, when measuring a H-polarised photon at Bob has a few additional features when compared to the previous measurement in Figure 7.3. Firstly, the pulsed nature of the experiment is seen by a series of peaks in the triple coincidences along the τ_1 axis, where the period corresponds to the $f = 1.07$ GHz repetition rate used. Secondly, the triple coincidences are uniformly pulsed along this axis, due to the fact that here the D_H detection begins the time-tagging of subsequent events. Therefore, the QD is the trigger and so the cascade happens for all τ_1 when the laser is present. The pulsed nature is exaggerated here due an imbalance of the laser and QD intensity, which has no effect on the measurement outcome, since there is no requirement on the TPI in order to perform this correlation. For the same reason as discussed in Section 7.2, the additional features relating to the re-excitation events can be seen, as well as in Figure 7.9b. The corresponding fidelity map $f_V^T(\tau_1,\tau_2)$ shown in Figure 7.9c displays similar behaviour as before, where this time the alignment of the BSM is much improved, as evidenced by the lack of weak oscillatory features. The improvement here is attributed to a careful optimisation of the QD HV basis, and results in an improved teleportation fidelity of $f_V^T = 0.98 \pm 0.02$, as shown by the cut through in Figure 7.9d, where the non-unity value is due to the non-unity correlation coefficient, even after some optimisation of the basis.

For the more interesting superposition state teleportation, the input laser is prepared with a phase leading to equal intensity pulses, which is then mapped to the QD $|A\rangle$ state at Charlie. The delay between the laser pulse and QD pulse is adjusted so the two pulses overlap at the beamsplitter. The peak intensities are set to be equal corresponding to similar conditions for the TPI as before, verified by a separate TPI under pulsed excitation (achieving a similar visibility to that in Section 5.10). The results for this input state are shown in Figure 7.10, where the expected (unexpected) correlations when measuring $A(D)$-polarised photons at Bob show similar behaviour as measured previously. The increase (absence) in triple coincidences at the origin signals the successful teleportation. The mean fidelity map $f_A^T(\tau_1,\tau_2)$ shown in Figure 7.10c confirms the high fidelity peak, where a maximum of $f_A^T = 0.75 \pm 0.03$ is found. The appearance of weak oscillations in the fidelity map again indicates a small misalignment of the BSM, highlighting the sensitivity in this alignment procedure.

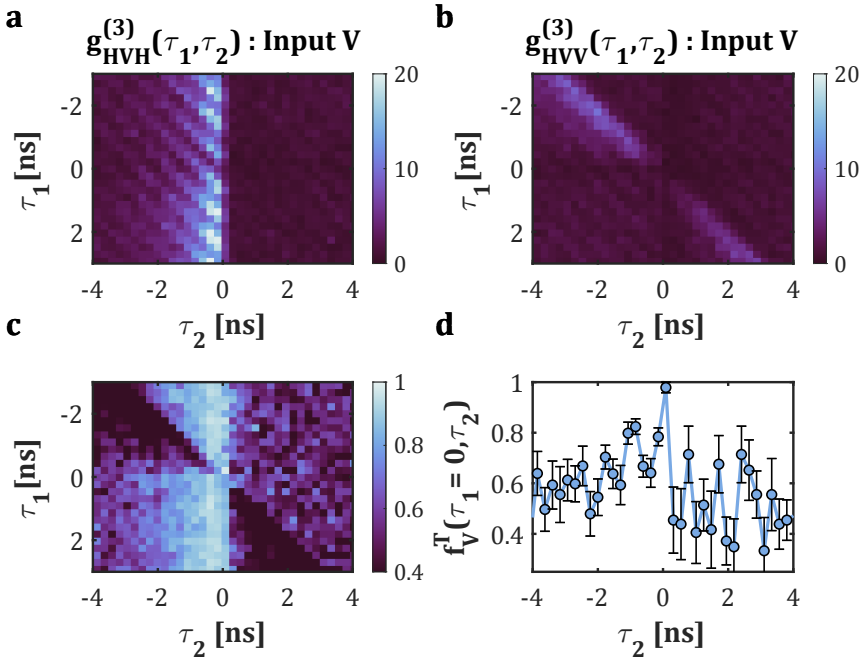

Figure 7.9: Teleportation of e states onto H polarised XX photons. a Third-order correlation $g^{(3)}_{HVH}(\tau_1,\tau_2)$. **b** Third-order correlation $g^{(3)}_{HVV}(\tau_1,\tau_2)$. **c** Corresponding teleportation fidelity $f^T_V(\tau_1,\tau_2)$. **d** Slice at $\tau_1 = 0$ along τ_2 of f^T_V. Data shown for a post-selection window size of $\Delta\tau_1$ x $\Delta\tau_2$ = 224 x 232 ps.

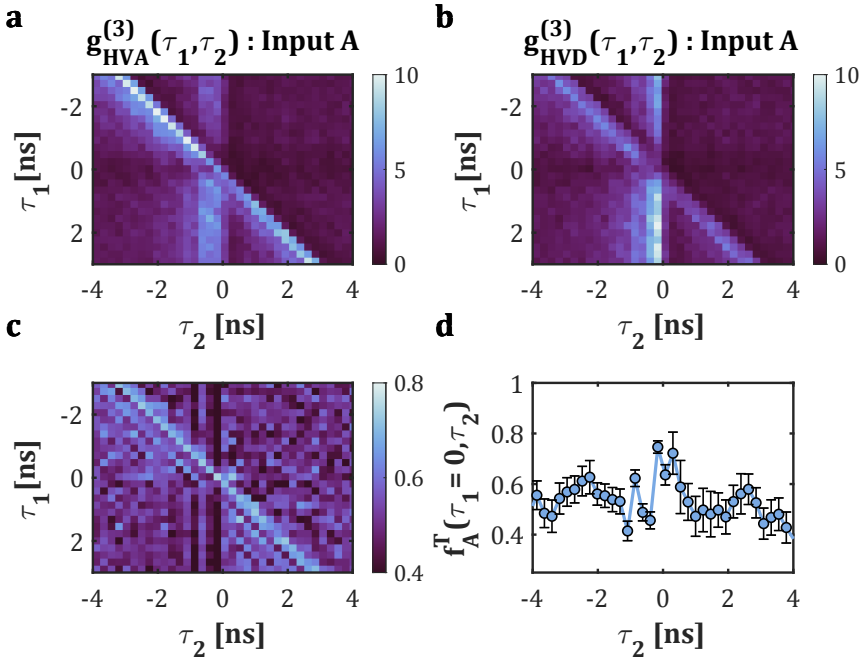

Figure 7.10: Teleportation of superposition time-bin state onto A polarised XX photons. a Third-order correlation $g^{(3)}_{HVA}(\tau_1,\tau_2)$. **b** Third-order correlation $g^{(3)}_{HVA}(\tau_1,\tau_2)$. **c** Corresponding teleportation fidelity $f^T_A(\tau_1,\tau_2)$. **d** Slice at $\tau_1 = 0$ along τ_2 of f^T_A. Data shown for a post-selection window size of $\Delta\tau_1$ x $\Delta\tau_2$ = 224 x 234 ps.

Repeating this measurement for a third orthogonal input state, mapped to the QD $|L\rangle$ state, is required in order to verify that the mean fidelity violates the classical threshold for general teleportation [232], since any state can be made from a linear combination of these three states. The resulting individual mean fidelities are shown in Figure 7.11, where a maximum of $f_L^T = 0.73 \pm 0.03$ leads to a mean fidelity of $f_{\text{Mean}}^T = 0.82 \pm 0.01$, beating the classical threshold by 10.4 σ. Again, the bin size here ($\Delta\tau_1$ x $\Delta\tau_2$ = 224 x 234 ps) is defined to give the most statistically meaningful teleportation. The fidelity for the superposition states is lower than those measured under CW excitation. This is, in part, due to the difficulty in alignment for the superposition state detection, relating to the anomalous splitting of the QD used here. There is also a contribution from the stabilisation of the qubit transcoders, where fluctuations in phase lead to fluctuations in the output qubit polarisation. This leads to a higher number of incorrectly heralded detections, thus reducing the fidelity. In each case, the individual fidelities are similar to the values obtained in the CW measurement, and are above the classical threshold verifying the quantum nature of the teleportation.

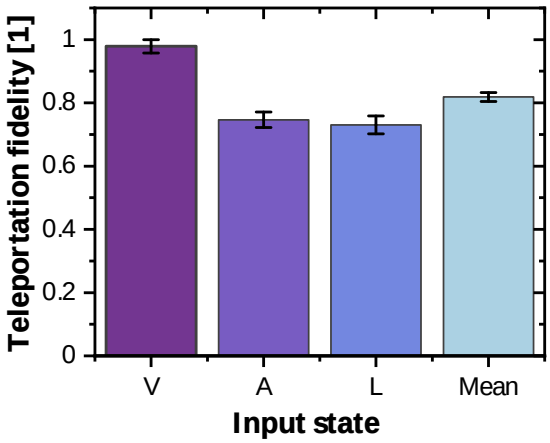

Figure 7.11: Teleportation fidelities for a complete set of input states. The results for the most statistically significant post-selection window size of $\Delta\tau_1$ x $\Delta\tau_2$ = 224 x 232 ps are shown. Each state surpasses the classical threshold, with a mean fidelity of 0.82 ± 0.01.

7.3.3 Measuring Time-Bin Output States

In the final step of this experiment, the teleported output photon can then be converted back into time-bin encoding, before sending it onwards to measurement at Bob. The proof-of-principle operation of this is verified here for the logical states by sending the XX photons back through the decoding qubit transcoder, which automatically guarantees phase stabilisation of the XX output photon to the time-bin input photon. This is achieved through the use of circulators placed on either side of the decoding transcoder unit. For the laser input qubits $|V\rangle \rightarrow |e\rangle$ and $|H\rangle \rightarrow |l\rangle$, the polarisation to time-bin conversion means that there will be a mapping of $|e\rangle \rightarrow |l\rangle$ and $|l\rangle \rightarrow |e\rangle$ at Bob.

In order to determine the success of the operation, three-order correlations $g^{(3)}_{HVEL}(\tau_1,\tau_2)$ are measured by correlating the successful BSM with the arrival time of the photons at Bob. The results of this can be seen in Figure 7.12a for the $|e\rangle$ input state (left) and $|l\rangle$ input state (right). Considering first the case of the $|e\rangle$ input qubit, there are several familiar features. The first thing to note is that as the Bob measurement correlates arrival times, the features for both H- and V-polarised photons are present, offset along the τ_1 axis by ~ 5 ns, according to the transcoder unit delay. There is a peak of coincidences at the $\tau_1 = \tau_2 = 0$ and an absence at $\tau_2 = 5$ ns along the $\tau_1 = 0$ axis, which confirms that Bob's photon went through the long arm of the conversion interferometer. Here, the relative time axis is set to measure the arrival of the late pulse at $\tau_2 = 0$. The notable feature of this plot is the absence of coincidences along the $\tau_1 = \tau_2$ axis, demonstrating the lack of simultaneous detections of the laser/X and XX photons. The faint diagonal line along $\tau_1 = \tau_2 + 5$ corresponds to the detections of early V-polarised photons, similar to the measurement $g^{(3)}_{HVV}(\tau_1,\tau_2)$ of V-polarised photons in Figure 7.9b. Considering the case of the $|l\rangle$ input qubit, the opposite behaviour is seen when looking at the right panel of Figure 7.12a. The expected outcome is an early one, and is seen by the peak in triple coincidences at $\tau_2 = -5$ ns along $\tau_1 = 0$, which corresponds to a successful mapping of the late to early time bins. This time, the pulsed pattern appears along the $\tau_1 = \tau_2 + 5$, due to the laser photons now being on D_H at the BSM.

The situation is again highlighted by looking at a cut along the τ_1 axis, as shown by Figure 7.12b, where the arrival times of the early and late photons are seen by the XX-X cascades separated by the delay of the interferometer. The fidelity is calculated according to

$$f^T_{e/l} = \frac{g^{(3)}_{HVEL}(\tau_1 = 0, \tau_{l/e})}{g^{(3)}_{HVEL}(\tau_1 = 0, \tau_e) + g^{(3)}_{HVEL}(\tau_1 = 0, \tau_l)}, \tag{7.5}$$

where $\tau_{e/l}$ corresponds to the expected time bin of the early/late pulse, determined by the interferometer delay. The peak and absence of photons in the correct time bins results in a post-selected teleportation fidelity of $f^T_e = f^T_l = 0.89 \pm 0.04$ for both logical time-bin encoded input states. This fidelity is somewhat comparable to that reached without the time-bin conversion of Bob's photon, which confirms the accuracy of the conversion process. The limitations and reduction of the fidelity may correspond to the exact alignment of the logical basis BSM, as discussed previously. However, it

could also be the result of the increased noise when sending the Bob photons through the transcoder. The parasitic loss of this process resulted in a transmission of ~ 56% for the XX photons. This also limits the measurement of teleportation of a superposition state in time-bin encoding, since after the conversion, the output photons would need converting back into polarisation using another pass of the interferometer in order to determine if the phase was correctly mapped [242]. Such losses using the current device unfortunately made it infeasible to conduct such an experiment within a reasonable timescale.

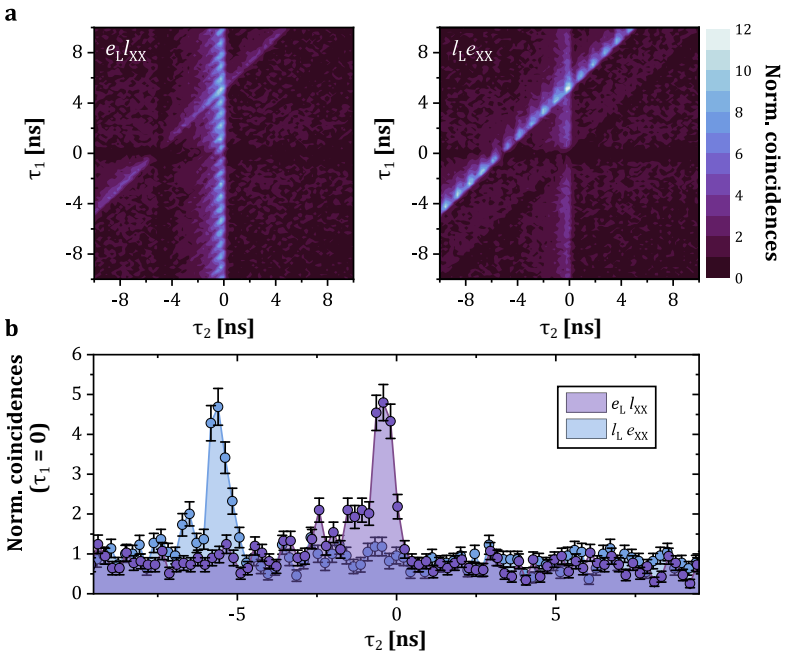

Figure 7.12: Time-bin logical-basis teleportation. a Third-order correlations $g^{(3)}_{HVEL}(\tau_1, \tau_2)$ for sending input laser qubits $|e\rangle$ (left) and $|l\rangle$ (right), which are mapped to $|l\rangle$ and $|e\rangle$ output states, respectively, after sending XX photons back through the decoding interferometer. **b** Cut along $\tau_1 = 0$ showing the mapping of the $|e\rangle$ input state to the $|l\rangle$ output state, corresponding to the polarisation mapping of $|V\rangle$ to $|H\rangle$.

7.4 Summary

In this chapter, the work of the thesis in demonstrating quantum interference and entanglement was combined in order to demonstrate a proof-of-principle quantum relay using a QD quantum light source emitting in the telecom *C*-band. Under CW excitation and polarisation encoding, high post-selected fidelities were achieved when considering a complete set of six input states, overcoming even the threshold for secure implementations of secret key sharing protocols. This scheme was extended further to the pulsed excitation regime at a repetition rate of 1 GHz, where the teleportation of initially time-bin encoded qubits was demonstrated to again overcome the classical and fault-tolerant thresholds. A final demonstration showed the possibility for extending this scheme by converting the output photons back into time-bin encoding qubits, making it compatible with existing QKD infrastructure.

Chapter 8

Conclusions and Outlook

The work in this thesis has described the experimental efforts towards the development of a semiconductor QD quantum light source operating near the minimum absorption wavelength window of optical fibre, centred on the telecom *C*-band (1530 – 1565 nm). Such a source is an ideal candidate for transmission over the standard telecommunication optical fibre network infrastructure for quantum information applications. The ultimate aim was to demonstrate proof-of-principle quantum teleportation of telecom *C*-band laser qubits, enabling such a platform to form an interface with current QKD systems in the future.

8.1 Summary

The thesis began by performing a characterisation of the source, DE grown InAs/InP QDs embedded in a *p*-*i*-*n* diode structure with a weak planer cavity, by looking at the spectral and time-resolved emission under non-resonant optical excitation. Spectral analysis revealed that the QDs tended to form with remarkably consistent energetic structure, displaying a rigid pattern of exciton charge configurations. Polarisation analysis was used to identify the neutral exciton transitions, which would form the basis of all subsequent measurements. Time-resolved analysis further showed that the main transitions displayed highly non-classical photon statistics under both non-resonant CW and 1-GHz pulsed excitation, with strong evidence of multilevel dynamics as a result of the excitation scheme used. Such demonstration of non-classical emission could, in theory, form the basis of a true single-photon telecom *C*-band source for QKD over fibre. In order to characterise the suitability of this source for quantum interference-based applications, a subsequent analysis of the coherence in the emission was then performed using a standard telecom fibre MI. This characterisation revealed unprecedented coherence times for the DE QDs, comparable to state of the art GaAs-based systems under comparable excitation conditions. A strong limit was found on the coherence for elevated temperatures where non-resonant electrical excitation would be possible.

Using the demonstration of highly-coherent emission, the HOM-type interference of unpolarised single photons from the neural *X* was then considered. It was shown that for high and low power

regimes, high post-selected visibilities were achieved despite the non-resonant excitation, showing the potential of this platform as a source of indistinguishable photons. Using the high interference visibility, the first key element of the teleportation protocol for the teleportation of laser qubits, the interference with a weak coherent state, was performed. Again, it was found that the high post-selected visibility was mainly limited by background contributions in both experimental conditions considered.

Following this, the entanglement properties, forming the second key element of a teleportation protocol, were considered under both CW and pulsed optical excitation. Measurement of the correlation coefficient in five complementary bases under CW excitation revealed a post-selected maximum entanglement fidelity of 0.90 ± 0.01 and a counts-weighted average fidelity of 0.72 ± 0.01 to the expected Bell state, constituting a record-high measurement for this type of solid-state quantum emitter. A violation of the Bell parameter was also measured in three orthogonal planes of the Poincaré sphere. When looking towards pulsed excitation, an unusual feature of the FSS found in a large number these QDs was revealed and further investigated by considering an ensemble of 90 FSS measurements. The statistics gathered from this data strongly correlated with the proposed model, which detailed the modification of the FSS and the photon polarisation resulting from a magnetic-field type interaction, developed in [206]. A method to recover the QD eigenstates from the measurement of the two-photon density matrix was then considered, which after determination of the QD basis using this method, resulted in a reconstruction of the full QD density matrix. This was found to bear strong resemblance to the expected Bell state, with a maximum fidelity of 0.88 ± 0.01 and a concurrence of 0.80 ± 0.01.

Combining the work of this thesis, a proof-of-principle quantum relay using a QD quantum light source emitting in the telecom *C*-band was then demonstrated. With CW excitation and polarisation encoding, high post-selected fidelities were achieved when considering a complete set of six input states, overcoming even the threshold for secure implementations of secret key sharing protocols. The scheme was then extended further, using the previously determined measurement basis, to a 1 GHz pulsed excitation regime, where the teleportation of initially time-bin encoded qubits was demonstrated. The last part of this thesis then considered how, in the future, a further extension could be made by considering the possibility of full teleportation of time-bin qubits. Such a scheme, while unattainable during the work of this thesis, would allow for a direct interface between the quantum relay and existing QKD infrastructure, allowing for the enhancement in the security of a quantum link, and the possibility to extend the distance.

8.2 Future Work

Development of the sample structure to enable lower operating temperature under electrical excitation in order to access the longer coherence times could be one potential avenue for future work, towards the development of remote systems where experimental complexity is undesirable. This avenue could also consider the use of recently demonstrated 'on-chip' pumping schemes [134, 174], where carriers excited into the quantum well surrounding the QD recombine to quasi-resonantly excite QDs in a nearby mesa. Such structures have enabled fully electrically tunable and electrically-driven emission of a QD source in the telecom *O*-band [134].

Work towards resonant excitation schemes would also be an interesting area for future work. In this regime, not only is the single-photon purity greatly enhanced, but the pure dephasing is also reduced significantly such that transform-limited emission is possible [166, 175]. This would enable highly indistinguishable and pure telecom *C*-band single photons, a suitable candidate for integration with silicon-integrated photonics [176, 177]. Utilising resonant excitation schemes in order to remove dephasing associated with carrier relaxation processes [165, 166, 171, 200] would be the natural first step here. In terms of experiments involving laser photon interference, reduction of the pure dephasing and emitter lifetime would naturally reduce the time-gate restriction, allowing wider gates to be used and more efficient use of the QD photons.

When considering the entanglement-based applications, future work in this area would be to operate the system under resonant two-photon excitation. Similar benefits to operation under resonant excitation could be achieved, with an additional increase of the entanglement fidelity of the emitted photons [72]. Such a scheme would further increase the utility for entanglement and interference-based applications, such as teleportation [42, 227] or entanglement swapping [43, 44]. In all cases, engineering of the photonic structure by incorporation into a cavity, such as those recently demonstrated [189, 190, 201], would improve the overall source brightness, indistinguishability and efficiency. Such improvements would be universally beneficial for all quantum information applications using this type of source. Such a cavity would enhance the coupling of the QD to the cavity, leading to a reduction of the radiative lifetime. This would not only support the development of Fourier-limited emission, but would additionally support the on-demand operation and efficiency of the source, allowing all photon events to be considered; removing the need for post-selection. The increased brightness from the higher obtainable collection efficiency would drastically improve the operation of all interference-based measurements, as well as three and four-photon measurements such as teleportation and entanglement swapping, due to the way that the rate of detection events scales with emission intensity. This would also be critical when looking towards deployed fibre applications [133, 134], where fibre losses over distance and interconnects becomes a limiting factor for even entanglement-based applications. Work towards such improvements using circular Bragg gratings optimised for telecommunications wavelengths has already been demonstrated [228], and has the potential to push this technology towards truly useful quantum information applications.

References

[1] Rivest, R. L., Shamir, A. & Adleman, L. A method for obtaining digital signatures and public-key cryptosystems. *Commun. ACM* **21**, 120–126 (1978).

[2] Dolev, D. & Yao, A. On the security of public key protocols. *IEEE Trans. Inf. theory* **29**, 198–208 (1983).

[3] Fox, M. *Quantum optics: an introduction*, vol. 15 (OUP Oxford, 2006).

[4] Feynman, R. P. Simulating physics with computers. *Int. J. Theor. Phys.* **21**, 467–488 (1982).

[5] Shor, P. W. Algorithms for quantum computation: Discrete logarithms and factoring. In *Found. Comput. Sci. 1994 Proceedings., 35th Annu. Symp.*, 124–134 (IEEE, 1994).

[6] Shor, P. W. Polynomial-time algorithms for prime factorization and discrete logarithms on a quantum computer. *SIAM Rev.* **41**, 303–332 (1999).

[7] Grover, L. K. A fast quantum mechanical algorithm for database search. In *Proc. twenty-eighth Annu. ACM Symp. Theory Comput.*, 212–219 (ACM, 1996).

[8] Deutsch, D. & Jozsa, R. Rapid solution of problems by quantum computation. In *Proc. R. Soc. London A Math. Phys. Eng. Sci.*, vol. 439, 553–558 (The Royal Society, 1992).

[9] Gisin, N., Ribordy, G., Tittel, W. & Zbinden, H. Quantum cryptography. *Rev. Mod. Phys.* **74**, 145 (2002).

[10] Kimble, H. J. The quantum internet. *Nature* **453**, 1023–1030 (2008).

[11] Wootters, W. K. & Zurek, W. H. A single quantum cannot be cloned. *Nature* **299**, 802 EP – (1982).

[12] Arute, F. *et al.* Quantum supremacy using a programmable superconducting processor. *Nature* **574**, 505–510 (2019).

[13] Google AI Quantum. Hartree-Fock on a superconducting qubit quantum computer. *Science.* **369**, 1084–1089 (2020).

[14] Bell, J. S. On the Einstein Podolsky Rosen paradox. *Phys. Phys. Fiz.* **1**, 195–200 (1964).

[15] Einstein, A., Podolsky, B. & Rosen, N. Can quantum-mechanical description of physical reality be considered complete? *Phys. Rev.* **47**, 777–780 (1935).

[16] Clauser, J. F., Horne, M. A., Shimony, A. & Holt, R. A. Proposed experiment to test local hidden-variable theories. *Phys. Rev. Lett.* **23**, 880–884 (1969).

[17] Aspect, A., Dalibard, J. & Roger, G. Experimental test of Bell's inequalities using time- varying analyzers. *Phys. Rev. Lett.* **49**, 1804–1807 (1982).

[18] Weihs, G., Jennewein, T., Simon, C., Weinfurter, H. & Zeilinger, A. Violation of bell's inequality under strict einstein locality conditions. *Phys. Rev. Lett.* **81**, 5039–5043 (1998).

[19] Young, R. J. *et al.* Bell-inequality violation with a triggered photon-pair source. *Phys. Rev. Lett.* **102**, 030406 (2009).

[20] Giustina, M. *et al.* Significant-Loophole-Free Test of Bell's Theorem with Entangled Photons. *Phys. Rev. Lett.* **115**, 250401 (2015).

[21] Abellán, C. *et al.* Challenging local realism with human choices. *Nature* **557**, 212–216 (2018).

[22] Kim, Y.-H., Kulik, S. P. & Shih, Y. Quantum Teleportation of a Polarization State with a Complete Bell State Measurement. *Phys. Rev. Lett.* **86**, 1370–1373 (2001).

[23] Bennett, C. H. & Brassard, G. Quantum Cryptography: Public Key Distribution and Coin Tossing. In *Proc. IEEE Int. Conf. Comput. Syst. Signal Process.*, 175–179 (IEEE Press, New York, 1984).

[24] Lütkenhaus, N. Security against individual attacks for realistic quantum key distribution. *Phys. Rev. A* **61**, 52304 (2000).

[25] Sangouard, N. & Zbinden, H. What are single photons good for? *J. Mod. Opt.* **59**, 1458–1464 (2012).

[26] Jacobs, B. C., Pittman, T. B. & Franson, J. D. Quantum relays and noise suppression using linear optics. *Phys. Rev. A* **66**, 6 (2002).

[27] Briegel, H. J., Dür, W., Cirac, J. I. & Zoller, P. Quantum repeaters: The role of imperfect local operations in quantum communication. *Phys. Rev. Lett.* **81**, 5932–5935 (1998).

[28] Sangouard, N., Simon, C., De Riedmatten, H. & Gisin, N. Quantum repeaters based on atomic ensembles and linear optics. *Rev. Mod. Phys.* **83**, 33 (2011).

[29] Monroe, C. Quantum information processing with atoms and photons. *Nature* **416**, 238–246 (2002).

[30] Lounis, B. & Moerner, W. E. Single photons on demand from a single molecule at room temperature. *Nature* **407**, 491–493 (2000).

[31] Jelezko, F. & Wrachtrup, J. Single defect centres in diamond: A review. *Phys. status solidi* **203**, 3207–3225 (2006).

[32] Shields, A. J. Semiconductor quantum light sources. *Nat. Photonics* **1**, 215–223 (2007).

[33] Buckley, S., Rivoire, K. & Vučković, J. Engineered quantum dot single-photon sources. *Reports Prog. Phys.* **75**, 126503 (2012).

[34] Gerry, C. & Knight, P. *Introductory Quantum Optics* (Cambridge University Press, 2004).

[35] Lo, H. K., Ma, X. & Chen, K. Decoy state quantum key distribution. *Phys. Rev. Lett.* **94**, 230504 (2005).

[36] Peng, C. Z. *et al.* Experimental long-distance decoy-state quantum key distribution based on polarization encoding. *Phys. Rev. Lett.* **98**, 010505 (2007).

[37] Rosenberg, D. *et al.* Long-distance decoy-state quantum key distribution in optical fiber. *Phys. Rev. Lett.* **98**, 010503 (2007).

[38] Sangouard, N. & Zbinden, H. What are single photons good for? *J. Mod. Opt.* **59**, 1458–1464 (2012).

[39] Somaschi, N. *et al.* Near-optimal single-photon sources in the solid state. *Nat. Photonics* **10**, 340–345 (2016).

[40] Intallura, P. M. *et al.* Quantum key distribution using a triggered quantum dot source emitting near 1.3 μm. *Appl. Phys. Lett.* **91**, 161103 (2007).

[41] Schimpf, C. *et al.* Quantum cryptography with highly entangled photons from semiconductor quantum dots. *Sci. Adv.* **7**, eabe8905 (2021).

[42] Nilsson, J. *et al.* Quantum teleportation using a light-emitting diode. *Nat. Photonics* **7**, 311–315 (2013).

[43] Basso Basset, F. *et al.* Entanglement Swapping with Photons Generated on Demand by a Quantum Dot. *Phys. Rev. Lett.* **123**, 160501 (2019).

[44] Zopf, M. *et al.* Entanglement Swapping with Semiconductor-generated Photons. *Phys. Rev. Lett.* **123**, 160502 (2019).

[45] Loredo, J. C. *et al.* Boson Sampling with Single-Photon Fock States from a Bright Solid-State Source. *Phys. Rev. Lett.* **118**, 130503 (2017).

[46] Mandel, L. & Wolf, E. *Optical coherence and quantum optics* (Cambridge university press, 1995).

[47] Brown, R. H. & Others. Correlation between photons in two coherent beams of light. *Nature* **177**, 27–29 (1956).

[48] Knill, E., Laflamme, R. & Milburn, G. J. A scheme for efficient quantum computation with linear optics. *Nature* **409**, 46–52 (2001).

[49] Gottesman, D. & Chuang, I. L. Demonstrating the viability of universal quantum computation using teleportation and single-qubit operations. *Nature* **402**, 390–393 (1999).

[50] Nielsen, M. A. & Chuang, I. L. *Quantum computation and quantum information* (Cambridge university press, 2000).

[51] Bouwmeester, D. *et al.* Experimental quantum teleportation. *Nature* **390**, 575–579 (1997).

[52] Varnava, C. *et al.* An entangled-LED-driven quantum relay over 1 km. *npj Quantum Inf.* **2**, 145 (2016).

[53] Zwerger, M., Dür, W. & Briegel, H. J. Measurement-based quantum repeaters. *Phys. Rev. A* **85**, 062326 (2012).

[54] Munro, W. J., Stephens, A. M., Devitt, S. J., Harrison, K. A. & Nemoto, K. Quantum communication without the necessity of quantum memories. *Nat. Photonics* **6**, 777–781 (2012).

[55] Li, Z. D. *et al.* Experimental quantum repeater without quantum memory. *Nat. Photonics* **13**, 644–648 (2019).

[56] Hong, C. K., Ou, Z. Y. & Mandel, L. Measurement of subpicosecond time intervals between two photons by interference. *Phys. Rev. Lett.* **59**, 2044–2046 (1987).

[57] Feynman, R. P., Leighton, R. B. & Sands, M. *The Feynman Lectures on Physics, Vol. III: The New Millennium Edition: Quantum Mechanics.* The Feynman Lectures on Physics (Basic Books, 2011).

[58] Michler, P. *Single semiconductor quantum dots* (Springer, 2009).

[59] Bimberg, D., Grundmann, M. & Ledentsov, N. Quantum Dot Heterostructures (John Wiley & Sons, 1999).

[60] Agostini, G. & Lamberti, C. *Characterization of Semiconductor Heterostructures and Nanostructures* (Elsevier Science, 2013).

[61] Ashoori, R. C. Electrons in artificial atoms. *Nature* **379**, 413 (1996).

[62] Heitz, R. *et al.* Multiphonon-relaxation processes in self-organized InAs/GaAs quantum dots. *Appl. Phys. Lett.* **68**, 361–363 (1996).

[63] Santori, C., Fattal, D., Vučković, J., Solomon, G. S. & Yamamoto, Y. Indistinguishable photons from a single-photon device. *Nature* **419**, 594–597 (2002).

[64] Yuan, Z. *et al.* Electrically driven single-photon source. *Science* **295**, 102–105 (2002).

[65] Salter, C. L. *et al.* An entangled-light-emitting diode. *Nature* **465**, 594–597 (2010).

[66] Stevenson, R. M. *et al.* Indistinguishable entangled photons generated by a light-emitting diode. *Phys. Rev. Lett.* **108**, 040503 (2012).

[67] Kamada, H., Gotoh, H., Temmyo, J., Takagahara, T. & Ando, H. Exciton Rabi oscillation in a single quantum dot. *Phys. Rev. Lett.* **87**, 246401 (2001).

[68] Miyazawa, T. *et al.* Single-photon emission at 1.5 μm from an InAs/InP quantum dot with highly suppressed multi-photon emission probabilities. *Appl. Phys. Lett.* **109**, 132106 (2016).

[69] He, Y. M. *et al.* Coherently driving a single quantum two-level system with dichromatic laser pulses. *Nat. Phys.* **15**, 941–946 (2019).

[70] Brunner, K., Abstreiter, G., Böhm, G., Tränkle, G. & Weimann, G. Sharp-line photoluminescence and two-photon absorption of zero-dimensional biexcitons in a GaAs/AlGaAs structure. *Phys. Rev. Lett.* **73**, 1138–1141 (1994).

[71] Stufler, S. *et al.* Two-photon Rabi oscillations in a single Inx Ga1-x As GaAs quantum dot. *Phys. Rev. B* **73**, 125304 (2006).

[72] Müller, M., Bounouar, S., Jöns, K. D., Glässl, M. & Michler, P. On-demand generation of indistinguishable polarization-entangled photon pairs. *Nat. Photonics* **8**, 224–228 (2014).

[73] Urbaszek, B. *et al.* Fine Structure of Highly Charged Excitons in Semiconductor Quantum Dots. *Phys. Rev. Lett.* **90**, 4 (2003).

[74] Cade, N. I., Gotoh, H., Kamada, H., Nakano, H. & Okamoto, H. Fine structure and magneto-optics of exciton, trion, and charged biexciton states in single InAs quantum dots emitting at 1.3 μm. *Phys. Rev. B* **73**, 115322 (2006).

[75] Warburton, R. J. *et al.* Optical emission from a charge-tunable quantum ring. *Nature* **405**, 926–929 (2000).

[76] Stevenson, R. M. *et al.* A semiconductor source of triggered entangled photon pairs. *Nature* **439**, 179–182 (2006).

[77] Akopian, N. *et al.* Entangled photon pairs from semiconductor quantum dots. *Phys. Rev. Lett.* **96**, 130501 (2006).

[78] Bayer, M. *et al.* Fine structure of neutral and charged excitons in self-assembled In(Ga)As/(Al)GaAs quantum dots. *Phys. Rev. B* **65**, 195315 (2002).

[79] Stevenson, R. M. *et al.* Evolution of Entanglement Between Distinguishable Light States. *Phys. Rev. Lett.* **101**, 170501 (2008).

[80] Tartakovskii, A. *Quantum dots: optics, electron transport and future applications* (Cambridge University Press, 2012).

[81] Dusanowski, Ł. *et al.* Single-photon emission of InAs/InP quantum dashes at 1.55 μ m and temperatures up to 80 K. *Appl. Phys. Lett.* **108**, 163108 (2016).

[82] Young, R. J. *et al.* Inversion of exciton level splitting in quantum dots. *Phys. Rev. B* **72**, 113305 (2005).

[83] Felle, M. *et al.* Interference with a quantum dot single-photon source and a laser at telecom wavelength. *Appl. Phys. Lett.* **107**, 131106 (2015).

[84] Felle, M. *Telecom Wavelength Quantum Devices.* Ph.D. thesis, University of Cambridge (2017).

[85] Portalupi, S. L., Jetter, M. & Michler, P. InAs quantum dots grown on metamorphic buffers as non-classical light sources at telecom C-band: a review. *Semicond. Sci. Technol.* **34**, 053001 (2019).

[86] Kors, A., Reithmaier, J. P. & Benyoucef, M. Telecom wavelength single quantum dots with very small excitonic fine-structure splitting. *Appl. Phys. Lett.* **112**, 172102 (2018).

[87] Benyoucef, M., Yacob, M., Reithmaier, J. P., Kettler, J. & Michler, P. Telecom-wavelength (1.5 μm) single-photon emission from InP-based quantum dots. *Appl. Phys. Lett.* **103**, 162101 (2013).

[88] Gurioli, M., Wang, Z., Rastelli, A., Kuroda, T. & Sanguinetti, S. Droplet epitaxy of semiconductor nanostructures for quantum photonic devices. *Nat. Mater.* **18**, 799–810 (2019).

[89] Liu, X. *et al.* Vanishing fine-structure splittings in telecommunication-wavelength quantum dots grown on (111)A surfaces by droplet epitaxy. *Phys. Rev. B* **90**, 081301 (2014).

[90] Skiba-Szymanska, J. *et al.* Universal Growth Scheme for Quantum Dots with Low Fine-Structure Splitting at Various Emission Wavelengths. *Phys. Rev. Appl.* **8**, 014013 (2017).

[91] Yamamoto, Y., Santori, C. & Pelton, M. Regulated and entangled photons from a single quantum dot. *Phys. Rev. Lett.* **84**, 2513–2516 (2000).

[92] Santori, C., Fattal, D., Pelton, M., Solomon, G. S. & Yamamoto, Y. Polarization-correlated photon pairs from a single quantum dot. *Phys. Rev. B* **66**, 1–4 (2002).

[93] Fafard, S., Wasilewski, Z., McCaffrey, J., Raymond, S. & Charbonneau, S. InAs self-assembled quantum dots on InP by molecular beam epitaxy. *Appl. Phys. Lett.* **68**, 991–993 (1996).

[94] Takemoto, K., Sakuma, Y., Hirose, S., Usuki, T. & Yokoyama, N. Observation of Exciton Transition in 1.3-1.55 μm Band from Single InAs/InP Quantum Dots in Mesa Structure. *Jpn. J. Appl. Phys.* **43**, L349–L351 (2004).

[95] Takemoto, K. *et al.* An optical horn structure for single-photon source using quantum dots at telecommunication wavelength a. *J. Appl. Phys.* **101**, 81720 (2007).

[96] Yacob, M., Reithmaier, J. P. & Benyoucef, M. Low-density InP-based quantum dots emitting around the 1.5 μ m telecom wavelength range. *Appl. Phys. Lett.* **104**, 022113 (2014).

[97] Gong, M. *et al.* Electronic structure of self-assembled In As/ In P quantum dots: Comparison with self-assembled In As/ Ga As quantum dots. *Phys. Rev. B* **77**, 45326 (2008).

[98] Marchand, H. *et al.* Metalorganic vapor phase epitaxy of coherent self-assembled InAs nanometer-sized islands in InP(001). *Appl. Phys. Lett.* **71**, 527–529 (1997).

[99] Müller, T. *et al.* A quantum light-emitting diode for the standard telecom window around 1,550 nm. *Nat. Commun.* **9**, 1–6 (2018).

[100] Ellis, D. J., Bennett, A. J., Shields, A. J., Atkinson, P. & Ritchie, D. A. Electrically addressing a single self-assembled quantum dot. *Appl. Phys. Lett.* **88**, 133509 (2006).

[101] Stevenson, R. M. *et al.* Quantum teleportation of laser-generated photons with an entangled-light-emitting diode. *Nat. Commun.* **4**, 2859 (2013).

[102] Bennett, A. J. *et al.* Single-photon-emitting diodes: A review. *Phys. Status Solidi* **243**, 3730–3740 (2006).

[103] Boretti, A., Rosa, L., Mackie, A. & Castelletto, S. Electrically Driven Quantum Light Sources. *Adv. Opt. Mater.* **3**, 1012–1033 (2015).

[104] Lochmann, A. *et al.* Electrically pumped, micro-cavity based single photon source driven at 1GHz. *Electron. Lett.* **45**, 566–567 (2009).

[105] Hargart, F. *et al.* Electrically driven quantum dot single-photon source at 2 GHz excitation repetition rate with ultra-low emission time jitter. *Appl. Phys. Lett.* **102**, 011126 (2013).

[106] Schlehahn, A. *et al.* An electrically driven cavity-enhanced source of indistinguishable photons with 61% overall efficiency. *APL Photonics* **1**, 011301 (2016).

[107] Mizuochi, N. *et al.* Electrically driven single-photon source at room temperature in diamond. *Nat. Photonics* **6**, 299–303 (2012).

[108] Deshpande, S. & Bhattacharya, P. An electrically driven quantum dot-in-nanowire visible single photon source operating up to 150 K. *Appl. Phys. Lett.* **103**, 241117 (2013).

[109] Lin, X. *et al.* Electrically-driven single-photon sources based on colloidal quantum dots with near-optimal antibunching at room temperature. *Nat. Commun.* **8**, 1132 (2017).

[110] Ward, M. B. *et al.* Electrically driven telecommunication wavelength single-photon source. *Appl. Phys. Lett.* **90**, 063512 (2007).

[111] Miyazawa, T. *et al.* Exciton dynamics in current-injected single quantum dot at 1.55 μm. *Appl. Phys. Lett.* **92**, 161104 (2008).

[112] Varnava, C. *Quantum dot-based Entangled-Light Emitting Diodes (E-LED) for quantum relays.* Ph.D. thesis, University of Cambridge (2018).

[113] Chen, Z. B. *et al.* Preferential nucleation and growth of InAs/GaAs(0 0 1) quantum dots on defected sites by droplet epitaxy. *Scr. Mater.* **69**, 638–641 (2013).

[114] Costantini, G., Manzano, C., Songmuang, R., Schmidt, O. G. & Kern, K. InAs/GaAs(001) quantum dots close to thermodynamic equilibrium. *Appl. Phys. Lett.* **82**, 3194–3196 (2003).

[115] Davanço, M., Hellberg, C. S., Ates, S., Badolato, A. & Srinivasan, K. Multiple time scale blinking in InAs quantum dot single-photon sources. *Phys. Rev. B* **89**, 161303 (2014).

[116] Berthelot, A. *et al.* Unconventional motional narrowing in the optical spectrum of a semiconductor quantum dot. *Nat. Phys.* **2**, 759–764 (2006).

[117] Kuhlmann, A. V. *et al.* Charge noise and spin noise in a semiconductor quantum device. *Nat. Phys.* **9**, 570–575 (2013).

[118] Goldstein, D. H. *Polarized light: Third edition* (CRC Press, 2017).

[119] Wang, S. *et al.* 2 GHz clock quantum key distribution over 260 km of standard telecom fiber. *Opt. Lett.* **37**, 1008 (2012).

[120] Boaron, A. *et al.* Simple 2.5 GHz time-bin quantum key distribution. *Appl. Phys. Lett.* **112**, 171108 (2018).

[121] Legero, T., Wilk, T., Kuhn, A. & Rempe, G. Time-resolved two-photon quantum interference. In *Appl. Phys. B Lasers Opt.*, vol. 77, 797–802 (2003).

[122] Kammerer, C. *et al.* Interferometric correlation spectroscopy in single quantum dots. *Appl. Phys. Lett.* **81**, 2737–2739 (2002).

[123] Zwiller, V., Aichele, T. & Benson, O. Single-photon Fourier spectroscopy of excitons and biexcitons in single quantum dots. *Phys. Rev. B* **69**, 165307 (2004).

[124] Adachi, S., Yatsu, N., Kaji, R., Muto, S. & Sasakura, H. Decoherence of exciton complexes in single InAlAs quantum dots measured by Fourier spectroscopy. *Appl. Phys. Lett.* **91**, 161910 (2007).

[125] Loudon, R. *The Quantum Theory of Light* (OUP Oxford, 2000).

[126] Gold, P. *et al.* Two-photon interference from remote quantum dots with inhomogeneously broadened linewidths. *Phys. Rev. B* **89**, 35313 (2014).

[127] Paul, M. *et al.* Single-photon emission at 1.55 μ m from MOVPE-grown InAs quantum dots on InGaAs/GaAs metamorphic buffers. *Appl. Phys. Lett.* **111**, 033102 (2017).

[128] Carmesin, C. *et al.* Structural and optical properties of InAs/(In)GaAs/GaAs quantum dots with single-photon emission in the telecom C-band up to 77 K. *Phys. Rev. B* **98**, 125407 (2018).

[129] Zeuner, K. D. *et al.* A stable wavelength-tunable triggered source of single photons and cascaded photon pairs at the telecom C-band. *Appl. Phys. Lett.* **112**, 173102 (2018).

[130] Birowosuto, M. D. *et al.* Fast Purcell-enhanced single photon source in 1,550-nm telecom band from a resonant quantum dot-cavity coupling. *Sci. Rep.* **2**, 321 (2012).

[131] Ha, N. *et al.* Single photon emission from droplet epitaxial quantum dots in the standard telecom window around a wavelength of 1.55 μm. *Appl. Phys. Express* **13**, 025002 (2020).

[132] Musiał, A. *et al.* High-Purity Triggered Single-Photon Emission from Symmetric Single InAs/InP Quantum Dots around the Telecom C-Band Window. *Adv. Quantum Technol.* **3**, 1900082 (2020).

[133] Xiang, Z. H. *et al.* Long-term transmission of entangled photons from a single quantum dot over deployed fiber. *Sci. Rep.* **9**, 1–6 (2019).

[134] Xiang, Z.-H. *et al.* A tuneable telecom wavelength entangled light emitting diode deployed in an installed fibre network. *Commun. Phys.* **3**, 121 (2020).

[135] Grundmann, M. & Bimberg, D. Theory of random population for quantum dots. *Phys. Rev. B* **55**, 9740–9745 (1997).

[136] Sk, G., Musiał, A., Podemski, P. & Misiewicz, J. On the applicability of a few level rate equation model to the determination of exciton versus biexciton kinetics in quasi-zero-dimensional structures. *J. Appl. Phys.* **108**, 033507 (2010).

[137] Rodt, S., Schliwa, A., Pötschke, K., Guffarth, F. & Bimberg, D. Correlation of structural and few-particle properties of self-organized InAs GaAs quantum dots. *Phys. Rev. B* **71**, 155325 (2005).

[138] Lelong, P. & Bastard, G. Binding energies of excitons and charged excitons in GaAs/Ga(In)As quantum dots. *Solid State Commun.* **98**, 819–823 (1996).

[139] Cade, N. I. *et al.* Charged exciton emission at 1.3 μm from single InAs quantum dots grown by metalorganic chemical vapor deposition. *Appl. Phys. Lett.* **87**, 1–3 (2005).

[140] Löbl, M. C. *et al.* Excitons in InGaAs quantum dots without electron wetting layer states. *Commun. Phys.* **2**, 1–7 (2019).

[141] Favero, I. *et al.* Acoustic phonon sidebands in the emission line of single InAs/GaAs quantum dots. *Phys. Rev. B* **68**, 233301 (2003).

[142] Takagahara, T. Theory of exciton dephasing in semiconductor quantum dots. *Phys. Rev. B* **60**, 2638–2652 (1999).

[143] Krummheuer, B., Axt, V. M. & Kuhn, T. Theory of pure dephasing and the resulting absorption line shape in semiconductor quantum dots. *Phys. Rev. B* **65**, 1–12 (2002).

[144] Schlehahn, A. *et al.* A stand-alone fiber-coupled single-photon source. *Sci. Rep.* **8**, 1340 (2018).

[145] Musiał, A. *et al.* Plug&Play Fiber-Coupled 73 kHz Single-Photon Source Operating in the Telecom O-Band. *Adv. Quantum Technol.* **3**, 2000018 (2020).

[146] Besombes, L., Kheng, K., Marsal, L. & Mariette, H. Acoustic phonon broadening mechanism in single quantum dot emission. *Phys. Rev. B* **63**, 155307 (2001).

[147] Baier, M. H., Malko, A., Pelucchi, E., Oberli, D. Y. & Kapon, E. Quantum-dot exciton dynamics probed by photon-correlation spectroscopy. *Phys. Rev. B* **73**, 205321 (2006).

[148] Sallen, G. *et al.* Exciton dynamics of a single quantum dot embedded in a nanowire. *Phys. Rev. B* **80**, 085310 (2009).

[149] Rezai, M., Wrachtrup, J. & Gerhardt, I. Coherence Properties of Molecular Single Photons for Quantum Networks. *Phys. Rev. X* **8**, 031026 (2018).

[150] Gottesman, D., Hoi-Kwonglo, L. O., Lütkenhaus, N. & Preskill, J. Security of quantum key distribution with imperfect devices. *Quantum Inf. Comput.* **4**, 325–360 (2004).

[151] Waks, E. *et al.* Secure communication: Quantum cryptography with a photon turnstile. *Nature* **420**, 762 (2002).

[152] Michler, P. *et al.* A quantum dot single-photon turnstile device. *Science* **290**, 2282–2285 (2000).

[153] Santori, C., Pelton, M., Solomon, G., Dale, Y. & Yamamoto, Y. Triggered single photons from a quantum dot. *Phys. Rev. Lett.* **86**, 1502–1505 (2001).

[154] Yuan, Z. L., Kardynal, B. E., Sharpe, A. W. & Shields, A. J. High speed single photon detection in the near infrared. *Appl. Phys. Lett.* **91**, 041114 (2007).

[155] Yuan, Z. L., Dixon, A. R., Dynes, J. F., Sharpe, A. W. & Shields, A. J. Gigahertz quantum key distribution with InGaAs avalanche photodiodes. *Appl. Phys. Lett.* **92**, 201104 (2008).

[156] Jöns, K. D. *et al.* Bright nanoscale source of deterministic entangled photon pairs violating Bell's inequality. *Sci. Rep.* **7**, 1–11 (2017).

[157] Kitson, S. C., Jonsson, P., Rarity, J. G. & Tapster, P. R. Intensity fluctuation spectroscopy of small numbers of dye molecules in a microcavity. *Phys. Rev. A* **58**, 620–627 (1998).

[158] Takemoto, K. *et al.* Transmission experiment of quantum keys over 50km using high-performance quantum-dot single-photon source at 1.5μm wavelength. *Appl. Phys. Express* **3**, 092802 (2010).

[159] Heindel, T. *et al.* Quantum key distribution using quantum dot single-photon emitting diodes in the red and near infrared spectral range. *New J. Phys.* **14**, 083001 (2012).

[160] Takemoto, K. *et al.* Quantum key distribution over 120km using ultrahigh purity single-photon source and superconducting single-photon detectors. *Sci. Rep.* **5**, 14383 (2015).

[161] Kupko, T. *et al.* Tools for the performance optimization of single-photon quantum key distribution. *npj Quantum Inf.* **6**, 1–8 (2020).

[162] Sasakura, H. *et al.* Longitudinal and transverse exciton-spin relaxation in a single InAsP quantum dot embedded inside a standing InP nanowire using photoluminescence spectroscopy. *Phys. Rev. B* **85**, 075324 (2012).

[163] Favero, I. *et al.* Temperature dependence of the zero-phonon linewidth in quantum dots: An effect of the fluctuating environment. *Phys. Rev. B* **75**, 73308 (2007).

[164] Patel, R. B. *et al.* Postselective Two-Photon Interference from a Continuous Nonclassical Stream of Photons Emitted by a Quantum Dot. *Phys. Rev. Lett.* **100**, 207405 (2008).

[165] Nawrath, C. *et al.* Coherence and indistinguishability of highly pure single photons from non-resonantly and resonantly excited telecom C-band quantum dots. *Appl. Phys. Lett.* **115**, 023103 (2019).

[166] Bennett, A. J. *et al.* Cavity-enhanced coherent light scattering from a quantum dot. *Sci. Adv.* **2**, e1501256 (2016).

[167] Tighineanu, P. *et al.* Decay dynamics and exciton localization in large GaAs quantum dots grown by droplet epitaxy. *Phys. Rev. B* **88**, 155320 (2013).

[168] Dekel, E. *et al.* Cascade evolution and radiative recombination of quantum dot multiexcitons studied by time-resolved spectroscopy. *Phys. Rev. B* **62**, 11038–11045 (2000).

[169] Narvaez, G. A., Bester, G., Franceschetti, A. & Zunger, A. Excitonic exchange effects on the radiative decay time of monoexcitons and biexcitons in quantum dots. *Phys. Rev. B - Condens. Matter Mater. Phys.* **74**, 205422 (2006).

[170] Huber, T. *et al.* Measurement and modification of biexciton-exciton time correlations. *Opt. Express* **21**, 9890 (2013).

[171] Schöll, E. *et al.* The crux of using the cascaded emission of a 3-level quantum ladder system to generate indistinguishable photons. *arXiv Prepr. arXiv2006.05476* (2020).

[172] Simon, C. & Poizat, J. P. Creating single time-bin-entangled photon pairs. *Phys. Rev. Lett.* **94**, 030502 (2005).

[173] Kamada, H. & Kutsuwa, T. Broadening of single quantum dot exciton luminescence spectra due to interaction with randomly fluctuating environmental charges. *Phys. Rev. B* **78**, 155324 (2008).

[174] Lee, J. P. *et al.* Electrically driven and electrically tunable quantum light sources. *Appl. Phys. Lett.* **110**, 071102 (2017).

[175] Kuhlmann, A. V. *et al.* Transform-limited single photons from a single quantum dot. *Nat. Commun.* **6**, 1–6 (2015).

[176] Zadeh, I. E. *et al.* Deterministic Integration of Single Photon Sources in Silicon Based Photonic Circuits. *Nano Lett.* **16**, 2289–2294 (2016).

[177] Kim, J. H. *et al.* Hybrid Integration of Solid-State Quantum Emitters on a Silicon Photonic Chip. *Nano Lett.* **17**, 7394–7400 (2017).

[178] Beugnon, J. *et al.* Quantum interference between two single photons emitted by independently trapped atoms. *Nature* **440**, 779–782 (2006).

[179] Maunz, P. *et al.* Quantum interference of photon pairs from two remote trapped atomic ions. *Nat. Phys.* **3**, 538–541 (2007).

[180] Lettow, R. *et al.* Quantum interference of tunably indistinguishable photons from remote organic molecules. *Phys. Rev. Lett.* **104**, 123605 (2010).

[181] De Riedmatten, H., Marcikic, I., Tittel, W., Zbinden, H. & Gisin, N. Quantum interference with photon pairs created in spatially separated sources. *Phys. Rev. A* **67**, 5 (2003).

[182] Prabhakar, S. *et al.* Two-photon quantum interference and entanglement at 2.1 μm. *Sci. Adv.* **6**, 5195–5222 (2020).

[183] Rosenfeld, L. M. *et al.* Mid-infrared quantum optics in silicon. *Opt. Express* **28**, 37092 (2020).

[184] Varoutsis, S. *et al.* Restoration of photon indistinguishability in the emission of a semiconductor quantum dot. *Phys. Rev. B* **72**, 041303 (2005).

[185] Wang, H. *et al.* Towards optimal single-photon sources from polarized microcavities. *Nat. Photonics* **13**, 770–775 (2019).

[186] Wang, H. *et al.* Near-Transform-Limited Single Photons from an Efficient Solid-State Quantum Emitter. *Phys. Rev. Lett.* **116**, 213601 (2016).

[187] Ollivier, H. *et al.* Reproducibility of High-Performance Quantum Dot Single-Photon Sources. *ACS Photonics* **7**, 1050–1059 (2020).

[188] Huber, D. *et al.* Highly indistinguishable and strongly entangled photons from symmetric GaAs quantum dots. *Nat. Commun.* **8**, 15506 (2017).

[189] Liu, J. *et al.* A solid-state source of strongly entangled photon pairs with high brightness and indistinguishability. *Nat. Nanotechnol.* **14**, 586–593 (2019).

[190] Wang, H. *et al.* On-Demand Semiconductor Source of Entangled Photons Which Simultaneously Has High Fidelity, Efficiency, and Indistinguishability. *Phys. Rev. Lett.* **122**, 113602 (2019).

[191] Weber, J. H. *et al.* Two-photon interference in the telecom C-band after frequency conversion of photons from remote quantum emitters. *Nat. Nanotechnol.* **14**, 23–26 (2019).

[192] Kim, J.-H., Cai, T., Richardson, C. J. K., Leavitt, R. P. & Waks, E. Two-photon interference from a bright single-photon source at telecom wavelengths. *Optica* **3**, 577 (2016).

[193] Bylander, J., Robert-Philip, I. & Abram, I. Interference and correlation of two independent photons. *Eur. Phys. J. D* **22**, 295–301 (2003).

[194] Lydersen, L., Makarov, V. & Skaar, J. Secure gated detection scheme for quantum cryptography. *Phys. Rev. A* **83**, 032306 (2011).

[195] Reimer, M. E. *et al.* Overcoming power broadening of the quantum dot emission in a pure wurtzite nanowire. *Phys. Rev. B* **93**, 195316 (2016).

[196] Legero, T., Wilk, T., Hennrich, M., Rempe, G. & Kuhn, A. Quantum beat of two single photons. *Phys. Rev. Lett.* **93**, 070503 (2004).

[197] Patel, R. B. *et al.* Quantum interference of electrically generated single photons from a quantum dot. *Nanotechnology* **21**, 274011 (2010).

[198] Bennett, A. J., Patel, R. B., Nicoll, C. A., Ritchie, D. A. & Shields, A. J. Interference of dissimilar photon sources. *Nat. Phys.* **5**, 715–717 (2009).

[199] Huwer, J. *et al.* Quantum-dot-based telecommunication-wavelength quantum relay. *Phys. Rev. Appl.* **8**, 024007 (2017).

[200] Zeuner, K. D. *et al.* On-demand generation of entangled photon pairs in the telecom C-band for fiber-based quantum networks. *arXiv Prepr. arXiv1912.04782* (2019).

[201] Yang, J. *et al.* Quantum dot-based broadband optical antenna for efficient extraction of single photons in the telecom O-band. *Opt. Express* **28**, 19457 (2020).

[202] Fattal, D. *et al.* Entanglement Formation and Violation of Bell's Inequality with a Semiconductor Single Photon Source. *Phys. Rev. Lett.* **92**, 4 (2004).

[203] Kuroda, T. *et al.* Symmetric quantum dots as efficient sources of highly entangled photons: Violation of Bell's inequality without spectral and temporal filtering. *Phys. Rev. B* **88**, 041306 (2013).

[204] Fognini, A. *et al.* Dephasing Free Photon Entanglement with a Quantum Dot. *ACS Photonics* **6**, 1656–1663 (2019).

[205] Keil, R. *et al.* Solid-state ensemble of highly entangled photon sources at rubidium atomic transitions. *Nat. Commun.* **8**, 15501 (2017).

[206] Stevenson, R. M., Bennett, A. J. & Shields, A. J. Electrically operated entangled light sources based on quantum dots. In *Quantum Dots Opt. Electron Transp. Futur. Appl.*, vol. 9781107012, 319–340 (Cambridge University Press, 2012).

[207] Zhang, J. *et al.* High yield and ultrafast sources of electrically triggered entangled-photon pairs based on strain-tunable quantum dots. *Nat. Commun.* **6**, 1–8 (2015).

[208] Ward, M. *et al.* Coherent dynamics of a telecom-wavelength entangled photon source. *Nat. Commun.* **5**, 3316 (2014).

[209] Olbrich, F. *et al.* Polarization-entangled photons from an InGaAs-based quantum dot emitting in the telecom C-band. *Appl. Phys. Lett.* **111**, 133106 (2017).

[210] Ekert, A. K. Quantum cryptography based on Bell's theorem. *Phys. Rev. Lett.* **67**, 661–663 (1991).

[211] Hudson, A. J. *et al.* Coherence of an Entangled Exciton-Photon State. *Phys. Rev. Lett.* **99**, 266802 (2007).

[212] Stievater, T. H. *et al.* Measurement of relaxation between polarization eigenstates in single quantum dots. *Appl. Phys. Lett.* **81**, 4251–4253 (2002).

[213] Ulrich, S. M., Strauf, S., Michler, P., Bacher, G. & Forchel, A. Triggered polarization-correlated photon pairs from a single CdSe quantum dot. *Appl. Phys. Lett.* **83**, 1848–1850 (2003).

[214] Trotta, R., Wildmann, J. S., Zallo, E., Schmidt, O. G. & Rastelli, A. Highly entangled photons from hybrid piezoelectric-semiconductor quantum dot devices. *Nano Lett.* **14**, 3439–3444 (2014).

[215] Fognini, A., Ahmadi, A., Daley, S. J., Reimer, M. E. & Zwiller, V. Universal fine-structure eraser for quantum dots. *Opt. Express* **26**, 24487 (2018).

[216] Zeeshan, M., Sherlekar, N., Ahmadi, A., Williams, R. L. & Reimer, M. E. Proposed Scheme to Generate Bright Entangled Photon Pairs by Application of a Quadrupole Field to a Single Quantum Dot. *Phys. Rev. Lett.* **122**, 227401 (2019).

[217] Blackwood, E., Snelling, M. J., Harley, R. T., Andrews, S. R. & Foxon, C. T. Exchange interaction of excitons in GaAs heterostructures. *Phys. Rev. B* **50**, 14246–14254 (1994).

[218] Akimov, I. A., Hundt, A., Flissikowski, T. & Henneberger, F. Fine structure of the trion triplet state in a single self-assembled semiconductor quantum dot. *Appl. Phys. Lett.* **81**, 4730–4732 (2003).

[219] Akimov, I. A., Kavokin, K. V., Hundt, A. & Henneberger, F. Electron-hole exchange interaction in a negatively charged quantum dot. *Phys. Rev. B* **71**, 075326 (2005).

[220] Stevenson, R. M. *et al.* Magnetic-field-induced reduction of the exciton polarization splitting in InAs quantum dots. *Phys. Rev. B* **73**, 033306 (2006).

[221] Khaetskii, A. V., Loss, D. & Glazman, L. Electron spin decoherence in quantum dots due to interaction with nuclei. *Phys. Rev. Lett.* **88**, 1868021–1868024 (2002).

[222] Sallen, G. *et al.* Nuclear magnetization in gallium arsenide quantum dots at zero magnetic field. *Nat. Commun.* **5**, 1–7 (2014).

[223] Seguin, R. *et al.* Size-dependent fine-structure splitting in self-organized InAs/GaAs quantum dots. *Phys. Rev. Lett.* **95**, 257402 (2005).

[224] Young, R. J. *et al.* Entangled photons from the biexciton cascade of quantum dots. *J. Appl. Phys.* **101**, 081711 (2007).

[225] James, D. F., Kwiat, P. G., Munro, W. J. & White, A. G. Measurement of qubits. *Phys. Rev. A* **64**, 15 (2001).

[226] Wootters, W. K. Entanglement of formation of an arbitrary state of two qubits. *Phys. Rev. Lett.* **80**, 2245–2248 (1998).

[227] Reindl, M. *et al.* All-photonic quantum teleportation using on-demand solid-state quantum emitters. *Sci. Adv.* **4**, eaau1255 (2018).

[228] Rickert, L., Kupko, T., Rodt, S., Reitzenstein, S. & Heindel, T. Optimized designs for telecom-wavelength quantum light sources based on hybrid circular Bragg gratings. *Opt. Express* **27**, 36824 (2019).

[229] de Riedmatten, H. *et al.* Long Distance Quantum Teleportation in a Quantum Relay Configuration. *Phys. Rev. Lett.* **92**, 4 (2004).

[230] Jin, X. M. *et al.* Experimental free-space quantum teleportation. *Nat. Photonics* **4**, 376–381 (2010).

[231] Valivarthi, R. *et al.* Quantum teleportation across a metropolitan fibre network. *Nat. Photonics* **10**, 676–680 (2016).

[232] Metcalf, B. J. *et al.* Quantum teleportation on a photonic chip. *Nat. Photonics* **8**, 770–774 (2014).

[233] Bruß, D. Optimal eavesdropping in quantum cryptography with six states. *Phys. Rev. Lett.* **81**, 3018–3021 (1998).

[234] Chau, H. F. Practical scheme to share a secret key through a quantum channel with a 27.6% bit error rate. *Phys. Rev. A* **66**, 060302 (2002).

[235] Brendel, J., Gisin, N., Tittel, W. & Zbinden, H. Pulsed energy-time entangled twin-photon source for quantum communication. *Phys. Rev. Lett.* **82**, 2594–2597 (1999).

[236] Dynes, J. F. *et al.* Efficient entanglement distribution over 200 kilometers. *Opt. Express* **17**, 11440 (2009).

[237] Lee, J. P. *et al.* Controllable Photonic Time-Bin Qubits from a Quantum Dot. *Phys. Rev. X* **8**, 021078 (2018).

[238] Pathak, P. K. & Hughes, S. Coherent generation of time-bin entangled photon pairs using the biexciton cascade and cavity-assisted piecewise adiabatic passage. *Phys. Rev. B* **83**, 245301 (2011).

[239] Jayakumar, H. *et al.* Time-bin entangled photons from a quantum dot. *Nat. Commun.* **5**, 4251 (2014).

[240] Huber, T. *et al.* Coherence and degree of time-bin entanglement from quantum dots. *Phys. Rev. B* **93**, 201301 (2016).

[241] Sanaka, K., Kawahara, K. & Kuga, T. Experimental probabilistic manipulation of down-converted photon pairs using unbalanced interferometers. *Phys. Rev. A* **66**, 4 (2002).

[242] Versteegh, M. A. *et al.* Single pairs of time-bin-entangled photons. *Phys. Rev. A* **92**, 033802 (2015).